Noninvasive Thrombolysis Using Histotripsy Pulsed Ultrasound Cavitation Therapy

by

Adam D. Maxwell

A dissertation submitted in partial fulfillment
of the requirements for the degree of
Doctor of Philosophy
(Biomedical Engineering)
in The University of Michigan
2012

Doctoral Committee:

Assistant Professor Zhen Xu, Chair
Professor Charles A. Cain
Professor J. Brian Fowlkes
Associate Professor Hitinder S. Gurm

To my wife, Jessie, who has shown me unconditional love and patience during my many years as a student, and to my parents, Doug and Leanne, who have always encouraged my passion for learning and supported me in all of my endeavors.

Acknowledgments

I would like first and foremost to express my gratitude to my advisor, Zhen, whose patient guidance has helped me continually improve as a researcher over the past years. Her curiosity and enthusiasm for our research has made this work as enjoyable and interesting today as when I first began, and I appreciate the freedom that she gave me to explore so many facets of histotripsy. I'd also like to thank the other members of my committee, who provided me with feedback and suggestions during my many projects. Charles' ability to turn observations and problems in experiments into features has taken many of these projects in new, exciting directions. I've benefitted greatly from discussions with Brian on my observations of cavitation in my experiments and the mechanisms behind histotripsy. Hitinder has provided valuable insight on the clinical relevance of these experiments and much needed guidance on translating the technology towards clinical use.

I would also like to thank the other members of the histotripsy lab: Tim, Tzu-Yin, Yohan, Ryan, Alex, Kuang-Wei, Simone, Eli, and Steven for all of their help and for creating such a wonderful working environment which promotes respect and teamwork. I've greatly appreciated the group's willingness to help out me and each other, whether it's devising experiments, assembling a transducer, or mopping up one of the 'floods' in the lab. Thanks to Alex Chiao as well, for giving me the opportunity to act as a mentor and learn from it.

Thanks to Gabe for his continual dedication to the thrombolysis project, and to Kim for putting up with our many long days. I also appreciate the help of the Radiology group for their advice with experimental setups, particularly the high-speed camera. I would like to thank Will for letting me observe many of your experiments and learn from them. Additionally, thanks to those around UM who've given me technical advice and been willing to fill in the many gaps in my knowledge: Professors Jim Grotberg, Ben Vaughan, Dan Myers and Eric Johnsen.

There are also several people outside of the University who have provided me with additional support. The Histosonics team has given me as a student the rare opportunity to observe and participate in another side of this research, and see first-hand how we might one day translate this work to clinical practice. I would like to also thank Mike Bailey and many others in CIMU at University of Washington, for introducing me to the world of therapeutic ultrasound and for their continued collaboration and friendship during my years at Michigan. Many thanks as well to my friends here in Michigan and back in Washington who have checked in with me from time to time. It has been great motivation just to share my progress with you. Thanks to all of my family, especially my parents, who have shown similar interest in my graduate career and have often kept me from losing sight of the big picture. Finally, I'd like to say how fortunate and grateful I am to have my wife, Jessie, who has always given me her love and support throughout the challenges I've faced as a graduate student.

Table of Contents

List of Figures

List of Tables

CHAPTER 1

Introduction

This dissertation addresses several aspects of histotripsy pulsed ultrasound cavitation therapy and its prospective application as a noninvasive method of thrombolysis. The research is separated primarily into two categories: investigations of the physical mechanisms of histotripsy and the development of histotripsy technology to optimally treat instances of thrombosis. While these studies have shown promising results for this application, additional work in this area is needed to demonstrate its long-term safety and efficacy prior to clinical implementation.

1.1 Thrombosis

Several diseases prevalent in the western world are commonly the result of the pathologic formation of a blood clot in the vasculature (thrombosis). In the United States, such cardiovascular diseases are estimated to account for greater than 35% of all deaths annually[1]. These ailments are exacerbated by the population's increasingly sedentary lifestyle, incidence of obesity, smoking, diabetes, and other risk factors in the western world[2]. Additionally, vascular diseases of this nature are becoming increasingly common in developing

countries[3]. Based on these trends, it is likely that problems associated with thrombosis will continue to present themselves in a large number of individuals.

Depending on the site of the thrombus and its occupation of the vessel cross-section, thrombotic events can range in severity from asymptomatic to fatal. Myocardial infarction[4] and ischemic stroke[5, 6] are the result of clots in the coronary and cerebral arteries respectively, and are considered the most severe forms of thrombosis. Myocardial infarction has a case fatality rate between 10-20%, and ischemic stroke can be fatal 20%-50% of the time depending on a number of risk factors[1]. Pulmonary embolism (PE)[7] (large clots in the major vessels of the lungs) can also be fatal and often goes undiagnosed even though the case fatality rate is thought to be similar to myocardial infarction and stroke[8, 9]. The source of emboli in PE can often be clots in the veins of the legs, a condition called deep vein thrombosis (DVT)[10]. DVT can cause swelling and pain in the legs or may generate no symptoms at all, and is usually not treated aggressively unless there is a strong possibility of PE. The estimated number of new DVT cases each year is approximately 300,000, and likely over 1,000,000 including recurrent and undiagnosed instances[11, 12]. The number of mortalities, high cost of treatments, and overall prevalence of these diseases make it highly desirable to develop treatments which are more effective with fewer side effects.

There are multiple pathways to the formation of clots. Clotting is a beneficial response to vascular injury to prevent continuous bleeding. However, nonideal conditions in the blood or surrounding vessel can cause clotting in the lumen of the vessel, obstructing blood flow. Three broad categories for causes of thrombosis are (i) alteration in blood flow, (ii) changes in the constitution of blood, and (iii) injury to the vascular endothelium. These conditions are known as Virchow's triad[13]. Different diseases are affected predominantly by different underlying causes. For instance, buildup of atherosclerotic plaque in the

coronary arteries is commonly observed postmortem in victims of myocardial infarction. While this stenotic material may result in an alteration of blood flow [14], it is most commonly thought that the rupture of an atheroma, and the subsequent introduction of a large concentration of lipids locally triggers the coagulation cascade and thrombus formation, causing complete obstruction [15, 16]. However, increased blood flow through the vessel due to physical exertion can cause shear stress and be the primary triggering event for such plaque rupture[17]. Ischemic stroke can result from a similar formation of a cardiac clot which dislodges (an embolus) and flows to the cerebral vasculature, occluding a smaller artery[18]. Most forms of venous thrombosis appear to be precipitated by multiple simultaneous factors[19]. Generally, the patient may have an underlying propensity for coagulation, either by vessel injury, genetic factors, or enhanced expression of procoagulants by another disease such as cancer. However, a clot often forms only with an additional acute stimulating factor, such as long-term blood stasis caused by inactivity or vascular trauma[20]. Clot formation is thus a more complex interplay between the three criteria of Virchow's triad rather than a simple occurrence of one condition.

Clots can progress quickly or slowly depending on their site and cause of formation. When serious risks are present, such as the cases of myocardial infarction or stroke, it can be only a matter of hours before treatment is administered. The clot composition in these situations is red blood cells, fibrin, platelets and inflammatory cells, either intermixed or in striations[21]. However, long term insufficiency of blood flow causes reorganization of the clot structure, and differentiation between the clot and vessel wall becomes difficult. After several weeks or months, the entire vessel lumen can become occupied with fibrotic hyperplasia, and newly developed microvasculature can occur[22, 23]. Clots such as those in deep vein thrombosis can be asymptomatic for extended periods

and may not be diagnosed until after remodeling of the vessel wall occurs. Older clots in particular are more similar in stiffness to the surrounding soft tissue. Characterization of a thrombus age can contribute significantly to planning the course of treatment[24]. Ultrasound has been found to be a good method to evaluate clot stiffness and age, by B-Mode imaging or elastography and strain imaging [25-27].

1.2 Current Thrombolysis Techniques

Depending on the location, severity, and age of thrombosis, several current treatment options are utilized, including anticoagulant therapy [28], thrombolytic drugs[29], or percutaneous catheter-based mechanical thrombectomy[30], direct surgical thrombectomy[31], or combinations thereof. Anticoagulants such as heparin and warfarin are used in cases where rapid clot dissolution is not necessary, as is common practice with many instances of DVT[32]. This treatment does not actively cause thrombolysis by rather relies on the body's natural fibrinolytic system to eliminate the clot, and often does not achieve recanalization of the afflicted vessel, even after several months[33]. Additionally, these drugs increase the risk of serious bleeding during their administration[34]. Because chronic DVTs are often fibrotic tissue rather than fibrin clots, these cannot be recanalized by anticoagulant therapy, and clinicians often opt for oral anticoagulation by drugs such as warfarin to simply prevent further proliferation provided the patient's symptoms are manageable or asymptomatic.

Thrombolytic drugs (e.g. t-Pa, streptokinase, urokinase, and anistreplase) actively dissolve clots by inducing fibrinolytic activity. These agents are specific to breaking down certain components of a thrombus, and are thus not effective in all cases[35, 36]. In particular, clots which are primarily composed of platelets do

not respond as completely as those composed of fibrin[35]. Thrombolytic agents present greater risks of bleeding than anticoagulants due to their breakdown of fibrin structures (including those for repair of injury in the vessel wall). These drugs are most successful when applied within a few hours after an acute event, after which, the risks of administration are considered to outweigh its benefits[37]. Because of these limitations, thrombolytics are only indicated in a small percentage of the population who can tolerate the risk of bleeding and present immediately (which studies have shown to be as low as 16% of cases) [38, 39]. Thus, these drugs cannot always be adopted as a first line of treatment. Catheters may be used to administer the drug locally to minimize the risk of bleeding outside of the treatment zone[40]. However, even with directed thrombolysis, bleeding risks are still significant – a multicenter study of treating DVT with this method found severe bleeding (necessitating blood transfusion) occurred in 11% of treatments[40].

An alternative to drug-based thrombolysis is the use of catheter-based mechanical thrombectomy devices, which have become more accepted in recent years as a minimally-invasive and effective method of treatment for all types of thrombi. Several devices with different mechanisms of action are available[30], relying on use of mechanical or hydraulic forces to actively fragment the clot into small particles and aspiration to remove these particles. However, catheters are invasive and also carry a risk of bleeding, as well as vascular injury or perforation, hemolysis, and infection [41]. Because of these limitations, there is a great need for safer, more effective treatments.

The ability of ultrasound to augment both catheter-based thrombectomy and thrombolytic drugs has been acknowledged for several decades [42-44]. Trubestein et al. were first to incorporate ultrasound into such a treatment, with the introduction of a 20 kHz vibrating guide-wire as a catheter-based thrombectomy device in 1976[42]. Since then, ultrasound has been combined with currently

existing thrombolysis techniques or even used as a standalone procedure in treating clots. Starting with Kudo in 1989, several groups demonstrated *in-vitro* that ultrasound enhanced the rate of clot dissolution by tPa[45-47]. Many studies since then have focused on the synergistic effect of drugs with low-intensity ultrasound. For example, one *in-vitro* study found a reduction in average lysis time from 3 hours to 30 minutes has been achieved for combined ultrasound + rt-PA therapy compared with just rt-PA alone[48]. Delivery methods include the systemic administration of drugs and transcutaneous ultrasound or catheter-based ultrasound/drug delivery. A further beneficial effect appears to be the combined use of microbubble contrast agents with the drugs and ultrasound[49]. The interaction of ultrasound with the microbubbles can cause streaming of the blood, increasing convective delivery of the drug to the clot and enhancing its dissolution. Several catheter-based thrombectomy systems have incorporated ultrasound through a guidewire, although the benefit provided by these appears less appreciable[50].

Some preliminary studies have also shown that high-intensity focused ultrasound pulses can induce very rapid clot breakdown without administration of fibrinolytics[51-53]. Compared with drugs, which can require several hours to achieve reperfusion[54, 55], these techniques may destroy clots within a few minutes[53]. In thrombolysis procedures, rapid recanalization is highly desirable to preserve the function of the afflicted organs[56, 57]. For instance, myocardium shows signs of necrosis and permanent loss of function within a few hours of an ischemic event[58]. Thus, a rapid, noninvasive thrombolysis technique using focused ultrasound has the potential to combine the locality of catheter-based procedures and noninvasive characteristics of pharmaceuticals, while increasing the safety and reducing the side effects of the treatment to improve the clinical outcome. The purpose of the work in this dissertation was to investigate one

such noninvasive ultrasound modality which can potentially achieve rapid clot dissolution, called 'histotripsy'.

1.3 Histotripsy Ultrasound Therapy

Histotripsy is a relatively new technology which uses short, high-amplitude, focused ultrasound pulses to noninvasively cause targeted fractionation of soft tissues. Although tissue ablation with ultrasound has been investigated for the last 70 years[59-61], most of this work has utilized heat generated by ultrasound attenuation to thermally denature tissues. While this method has been successful in treating several diseases, it cannot be used for thrombolysis, because it leaves the mechanical structure of the tissue intact. Histotripsy, on the other hand, uses acoustic cavitation generated at the focus to mechanically break apart the tissue structure and in many cases completely liquefy it into subcellular components[62]. Histotripsy has been demonstrated to debulk several soft tissue structures, for treatment of benign prostate hyperplasia (BPH)[63], kidney tumors[64], and hypoplastic left heart syndrome (HLHS)[65], leaving a void or hole in the tissue filled with liquid. The rapid fractionation of tissue and characteristically small debris in the homogenate make histotripsy a potentially strong candidate for eliminating clots as well.

The large tensile pressure generated at the focus causes a cloud of acoustic cavitation bubbles to form above certain thresholds, which creates localized stress in the tissue and mechanical breakdown without significant heat deposition. Several studies have shown strong correlation between this cavitation cloud and tissue disruption[66, 67], and at pressure levels where cavitation is not generated, minimal effect is observed on the tissue at the focus. This cavitation is observed only at pressure levels significantly greater than those

which define the inertial cavitation threshold in water for similar pulse durations[68, 69], on the order of 10-20 MPa peak negative pressure. However, the mechanisms of how cavitation clouds form and how cavitation interacts with tissue have not been fully understood. The first part of this dissertation is dedicated to investigating these relations, and examining the necessary acoustic conditions for cavitation and associated tissue breakdown.

Histotripsy can be performed in two modalities depending on the location of the bubble cloud with respect to the target tissue. In the first technique, cavitation is directly generated within the tissue, inducing a liquefaction of the medium[70]. An example of this is the treatment of BPH, where a volume of tissue in the middle of the prostate is targeted to destroy it. Alternatively, cavitation can be generated in a fluid at an interface with a solid tissue, which causes an erosion of this adjacent layer[69]. This method is beneficial in treating HLHS, where a hole in the atrial septum of the heart can be created by generating a cavitation cloud in the blood in the atrium next to the septum. These two methods use significantly different acoustic parameters to generate optimal tissue breakdown in each case[71, 72]. However, both of these methods may be useful for inducing thrombolysis depending on the morphology of the treated clots.

Histotripsy is performed noninvasively by coupling a focused transducer to the skin of the patient and transmitting the acoustic pulses transcutaneously through the overlying tissue to the focal zone. Because the surgeon does not have optical access to the target, real-time ultrasound imaging is used to align the focus with the target tissue, monitor the treatment progression, and determine the treatment outcome. The bubble cloud generated by histotripsy is visible as a highly-dynamic, echogenic region on a B-Mode ultrasound image, allowing confirmation of accurate targeting prior to treatment. Meanwhile, the fractionated tissue shows a reduction in echogenicity compared with intact

tissue, which can be used to evaluate progression of treatment[73, 74]. Both Hall et al[73] and Wang et al[75] found an approximately 10-fold decrease in backscatter amplitude of imaged homogenized tissue vs. untreated tissue *in-vitro*. In vascular applications, clots can similarly be detected based on echogenicity[27] and may show a B-mode amplitude reduction upon treatment. Doppler ultrasound may also provide feedback on the thrombus location and extent, and confirm restoration of flow after thrombolysis. These capabilities to efficiently fractionate tissue and monitor therapy using image-guided real-time feedback are primary motivations to explore histotripsy as a potential noninvasive thrombolysis method.

1.4 Organization of the Dissertation

In the first chapters, the physical mechanisms of histotripsy are explored to understand how cavitation clouds form and the interaction of cavitation bubbles with cells and tissue to cause their disruption. In Chapter 2, a novel mechanism by which cavitation clouds form in response to shocked ultrasound pulses is described. In Chapter 3, the intrinsic pressure thresholds for achieving cloud cavitation are measured. Chapter 4 describes the development of a tissue phantom allowing direct visualization of cavitation clouds and fractionated cell damage in histotripsy. In the following chapters, the clinical potential for histotripsy thrombolysis is evaluated and new technologies are developed specifically for this application. Chapter 5 presents *in-vitro* experiments which evaluate histotripsy's efficacy and address potential safety concerns in performing thrombolysis. Chapter 6 introduces a noninvasive technique for capturing and destroying blood clot emboli, which may further enhance the safety of histotripsy thrombolysis. In Chapter 7, the design and fabrication of

transducers for histotripsy thrombolysis *in-vivo* are described. Chapter 8 presents an *in-vivo* study demonstrating the feasibility of histotripsy thrombolysis in a porcine model of deep-vein thrombosis, as well as evaluations of the prototype transducers *in-vivo*. Finally, Chapter 9 summarizes this work and provides suggestions for future research into histotripsy thrombolysis and its mechanisms.

1.5 References

1. Lloyd-Jones D, Adams R, Carnethon M, De Simone G, Ferguson TB, Flegal K, Ford E, Furie K, Go A, Greenlund K, Haase N, Hailpern S, Ho M, Howard V, Kissela B, Kittner S, Lackland D, Lisabeth L, Marelli A, McDermott M, Meigs J, Mozaffarian D, Nichol G, O'Donnell C, Roger V, Rosamond W, Sacco R, Sorlie P, Stafford R, Steinberger J, Thom T, Wasserthiel-Smoller S, Wong N, Wylie-Rosett J, Hong Y. Heart disease and stroke statistics--2009 update: A report from the American Heart Association Statistics Committee and Stroke Statistics Subcommittee. Circulation. 2009;119:480-486

2. Yusuf S, Hawken S, Ounpuu S, Dans T, Avezum A, Lanas F, McQueen M, Budaj A, Pais P, Varigos J, Lisheng L. Effect of potentially modifiable risk factors associated with myocardial infarction in 52 countries (the interheart study): Case-control study. Lancet. 2004;364:937-952

3. Reddy KS. India wakes up to the threat of cardiovascular diseases. J. Am. Coll. Cardiol. 2007;50:1370-1372

4. Fuster V. Mechanisms leading to myocardial infarction: Insights from studies of vascular biology. Circulation. 1994;90:2126-2146

5. Lees KR. Management of acute stroke. Lancet Neurol. 2002;1:41-50

6. Lavados PM, Hennis AJ, Fernandes JG, Medina MT, Legetic B, Hoppe A, Sacks C, Jadue L, Salinas R. Stroke epidemiology, prevention, and management strategies at a regional level: Latin america and the caribbean. Lancet Neurol. 2007;6:362-372

7. Kucher N, Rossi E, De Rosa M, Goldhaber SZ. Massive pulmonary embolism. Circulation. 2006;113:577-582

8. Giuntini C, Di Ricco G, Marini C, Melillo E, Palla A. Epidemiology. Chest. 1995;107:3S-9S

9. Goldhaber SZ, Elliott CG. Acute pulmonary embolism: Part I. Circulation. 2003;108:2726-2729

10. Lopez JA, Kearon C, Lee AYY. Deep venous thrombosis. Hematology. 2004;2004:439-456

11. Heit JA. The epidemiology of venous thromboembolism in the community. Arterioscler. Thromb. Vasc. Biol. 2008;28:370-372

12. Goldhaber SZ, Fanikos J. Prevention of deep vein thrombosis and pulmonary embolism. Circulation. 2004;110:e445-e447

13. Brotman DJ, Deitcher SR, Lip GYH, Matzdorff AC. Virchow's triad revisited. South. Med. J. 2004;97

14. Ku DN. Blood flow in arteries. Ann. Rev. Fluid Mech. 1997;29:399-434

15. Erling F. Coronary thrombosis: Pathogenesis and clinical manifestations. Am. J. Cardiol. 1991;68:B28-B35

16. Rauch U, Osende JI, Fuster V, Badimon JJ, Fayad Z, Chesebro JH. Thrombus formation on atherosclerotic plaques: Pathogenesis and clinical consequences. Ann. Intern. Med. 2001;134:224-238

17. Willich SN, Lewis M, Lowel H, Arntz H-R, Schubert F, Schroder R. Physical exertion as a trigger of acute myocardial infarction. N. Engl. J. Med. 1993;329:1684-1690

18. Rana BS, Monaghan MJ, Ring L, Shapiro LS, Nihoyannopoulos P. The pivotal role of echocardiography in cardiac sources of embolism. Euro. J. Echocardiography. 2011;12:i25-i31

19. Rosendaal FR. Venous thrombosis: A multicausal disease. Lancet. 1999;353:1167-1173

20. Kyrle PA, Eichinger S. Deep vein thrombosis. Lancet. 2005;365:1163-1174

21. Marder VJ, Chute DJ, Starkman S, Abolian AM, Kidwell C, Liebeskind D, Ovbiagele B, Vinuela F, Duckwiler G, Jahan R, Vespa PM, Selco S, Rajajee V, Kim D, Sanossian N, Saver JL. Analysis of thrombi retrieved from cerebral arteries of patients with acute ischemic stroke. Stroke. 2006;37:2086-2093

22. Fineschi V, Turillazzi E, Neri M, Pomara C, Riezzo I. Histological age determination of venous thrombosis: A neglected forensic task in fatal pulmonary thrombo-embolism. Forensic Sci. Int. 2009;186:22-28

23. Bonderman D, Jakowitsch J, Redwan B, Bergmeister H, Renner M-K, Panzenböck H, Adlbrecht C, Georgopoulos A, Klepetko W, Kneussl M, Lang IM. Role for staphylococci in misguided thrombus resolution of chronic thromboembolic pulmonary hypertension. Arterioscler. Thromb. Vasc. Biol. 2008;28:678-684

24. Buller HR, Agnelli G, Hull RD, Hyers TM, Prins MH, Raskob GE. Antithrombotic therapy for venous thromboembolic disease: The seventh accp conference on antithrombotic and thrombolytic therapy. Chest. 2004;126:401S-428S

25. Xie H, Kim K, Aglyamov SR, Emelianov SY, Chen X, O'Donnell M, Weitzel WF, Wrobleski SK, Myers DD, Wakefield TW, Rubin JM. Staging deep venous thrombosis using ultrasound elasticity imaging: Animal model. Ultrasound Med Biol. 2004;30:1385-1396

26. Emelianov SY, Chen X, O'Donnell M, Knipp B, Myers D, Wakefield TW, Rubin JM. Triplex ultrasound: Elasticity imaging to age deep venous thrombosis. Ultrasound Med Biol. 2002;28:757-767

27. Fowlkes JB, Strieter RM, Downing LJ, Brown SL, Saluja A, Salles-Cunha S, Kadell AM, Wrobleski SK, Wakefield TW. Ultrasound echogenicity in experimental venous thrombosis. Ultrasound Med Biol. 1998;24:1175-1182

28. Kearon C, Kahn SR, Agnelli G, Goldhaber S, Raskob GE, Comerota AJ. Antithrombotic therapy for venous thromboembolic disease: American college of chest physicians evidence-based clinical practice guidelines (8th edition). Chest. 2008;133:454S-545S

29. Goldenberg NA, Durham JD, Knapp-Clevenger R, Manco-Johnson MJ. A thrombolytic regimen for high-risk deep venous thrombosis may substantially reduce the risk of postthrombotic syndrome in children. Blood. 2007;110:45-53

30. Sharafuddin MJA, Hicks ME. Current status of percutaneous mechanical thrombectomy. Part ii. Devices and mechanisms of action. J. Vasc Interv. Radiol. 1998;9:15-31

31. Gutt CN, Oniu T, Wolkener Fdr, Mehrabi A, Mistry S, Buchler MW. Prophylaxis and treatment of deep vein thrombosis in general surgery. Am. J. Surg 2005;189:14-22

32. Bates SM, Ginsberg JS. Treatment of deep-vein thrombosis. N Engl J Med. 2004;351:268-277

33. Caprini JA, Arcelus JI, Reyna JJ, Motykie GD, Mohktee D, Zebala LP, Cohen EB. Deep vein thrombosis outcome and the level of oral anticoagulation therapy. J Vasc Surg. 1999;30:805-811

34. Singer OC, Humpich MC, Fiehler J, Albers GW, Lansberg MG, Kastrup A, Rovira A, Liebeskind DS, Gass A, Rosso C, Derex L, Kim JS, Neumann-Haefelin T. Risk for symptomatic intracerebral hemorrhage after thrombolysis assessed by diffusion-weighted magnetic resonance imaging. Ann Neurol. 2008;63:52-60

35. Jang IK, Gold HK, Ziskind AA, Fallon JT, Holt RE, Leinbach RC, May JW, Collen D. Differential sensitivity of erythrocyte-rich and platelet-rich arterial thrombi to lysis with recombinant tissue-type plasminogen activator. A possible explanation for resistance to coronary thrombolysis. Circulation. 1989;79:920-928

36. Molina CA, Montaner J, Arenillas JF, Ribo M, Rubiera M, Alvarez-Sabin J. Differential pattern of tissue plasminogen activator-induced proximal middle cerebral artery recanalization among stroke subtypes. Stroke. 2004;35:486-490

37. Tissue plasminogen activator for acute ischemic stroke. N. Engl. J. Med. 1995;333:1581-1588

38. Cragg DR, Friedman HZ, Bonema JD, Jaiyesimi IA, Ramos RG, Timmis GC, O'Neill WW, Schreiber TL. Outcome of patients with acute myocardial infarction who are ineligible for thrombolytic therapy. Ann Intern Med. 1991;115:173-177

39. Krumholz HM, Friesinger GC, Cook EF, Lee TH, Rouan GW, Goldman L. Relationship of age with eligibility for thrombolytic therapy and mortality

among patients with suspected acute myocardial infarction. J Am Geriatr Soc. 1994;42:127-131

40. Mewissen MW, Seabrook GR, Meissner MH, Cynamon J, Labropoulos N, Haughton SH. Catheter-directed thrombolysis for lower extremity deep venous thrombosis: Report of a national multicenter registry. Radiol. 1999;211:39-49

41. Sharafuddin MJ, Hicks ME. Current status of percutaneous mechanical thrombectomy. Part I. General principles. J Vasc Interv Radiol. 1997;8:911-921

42. Trubestein G, Engel C, Etzel F, Sobbe A, Cremer H, Stumpff U. Thrombolysis by ultrasound. Clin Sci Mol Med Suppl. 1976;3:697s-698s

43. Luo H, Steffen W, Cercek B, Arunasalam S, Maurer G, Siegel RJ. Enhancement of thrombolysis by external ultrasound. Am Heart J. 1993;125:1564-1569

44. Kaul S. Sonothrombolysis: A universally applicable and better way to treat acute myocardial infarction and stroke? Who is going to fund the research? Circulation. 2009;119:1358-1360

45. Tachibana K. Enhancement of fibrinolysis with ultrasound energy. J Vasc Interv Radiol. 1992;3:299-303

46. Hong AS, Chae J-S, Dubin SB, Lee S, Fishbein MC, Siegel RJ. Ultrasonic clot disruption: An in vitro study. Am. Heart J. 1990;120:418-422

47. Kudo S. Thrombolysis with ultrasound effect. Tokyo Jikeikai Med J. 1989;104:1005-1012

48. Siegel RJ, Atar S, Fishbein MC, Brasch AV, Peterson TM, Nagai T, Pal D, Nishioka T, Chae JS, Birnbaum Y, Zanelli C, Luo H. Noninvasive transcutaneous low frequency ultrasound enhances thrombolysis in peripheral and coronary arteries. Echocardiography. 2001;18:247-257

49. Andrei V A. Ultrasound enhanced thrombolysis for stroke. Seminars in Cerebrovasc. Dis. Stroke. 2005;5:106-110

50. Pfaffenberger S. Ultrasound thrombolysis. Thromb. haemost. 2005;94:26

51. Westermark S, Wiksell H, Elmqvist H, Hultenby K, Berglund H. Effect of externally applied focused acoustic energy on clot disruption in vitro. Clin. Sci. 1999;97:67-71

52. Rosenschein U, Yakubov SJ, Guberinich D, Bach DS, Sonda PL, Abrams GD, Topol EJ. Shock-wave thrombus ablation, a new method for noninvasive mechanical thrombolysis. Am. J. Cardiol. 1992;70:1358-1361

53. Rosenschein U, Furman V, Kerner E, Fabian I, Bernheim J, Eshel Y. Ultrasound imaging-guided noninvasive ultrasound thrombolysis: Preclinical results. Circulation. 2000;102:238-245

54. Alexandrov AV, Molina CA, Grotta JC, Garami Z, Ford SR, Alvarez-Sabin J, Montaner J, Saqqur M, Demchuk AM, Moye LA, Hill MD, Wojner AW. Ultrasound-enhanced systemic thrombolysis for acute ischemic stroke. N. Engl. J. Med. 2004;351:2170-2178

55. Brodie BR, Stuckey TD, Wall TC, Kissling G, Hansen CJ, Muncy DB, Weintraub RA, Kelly TA. Importance of time to reperfusion for 30-day and late survival and recovery of left ventricular function after primary angioplasty for acute myocardial infarction. J. Am. Coll. Cardiol. 1998;32:1312-1319

56. Christou I, Alexandrov AV, Burgin WS, Wojner AW, Felberg RA, Malkoff M, Grotta JC. Timing of recanalization after tissue plasminogen activator therapy determined by transcranial doppler correlates with clinical recovery from ischemic stroke. Stroke. 2000;31:1812-1816

57. Brodie BR, Stuckey TD, Wall TC, Kissling G, Hansen CJ, Muncy DB, Weintraub RA, Kelly TA. Importance of time to reperfusion for 30-day and late survival and recovery of left ventricular function after primary angioplasty for acute myocardial infarction. J Am Coll Cardiol. 1998;32:1312-1319

58. Tsao PS, Aoki N, Lefer DJ, Johnson G 3rd, Lefer AM. Time course of endothelial dysfunction and myocardial injury during myocardial ischemia and reperfusion in the cat. Circulation. 1990;82:1402-1412

59. Fry W, Mosberg W, Barnard J, Fry F. Production of focal destructive lesions in the central nervous system with ultrasound. J. Neurosurg. 1954;11:471-478

60. Kennedy JE, ter Haar GR, Cranston D. High intensity focused ultrasound: Surgery of the future? Brit. J. Radiol. 2003;76:590-599

61. Lynn JG, Zwemer RL, Chick AJ, Miller AE. A new method for the generation and use of focused ultrasound in experimental biology. J. Gen.Physiol. 1942;26:179-193

62. Xu Z, Fan Z, Hall TL, Winterroth F, Fowlkes JB, Cain CA. Size measurement of tissue debris particles generated from pulsed ultrasound cavitational therapy - histotripsy. Ultrasound Med. Biol. 2009;35:245-255

63. Hall TL, Hempel CR, Lake AM, Kieran K, Ives K, Fowlkes JB, Cain CA, Roberts WW. Histotripsy for the treatment of bph: Evaluation in a chronic canine model. IEEE Ultrasonics Symposium, 2008. 2008:765-767

64. Styn NR, Wheat JC, Hall TL, Roberts WW. Histotripsy of vx-2 tumor implanted in a renal rabbit model. J. Endourol. 2010;24:1145-1150

65. Xu Z, Owens G, Gordon D, Cain C, Ludomirsky A. Noninvasive creation of an atrial septal defect by histotripsy in a canine model. Circulation. 2010;121:742-749

66. Xu Z, Fowlkes JB, Rothman ED, Levin AM, Cain CA. Controlled ultrasound tissue erosion: The role of dynamic interaction between insonation and microbubble activity. J. Acoust. Soc. Am. 2005;117:424-435

67. Parsons JE, Cain CA, Fowlkes JB. Spatial variability in acoustic backscatter as an indicator of tissue homogenate production in pulsed cavitational ultrasound therapy. IEEE Trans Ultrason Ferroelectr Freq Control. 2007;54:576-590

68. Fowlkes JB, Crum LA. Cavitation threshold measurements for microsecond length pulses of ultrasound. J. Acoust. Soc. Am. 1988;83:2190-2201

69. Xu Z, Fowlkes JB, Ludomirsky A, Cain CA. Investigation of intensity thresholds for ultrasound tissue erosion. Ultrasound Med. Biol. 2005;31:1673-1682

70. Roberts WW, Hall TL, Ives K, Wolf JJS, Fowlkes JB, Cain CA. Pulsed cavitational ultrasound: A noninvasive technology for controlled tissue ablation (histotripsy) in the rabbit kidney. J. Urol. 2006;175:734-738

71. Parsons JE, Cain CA, Abrams GD, Fowlkes JB. Pulsed cavitational ultrasound therapy for controlled tissue homogenization. Ultrasound Med. Biol. 2006;32:115-129

72. Xu Z, Ludomirsky A, Eun LY, Hall TL, Tran BC, Fowlkes JB, Cain CA. Controlled ultrasound tissue erosion. IEEE Trans Ultrason Ferroelectr Freq Control. 2004;51:726-736

73. Hall TL, Fowlkes B, Cain CA. A real-time measure of cavitation induced tissue disruption by ultrasound imaging backscatter reduction. IEEE Trans Ultrason Ferroelectr Freq Control. 2007;54:569-575

74. Wang T-y, Xu Z, Winterroth F, Hall TL, Fowlkes JB, Rothman ED, Roberts WW, Cain CS. Quantitative ultrasound backscatter for pulsed cavitational ultrasound therapy-histotripsy. IEEE Trans Ultrason Ferroelectr Freq Control. 2009;56:995-1005

75. Wang TY, Xu Z, Winterroth F, Hall TL, Fowlkes JB, Rothman ED, Roberts WW, Cain CA. Quantitative image feedback for pulsed cavitational ultrasound therapy- histotripsy. IEEE Ultrasonics Symposium, 2008. 2008:867-870

CHAPTER 2

Cavitation Cloud Formation in Histotripsy

In this chapter, a physical mechanism for the formation of cavitating bubble clouds in histotripsy is hypothesized based on observations through high-speed imaging. A numerical model is employed to evaluate several features of this mechanism. The hypothesis is also tested through several experiments. Since tissue disruption in histotripsy is not observed without first initiating a bubble cloud, an understanding of how cavitation clouds form is of fundamental importance to designing effective therapy transducers and choosing appropriate pulsing strategies for histotripsy thrombolysis.

2.1 Cloud Cavitation in Focused Ultrasound

The cavitation cloud associated with histotripsy effects has only been observed at pressure excursions much greater than measured inertial cavitation thresholds for similar frequency and pulse lengths in water[1, 2]. A bubble cloud may be initiated during any pulse in a sequence of thousands of pulses[1], even if all incident pulses are identical. This observation is evidence that bubble cloud initiation is a probabilistic phenomenon. However, once a cloud is generated, it is

maintained by each pulse if the pulse repetition period is shorter than the time for the bubbles that make up the cloud to dissolve[3, 4].

Cloud cavitation at therapeutic ultrasound intensities has been observed in several forms in water, under conditions of both CW excitation[5-7] and lithotripsy shockwaves[8-11]. Cavitation clouds generated using focused ultrasound have been observed to form transiently in water with CW sonication at 2.5 MHz by Willard[6] and at 1 MHz by Neppiras and Coakley[7]. These transient events occurred when a heterogeneous bubble nucleus entered the focal region, causing it to explode into many bubbles which traveled as a cloud through the focal volume. Neppiras and Coakley proposed that surface waves on the bubbles cause their fragmentation into many smaller bubbles, which can then grow and each themselves fragment[7]. Pishchalnikov et al have also shown that bubble collapse after sonication can cause fracture and proliferation of bubbles in a cloud over several pulses[12].

Sankin and Teslenko[10] have also generated cavitation clouds in distilled water using a strong lithotripter shockwave, but within a single pulse. In their study, individual cavitation bubbles were apparent at low pressures, but cavitation clouds appeared consistently when a threshold of approximately 33 MPa peak negative pressure was exceeded[10, 13]. While it was found that cavitation clouds could be excited by direct action of the tensile tail of a shockwave, clouds were also observed to form by the reflection and inversion of the compressive shock from the water-air interface at the top of the tank. In an *in vivo* scenario, such cavitation may occur as a result of the reflection of strongly nonlinear waves from pre-existing gas bodies in tissues such as lung or intestine. Experimentally, Bailey *et al*.[14] found that isolated 1-MPa positive-pressure pulses caused equivalent hemorrhage as 1-MPa negative pressure pulses in tissue structures containing gas bodies. Church[15] proposed this could be due to cavitation activity

related to the reflection and inversion of the pulse from the gas body and that the true achievable negative pressure would be the peak-to-peak incident pressure.

Based on observations and experiments reported herein using high-speed photography, it is hypothesized that cavitation clouds in histotripsy evolve by reflection of a positive wave from single cavitation bubbles. Incidence of a shock front on a bubble within the central portion of the focus backscatters a negative-pressure pulse. This reflection incites cavitation proximal to the initial bubble, which produces a larger effective scattering surface for the next shock in the incident pulse. Thus, the process is self-reinforcing, being terminated only at the end of the pulse or when the cloud extends outside of the focus, where the pressure is too low to create sufficient scattering. Both the compressive and rarefaction phases of the wave, as well as the degree of nonlinear distortion, play a role in generating cavitation clouds under this mechanism.

In this chapter, the formation of bubble clouds observed during single pulses at the focus of a 1-MHz ultrasound transducer in a gelatin tissue-mimicking phantom using high-speed photography is described. The hypothesized mechanism of shock scattering is then evaluated by numerical models and three experiments. In the first experiment, we compare the region where bubble clouds form with the dimensions of the positive and negative pressure zones of the focus. In the second experiment, two transducers which produce the same peak negative focal pressure and frequency but different nonlinear waveform distortion are compared to evaluate their effect on producing clouds. In the third experiment, the shocks are acoustically filtered from the waveform while maintaining the same peak negative pressure to evaluate the importance of shock amplitude in generating clouds.

2.2 Observations of Cloud Formation by Shock Scattering

2.2.1 Methods: High Speed Photography

Bubble clouds were generated in tissue-mimicking phantoms composed of gelatin, which was chosen because of its high optical clarity for photography and similarity of its properties to those of soft tissue[16]. Type-A gelatin from porcine skin (G2500, Sigma-Aldrich, St. Louis, MO) and deionized water were combined at a ratio of 7 g gelatin per 100 mL water and then heated on a hot plate to melt the gelatin completely into solution. The mixture was placed in a degassing chamber at a vacuum of 74 kPa for 30 minutes. Next, the solution was carefully poured into a polycarbonate housing. The housing had one side open for ultrasound exposure and the opposite side had an acoustic window of 25-μm thickness polycarbonate. After all bubbles were skimmed from the surface of the molten gelatin, the phantom placed in refrigeration at 4^0C until solidified. Two hours prior to use, phantoms were submerged in degassed water at room temperature.

A high-speed framing camera (SIM 02, Specialised Imaging, Hertfordshire, UK) was used to observe bubble cloud formation at the focus of a histotripsy transducer during sonication. The camera is capable of capturing 16 frames at rates up to $2{\cdot}10^8$ frames per second (fps). Frame rates used in this study were between $5{\cdot}10^4 - 10^7$ fps. The transducer was a piezocomposite bowl of 10 cm aperture and 9 cm focal length (radius of curvature), with a 5 cm diameter concentric hole in the center (Imasonic, Voray sur l'Ognon, France). The working frequency was 1 MHz. The transducer was placed in a tank of filtered, degassed water at room temperature, attached to a 3-axis motorized positioning system. The transducer was driven by a class D amplifier with matching network

constructed in-house[17]. The tissue phantom was positioned such that the entire focus of the transducer was within the phantom. The camera was positioned to acquire axial-lateral images of the focal region of the transducer (Figure 2.1). Tominon macro-bellows lenses (Kyocera Optics, Nagano, Japan) were used to control magnification, focusing, and camera aperture. Images were backlit using one of two xenon flashlamps for either short-term or long-term exposure (IS 300 and ADA 500, Adapt Electronics, Hertsfordshire, UK). The flash lamp was coupled into a fiber optic bundle, whose output was passed through a convex lens to control the light beam diameter. This backlit shadowgraph method was used instead of front- or side-lighting in order to view ultrasound propagation and interaction with the cavitation, and to minimize the exposure time of the camera. The transducer was driven with a single pulse of 5 to 20 cycles duration and the camera recorded images as the pulse passed through the focal zone. For all experiments where the pressure levels are not explicitly specified in the results, each pulse had a peak positive/negative pressure of 85/19 MPa. Because cavitation damage changes the mechanical properties of the tissue phantom, the focus of the transducer was moved to a new location in the phantom for each pulse applied.

Ultrasound pressure waveforms were measured in degassed water using a fiber-optic hydrophone constructed in house[18]. The hydrophone's frequency response was calibrated by substitution comparison with a reference piezoelectric hydrophone (HGL-0085, Onda Corporation, Sunnyvale, CA). The measured waveforms were corrected using a deconvolution procedure to account for the frequency response of the hydrophone.

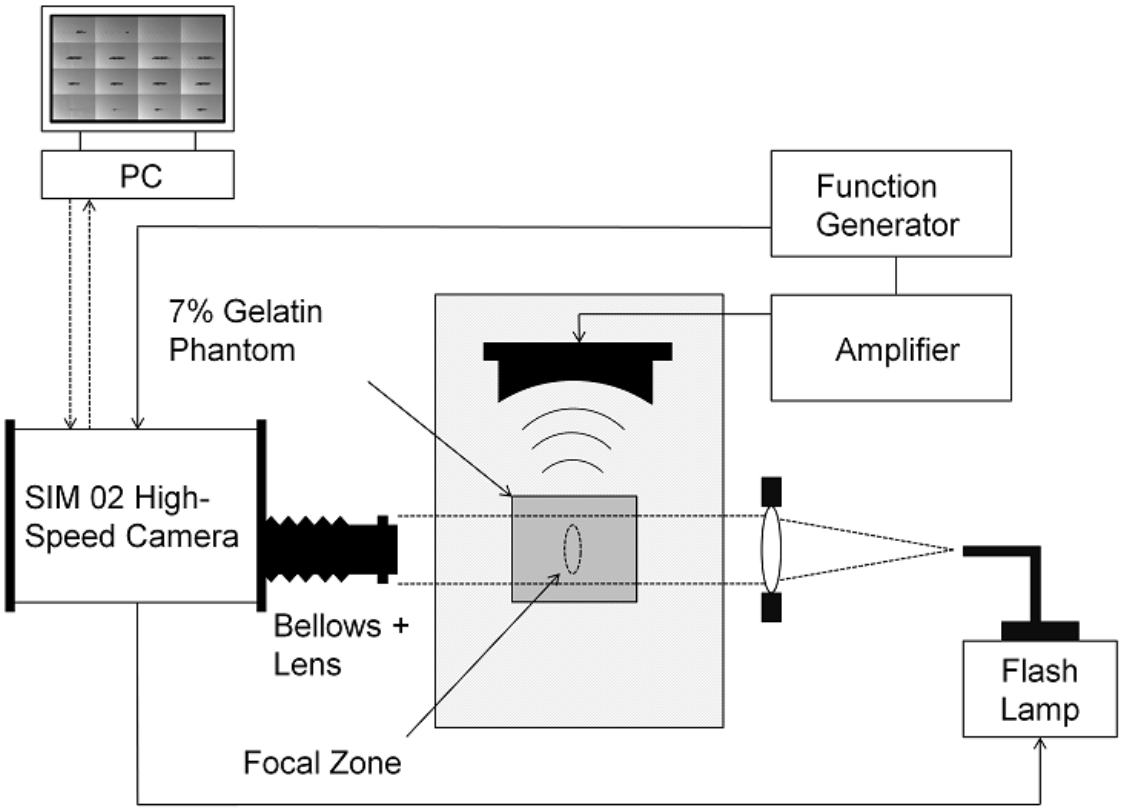

Figure 2.1. Apparatus for high-speed imaging of histotripsy bubble clouds. A fiber-coupled flash lamp was used to back-illuminate images captured by the camera. An ultrasound transducer placed in the water tank was focused into a gelatin-based tissue-mimicking phantom. The transducer was driven by a class D amplifier with matching circuit. A function generator was used to control the amplifier output and trigger the camera, which in turn triggered the flash lamp.

While the measurements were not recorded in the tissue phantom, they provide a good estimate of the focal pressure in the phantom, since the attenuation of the gelatin is low. Measurements were recorded with short pulses (3 cycles) to limit the potential for cavitation on the hydrophone and its confounding of the signal. It was found that the transducer output reached full amplitude by the third cycle, thus the peak pressure values recorded are the same for the longer pulses used in this study. The 3-cycle waveform is shown in Figure 2.2.

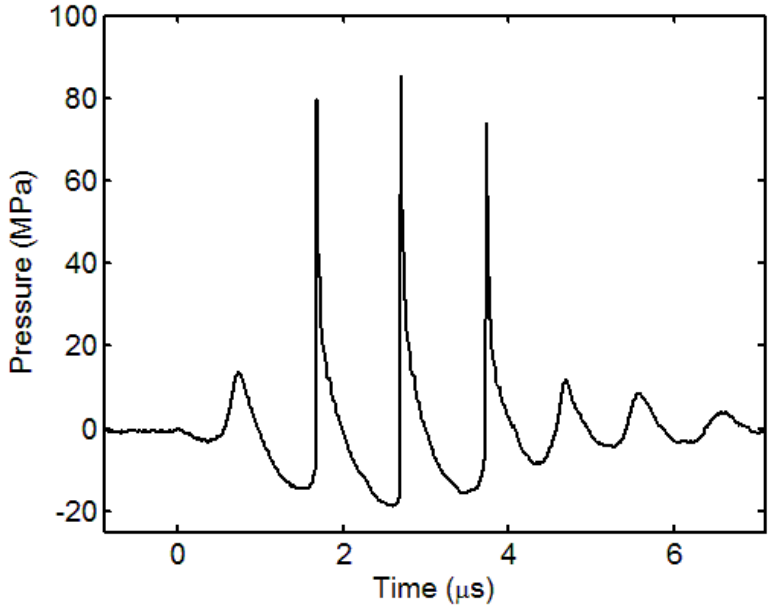

Figure 2.2. A 3-cycle focal pressure waveform of the histotripsy transducer used to generate bubble clouds. The waveforms are asymmetric with a larger positive-pressure excursion than negative-pressure excursion as a result of nonlinear acoustic propagation and diffraction. Pulse lengths of 5-20 cycles were used in this study for generating clouds.

2.2.2 Results: Cavitation Cloud Formation

Single cavitation bubbles were observed during all pulses, regardless of whether or not a bubble cloud formed. Single bubbles appeared in random positions throughout the focus. Bubbles would usually become visible within the first or second cycle of the pulse, growing and collapsing. During this time, collapses produced shockwaves radiating from the bubble which were visible by shadowgraph. After their first collapse, bubbles typically distorted with a flattened surface proximal to the transducer. Beyond the first 1-2 cycles, the bubbles remained at a relatively constant radius without collapsing and emitting radial shockwaves (Figure 2.3). Bubbles further distorted throughout the pulse, but the overall size remained approximately the same. Bubbles within the focus

grew to radii in the range of 40-90 μm, with a mean of 65 +/- 12 μm (n = 28). The minimum resolvable size for the camera system at this magnification was about 5 μm. This behavior of single bubbles in response to histotripsy pulses has also been observed previously in water[19].

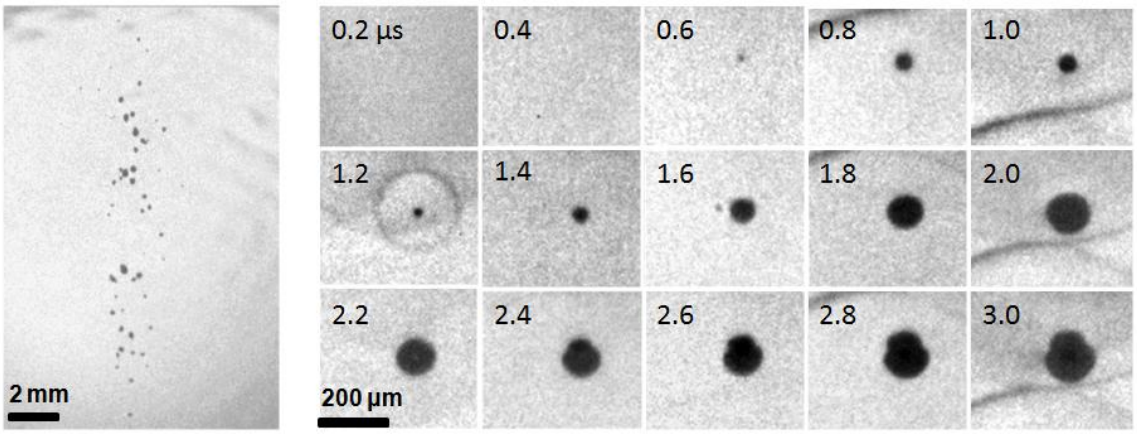

Figure 2.3. Single bubbles generated at the focus of a histotripsy transducer (top) and temporal behavior of an individual bubble during the first three cycles of a pulse (bottom). Ultrasound propagation was from left to right. Bubbles appeared in the initial cycles of the pulse, and underwent inertial collapse (an emitted shockwave is visible at t = 1.2 μs). However, bubbles did not continue to collapse during the later cycles, but instead deformed. Note, there is some small difference in the appearance and position of the shocks (dark lines) at t = 1.0, 2.0, and 3.0 μs due to transducer ring up and camera spatial jitter.

Bubble clouds consisted of dense clusters of bubbles that formed within the focus, distinct in morphology and much larger in size than single bubbles. Not all pulses created a bubble cloud. A bubble cloud did not start to form on the first cycle, but usually began forming within 3-4 cycles. Clouds initiated from a distal position within the focal volume and grew proximally, towards the transducer (Figure 2.4). Clouds grew at a nearly linear rate axially once they began to form during a pulse, but the lateral width remained constant throughout most of the pulse while the cloud was forming (Figure 2.5). As shown in Figure 2.5, the axial

growth rate was approximately 0.5 mm/μs (i.e. $\lambda/3$ per acoustic period). This growth pattern was different from that of single bubbles, which appeared in the proximal focus before the distal focus as the pulse propagated. After the pulse passed the focus, the bubble cloud continued to expand slightly and then disappeared after 50-200 μs, depending on size of the cloud. Bubble clouds created with a greater number of cycles in a pulse were longer in dimension along the acoustic axis, but nearly identical in lateral dimension (Figure 2.6). For instance, bubble clouds generated from a 5 cycle pulse extended 1.4 +/- 0.4 mm axially and 1.4 +/- 0.25 mm laterally, while clouds from a 20 cycle pulse were 4.8 +/- 1.1 mm axially and 1.8 mm +/- 0.2 mm laterally (n = 18). For longer pulses (15 – 20 cycles), multiple distinct clouds would occasionally form during a single pulse, separated axially within the focal region. There were two conditions under which cloud growth would terminate. The first was when the end of the pulse completely passed the focus (i.e. sonication was terminated). The second condition occurred when the cloud extended too far proximally, outside of the focal zone.

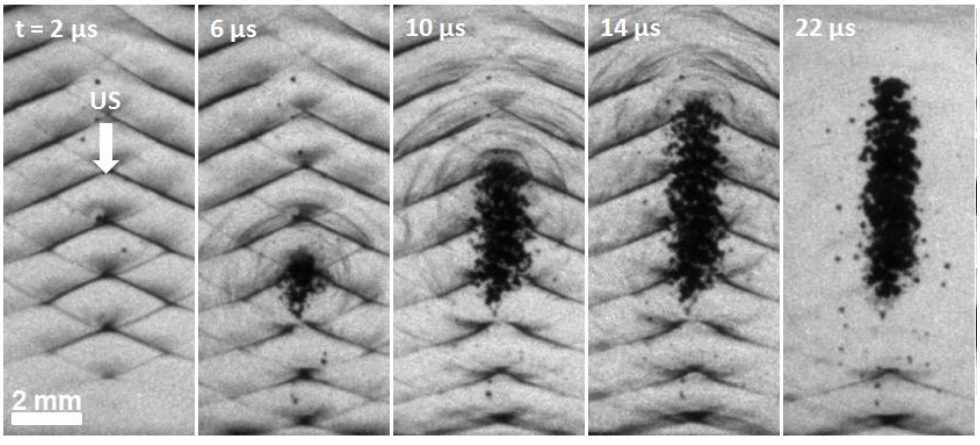

Figure 2.4. Growth of a bubble cloud at the focus during application of a 20-cycle pulse. Ultrasound propagation was from top to bottom. The cloud started from a distal location within the focal zone and grew towards the transducer along the acoustic axis. The dark lines in each frame are a shadowgraph pattern created by the shock fronts of each cycle of the wave.

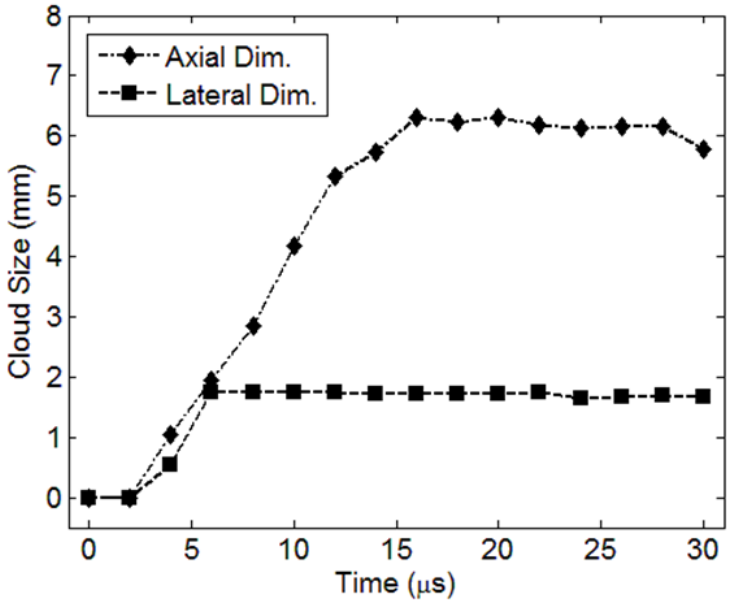

Figure 2.5. Plot of measured cloud dimensions vs. time for the photographic sequence in Figure 2.4. The cloud started to grow between t = 2 μs and 4 μs. The time when the final acoustic cycle passed the proximal end of the cloud (t = 16 μs) coincided with termination of cloud growth along the acoustic axis.

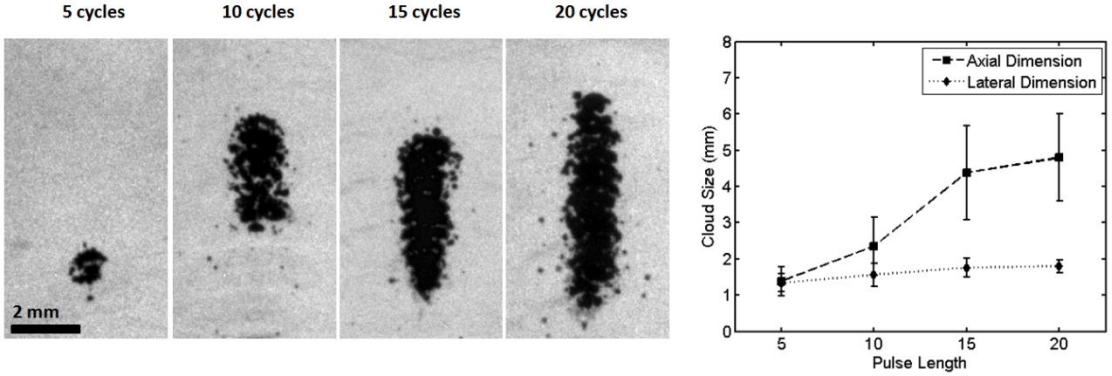

Figure 2.6. (Top) Typical size and shape of bubble clouds formed during 5, 10, 15, and 20 cycle pulses at 1 MHz. Ultrasound propagation was from top to bottom. All images have been aligned spatially relative to the focus. Note the widths of bubble clouds were similar, but the length increased with cycle number. (Bottom) Cloud dimensions vs. pulse length. The axial length of the cloud increased as the pulse length increased, but lateral size remained about the same.

Higher-magnification photographs of the initial formation of clouds revealed a relationship between the single bubbles formed at the beginning of the pulse and the cavitation clouds. Cavitation clouds were always observed to stem from a single bubble after a shock front of the wave impinged on the bubble (Figure 2.7). Following this event, a small cluster of cavitation appeared proximal to the bubble (cloud initiation). In Figure 2.7, the initial bubble cluster propagated behind the spherically diverging wave seen at t = 2.75 μs. Between t = 2.75 and 3.0 μs, the cloud grew about 360 μm along the acoustic axis and the cloud growth velocity during this period was calculated to be 1440 m/s, which was approximately the speed of sound in the medium. The scattered wave propagated at a similar velocity. Between t = 3.0 and 3.25 μs, the cloud grew by 0.110 μm, and did not grow between t = 3.25 and 3.5 μs. In the subsequent cycle, another cluster grew after the next shock front reached the first cluster. This process continued, with clusters of cavitation forming after each cycle. Although the average cloud growth rate as shown in Figure 2.5 was about 0.5 mm/μs, these results indicate that the cloud growth occurred in discrete steps with each cycle. The first cluster did not appear during the first cycle, but between cycles # 2-7, (mean 3.8 +/- 1.5 μs from the start of pulse, n = 35).

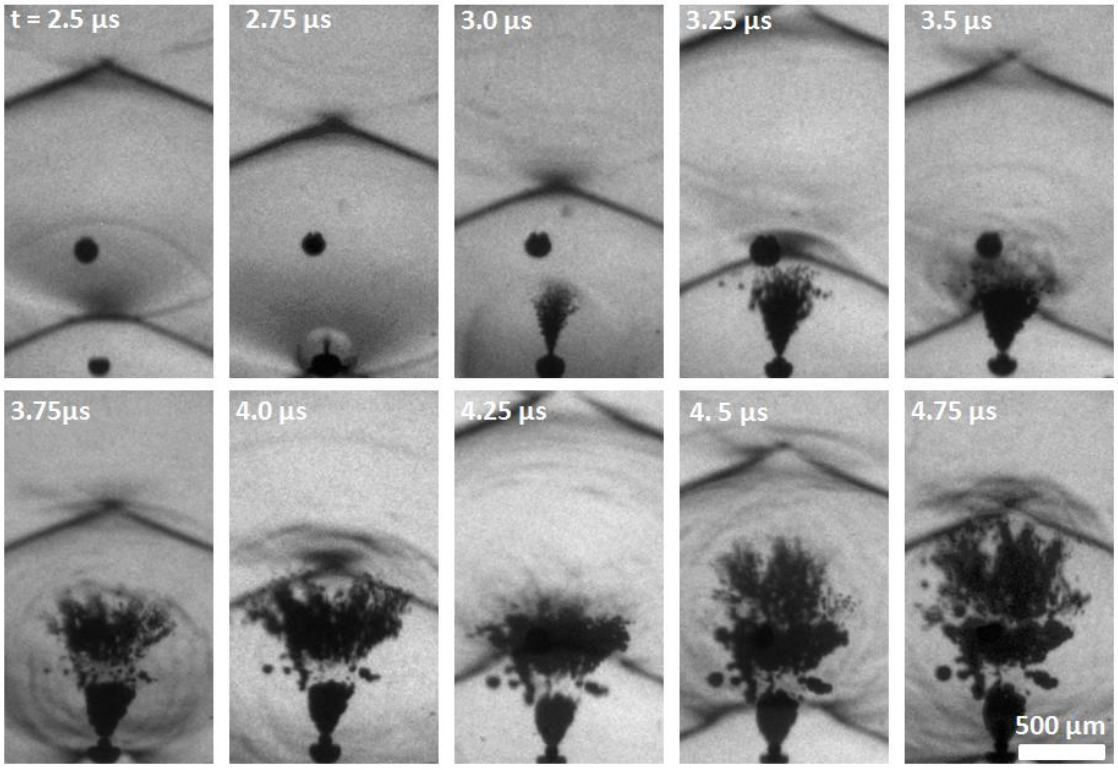

Figure 2.7. Initiation of a bubble cloud. Ultrasound propagation was from top to bottom. At t = 2.5 µs, a single bubble was present at the right side of the frame. After the shock impinged on the bubble (t = 2.75 µs), a spherical wave was visible, apparently scattered by the bubble. Over the next cycle, a cloud of bubbles stemmed from the center of the single bubble behind this scattered wave. A second cycle produced another section of the cloud between t = 3.5 µs and t = 4.0 µs, and a third section was produced between t = 4.25 µs and t = 4.75 µs. The timing in this figure corresponded to that in Figure 2.2 with the waveform at the position of the initial bubble.

2.3 Theoretical Evaluation of Shock Scattering Hypothesis

To evaluate the shock-scattering hypothesis and determine if a significant enhancement of tensile pressure is achieved in the presence of a scatterer, two models were employed to observe the transient and spatial characteristics of the interaction. High speed images often showed the single bubble from which the

cloud grows was deformed to a nearly hemispherical shape prior to cloud initiation (Figure 2.8), with the flattened surface facing the incident wave. This behavior of bubbles has also been predicted by numerical models in response to shock waves[20]. For weaker (less focused) transducers in particular, bubbles are almost always distorted prior to cloud initiation. Thus, models for both a spherical bubble and hemispherical bubble were used to examine the effects of waveform shape, bubble size, and bubble geometry on this scattering behavior and cloud formation.

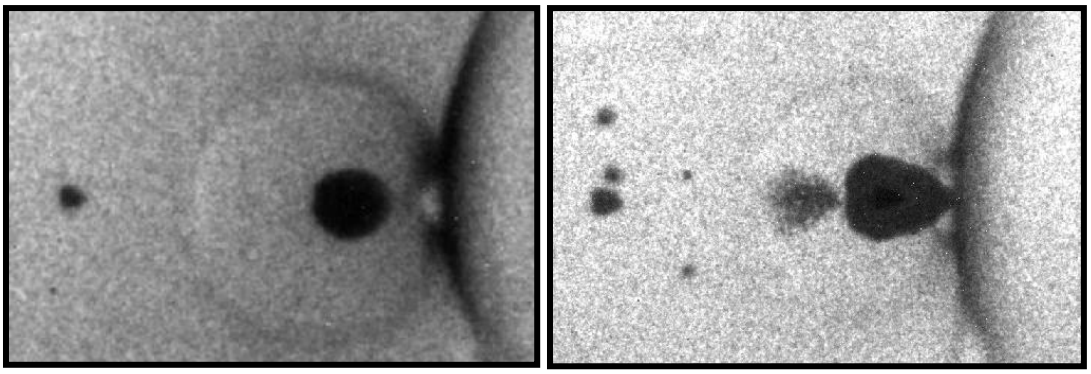

Figure 2.8. A spherical bubble (left) and flattened bubble (right). Cavitation clouds were observed to form behind both bubbles after these frames. Propagation of the incident wave is from left to right for these images.

2.3.1 Pulse Waveform

The focal pressure waveform for a histotripsy is a multi-cycle, nonlinear pulse. To simulate the incident wave on the surface of the bubble, an analytical model for a nonlinear pulse was applied [21]. Using this approach, a pulse with peak negative pressure of 20 MPa, peak positive pressure of 92 MPa, and rise time of 10 ns was created. These parameters are similar to the pulses used in section 2.2, which have been observed to produce cavitation clouds[22].

A nonlinear waveform was used to simulate the pressure profile[21]. This pressure pulse is given as

$$p_a(t) = p_f \sum_{m=1}^{\infty}\left[\frac{\sin\left(m\omega\left(t-\tau\right)+\phi\right)}{m+0.3}\right] \qquad 2.1$$

where p_f is the fundamental pressure amplitude, ω is the frequency, τ is chosen such that the start of the wave is at $p_a(0) = 0$, and φ is a phase shift to create waveform asymmetry. For this simulation, $\omega = 6.9 \times 10^6$ rad/s, $\tau = 1.25\ \pi / \omega$, and $\varphi = -\pi/4$. The infinite sum was truncated to $m = 100$. This gave a pressure profile which closely approximates the shape and ratio p_+/p_- given in Figure 2.2, and is displayed in Figure 2.9.

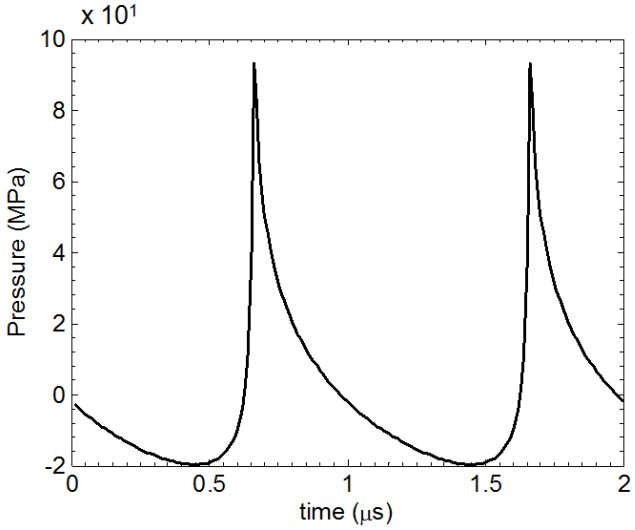

Figure 2.9. The standard nonlinear waveform used for simulation in this study, with p_-= 20 MPa, p_+ = 92 MPa, and rise time is 10 ns.

2.3.2 Hemispherical Scatterer

As a first order approximation, the deformed bubble was considered a hemisphere, with scattering occurring from the flat surface. Because only the backscattering is considered in this analysis, the problem reduces to scattering

from an acoustically soft disk. Unfortunately, no closed form solutions have been derived for the scattering from a disc everywhere in a field. Thus, a numerical procedure based on the Kirchoff integral is utilized which accounts for both low-frequency and high-frequency scattering of the first order.

Note that several approximations are made when compared with the experimental situation. First, the wave impinging on the bubble is considered to be plane instead of focused. This can be justified in that the wave actually defocuses to some extent due to nonlinear actions[25] and forms a flattened mach intersection at the center of the focus. Furthermore, the bubble is assumed to maintain its diameter throughout the simulation; no radial motion of the bubble itself is considered. It can also be observed in Figure 2.7 that this generally holds true, and that the radius of the bubble does not change significantly during the initial formation of the cavitation cloud.

The total velocity potential can be represented by the sum of incident and scattered waves:

$$\phi_t = \phi_i + \phi_s \tag{2.2}$$

At the surface of the soft disk, the total potential must vanish due to the boundary condition. The incident signal is a plane wave of known pressure, and thus the condition of the surface at all times can be determined. The scattered wave can then be found from the Kirchhoff integral for diffraction in a free field[26, 27]:

$$\phi_i(z,t) = \delta(t + z/c) \tag{2.3}$$

$$\phi_s(r,t) = \left(1 + \frac{z}{r'}\right)\iint_S \frac{\delta(t - r'/c)}{4\pi c r'} dS + \frac{z}{r'}\iint_S \frac{H(t - r'/c)}{4\pi r'^2} dS \tag{2.4}$$

where $r' = |r - r_0|$, r is a point in the field and r_0 a point on the surface, z is the distance normal to the surface, and dS is the area of a subelement on surface S.

This function can be considered the spatial impulse response of the disk, which is convolved with the temporal waveform *v(t)* to determine the total pressure:

$$p_s(r,t) = \rho \frac{d[\phi_s(r,t) * v_i(t)]}{dt} \qquad 2.5$$

These equations are solved by first discretization of the field and calculation of the individual spatial impulse response of each point on the disk. Eq. 2.4 is then used to compute the full field potential vs. time. Finally, Eq. 2.5 is used to determine the scattered wave pressure, which combined with Eq. 2.2, gives the total pressure field.

2.3.3 Spherical Scatterer

The Anderson model of for a fluid spherical scatterer was employed to determine the backscattered pressure from a bubble in response to a shocked waveform[23]. This model can be considered an exact solution to problem of scattering by an immovable fluid sphere i.e. it is valid for scatters of all size relative to the acoustic wavelength. This method makes use of decomposition of the plane and spherical waves into a sum of spherical harmonics and Legendre polynomials which can be implemented numerically. The theory by Feuillade is followed for a plane wave impinging on a sphere with acoustic impedance $Z = 0$ MRayl in water[24]. In this theory, the same approximations are used as for the hemispherical scatterer, that is, the incident wave is plane and the bubble size does not change throughout the simulation.

The plane wave pressure field is given as

$$P_i(f) = p_f \sum_{n=0}^{\infty} i^n (2n+1) L_n(\cos\theta) j_n(kr) \qquad 2.6$$

where p_f is amplitude of the wave for frequency ω at time t, k is the wave number, with L_n as the Legendre polynomial of n^{th} order, θ is the incidence angle, and j_n is the spherical Bessel function of n^{th} order. The scattered wave is a similar function:

$$P_s(f) = p_f \sum_{n=0}^{\infty} i^n A_n (2n+1) L_n(\cos\theta) h_n(kr) \qquad 2.7$$

with A_n being the amplitude of the scattered wave, and h_n is the spherical Hankel function. As the impedance of the sphere $Z \rightarrow 0$, the amplitudes of the value $A_n \rightarrow j_n(ka)/h_n(ka)$, a being the radius of the sphere. Thus the total pressure field can be determined by the sum of these incident and scattered waves at each frequency.

To numerically implement the scattering, the Fourier amplitudes of the transient waveform described in the section 2.3.1 are obtained. All the spherical functions and Legendre polynomials are calculated to n_{max} = 150. The incident and scattered waves at each time point are then computed by Eqs. 2.6 and 2.7. For all simulations, at least 1 full period is simulated to ensure the peak pressure amplitudes are reached everywhere in the field.

2.3.4 Transient Scattering Behavior

For the hemispherical case, the simulation reproduced the expected transient behavior according to the hypothesis. As the compressive shock impinged on the disk, a tensile transient wave was observed traveling back against the incident propagation direction (Figure 2.10). The tensile pressure was most greatly enhanced in the backscatter direction, with the scattered amplitude falling off with larger angle from the normal. Figure 2.11 shows a plot of the minimum pressure vs. position along the backscatter direction for simulation of different diameter hemispheres.

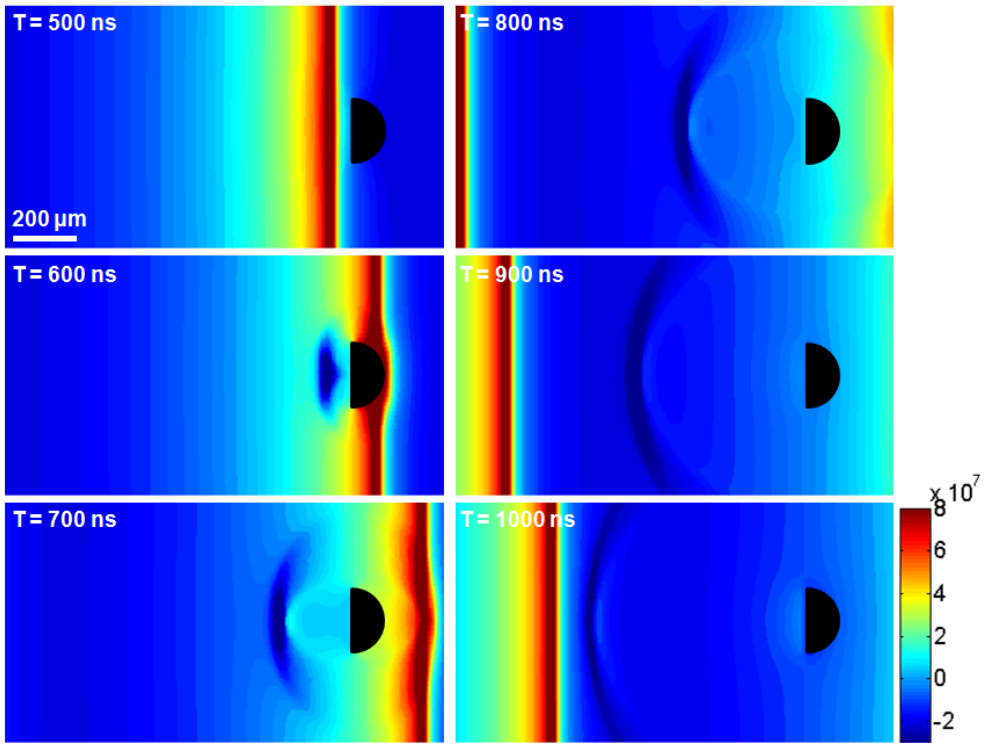

Figure 2.10. Transient pressure field for shocked plane wave scattering from a hemisphere (black) of 200 µm diameter. The incident wave propagates from left to right. The shock is scattered at 600 ns by the hemisphere, and temporarily generates an enhanced tensile pressure by constructive interference with the incident negative cycle of the waveform. Note this model is only valid in the backscatter plane, thus the pressure field beyond the bubble is not accurately predicted.

For smaller scatters (d < 100 µm), the largest peak negative pressures were generated where the scattered shock interfered with the following negative phase of the incident wave. However, this only increased the maximum negative pressure achieved at any point in space by up to 7 MPa. Larger hemispheres ($d \geq$ 100 µm), however, generated strong scattering which overwhelmed the incident wave, increasing the peak negative pressure to > 60 MPa in the case of a 200 µm diameter bubble (Figure 2.11). This suggests a 3-fold increase in peak negative pressure may occur transiently in the area behind the bubble. This large increase

in scattered pressure from 50-200 μm-diameter hemispheres is consistent with high speed images showing the single bubble from which the cloud grows is 80-200 μm in diameter for the 1 MHz transducer used in Section 2.2.

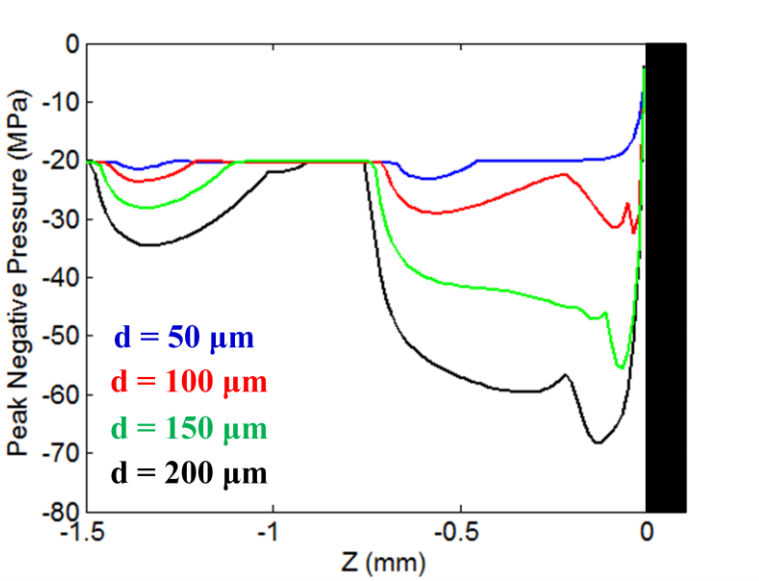

Figure 2.11. Peak negative pressure generated by backscattering from a hemisphere along the z-axis at $x = 0$ for different bubble diameters.

2.3.5 Effect of Bubble Shape on Scattering

The transient behavior of the scattering was similar to that in Figure 2.10, but the pressure wave was more divergent in the case of a sphere (Figure 2.12). Figure 2.13 shows the peak rarefactional pressure reached during simulation for a range of bubble diameters for a sphere and hemisphere. The scattered pressure level from a spherical bubble under identical inputs was significantly reduced compared with a hemisphere for bubbles in the size range of those observed in experiments. For instance, a 200 μm spherical bubble only enhanced the peak negative pressure about 9 MPa, whereas a disk of the same diameter enhanced the pressure by approximately 40 MPa. For very small bubbles, however, it can

be seen that the scattered pressure is similar for both cases (Figure 2.13). Although the fundamental wavelength is long, the shock thickness is much thinner than the bubble size, and thus, the shape appears to play an important role in the near-field interactions of the incident and scattered waves.

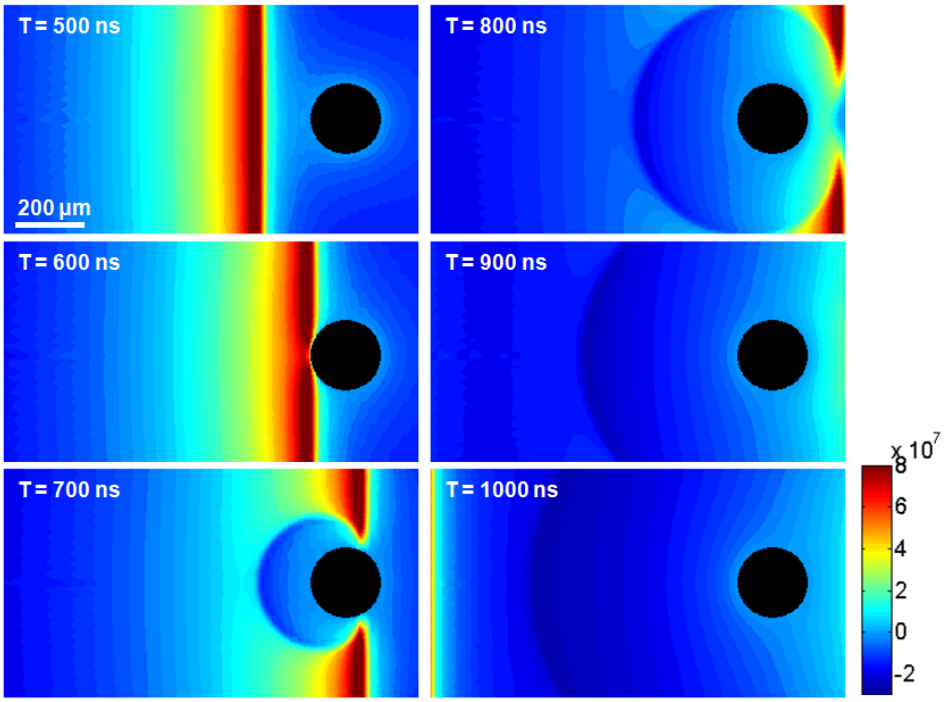

Figure 2.12. Transient pressure field for shocked plane wave scattering from a sphere (black) of 200 µm diameter. The shock is scattered at 600 ns by the sphere, and temporarily generates an enhanced tensile pressure by constructive interference with the incident negative cycle of the waveform.

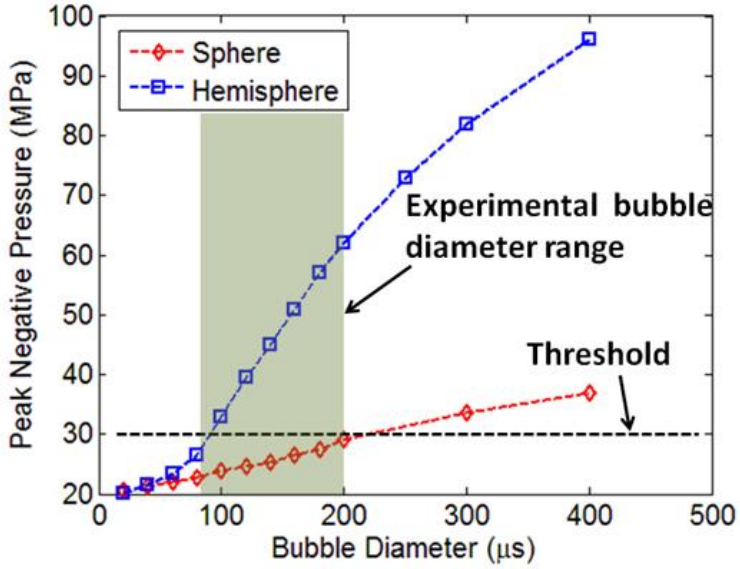

Figure 2.13. Comparison of peak negative pressure levels achieved by shock scattering for different bubble sizes for a hemisphere (blue) and a sphere (red). The gray region denotes the range of bubble diameters which initiate cavitation clouds observed using high speed images.

The spatial pressure field proximal to the bubble for both shapes was also evaluated. The peak negative pressure achieved at all points in the field over time was plotted, as shown in Figure 2.14, along with a photograph of a single cycle of the cavitation cloud formation. The simulation predicts that the peak negative pressure is enhanced in a cone behind the bubble for a hemisphere, up to ½ wavelength from the bubble, while the pressure for a sphere forms in a ring behind it where the tensile pressure of the scattered wave interferes with that of the incident wave. The observations of similar- sized bubbles (160 μm for the hemisphere and 200 μm for the sphere) show comparable patterns for the cavitation cloud. Thus, the model appears to explain the basic shape of cavitation clouds formed by this mechanism.

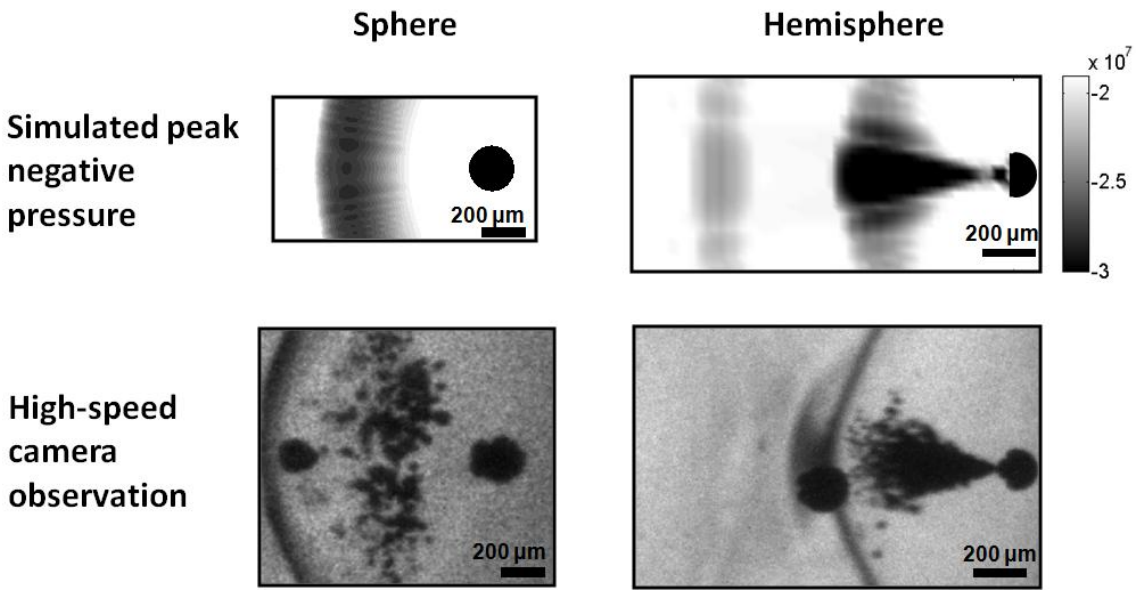

Figure 2.14. (Top) Simulated 2-dimensional peak negative pressure distribution over 1 cycle. The white color is set to the incident peak negative pressure in the simulation, and darker shades indicate enhancement of peak negative pressure by scattering. The sphere is 200 µm and the hemisphere is 160 µm. (Bottom) Cavitation cloud patterns observed by high speed camera with single bubbles corresponding to the size and shape in the simulation. Good agreement between the simulated negative pressure region and the experiment is observed. A smaller region is simulated for the sphere due to numerical limitation of the computer hardware implementing the model.

2.3.6 Effect of Waveform Shape on Scattering

To evaluate the importance of the high frequency harmonics in the wave, modified waveforms were also created by low-pass filtering the original signal at frequencies of 5, 10 and 20 MHz (Figure 2.15). Scattering of these waveforms were simulated using a 160 µm hemisphere. Filtering the higher harmonics above 5 MHz reduced the scattered field peak negative pressure level from 52 MPa to 22 MPa (Figure 2.15). Thus, the contribution of scattering to the peak negative pressure was minimal with this modified waveform.

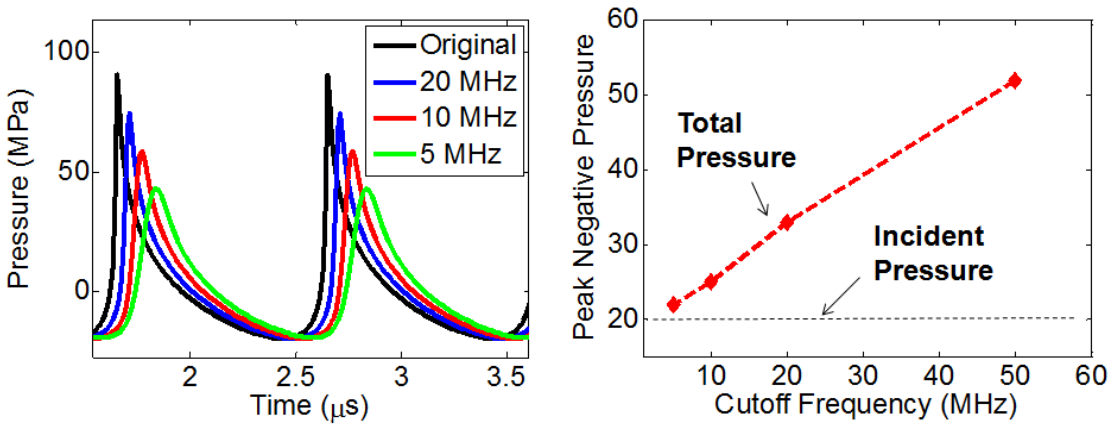

Figure 2.15. (Left) Filtered waveforms applied to evaluate the importance of harmonics to scattering. (Right) Peak negative pressure reached during simulation vs. waveform filter frequency. As the harmonics of the wave are decreased, the scattered pressure becomes insignificant compared with the incident wave.

Another modified incident waveform was created by artificially increasing the rise time of the shock without changing the peak positive or negative pressure (Figure 2.16). When the shock rise time of the waveform was increased to 100 ns, the total pressure achieved in the field was reduced from 52 MPa to 26 MPa. Even with identical peak positive and negative pressure levels, the scattering was reduced below the threshold due to the absence of a steep shock front. Thus, the criteria for strong shock scattering include both high amplitude and a steep shock front i.e. high frequency content. All of the scattering must occur at a single time point in each cycle to maximize the amplitude of the scattered wave. By extending the rise time, the scattering is 'spread out' over space as a wide, low amplitude signal which does not exceed the cavitation threshold.

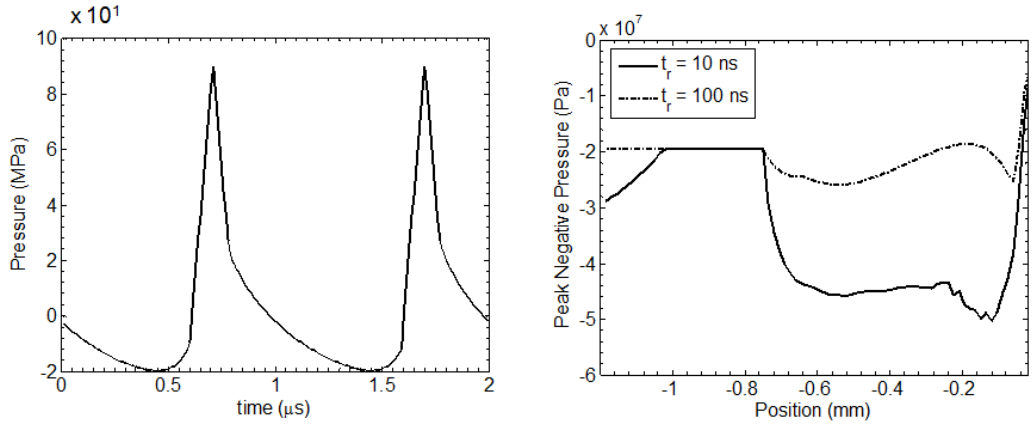

Figure 2.16. (Left) Modified waveform with equal peak pressure levels to that in Figure 2.9, but with rise time of the shock extended to 100 ns. (Right) Comparison of backscattered peak negative pressure with the shocked waveform and the waveform with extended rise time. Removal of only the steep shock strongly suppressed the backscatter.

2.4 Experimental Evaluation of Shock Scattering Hypothesis

Three experiments were also performed to evaluate the mechanism for bubble cloud initiation: The hypothesis is that bubble clouds are created when the incident positive pressure phase of the shocked pulse reflects and inverts from a single cavitation bubble. This negative transient backscattered wave incites a cloud of cavitation bubbles proximal to the scatterer.

2.4.1 Methods: Experiments

Test #1: *If cloud formation is dependent on the positive pressure, the initial position of cloud formation will be limited to the positive-pressure focal region instead of the negative-pressure focal region.* Histotripsy pulses are distorted from a sinusoidal shape because of nonlinear propagation. A typical pulse contains multiple cycles,

each cycle consisting of a steep shock front with a high-amplitude, positive-pressure phase followed by a lower-amplitude, negative-pressure phase (Figure 2.2). The waveform displays strong asymmetry, in that the peak positive pressure of the pulses is several times greater than the peak negative pressure because of the combined effects of nonlinear propagation and diffraction. The higher harmonics of the wave focus within a smaller zone and thus the volume over which the pulse has a high positive pressure is limited to a small region in the center of the focus[28, 29]. The peak negative pressure is distributed over a significantly larger region, similar to that defined by linear propagation when the waveform is sinusoidal. If scattering of the positive phase of the wave is the mechanism of cloud initiation, then it is expected that cloud initiation will occur only within the narrow central region of the focus where the positive pressure is high. To test this, we recorded the lateral and axial locations of the single bubbles from which clouds began to form.

Test #2: *If bubble cloud formation is dependent on scattering of the positive pressure phase, then a transducer outputting a lower positive pressure level for a given negative pressure level, i.e., a lower ratio* $p_+/|p_-|$ *, will have a higher threshold of negative pressure for bubble cloud formation.* The waveform asymmetry can be characterized by the ratio between peak positive and peak negative pressures $p_+/|p_-|$. The waveform asymmetric distortion is always pronounced in nonlinear acoustic beams because of the combined action of acoustic nonlinearity and diffraction, which results in $p_+ > |p_-|$[29]. In the case of focused beams, the asymmetry is usually strongest at the focus and depends on the transducer F-number (ratio of the transducer focal length to diameter). In this study, a 1-MHz, F# 0.9 transducer (diameter = 10 cm, focal length = 9 cm) and another 1-MHz, F# 0.6 transducer (diameter = 17 cm, focal length =10 cm) were used to generate different levels of waveform

asymmetry for a given peak negative pressure value. For the pressure range applied in this study, the transducer with a lower F# produced a waveform with a lower $p_+/|p_-|$ ratio. The -6 dB negative pressure lateral beamwidth is 2.2 mm and the axial beamwidth is 15 mm for the F# = 0.9 transducer. The lateral beamwidth is 1.2 mm and the axial beamdwidth is 7 mm for the F# = 0.6 transducer. For linear propagation, the peak positive beamwidth is the same as that for peak negative pressure. However, at higher amplitude, the positive pressure beamwidth is reduced because of stronger focusing of harmonics.

The negative pressure threshold at which bubble clouds were first observed to form was recorded with both transducers. Additionally, the probability of bubble cloud formation was recorded over a range of pressure levels using 15-cycle pulses for each transducer. Individual pulses were applied to the tissue phantom, and the presence or absence of a cloud on the high-speed camera image was noted in each case. The probability was defined as the fraction of pulses that generated a cavitation cloud visible on the high-speed camera images.

Test #3: *If shockwave scattering is the mechanism of cloud formation, then reduction of only the peak positive pressure of the incident wave will suppress cloud formation.* In order to accomplish this effect, thin brass sheets were placed between the transducer and focus aligned perpendicular to the propagation axis. The sheets act as a low-pass filter, primarily reducing the harmonics of the nonlinear wave. The outcome is that the positive peak focal pressure is more greatly reduced than the negative peak focal pressure when the sheets' thickness and material are chosen appropriately. The sheets must be placed near the focus to allow nonlinear distortion to develop before impinging on the filter. Once the filter was in place, the driving voltage on the transducer was increased to reach the same

peak negative focal pressure as the original incident wave without the filter. If shock scattering is the mechanism of bubble cloud formation, it is expected that bubble clouds will be suppressed under the modified waveform with reduced levels of harmonics, while single bubbles should still appear within the focal region. The appropriate thickness and material were determined by testing different sheets with the hydrophone at the focus and recording the waveforms with each in position. For this experiment, the filter consisted of 3 brass sheets each 0.075 mm thickness spaced 0.5mm apart, placed about 1 cm proximal of the focus center. The filter was assembled under water to ensure no air was trapped between the sheets. The pressure distribution in the plane normal to the acoustic axis was recorded with and without the sheets in place to ensure the peak pressure levels were measured at the true maximum. After recording pressure levels, the sheets were attached to the front of the tissue phantom holder, and the focus was positioned at the same distance from the sheets. High-speed images were recorded at the focus with and without the sheet to determine what effect the modified waveform had on the probability of generating bubble clouds.

2.4.2 Results: Cloud Formation Position

The proposed mechanism suggested that the rarefaction phase of the incident wave formed single bubbles, while the compressive shock was the source of scattering and the ensuing cavitation cloud. The experiments below were performed to determine the contribution of waveform asymmetry caused by nonlinearity and the positive phase of the wave to forming bubble clouds.

Test #1: *If cloud formation is dependent on the positive pressure, the initial cloud formation position will be limited to the positive-pressure focal region instead of the negative-pressure focal region.* The locations of single bubbles that initiated cloud formation were recorded (Figure 2.17). All cloud initiation events occurred at the

center of the focus laterally, within a range of +/- 118 μm (n = 35). The lateral -3dB peak positive pressure width was 270 μm, and the lateral -3dB peak negative pressure width was 1.6 mm. Axially, initiation occurred in a zone -3.5mm prefocal to +5.2 mm postfocal. The axial -3dB peak positive pressure extended from -3.5 mm to 5.5 mm, and from -4 mm to 6.3 mm for the negative pressure distribution. In this case, the -3dB positive pressure region defined accurately the range over which initiation events were observed. The bubbles which initiated the cloud lie within the region of the focus that forms a Mach intersection[30], due to the convergence of shock waves at the focus. This region defined the zone containing a single shock front resulting in a high peak positive pressure. Outside this region, the shock was spatially separated into two lower pressure peaks. In the outer region, the negative pressure remained nearly the same as the very center of the focus, but single bubbles visible in the outer region did not appear to create cavitation clouds.

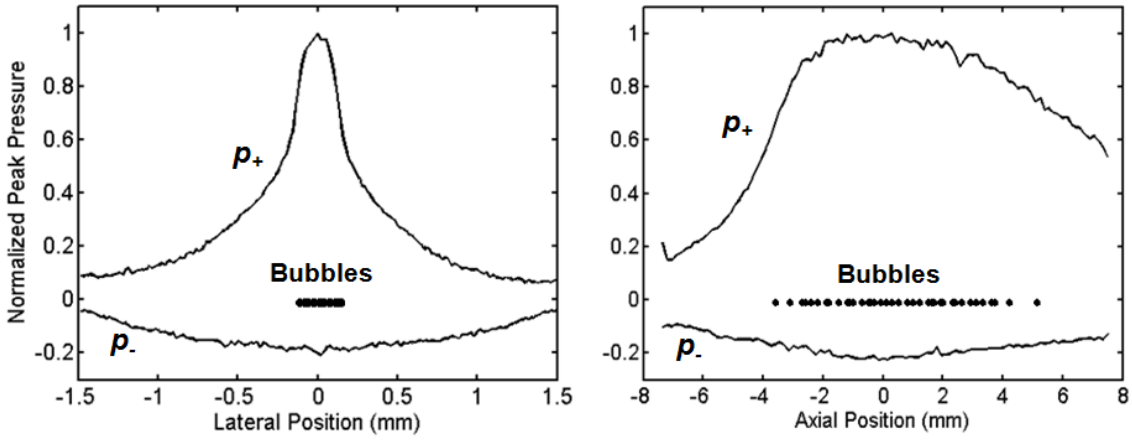

Figure 2.17. Positions of bubbles (black dots, n = 35) for cloud initiation, as well as peak positive (p_+) and negative pressure (p_-) distribution at the focus. (Top) Lateral profile of focus and initiation bubble positions. Note bubble clouds were only formed by bubbles +/- 118 μm from the center of the focus. The measured width of the -3dB positive pressure zone at this location was 270 μm. (Bottom) Axial profile of focus and initiating bubble positions.

2.4.3 Results: Cloud Formation vs. Waveform Asymmetry

Test #2: *If bubble cloud formation was dependent on scattering of the positive pressure phase, then a transducer outputting a lower positive pressure level for a given negative pressure level, i.e., a lower $p_+/|p_-|$ ratio, will have a higher threshold of negative pressure for bubble cloud formation.* Over the range of peak-negative pressure values examined in this study, the ratio $p_+/|p_-|$ was lower for the transducer with F# = 0.6 than for F# = 0.9. The probabilities of cloud formation as a function of peak negative/positive pressure are shown in Figure 2.18 for both transducers in degassed water and gelatin. An S-curve was fit to each of the data sets by least-squares regression. Each curve was defined by a cumulative distribution function for a normal distribution. Table 2.1 summarizes the p- and corresponding p+ pressure levels at which cavitation clouds were first observed, as well as the pressure values for where the fit curve reached probability = 0.5. In general, cavitation clouds were observed at lower pressures with the F# = 0.9 transducer in both water and gelatin. However, for higher pressures ($|p-| \geq 18.5$) in gelatin, the probabilities for both transducers were similar (Figure 2.18). Despite this, the F# = 0.9 transducer generated bubble clouds between $|p-|$ = 13.5-17 MPa, whereas clouds were not observed in this pressure range for F# = 0.6 transducer in gelatin. These data were consistent with the hypothesis in that peak negative pressure did not solely determine the threshold for cavitation clouds, even if the frequency of the transducers and pulse length are the same.

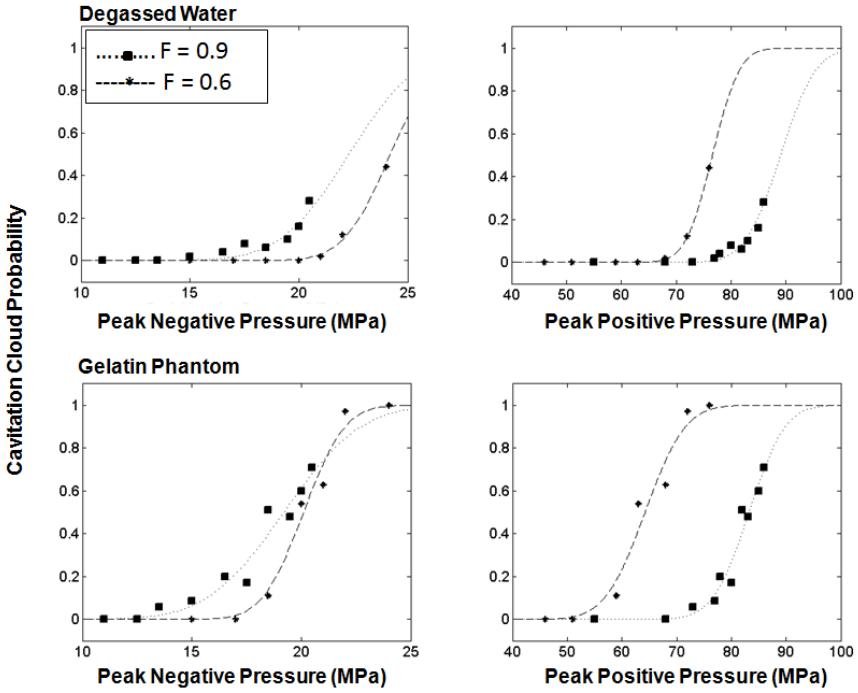

Figure 2.18. Fraction of pulses that produced bubble clouds vs. acoustic pressure for two different transducers with same frequency and focal length, but different F#. The upper two graphs show the bubble cloud formation probability in degassed, filtered water (n = 50, margin of error = $1/\sqrt{n}$ = 0.14) and the lower two graphs show the bubble cloud formation probability in gelatin (n = 35, margin of error = 0.17). Dashed lines are S-curves defined by a cumulative distribution function for a normal distribution, fit by nonlinear least squares analysis to the data.

Table 2.1. Pressure thresholds for cavitation clouds with the F# = 0.9 and F# = 0.6 transducers in water and gelatin. The value p_L defines the lowest pressure at which cavitation clouds were first observed on the high-speed camera. The value p_{50} is the pressure at which the curve fits to the data in Figure 2.18 give probability = 0.5.

		p_{L-} (MPa)	p_{50-} (MPa)	p_{L+} (MPa)	p_{50+} (MPa)
Water	**F# = 0.9**	-15	-22.3	78	89.0
	F# = 0.6	-21	-24.2	68	76.6
Gelatin	**F# = 0.9**	-13.5	-19.2	73	83.2
	F# = 0.6	-18.5	-20.1	60	64.2

2.4.4 Results: Cloud Formation with Reduced Shock Amplitude

Test #3: *If shockwave scattering is the mechanism of cloud formation, then reduction of only the peak positive pressure of the incident wave will suppress cloud formation.* To assess the importance of the positive phase of the wave, we used an acoustic filter to selectively prevent transmission of the higher harmonics of the shock to the focus. Without the filter in place, the peak positive/negative pressures were 85/19 MPa, and the rise time of the shock front was < 8 ns. The measured rise time is limited by the bandwidth of the hydrophone in this case. When the filter was positioned about 1 cm from the focal center and the drive voltage to the transducer increased, the peak positive/negative pressure was 38/19 MPa, and the rise time increased to 55 ns (Figure 2.19). The focus shifted slightly in the lateral direction when the filter was in position, and so the lateral 2-dimensional pressure distribution of the focus was recorded in each case to find the true maxima. The spatial width of the negative pressure region was also reduced slightly with the filter in place.

Without the filter, the probability of bubble cloud initiation with a 15 cycle pulse was 0.72 (n = 101). When the filter was inserted to reduce the shock amplitude, the probability of bubble cloud initiation was 0.01 (n = 96). A one-sided Z-test for the two proportions gives a p-value < 0.001. Single cavitation bubbles were visible on every pulse within the focal region in both cases. Thus, the reduction of the positive-pressure phase suppressed cloud initiation almost entirely, while single bubble cavitation was maintained.

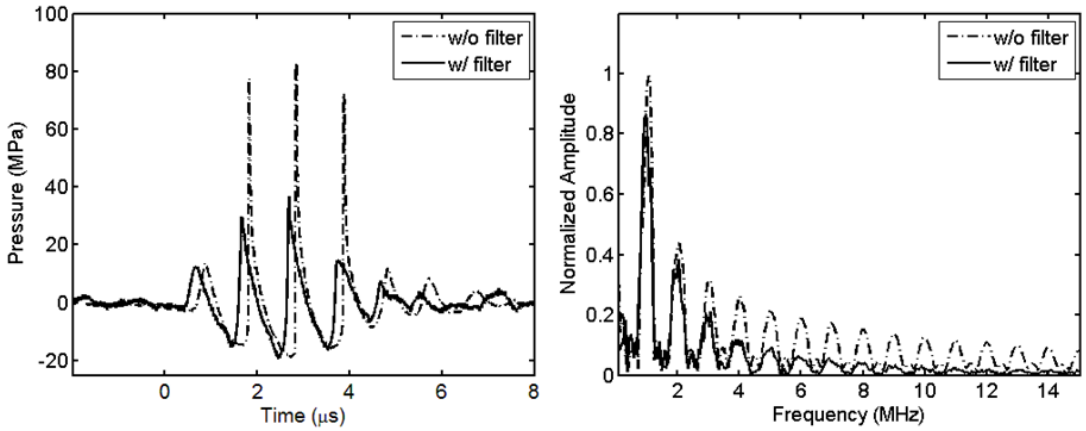

Figure 2.19. Comparison of the temporal waveforms (top) and frequency spectra (bottom) with and without the acoustic filter placed between the focus and transducer. The positive pressure was lowered with the filter, while the negative pressure remained the same after increasing the transducer drive voltage. In the frequency domain, the fundamental and second harmonics had nearly the same amplitude as the original signal, but higher harmonics were greatly reduced.

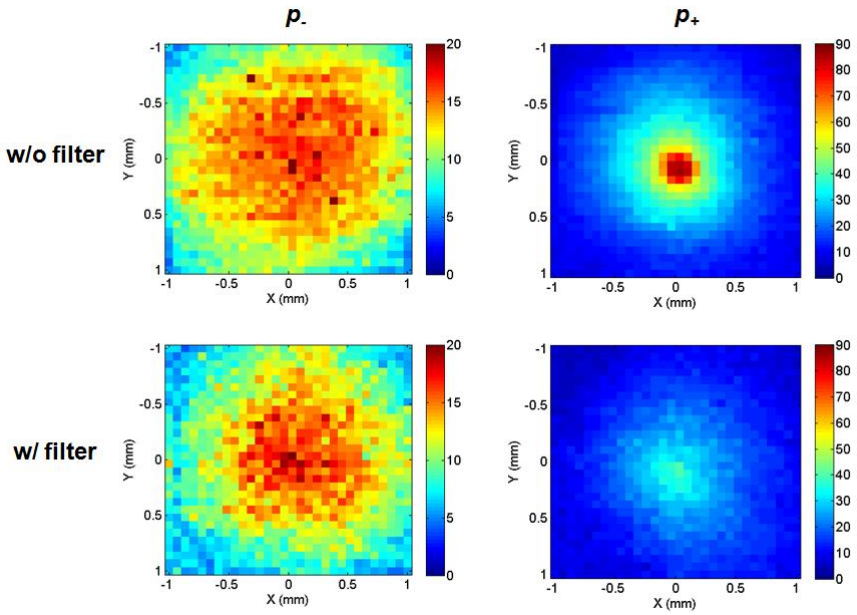

Figure 2.20. Transverse two-dimensional beam profiles of the transducer for peak negative pressure (left) and peak positive pressure (right) without (top) and with (bottom) the acoustic filter in position.

2.5 Discussion

In this article, we studied the mechanism by which bubble clouds form in a tissue phantom during histotripsy using high-speed photography. Two distinct types of cavitation activity were observed: single bubble cavitation and cavitation clouds. Single bubbles were observed to grow and collapse during the initial cycles of the pulse. However, bubbles remained in an expanded state during later cycles of the pulse after they had grown to ~100-μm diameter. The lack of collapse may have resulted from the temporal asymmetry caused by nonlinearity of the waveform[31], or the inability of the large bubble to respond within a period due to inertia. Because of this lack of collapse after the initial cycles, the cavitation bubbles acted as scatterers for the subsequent portions of the pulse. Note that although the reflecting bubble was fairly small, its diameter being only of order of 100 μm (see Figure 2.3), it was in fact large relative to the incident shock front thickness. The shock front thickness δ_s is determined by competition between the waveform steepening due to acoustic nonlinearity and smoothening due to viscosity. In classical liquids, $\delta_s = 2c\left(\varsigma + 4\eta/3\right)/\left(\beta \cdot p_s\right)$, where c is the speed of sound, ς and η are the bulk and shear viscosity coefficients, β is the parameter of acoustic nonlinearity, and p_s is the pressure jump at the shock front[33]. For instance, for water (ς =2.5·10^{-3} Pa·s, η =1.1·10^{-3} Pa·s, β =3.5) at p_s =50 MPa, the mentioned formula gives $\delta_s \approx 0.07$ μm, which is more than 1000 times smaller than the bubble diameter, i.e. the shock reflection indeed happens as a plane wave reflection from a pressure-release mirror.

Once cavitation clouds began to form, the clouds grew along the acoustic axis at a nearly constant rate throughout the pulse. As the shockwave scattered from the proximal cloud surface, a new section of the cloud was generated with each

cycle. The clouds often took on a layered structure, with small gaps without cavitation between layers separated by about 0.5 mm (near $\lambda/3$ for the fundamental frequency). This structure is evident in Figure 2.7. It probably arose because of the scattering of the wave creates the strongest rarefaction when it constructively interfered with the incident negative portion of the cycle, creating a position where cavitation was most dense. The process is analogous to a fracture process called spallation that plays a limited role in shock wave lithotripsy, where the wave reflects and inverts at an interface from solid to fluid or gas and fractures the distal end of the solid. However, here the wave was distorted and not sinusoidal so the constructive interference appeared near $\lambda/3$ instead of $\lambda/4$. The width and length of the cloud were limited by the focal zone, outside of which, the pressure was not sufficient to create strong scattering.

A numerical model supported the shock-scattering hypothesis, suggesting that high-amplitude transient waves can be generated upon reflection of a shock either a sphere or hemisphere. A surprising result is perhaps the importance that bubble geometry played in the scattering amplitude. Arguably, the use of two separate models for the sphere and hemisphere do not produce directly comparable simulations, particularly with one being a closed-form solution and the other being a numerical simulation. However, the pressure scattering results for very small and very large bubbles seem to converge, suggesting only in this intermediate bubble size range (bubble is larger than the shock front but smaller than the acoustic wavelength) is the difference noticeable. Furthermore, Iloreta et al., upon numerical simulation of shocks scattering from a convex and flat kidney stone, found a significant difference in backscattered pressure even for a slight curvature[32], supporting these results. The model also suggested that a steep, high-amplitude shock in particular is necessary to create this scattering.

Based on these results, tests to evaluate the shock scattering mechanism were conducted to demonstrate the importance of the positive pressure and asymmetry caused by nonlinearity of the waveform. Clouds were found to initiate by bubbles within a narrow region +/- 118 μm from the center of the focus laterally. In this region, a single, coherent strong shock front was formed with high peak positive pressure each cycle. The focusing of shocks and the pattern observed at the focus are explained in detail by Sturtevant and Kulkarny[33]. The region of cloud initiation corresponded well with the -3dB positive pressure region laterally (+/- 135 μm), and was considerably smaller than the -3dB negative pressure region of the focus (+/- 800 μm).

In another experiment, we compared the bubble cloud formation by two transducers with different F#. We observed that, in general, the lower F# transducer had higher a peak negative pressure threshold for generating bubble clouds. While the probabilities of cloud generation were similar for both transducers at $|p_-| \geq 18.5$ MPa in gelatin, clouds were only observed at $|p_-| < 18.5$ MPa with the F# = 0.9 transducer. It is difficult to predict the probabilities of cloud formation, since several variables, including difference in focal dimensions and different geometry of the focusing likely contribute. However, the results at lower focal pressures in gelatin, as well those in degassed water which show distinctly a lower $|p_-|$ threshold for the F# = 0.9 transducer lend support to the hypothesis. Meanwhile, the positive pressure level at which the clouds appeared was lower for the F# = 0.6 transducer than for the F# = 0.9 transducer. Effectively, the resulting negative pressure from the combined incident and scattered waves at their thresholds could be the same for these two different F# transducers.

In the third experiment, the positive pressure was reduced by inserting a filter plate into the focus. The higher harmonics of the wave were attenuated while the lower harmonics were transmitted to the focus. This effectively

lowered the peak positive pressure at the focus and suppressed bubble cloud formation, which was consistent with the hypothesis. Since the fundamental wavelength is larger than the initial bubble and therefore does not backscatter efficiently, it is likely that scattering of harmonics generated by nonlinear propagation is most important in initiating cloud growth. However, as the cloud grows in size laterally, it may reflect lower frequencies more efficiently, and the importance of the shock may be reduced in the later cycles.

While this mechanism appears to be dominant for acoustic parameters commonly used in histotripsy, this is not the only mechanism by which bubble clouds can form. There is a similar appearance of the bubble in the third frame of Figure 2.7 to that of a bubble counterjet described by Lauterborn et al[34]. It was observed that the counterjet is caused by the shock from the bubble collapse creating a small cluster of microbubbles. Despite the similarity, our experiments suggest that it was the shock from the incident wave which caused the initiation of the cavitation cloud in this case. After initiation of the first cluster of microbubbles, it is possible that the shocks which perpetuate the growth each cycle may be caused by microbubble collapse rather than the incident shock. Cavitation clouds have also been generated by applying very large tensile pulses to liquid with a single-cycle lithotripsy-type shockwave[10], when the peak negative pressure exceeded 33 MPa. However, it is exceptionally difficult to achieve such a negative-pressure level using a harmonic waveform, because of the limits imposed by nonlinear acoustic saturation[35, 36]. Alternatively, Canney *et al.* have demonstrated that under intense, millisecond-length focused pulses at 2 MHz, large bubbles can be achieved at the focus as a result of boiling[37]. These bubbles also demonstrate the ability to mechanically fractionate tissue. Rapid boiling is achieved primarily because of heating caused by nonlinear absorption and shockwave dissipation at the focus. Therefore, shocks also play an important

role in this mechanism of bubble formation. The cavitation clouds here also appear distinct from those observed by Willard [6] and Neppiras [7] in water under CW insonation. In liquids, it has been observed that such bubbles can proliferate into a cloud when they undergo fragmentation, either due to surface waves[38], deformation from shockwaves, or fragmentation of the bubbles upon collapse[12]. These observations suggest that bubble clouds and mechanical tissue disruption may be achievable by several mechanisms.

Based on the understanding of this mechanism, several strategies may improve initiation of bubble clouds. The source of probability in cloud formation is ultimately related to the position and dynamic behavior of the single cavitation bubble scatterers. While it is difficult to predict where these nuclei exist *in-vivo*, it may be possible to modify the therapy to improve the likelihood of cloud generation within a pulse. Injection of microbubble contrast agents could create a region more probable to generate a cloud by increasing the density of nuclei locally. If initiation is not achieved on a first pulse, then it is unlikely it will be achieved by application of further identical pulses in the same location in tissue unless a cavitation nucleus enters the focal region. It may instead be more efficient to 'search' for nuclei using a spatial dithering algorithm to slightly move the focus to a new location each pulse until cloud initiation is achieved. Other strategies for efficient initiation may incorporate creation of larger scattering bubbles. A lower frequency transducer could produce larger single bubbles and provide greater degree of scattering of the wave. A higher frequency transducer could then be used to create scattering from these large bubbles and generate clouds with precision, but at a lower threshold than by itself. Such techniques may improve the reliability of bubble cloud generation, particularly in applications with small acoustic windows where it is difficult produce large focal pressures. A similar effect of large bubble creation can also be achieved through

the rapid boiling mechanism when a focused transducer is excited by several millisecond duration (or longer) bursts[37].

2.6 References

1. Xu Z, Fowlkes JB, Rothman ED, Levin AM, Cain CA. Controlled ultrasound tissue erosion: The role of dynamic interaction between insonation and microbubble activity. J. Acoust. Soc. Am. 2005;117:424-435

2. Fowlkes JB, Crum LA. Cavitation threshold measurements for microsecond length pulses of ultrasound. J. Acoust. Soc. Am. 1988;83:2190-2201

3. Xu Z, Hall TL, Fowlkes JB, Cain CA. Optical and acoustic monitoring of bubble cloud dynamics at a tissue-fluid interface in ultrasound tissue erosion. J. Acoust. Soc. Am. 2007;121:2421-2430

4. Xu Z, Fowlkes JB, Cain CA. A new strategy to enhance cavitational tissue erosion by using a high intensity initiating sequence. IEEE Trans Ultrasonics Ferroelec Freq Control. 2006;53:1412-1424

5. Chen H, Li X, Wan M, Wang S. High-speed observation of cavitation bubble clouds near a tissue boundary in high-intensity focused ultrasound fields. Ultrasonics. 2009;49:289-292

6. Willard GW. Ultrasonically induced cavitation in water: A step-by-step process. J. Acoust. Soc. Am. 1953;25:669-686

7. Neppiras EA, Coakley WT. Acoustic cavitation in a focused field in water at 1 mhz. J. Sound Vibrat. 1976;45:341-373

8. Arora M, Junge L, Ohl CD. Cavitation cluster dynamics in shock-wave lithotripsy: Part 1. Free field. Ultrasound Med. Biol. 2005;31:827-839

9. Pishchalnikov YA, Sapozhnikov OA, Bailey MR, Williams JC, Cleveland RO, Colonius T, Crum LA, Evan AP, McAteer JA. Cavitation bubble cluster activity in the breakage of kidney stones by lithotripter shockwaves. J. Endourol. 2003;17:435-446

10. Sankin G, Teslenko V. Two-threshold cavitation regime. Dokl. Phys. 2003;48:665-668

11. Peter H, et al. Influence of shock wave pressure amplitude and pulse repetition frequency on the lifespan, size and number of transient cavities in the field of an electromagnetic lithotripter. Phys. Med. Biol. 1998;43:3113

12. Pishchalnikov YA, McAteer JA, Pishchalnikova IV, Williams JC, Jr, Bailey MR, Sapozhnikov OA. Bubble proliferation in shock wave lithotripsy occurs during inertial collapse. 18th International Symposium on Nonlinear Acoustics - ISNA 18. 2008;1022:460-463

13. Sankin G. Luminescence induced by spherically focused acoustic pulses in liquids. Acoust. Phys. 2005;51:338-346

14. Bailey MR, Dalecki D, Child SZ, Raeman CH, Penney DP, Blackstock DT, Carstensen EL. Bioeffects of positive and negative acoustic pressures in vivo. J. Acoust. Soc. Am. 1996;100:3941-3946

15. Church CC. A theoretical study of acoustic cavitation produced by "positive-only" and "negative-only" pressure waves in relation to in vivo studies. Ultrasound Med. Biol. 2003;29:319-330

16. Zhen X, Raghavan M, Hall TL, Mycek MA, Fowlkes JB, Cain CA. Evolution of bubble clouds induced by pulsed cavitational ultrasound therapy - histotripsy. Ultrasonics, Ferroelectrics and Frequency Control, IEEE Transactions on. 2008;55:1122-1132

17. Hall T, Cain C. A low cost compact 512 channel therapeutic ultrasound system for transcutaneous ultrasound surgery. AIP Conf. Proc. 2006;829:445-449

18. Parsons JE, Cain CA, Fowlkes JB. Cost-effective assembly of a basic fiber-optic hydrophone for measurement of high-amplitude therapeutic ultrasound fields. J. Acoust. Soc. Am. 2006;119:1432-1440

19. Wang T-Y, Maxwell AD, Park S, Xu Z, Fowlkes JB, Cain CA. Why are short pulses more efficient in tissue erosion using pulsed cavitational ultrasound therapy (histotripsy)? ISTU2009.1215:40-43

20. Johnsen E, Colonius T. Shock-induced collapse of a gas bubble in shockwave lithotripsy. J. Acoust. Soc. Am. 2008;124:2011-2020

21. Ayme EJ, Carstensen EL. Cavitation induced by asymmetric distorted pulses of ultrasound: Theoretical predictions. IEEE Trans Ultrason Ferroelectr Freq Control. 1989;36:32-40

22. Maxwell AD, Tzu-Yin W, Cain CA, Fowlkes JB, Sapozhnikov OA, Bailey MR, Zhen X. The role of compressional pressure in the formation of dense bubble clouds in histotripsy. IEEE Ultrasonics Symposium 2009. 2009:81-84.

23. Anderson VC. Sound scattering from a fluid sphere. J. Acoust. Soc. Am. 1950;22:426-431

24. Feuillade C. Animations for visualizing and teaching acoustic impulse scattering from spheres. J. Acoust. Soc. Am. 2004;115:1893-1904

25. Oleg VR, Oleg AS. Self-action effects for wave beams containing shock fronts. Phys.-Uspekhi. 2004;47:907

26. Emeterio JLS, Ullate LG. Diffraction impulse response of rectangular transducers. J. Acoust. Soc. Am. 1992;92:651-662

27. Guyomar D. Boundary effects on transient radiation fields from vibrating surfaces. J. Acoust. Soc. Am. 1985;77:907

28. Hamilton MF, Blackstock DT. Nonlinear acoustics. San Diego: Academic Press; 1998.

29. Canney MS, Bailey MR, Crum LA, Khokhlova VA, Sapozhnikov OA. Acoustic characterization of high intensity focused ultrasound fields: A combined measurement and modeling approach. J. Acoust. Soc. Am. 2008;124:2406-2420

30. Massey B, Ward-Smith J. Mechanics of fluids. New York: Taylor & Francis; 2006.

31. Kreider W, Bailey MR, Sapozhnikov OA, Khokhlova VA, Crum LA. The dynamics of histotripsy bubbles. 10th International Symposium on Therapeutic Ultrasound. 2010

32. Iloreta JI, Fung NM, Szeri AJ. Dynamics of bubbles near a rigid surface subjected to a lithotripter shock wave. Part 1. Consequences of interference between incident and reflected waves. J. Fluid Mech. 2008;616:43-61

33. Sturtevant B, Kulkarny VA. The focusing of weak shock waves. J. Fluid Mech. 1976;73:651-671

34. Lauterborn W, Ohl CD. The peculiar dynamics of cavitation bubbles. Appl. Sci. Res. 1997;58:63-76

35. Duck FA. Acoustic saturation and output regulation. Ultrasound Med. Biol. 1999;25:1009-1018

36. Bessonova O, Khokhlova V, Bailey M, Canney M, Crum L. Focusing of high power ultrasound beams and limiting values of shock wave parameters. Acoust. Phys. 2009;55:463-473

37. Canney MS, Khokhlova VA, Bessonova OV, Bailey MR, Crum LA. Shock-induced heating and millisecond boiling in gels and tissue due to high intensity focused ultrasound. Ultrasound Med. Biol.2010;36:250-267

38. Leighton TG. The acoustic bubble. San Diego: Academic Press; 1994.

CHAPTER 3

Cavitation Pressure Thresholds for Histotripsy

In the previous chapter, cavitation clouds appeared in response to a shocked pulse by creation of a strong tensile wave when the shocks scattered from a single bubble. This mechanism necessitates the existence of a bimodal distribution of cavitation nuclei – those which become the single scatterer bubbles and those which make up the resulting cloud. A primary question that was not addressed in the previous chapter is: what pressure level is necessary to excite these bubbles which form the cloud? This chapter discusses experiments measuring the pressure thresholds to form cloud cavitation. Thresholds for this cavitation were measured in several liquids, tissue phantoms, and tissues (including blood and thrombus). These observations also suggest a new method for performing histotripsy by intentionally avoiding the mechanism proposed in Chapter 2, which is possibly more predictable and consistent between pulses.

3.1 Cavitation Nuclei in Ultrasound

Cavitation pressure thresholds in water and tissues at ultrasonic frequencies have been studied in great detail, both theoretically[1-3] and experimentally[4-6].

These thresholds are of particular interest for understanding the limiting pressure levels which may cause cavitation-related tissue damage in diagnostic and therapeutic ultrasound. Cavitation nuclei are often separated into two categories: heterogeneous nuclei and homogeneous nuclei. The properties of these nuclei and previous studies relating to their measurement are discussed in this section.

3.1.1 Heterogeneous Nucleation

Under standard atmospheric conditions, a free gas bubble in water is unstable and will either dissolve due to the Laplace pressure from surface tension at the bubble wall, or rise out of the system due to buoyancy. However, numerous studies have suggested the presence of stabilized bubbles in water and other media. Thus, either some mechanism prevents this instability to allow the bubble to remain indefinitely, or the bubbles only exist transiently due to application of some external energy. The term 'heterogeneous nucleation' describes such gas bodies. Multiple models have been used to successfully describe how gas bodies may exist indefinitely in the liquid. The crevice model[7, 8], described by Harvey, demonstrated how a gas bubble can be stabilized in a crack in the wall of a container filled with liquid, or in a free-floating dirt particle. The variably-permeable skin model[9], the most well-known described by Yount in 1979, describes potential organic molecular impurities in a liquid which form a skin around the bubble and prevent gas diffusion from the bubble into the liquid. Neither model appears to completely describe experiments with micron-sized nuclei. Instead, both models may be relevant under different conditions[10-12]. More recently, an additional method of ionic stabilization has been proposed, which suggests dissolved ionic species may also stabilize against surface tension[13] . Gas bubbles can also be generated without stabilization through radiation-induced

cavitation, such as with a neutron source or by cosmic rays. However, these only exist temporarily before their dissolution back into the liquid.

Several studies in water have found short ultrasound pulses can induce inertial cavitation between 0.5 – 2 MPa peak negative pressure at 1 MHz, which agree well with theory for heterogeneous cavitation for nuclei of radii on the order of microns[6, 14-16]. Cavitation and potentially related tissue damage has been detected in-vivo under similar acoustic conditions, particularly with the introduction of contrast agents or in the presence of gas bodies such as lung or intestine[5, 17]. However, such cavitation events are strongly related to the heterogeneous distribution of micron-sized nuclei at the site of insonation, which appear to be rare *in-vivo*[18]. However, it is possible that smaller stabilized bubbles exist which grow during insonation by rectified diffusion or tissue outgassing from heating during treatment.

3.1.2 Homogeneous Nucleation

In the absence of impurities, another form of nuclei may still exist in the body of the medium. Homogeneous or spontaneous nucleation can occur within the medium when thermal or electrical fluctuations of an individual group of molecules create a favorable energetic condition such that the energy to create a nucleus of a given radius is lower than a critical value[19]. Since the nuclei are intrinsic to the pure material in this situation, cavitation of this nature can be considered a measure of the tensile strength of liquids[20]. Classical nucleation theory provides an estimate for the tensile strength of a liquid based on the formation of such nuclei[21]. For water, this value is $p \cong$ -140 MPa. Alternative models of water's tensile strength exist with lower values between 27 MPa – 100 MPa[22, 23].

Due to the delicate nature of the measurement, experimental results for such a pressure threshold have varied significantly. However, multiple independent measurements have found a distinct threshold in the range of 24-33 MPa. These methods include application of a quasi-static tension by a rotating capillary tube[20], application of highly focused sinusoidal pulses[24, 25], and focused shock waves[26, 27]. Herbert et al. noted that this cavitation threshold was remarkably consistent between samples and even water with different purity levels[25]. In another study, Sankin and Teslenko proposed the existence of two distinct sets of nuclei: micron-sized impurities which are responsible for heterogeneous cavitation, and ubiquitous nano-sized nuclei which are excited by a threshold of ~33 MPa[26]. The range of pressure values in these studies is far from the theoretical threshold from classical nucleation theory for water. One group has experimentally reached nearly 140 MPa tensile pressure by water in small quartz inclusions, but these pressure levels were indirectly determined from an extrapolation of an equation of state[28].

Cavitation-based ablation of tissue as with histotripsy[29, 30] depends on the generation of a dense cavitation cloud, and thus it is important to obtain knowledge of the cavitation nuclei distribution in tissues and tissue phantoms. Thresholds for cavitation clouds in histotripsy have been reported in several studies, and vary between peak negative pressures of 6-15 MPa in degassed water[31-33] and between 13.5-21 MPa in tissue and tissue phantoms[34, 35]. In light of the results from the previous chapter that the mechanism of cloud formation depends on multiple factors, not just peak negative pressure, the variation in threshold is somewhat explicable. Similar pressure levels are applied for *in-vivo* experiments, although the exact pressure at the focus is not known because reflection, aberration, and attenuation of the wave during these experiments alter

the effective focal pressure. The pulse durations, pulse repetitions, and time to initiate cavitation also vary between these different studies.

In the experiments described in this chapter, these factors are minimized by simply applying a single focused pulse which contains a single high-amplitude pressure cycle to cavitate the medium within a time from of hundreds of nanoseconds. This minimizes the possibilities of rectified diffusion over many cycles[36], residual nuclei from previous pulses[37], and heterogeneous nuclei caused by impurities from artificially lowering this 'intrinsic' pressure threshold.

3.2 Measurement of Cavitation Thresholds

3.2.1 Methods: Exposure Chamber

A chamber was constructed to allow sonication of the sample and simultaneous visualization of the region of interest in transparent samples to observe cavitation (Figure 3.1). The chamber was made from PTFE, glass, and 316 stainless steel to operate over a wide temperature range and with a variety of chemicals. Two glass windows were inserted in the walls of the chamber to facilitate high-speed photography of the cavitation activity at the interface. Acoustic windows in the front and back made from a 12-μm thickness low-density polyethylene membranes were added to contain fluids in the chamber and allow ultrasound propagation into the sample. A fluid inlet and outlet port were embedded in the top and bottom of the chamber for circulation of fluid when necessary. The chamber was cleaned between experiments by first washing in a detergent solution, then soaking in acetone, and finally rinsing thoroughly with distilled water.

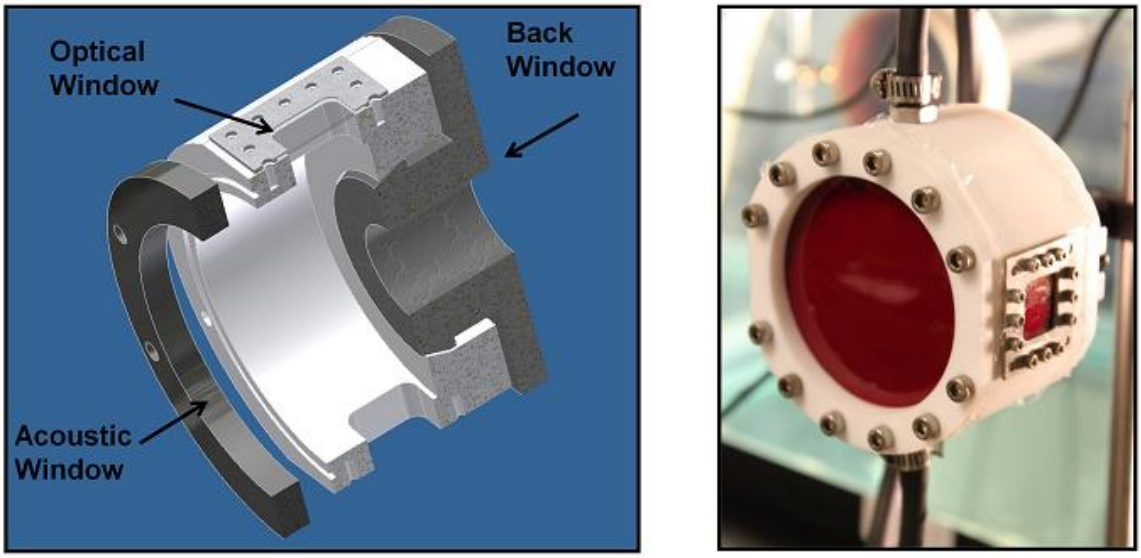

Figure 3.1. CAD cross-section (left) and photograph (right) of the sample chamber used to contain materials during experiments. A large acoustic window is present in the front and a small window in the back to allow ultrasound transmission to the medium. Two optical windows are positioned 180 degrees for backlit photography of cavitation.

3.2.2 Methods: Sample Preparation

The cavitation threshold of several liquid media, tissue phantoms, and canine tissue specimens were tested. Tap and distilled water and 1,3-butanediol were degassed by rigorously boiling the liquid in a 1-liter Pyrex flask on a hot plate for 10 minutes while stirring with a Teflon-coated magnetic stir bar, then sealing the flask and cooling the liquid to room temperature for the experiment before unsealing. Using this method, gas levels of ~10% O_2 saturation could be achieved in water.

Tissue phantoms were made from a mixture of gelatin or agarose powder and water. Gelatin and was chosen for its optical clarity. Gelatin powder (G2500, Sigma Aldrich, St. Louis, MO) was added to distilled water at 5%-15% wt/vol. The solutions were heated in a Pyrex flask on a hot plate to boiling temperature

to completely dissolve all powder, and allowed to boil for 10 minutes while stirring. The flask was then sealed until the temperature was lowered to 40°C, then added to the test chamber and allowed to cool to room temperature before the experiment.

Blood and tissue samples were acquired from canine research subjects immediately post-mortem in an unrelated study. Tissue was placed in room temperature saline in a polypropylene container and experiments were conducted within 24 hours of harvest. Each sample was embedded in the chamber in 5% gelatin, which was prepared as described above.

Blood was collected and placed in a citrate-phosphate-dextrose solution (C7165, Sigma Aldrich, St. Louis, MO) with a ratio of 9:1, and then stored in refrigeration at 4°C in a polypropylene container. The blood was added to the chamber directly, and allowed to return to room temperature before sealing the chamber prior to experiment. Blood clots were created from whole blood at room temperature by addition of 0.05 mL of 0.5 M $CaCl_2$ per 1 mL of blood. After adding the mixture to the chamber, the chamber was placed in a water bath at 37°C for 2 hours to allow incubation of the clot. The chamber was then allowed to return to room temperature, sealed, and positioned in the water tank for the experiment.

3.2.3 Methods: Pressure Pulse Generation

In order to measure the cavitation threshold, a predictable, high amplitude negative pressure must be developed in the body of the medium under test. A spherically-focused transducer with a center frequency of 1.1 MHz was used to generate ultrasound pulses. The transducer consisted of 8-element array of 2-cm diameter focused elements aligned confocally with a radius of curvature of 5 cm. The overall aperture of the transducer array was 8.5 x 7 cm. The multi-element

transducer allows characterization of each element output to estimate the focal pressure beyond the cavitation threshold, as described in section 3.2.4. The transducer was connected to a class D amplifier developed in our lab[38] through a matching network, which provided high driving voltage signal to each element, up to 1600 V_{pp}.

The amplifier signal was controlled by a field-programmable gate array (FPGA) logic board (Altera, San Jose, CA, USA). The transducer was driven with a 2-cycle sinusoidal electrical signal. Due to the limited transducer bandwidth of ~ 50%, only the second cycle of the pulse reaches the maximum amplitude, meaning that there is only one negative pressure excursion with the peak amplitude (Figure 3.2). This very short pulse prevents cavitation occurring through shock scattering so that cavitation is only generated by the negative pressure excursion of the incident wave. The pulse repetition frequency for the transducer was kept very low (0.33 Hz) to minimize the possibility of cavitation from a pulse from changing the probability of cavitation on a subsequent pulse. Preliminary experiments revealed that for PRFs > ~ 1 Hz, cavitation during a pulse increased the likelihood of cavitation on the following pulse, which could artificially lower the apparent cavitation threshold. Below this value, the probability did not change significantly with PRF. The lifetime of remnant bubble nuclei in histotripsy has been investigated previously, and was found to be on the order of tens of milliseconds[37], although the sonication pressure in that study was lower amplitude.

In solid materials, the focus was translated for each pulse by 1 mm transverse to the acoustic propagation direction in a 10 x 10 grid for each pressure level to minimize the effects of cavitation damage to the solid sample from altering the probability of cavitation. Each focal volume in the solid received no more than 1 pulse at each acoustic pressure level, and only with a fraction of these pulses did

cavitation occur. One hundred pulses were applied to the sample at each pressure level tested. The pressure levels were varied in a randomized order to minimize any possible hysteretic effects of pressure level on cavitation activity.

3.2.4 Methods: Transducer Focal Pressure Measurement

Measurements of the focal pressure were recorded with a calibrated fiber-optic probe hydrophone (FOPH)[39]. The FOPH was calibrated by substitution comparison with two piezoelectric reference hydrophones (HGL-0085 and HGL-0200, Onda Corporation, Sunnyvale, CA). Each hydrophone had a reported calibration uncertainty at 1.1 MHz of ± 1 dB (~ ± 12%), thus the sensitivity was taken from the average of both measurements with uncertainty $\varepsilon/\sqrt{n} = \pm 8.5\%$. Both reference hydrophones' calibrations were in agreement at low pressure levels (up to 3 MPa) within 4%. The measurements were captured in a free-field condition in water degassed to 25% O_2. Pressure levels up to 23 MPa peak negative pressure could be recorded in water with the FOPH. Above this level, cavitation occurred on the hydrophone often or the fiber tip fractured, which precluded further measurements. Thus, it was not possible to directly measure the focal pressure in water up to the maximum transducer output. Two separate indirect measurement techniques were employed to determine the peak negative pressure at the focus vs. transducer driving voltage.

For the first technique, the fiber optic hydrophone was positioned in another liquid which was found to have a higher threshold for cavitation: 1,3 butanediol. This method has been used with piezoelectric hydrophones in castor oil to prevent cavitation damage to their surface from lithotripter shockwaves[40]. Butanediol has a density (ϱ = 1005 kg/m^3) and sounds speed (c = 1505 m/s) very similar to water (ϱ = 1000 kg/m^3 and c = 1484 m/s), eliminating any significant acoustic reflection at the interface between the two. The fiber probe was

positioned in a small container of butanediol with an acoustic window of 12-μm low-density polyethylene facing the transducer. To ensure the attenuation in butanediol did not alter the measurement significantly, the probe tip was positioned only 5 mm from the interface. The sensitivity of the fiber optic hydrophone in butanediol was calculated by comparison of the focal pressures measured in water with the FOPH and piezoelectric hydrophones at low pressure values.

The second technique used to estimate the focal pressure was summation of measurements from individual elements' pressure output at the focus. Each of the 8 elements in the transducers was driven separately, and the pressure waveforms were measured at the transducer focus in degassed water with the fiber optic hydrophone. The waveforms from each element for a given driving voltage were then summed to estimate the pressure waveform generated by the transducer when all 8 elements are driven in phase. Generally, this technique is not acceptable for high-amplitude measurements, because nonlinear propagation is dependent on the pressure amplitude along the path from the transducer to focus. When an element is driven individually, the pressure in and around the focus is lower, meaning the waveforms measured independently will be less distorted than the waveform with all elements driven simultaneously. This can lead to significant errors in pressure. In this study, however, the elements are each focused individually and the beam paths from each element do not overlap except at the transducer focus, which is only a few mm distance. Thus, most of the nonlinear distortion develops in the nearfield of each element, independent of the others. This assertion was verified by comparing the measurements at lower pressures with focal waveforms captured with all 8 transducer elements driven at the same time. The pressure calibrations for the three methods described are shown in Figure 3.2.

With the FOPH in butanediol, the pressure measurement error compared with the standard measurement in water up to supply voltage = 230 V (p_- = 23 MPa) was $\varepsilon \leq 10\%$, and ε_{mean} = 2.6%. Using the method of element summation to predict the focal pressure, the error compared with the standard measurement was $\varepsilon \leq 15\%$, and ε_{mean} = 8.7%. At higher transducer output where the standard measurement could not be made in water, the two methods agreed within 15% of each other for all measurements. Based on the excellent agreement of the data in water and butanediol, the measurements in butanediol were used fit to a 5th order polynomial which was used to determine the peak negative pressure vs. voltage. The overall uncertainty for the absolute value of peak pressure is estimated to be ± 8.9% based on the combined uncertainty of the reference hydrophone and comparison between water and butanediol measurements.

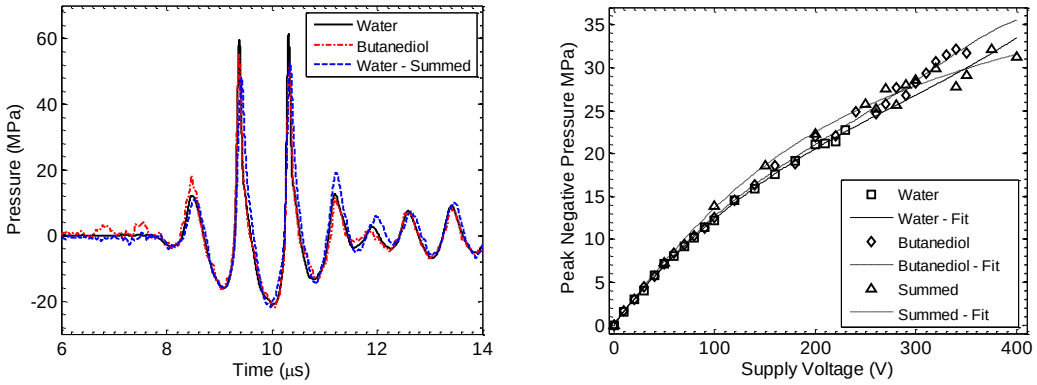

Figure 3.2. Focal waveforms at p_- = -21.5 MPa (left) and peak negative pressure vs. transducer voltage (right) for the two measurement techniques used to measure large tensile pressures as well as focal measurements in water. Waveforms with the three measurements appeared nearly identical in peak negative pressure value, although the peak positive pressure was slightly reduced for the two experimental measurement techniques. The error in peak negative pressure between measurement techniques was no greater than 15% for any pressure value, and the maximum error between the three polynomial curve fits is 11%.

3.2.5 Methods: Image Capture and Processing

A high speed camera (V210, Vision Research, Wayne, NJ) was used to capture images of the focal zone directly after the propagation of each pulse through the focus in all transparent media. The camera was focused with a macro-bellows lens (Tominon, Kyocera, Kyoto, Japan) through the window of the chamber to observe the focal region. The camera was backlit by a continuous light source to produce shadowgraphic images of the cavitation activity. The camera was triggered to record one image for each pulse applied, 3 μs after the pulse reached the focal center. The camera exposure time was 2 μs. The minimum resolvable size of a bubble was about 15 μm at the magnification of the described experimental arrangement.

Images were converted from grayscale to binary by an image intensity threshold determined by the background intensity of the images in image processing software (MATLAB, The Mathworks, Natick, MA). Bubbles were indicated as any dark regions > 5 pixels in area. The number of frames which contained detected cavitation bubbles on an image was recorded and the fraction of total frames for which any cavitation was detected was recorded as the probability.

3.2.6 Methods: PCD Measurements and Signal Processing

While high-speed photography provides excellent detection of cavitation in transparent media, it cannot be used with most tissue samples. Additionally, the camera only detects the presence of cavitation at one time point, and does not provide information regarding the cavitation dynamics. An acoustic method was also used to detect cavitation in all media, using a broadband transducer to detect emissions in the focal region. A passive cavitation detector (PCD) consisting of a broadband 5-MHz focused transducer with focal length = 10 cm

was positioned behind the therapy transducer with their foci overlapping. The central hole in the therapy transducer provided an unobstructed aperture for the PCD. The PCD was connected to a signal amplifier (PR5072, Panametrics NDT, Waltham, MA), which was in turn connected to an oscilloscope (LT372, Lecroy, Chestnut Ridge, NY). The time window for the signal was set so that the PCD voltage was recorded starting 5 μs before the first cycle of the pulse arrived at the focus, and lasting for 200 μs. This window allowed recording of backscatter of the pressure pulse from cavitation bubbles[41], as well as emissions from bubble collapse well after the pulse passed the focus[42, 43].

To determine whether cavitation occurs in a given pulse, the signal caused by backscattering of the incident pulse from the focus was evaluated. In the presence of a cavitation bubble, part of the focused wave scatters from the bubble, greatly increasing the backscattered pressure received by the PCD. This signal appeared on the PCD at the time point based on the time of flight between the focal lengths of both transducers. Since all surfaces in the chamber were at least 1.5 cm from the focus, the possibility of the scattering from other sources besides cavitation was ruled out by time windowing the signal. The integrated frequency power spectrum of this backscatter signal $\beta(t)$ was used as a measure of whether cavitation occurred during the pulse. The signal's Fourier transform, $B(f)$, was first calculated, and the integrated power spectrum, S, was calculated by:

$$S = \sum_{f_1}^{f_2} |B(f)|^2 \qquad 3.1$$

It is common to evaluate subharmonic or superharmonic emissions which are generated solely by cavitation under lower-amplitude long-burst excitation, when these frequencies are not present in the incident pressure waveform[44, 45]. However, the short, high-amplitude pulse applied in this study was very

broadband because of the many harmonics from nonlinear distortion and short pulse duration. The largest component of the backscatter was near the center frequency (1.1 MHz), and thus the power spectrum of the backscatter signal around this frequency (0.6 – 1.6 MHz) was used as a measure of cavitation presence.

The cavitation threshold was defined by scaling the expected value for S based on the focal pressure curve obtained from calibration measurements. The following procedure was applied:

1. The integrated power spectrum, S_F, for the focal pressure waveforms captured by fiber optic hydrophone was calculated using Eq. 3.1.
2. The integrated power spectrum, S_{PCD}, for the pressure signals received by the PCD was calculated. The mean and standard deviation in S_{PCD} for 100 pulses were calculated.
3. Since it is expected that the backscatter signal will increase in proportion with focal pressure, a plot of S_{PCD} vs. S_F at low pressures (where cavitation does not occur) should follow a linear relationship. The expected value of S_{PCD} vs. S_F is given by:

$$S_{PCD}(V_n) = \frac{S_F(V_n)}{S_F(V_{n-1})} \cdot S_{PCD}(V_{n-1}) \qquad 3.2$$

   If, for a single pulse at a voltage V_n, the value S_{PCD} exceeds the expected value given in Eq. 3.2 + 3 standard deviations, it is considered a cavitation event. The voltage V_{n-1} is then chosen as the last point for the linear fit.
4. The mean values and standard deviations for $S_{PCD}(V_n, V_{n+1},\ldots,V_N)$ are estimated by a least-squares linear regression to the values $S_{PCD}(V_1, V_2,\ldots,V_{n-1})$ and linear extrapolation with respect to S_F.

5. For each of the signals recorded by PCD for $(V_n, V_{n+1}, \ldots, V_N)$, the value S_{PCD} is compared with the expected value calculated in step 4. If this value is greater than expected + 3 standard deviations, the signal is considered a cavitation event.

This method allowed a quantitative way to define whether the signal was above a certain threshold for cavitation, based on whether the backscattered signal was 'much larger' than expected. It is assumed that cavitation does not occur at the lowest pressure values tested so that a linear relationship for backscatter vs. focal pressure can be established. At least 5 points were measured where the relationship was found to be linear as determined by Step 3. The assumption of a linear extrapolation with respect to S_F was verified in water at higher amplitudes by extracting the mean value of S_{PCD} for pulses where high-speed photography did not observe cavitation.

Additional analysis of the PCD signal was performed to determine the collapse times for bubbles based on a secondary emission recorded at a later time than the backscatter signal (Figure 3.3). This signal consists of a short, positive pressure spike created by inertial collapse of the bubble. This signal has been characterized in previous research using passive cavitation detectors or hydrophones to measure the bubble collapse pressure[42, 43, 46]. The collapse time was characterized by the time difference between the backscatter signal and the collapse signals.

3.2.7 Results: Cavitation Threshold in Water

Cavitation bubbles were observed on high speed camera when a certain negative pressure threshold was exceeded (Figure 3.3). As the pressure was increased, the probability of observing cavitation in the focal volume, calculated

as the number of trials out of 100 in which cavitation was observed, followed a sigmoid function, given by

$$f(p_-) = \frac{1}{2}\left[1 + erf\left(\frac{p_- - \mu}{\sqrt{2\sigma^2}}\right)\right], \quad 3.3$$

where *erf* is the error function, μ is the pressure at which the probability $P = 0.5$ point and σ is a variable corresponding to the width of the transition between $P = 0$ and $P = 1$, with $\pm\sigma$ giving the difference in pressure from about $P = 0.15$ to $P = 0.85$ for the fit. The threshold in distilled, degassed water was found to be $\mu = 28.1$ MPa and $\sigma = 1.7$ MPa. Note that at lower values of p_-, cavitation was occasionally observed which did not follow the curve function. These cavitation events are likely due to contamination of the sample by heterogeneities in the liquid, which could not be entirely avoided throughout the experiment. In the experimental data, cavitation was observed with $P = 1$ for $p_- > -30$ MPa. As P approaches 1, multiple cavitation bubbles were observed by high-speed photography each pulse within the focal region, and the area over which the bubbles was observed increased as well. The bubbles' diameters were consistent at the time point captured by the camera.

The PCD detected a distinct signal in the presence of single or multiple cavitation events. First, a multicycle burst with a center frequency about 1.1 MHz was detected with a time delay corresponding to the time for the therapy pulse to travel from the transducer to the focus to the PCD - between 100 - 110 μs from the time the test pulse was emitted. Between 10 – 100 μs after this burst signal was received, one or more short positive pressure spikes were observed on the PCD signal, indicating shocks emitted during bubble collapse[43]. When no cavitation was observed on high-speed camera, both of these signals were absent (Figure 3.3). The accuracy of detection is validated in the set of data for water.

Figure 3.4 shows the value S_{PCD} vs. pulse number for 100 pulses near the cavitation pressure threshold μ in degassed, distilled water. Overall, an error rate between 1-2% is observed for a data set at one pressure level. Errors in detection generally occurred when a cavitation bubble at the edge or outside the focus was present, where the scattered signal received by the PCD was weaker than cavitation in the focus.

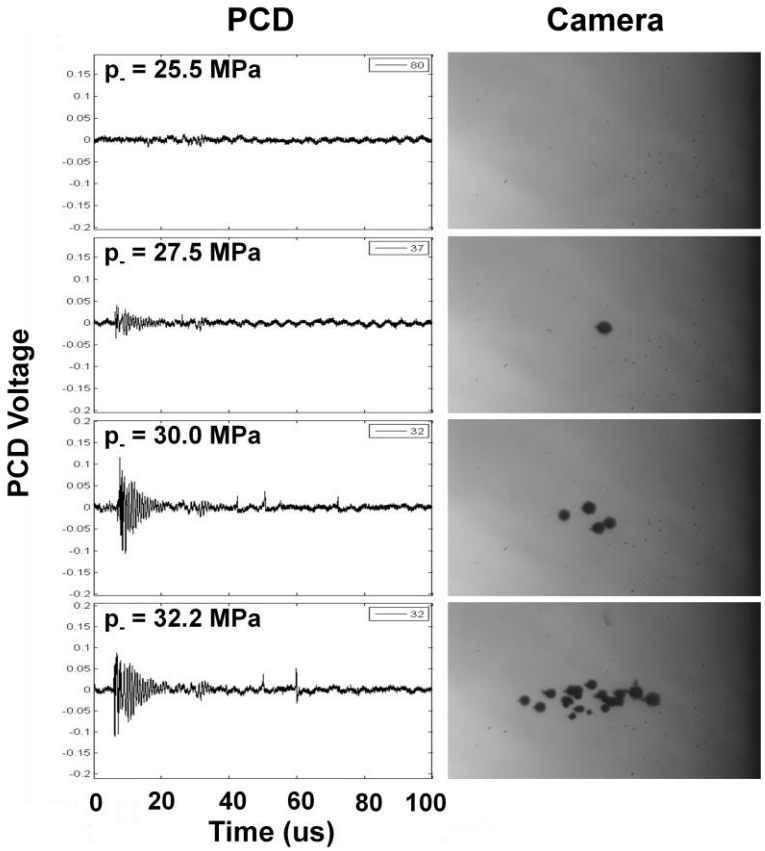

Figure 3.3. Sample PCD temporal signals (left) and camera photographs (right) of cavitation at the transducer focus. The PCD signals show an initial burst near the therapy frequency due to backscatter from the cavitation bubbles, as well as one or more short positive pulses – shockwaves from cavitation collapse. A small signal around 30 μs is caused by a reflection of the therapy pulse from the back membrane of the housing, and is windowed out of the signal from evaluating cavitation with the PCD. Ultrasound propagation in these images is from right to left.

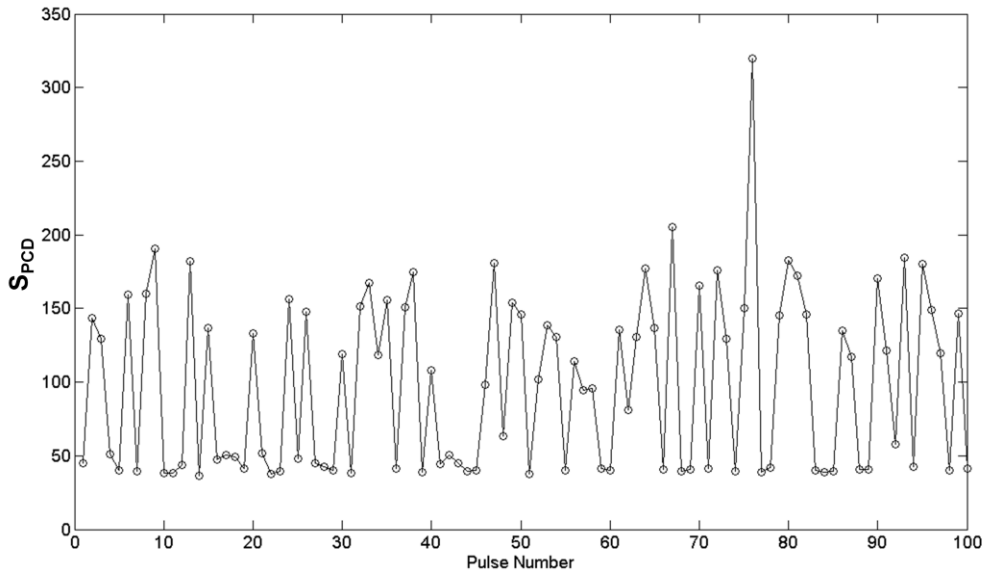

Figure 3.4. Integrated power spectrum (S_{PCD}) for the signal in distilled water vs. pulse number for 100 pulses. The peak negative pressure for this data set was p_- = 28.6 MPa - near the 50% threshold for cavitation. A bimodal distribution of values is present, with the lower consistent values indicating a lack of cavitation, and the larger more variable values indicating the presence of one or more bubbles. The threshold for distinguishing cavitation was set according to the statistical procedure described in the methods.

Purity and gas concentration of the water sample had a small effect on the cavitation threshold probability curve. In unfiltered tap water which was only mildly degassed to 90% O_2 concentration, μ = 26.4 MPa and σ = 1.3 MPa gave the best fit to the data set, compared with μ = 28.1 MPa and σ = 1.7 MPa for distilled water with about 10% O_2 concentration. The experimental and fit probability curves for both media are displayed in Figure 3.5.

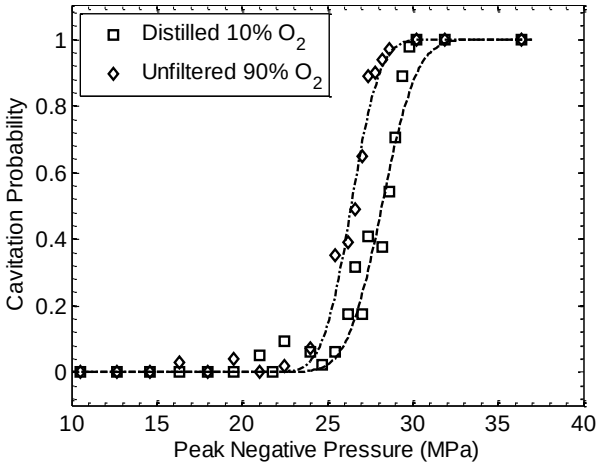

Figure 3.5. The cavitation threshold probability data and fit curves in distilled and tap water. The two both indicated a sigmoidal trend in probability with peak negative pressure. The fit values for the curves indicated by Eq. 3.3 are μ = 28.1 MPa and σ = 1.7 MPa for distilled water with 10% O_2 saturation and μ = 26.4 MPa and σ = 1.3 MPa for unfiltered water with 90% O_2 saturation.

3.2.8 Results: Cavitation Thresholds in Other Media

A similar function of cavitation probability vs. pressure was observed in all water-based media. Additionally, the cavitation pressure threshold value μ was also similar in these materials. The fit curves for the experimental cavitation probability data in tissue mimicking materials of 5% and 15% gelatin in distilled water gave μ = 26.5 MPa and μ = 26.4 MPa respectively, with σ = 2.2 and 0.8. One difference between the samples was that the bubbles were generally smaller in size at the time point captured by the camera for the 15% gelatin than the 5% gelatin or water (Figure 3.6). However, the region over which cavitation occurs in each sample was similar at the same pressure levels. While the initial backscatter signal was detected in both 5% and 15% gelatin samples, bubble collapses were undetectable in nearly all of the signals, while at a similar pressure level in 5% gelatin and water they were observed every pulse.

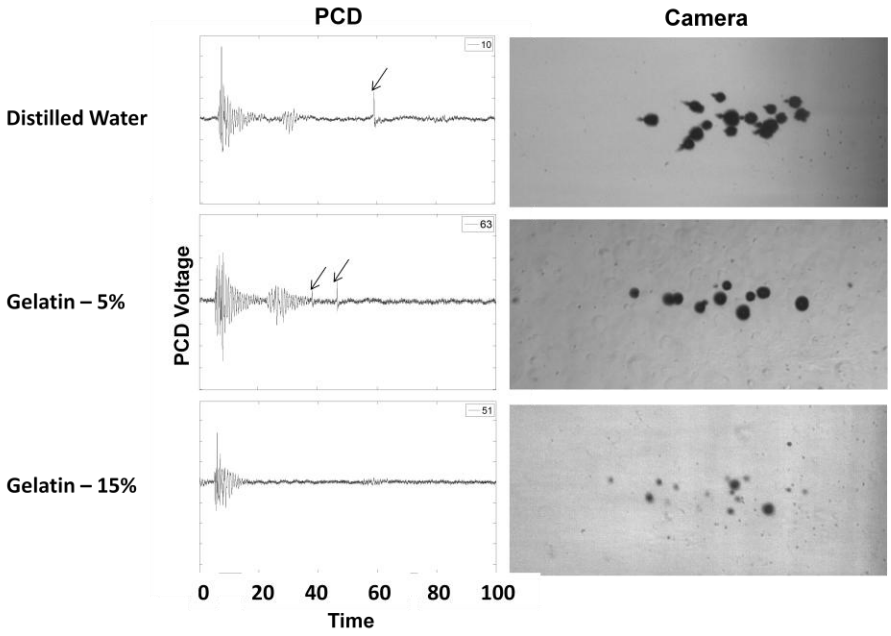

Figure 3.6. Example PCD signals (left) and corresponding high-speed photographs (right) of cavitation in distilled water and gelatin at 5 and 15% concentrations. Note that the diameters of the bubbles in 15% gelatin is significantly reduced compared with the other two samples, although they cavitate in roughly the same volume. Ultrasound propagation in these images is from right to left.

A similar threshold was also observed in canine blood, clotted blood, and kidney. In these materials, no images could be captured by the camera, but the same cavitation backscatter signals and bubble collapse signals were observed in all three materials. Blood and blood clot had μ = 27.6 and 26.7 MPa, respectively. Kidney tissue (cortex) was slightly higher with μ = 30.0 MPa. The value σ was 0.7 for both clotted and unclotted blood, and 2.2 kidney. The least negative pressure at which cavitation was observed in these three samples was p_- = 16.2 MPa with P = 0.01, indicating similarly few weak nuclei in the tissue samples.

Experiments were also performed in three materials which were not primarily water-based: 1,3 butanediol, olive oil, and canine visceral fat. The threshold in butanediol (μ= 35.6) and olive oil ($\mu \geq 36$) were greater than any of the water-based samples. In olive oil, the curve could not be well-fit to a

threshold because the probability of cavitation was low even at the maximum pressure output from the transducer. However, it is assumed that P approaches 1 at pressures much greater than the range in this study, similar to other media. Bubble expansion and collapse were also suppressed in butanediol and olive oil; cavitation bubbles appeared similar size to those in 15% gelatin and cavitation collapses were not detected with the PCD. Two samples of canine visceral fat to were tested to produce two independent probability curves. The threshold was significantly lower than in any of the above media, with μ = 15.6 and 16.9 MPa for the two specimens, and σ = 0.8 and 0.5 respectively.

The individual curves for different materials are given in Figure 3.7, and a summary of the relevant properties of the different samples is given in Table 3.1.

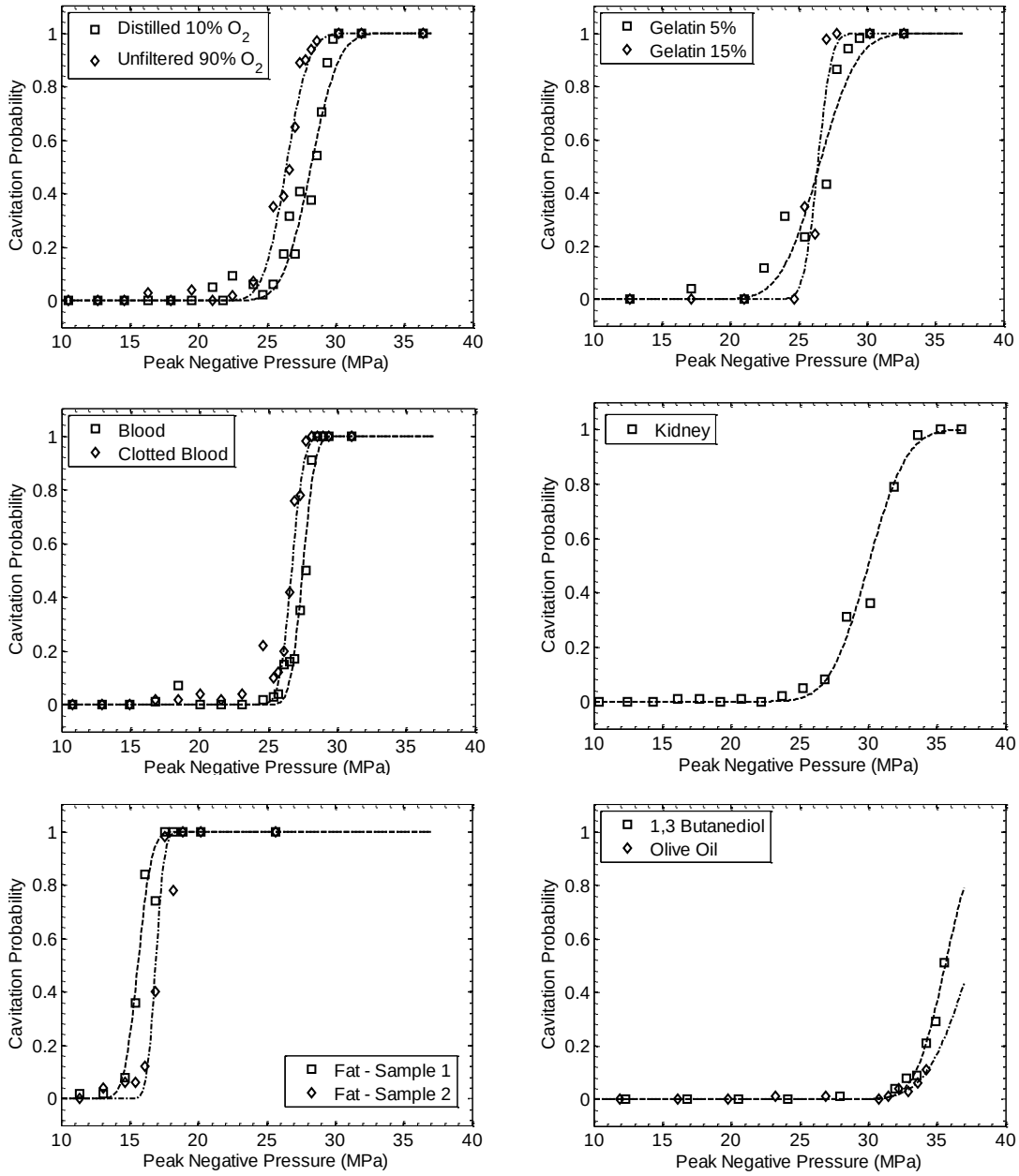

Figure 3.7. Probability data and fit curves for all media tested. Each data point is the fraction of 100 pulses where cavitation was detected. Curves are fit by nonlinear least-squares regression to each data set.

Table 3.1. Acoustic and mechanical properties of tissue at 1 MHz. The two water samples (D – 10) and (U – 90) are distilled water with 10% O_2 saturation and unfiltered water with 90% O_2 saturation, respectively. The cavitation threshold in olive oil could not be accurately determined since the transducer could not generate large enough pressure amplitude to cause consistent cavitation. The uncertainties listed for μ are the combined absolute uncertainty of the pressure measurement and standard errors of the fits for μ. The uncertainties listed for σ are the standard errors for the fits for σ.

Material	ρ (kg/m^3)	c (m/s)	α (dB/cm)	η (mPa-s)	γ (mN-m)	E (kPa)	Pressure Threshold μ (MPa)	Width σ (MPa)
Water (D 10)	998	1484	0.0022	1	72		28.1 ± 2.7	1.7 ± 0.3
Water (U 90)	998	1484	0.0022	1	72		26.4 ± 2.5	1.4 ± 0.3
Gelatin 5%	1015	1505	0.1	40	40	4.5	26.5 ± 3.0	2.2 ± 0.9
Gelatin 15%	1045	1550	0.1		40	36.0	26.4 ± 2.8	0.8 ± 0.6
Blood	1060	1584	0.2	3	60		27.6 ± 2.6	0.7 ± 0.6
Blood Clot	1060	1584	0.2	3	60	0.1-1.0	26.7 ± 2.5	0.7 ± 0.2
Kidney	1050	1560	1.0	30		5.7	30.0 ± 3.0	2.2 ± 0.4
Fat (1)	950	1478	0.5	12		1.9	15.6 ± 1.6	0.8 ± 0.3
Fat (2)	950	1478	0.5	12		1.9	16.9 ± 1.7	0.5 ± 0.3
Butanediol	1000	1522	0.1	97	37		35.6 ± 3.4	1.7 ± 0.3
Olive Oil	915	1440	0.2	84	36		> 36	

*References: Gelatin[47, 48]. Blood[49-51],Clot[52], Kidney[50, 53, 54],Fat[50, 55, 56],Butanediol[57, 58], Olive Oil[59, 60].
†Symbols: ϱ = density, c = sound speed, α = attenuation @ 1 MHz, η = dynamic viscosity, γ = surface tension, and E = elastic (Young's) modulus.

The fit curves were analyzed statistically to determine if the difference in the values μ were significantly different from each other. The standard errors for the parameters μ were estimated by a covariance matrix using the delta method[61]. The curves were compared with a two-sample t-test with statistic $t\left(\mu_1-\mu_2,\sqrt{SE_1^{\,2}+SE_2^{\,2}}\right)$ with a 95% confidence interval. Note that the standard error does not include the uncertainty in absolute pressure, only the uncertainty in the fit, because the values μ are relative. The differences between μ for unfiltered water, gelatin at 5% and 15% concentration, and blood clot were not

significantly different (p-value > 0.15). All other materials were statistically different for these four and from each other (p-value < 0.023).

3.3 Theoretical Analysis of Cavitation Thresholds

3.3.1 Numerical Model

A single bubble cavitation model was implemented to evaluate the pressure threshold response of cavitation nuclei related to the measured threshold. Since the primary focus of this study is the threshold behavior and expansion phase of the bubble, a simple model was used which does not account for extreme conditions under bubble collapse, although accounts for liquid compressibility. The Keller-Miksis equation[62], modified by Yang and Church to include elasticity[1], was used to describe the radius-time behavior of cavitation bubbles in a viscoelastic medium, given as:

$$\left(1-\frac{\dot{R}}{c}\right)R\ddot{R}+\left(1-\frac{\dot{R}}{3c}\right)\frac{3}{2}\dot{R}^2=\left(1-\frac{\dot{R}}{c}\right)\frac{P(\dot{R},R,t)}{\rho}+\frac{R}{\rho c}\frac{\partial P}{\partial t} \qquad 3.4$$

where R is bubble radius, the dot is a time derivative, c is the speed of sound in the medium, ρ is the medium density. P is the pressure at the bubble wall in the liquid, which includes terms for the internal gas pressure in the bubble following adiabatic conditions, as well as pressure due to surface tension, viscosity, and acoustic pressure:

$$P\left(\dot{R},R,t\right)=\left(p_0-p_v+\frac{2\sigma}{R_0}\right)\left(\frac{R_0}{R}\right)^{3\kappa}-p_0-\frac{2\sigma}{R}-\frac{4G}{3R^3}\left(R^3-{R_0}^3\right)-\frac{4\eta\dot{R}}{R}-p_a(t) \qquad 3.5$$

In Eq. 3.5, p_0 is the ambient pressure far from the bubble wall in the liquid, p_v is the vapor pressure in the bubble, σ is the surface tension of the liquid, R_0 is the initial bubble radius at time t = 0, κ is the polytropic index (ratio of specific

heats), G is the shear modulus, η is dynamic viscosity, and $p_a(t)$ is the time-varying acoustic pressure applied to the bubble. The values of c, ρ, p_v, σ, and η were chosen with respect to the temperature of the medium (297 K) for simulation. To numerically simulate the bubble response, the initial conditions for pressure are first found by Eq. 3.5. Next, the bubble radius vs. time is found with Eq. 3.4 using a variable order solver based on numerical differentiation formulas (ode15s, Matlab, The Mathworks, Natick, MA).

A nonlinear pulse model with a Gaussian pulse envelope was used to simulate the 2-cycle pressure waveform[63]. This pressure pulse is given as

$$p_a(t) = p_f \sum_{m=1}^{\infty}\left[\frac{\sin\left(m\omega\left(t-\tau\right)+\phi\right)}{m}\right]\cdot\exp\left[-\left(\frac{t-\delta}{\xi}\right)^2\right] \qquad 3.6$$

where p_f is the fundamental pressure amplitude, ω is the frequency, τ is chosen such that the start of the wave is at $p_a(0) = 0$, φ is a phase shift to create waveform asymmetry, δ is the time delay to the center of the pulse, and ξ defines the pulse width. For this simulation, $\omega = 6.91 \times 10^6$ rad/s, $\tau = 1.25\,\pi / \omega$, $\varphi = -\pi/4$, $\delta = 2.85$ μs, and $\xi = 1.2$ μs. The infinite sum was truncated to $m = 100$. This gave a pulse which closely approximates the shape and ratio p_+/p_- given in Figure 3.2.

The threshold in water was used to determine the radius of a model bubble nucleus which cavitates at the pressure threshold μ. Simulating a single spherical bubble in water, the bubble initial radius r_0 and peak negative pressure of the applied pulse was varied to evaluate the bubble response. Bubbles expansion was minimal ($r_{max} < 2r_0$) below a certain value for p_-, while above this value, large bubble growth and collapse was observed ($r_{max} > 10^4 r_0$). This pressure threshold was defined as the threshold for inertial cavitation. To achieve this threshold around $p_- = 28.1$ MPa (the same as distilled water), the necessary initial bubble radius is ~2.5 nm. The threshold was very distinct in water; a change in the

applied p_- of 1 kPa caused r_{max} to change from 4.2 nm to 30 μm (Figure 3.8). This characteristic is not observed for bubbles of 0.1 – 1 μm radius in response to ultrasound, which undergo a less well defined transition behavior between small linear oscillation and large inertia-dominated bubble growth and collapse as pressure amplitude is increased[64].

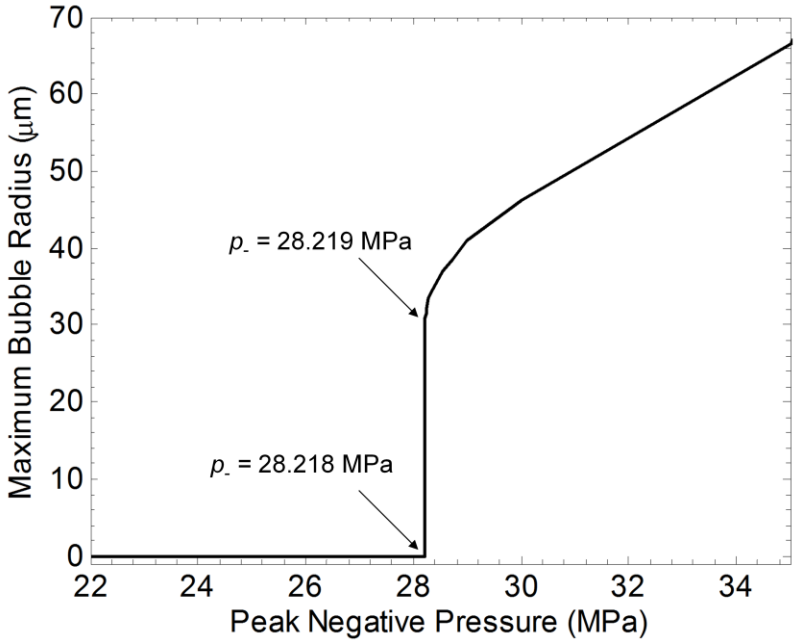

Figure 3.8. Maximum bubble radius achieved in response to a 2-cycle pulse vs. peak negative pressure of the pulse for a 2.5nm initial radius. Bubbles in this size range display a sharp threshold, in this case near p_- = 28.2 MPa.

The nuclei in this situation are much smaller than the corresponding resonant diameter for a 1.1 MHz wave in water. Because of this small size of the bubble, the cavitation threshold is nearly independent of in the frequency range of interest for ultrasound therapy (28.1 MPa at 0.1 MHz vs. 28.4 MPa at 10 MHz). The pressure threshold for bubbles this size is strongly dominated by surface tension of the medium. Despite the differences in measured surface tension of the tissues and tissue phantoms from pure water, their thresholds are similar, indicating either the radius of the model nucleus is different between them, or

the surface tension on the nanometer scale is similar to water. Butanediol, which does not contain water however, has a surface tension is 37 mN/m and the viscosity is 97 Pa-s. The bubble radius that fits the threshold of 35.6 MPa is 1.1 nm.

Other mechanical properties had a minimal effect of the threshold at 1.1 MHz. However, increasing viscosity created a stronger frequency-dependency for the threshold (Figure 3.9), a trend similar to that shown by Allen et al[2]. Additionally, at higher frequencies, the bubble expansion is lower. At 1.1 MHz, the threshold is 28.1-29.3 MPa for η = 0.001-0.1 Pa-s. Increased viscosity produced smaller growth, but did not change the threshold significantly. Change in the elasticity in the range G = 0 – 100 kPa (the approximate range for soft tissues) also did not significantly affect the threshold nor the maximum radius of the bubble (Figure 3.9). These data from the model support photographic observations which suggest that the threshold does not change significantly due to these properties, although the maximum growth and dynamic behavior of bubbles is suppressed specifically by higher viscosity or elasticity of a tissue.

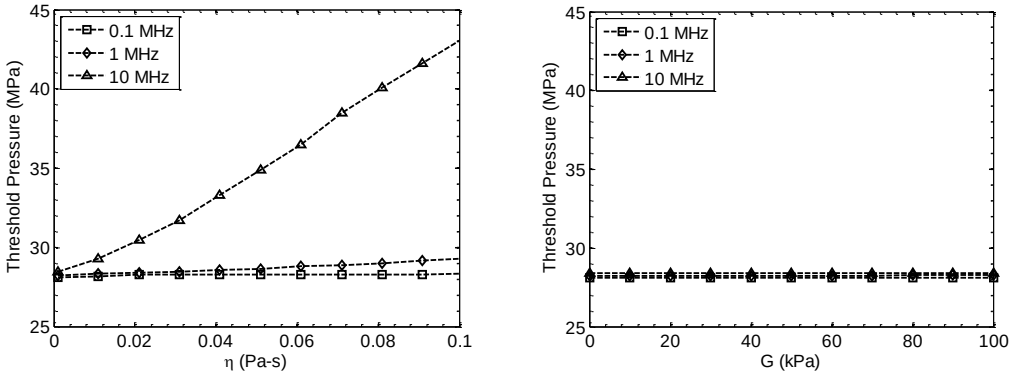

Figure 3.9. Cavitation threshold pressure for a 2.5-nm radius bubble vs. viscosity (left) and elasticity (right) for pulse center frequencies of 0.1, 1.1, and 10 MHz.

3.3.2 Simulation of Cavitation-Induced Lesions

Near the threshold pressure, single cavitation bubbles appeared primarily in a region near the center of the focal zone. When the focal pressure was significantly in excess of the cavitation threshold, cavitation bubbles occupied a region similar in shape to the focal zone each pulse. The area over which cavitation was observed was similar to the area which exceeded the pressure threshold μ. By integrating all 100 images of the cavitation observed by the camera at a given pressure level, the total region within the frame where cavitation was observed can be analyzed. This provides some indication for histotripsy ultrasound therapy of where damage would be expected to occur[65] (see Chapter 4). Figure 3.10 shows the integrated cavitation maps for water and 15% gelatin. Note that the extent of the bubble locations is similar at the same p_-, but the extent of the total cavitated region is smaller because of the suppressed bubble expansion in gelatin.

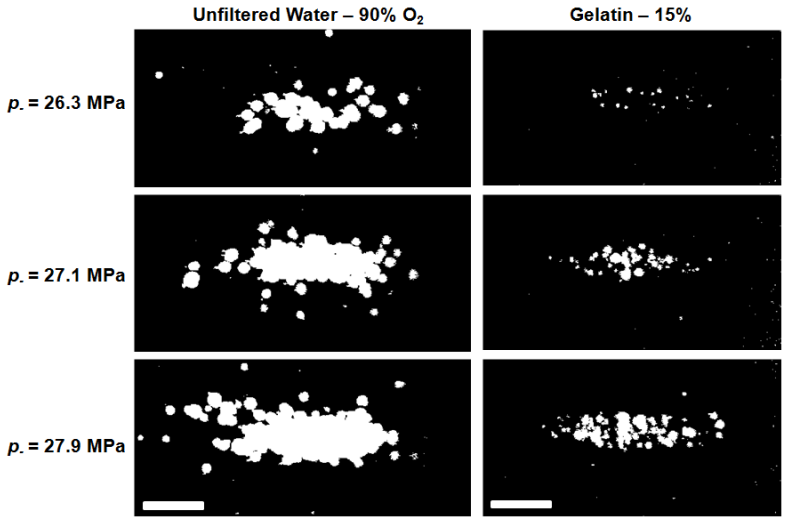

Figure 3.10. Integrated images of the locations where cavitation occurred over 100 pulses, shown in white for two materials with identical thresholds μ = 26.4 MPa. Over several pulses, the positions of cavitation add to generate a pattern similar to the focal zone of the transducer. Ultrasound propagation in these images is from right to left.

The data suggested the location and area of cavitation bubble generation is determined by where p_- is greater than the threshold. Assuming one has accurate knowledge of the peak pressure focal distribution, cavitation probability vs. pressure, and the cavitation radial dynamics, it should be possible to predict the area and extent of cavitation as a result of a set number of ultrasound pulses with a given p_-. First, the peak negative pressure vs. position can be mapped for a transducer from hydrophone measurements. Although the pulse in our case was distorted by nonlinear propagation, the beam profile for the peak negative pressure was similar to that in a linear simulation[66]. Next, the peak radius of a bubble vs. pressure can be determined by a simulation similar to that described above. Finally, the curves given in Figure 3.7 can be used to determine the probability of cavitation $P(x,z)$ as a function of pressure level $p(x,z)$. Due to the finite size of the area tested in the experiments above, however, the probabilities recorded are for the entire focal zone. Thus, P must be normalized to the volume of the focal zone. A Monte-Carlo-type simulation is then performed, where the probability $P(x,z)$ is compared with a random value between 0 and 1 at each spatial point for each pulse. Cavitation then occurs at point (x,z) for pulse n if the probability value is greater than a random number between 0 and 1 (i.e. $P_{norm}(x,y,z) > rand(x,y,z)$). This simulation then predicts the cavitation field for a given pulse. P_{norm} is obtained by multiplying P by a coefficient, determined by matching the simulation to the experiment such that the probability of cavitation occurring anywhere in the field of the simulation for 1 pulse is ~0.5 when $p_- = \mu$. Figure 3.11 shows an example of the total cavitated region from the simulation for different peak negative pressures, as well as the corresponding experimentally observed cavitated regions. Figure 3.12 gives the measured axial and lateral dimensions of the cavitated regions from simulation vs. p_-. Good

agreement is seen for the axial dimension, although the transverse dimension was somewhat smaller than in the experiment, possibly due to over-discretization of the field in simulation.

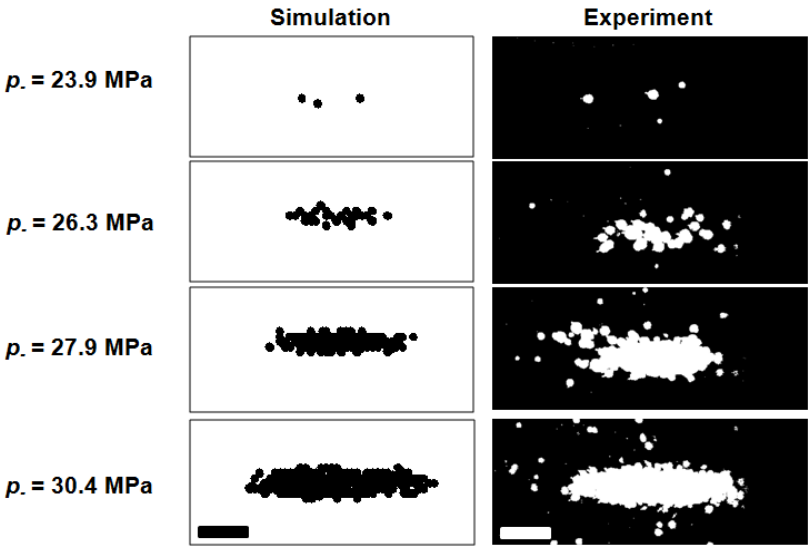

Figure 3.11. (Left) Integrated 2D cavitation map for n = 100 pulses resulting from a Monte-Carlo simulation using the probability curve, pressure map, and peak bubble radius for different peak negative pressures in unfiltered water (μ = 26.4 MPa, σ = 1.3 MPa). (Right) Binary image of the experimentally observed cavitation by high speed camera, integrated over n = 100 pulses for the same focal pressure levels in unfiltered water.

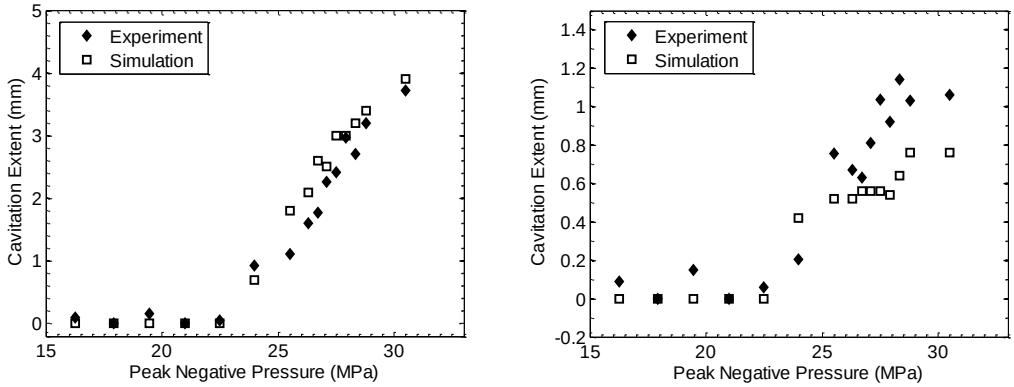

Figure 3.12. Dimensions of the cavitation regions vs. peak negative pressure for simulation and experiment in unfiltered water. (Left) Axial dimension of the cavitation zone (excluding bubbles outside the focus for experimental measurements). (Right) Measured and simulated transverse dimension of the cavitation region at the focus.

3.4 Discussion

In this chapter, a distinct negative pressure threshold for cavitation was observed in response to a single, microsecond-length pulse in a range of tissues and tissue-mimicking media. A similar pressure threshold has been observed specifically in water in several past investigations by other groups applying quasi-static tension[20], high amplitude shock waves[26, 27] or acoustic pulses[25], and the pressure values reported (24 – 33 MPa) are among the greatest measured for cavitation thresholds in water, with the exception of work in quartz inclusions[28]. Perhaps the most thorough work on this has been reported by Herbert et al[25], who used a similar acoustic method to apply 1 MHz 4-cycle pulses to a purified water sample. The authors found a peak negative pressure threshold near 24 MPa, although the reported values vary slightly for different methods of pressure measurement between 24 – 28 MPa at 20°C[25, 67]. The cavitation probability followed a sigmoid curve with similar pressure-probability width to our measurements. Their results also indicated that the threshold was independent of the purity by introducing 'dirt' into the water sample. While cavitation was occasionally observed at lower pressures, the higher probabilities ($P > 0.1$) were not observed until $p_- > 20$ MPa. Likewise, measurements recorded for the present study indicated only a minor variation in threshold between unfiltered water and distilled water (μ = 28.1 vs. 26.4 MPa). Thus, the results of our study are in agreement with the observations of Herbert et al.

This threshold was similar in all materials which were primarily water-based (water, gelatin, blood, clot, and kidney), despite the variety of other molecular species within these samples. The water content of these materials ranges from ~65% - 100% [68-70]. No discernable trend was found between percentage of water and threshold, nor other bulk properties of the media such as viscosity, elasticity,

surface tension, or acoustic impedance. While the macroscopic properties of these materials can vary significantly, we hypothesize that the cavitation nuclei environment at the nanometer scale determines the cavitation threshold in the medium. With water-based materials tested other than fat, free water appears to have a lower threshold than other nanometer-scale substances. Although many of these materials are an extremely diverse combination of molecules and almost certainly vary from position to position within the tissue structure, their common water content appears to be the best predictor of this threshold. Unfortunately, it was not possible to discern in this study whether cavitation was preferentially located within specific cellular or structural regions of tissue. There was some difference in the thresholds between the samples. Differences in acoustic attenuation and reflection may have contributed to unequal pressure levels at the focus for a given applied voltage to the transducer. However, based on literature values, the maximum attenuation was no more than 0.5 dB in any tissue sample. The maximum difference in acoustic impedance with water gives a reflection coefficient at the water/sample interface of < 0.06. Both of these effects were taken into account in the focal pressure estimation, thus the error in pressure estimation because of acoustic mismatch and attenuation is likely small. Possibly, the threshold differences may have arrived because of the necessarily different preparation methods of the samples, which resulted in unequal gas concentration. Despite this variation, the presence of water appeared to be a significant predictor of the cavitation threshold.

Materials which were not primarily water-based had much greater discrepancy in threshold compared with those described above. Butanediol is a hydroscopic liquid with similar acoustic properties to water, but a higher viscosity. This material has been proposed as a potential tissue mimicking material for ultrasound studies[71]. The higher threshold in this material and the

similarity of acoustic properties to water allowed us to record pressure measurements with $p_- > 30$ MPa, a technique which we validated by comparison with measurements in water. Canine visceral fat was found to contain a lower threshold of ~ 16 MPa. Triglycerides constitute about 80% of fat (composed of ~47% oleic acid, 24% palmitic acid, 15% linoleic acid, 14% others) and about 20% water [69, 72]. While this suggested that perhaps the nonpolar oil substances contain a lower cavitation threshold, olive oil which is nearly 100% triglycerides (composed of ~70% oleic acid, 13% palmitic acid, 10% linoleic acid, and 7% others) had a considerably higher threshold than either water or fat. It is likely that the fat/water interfaces are in fact the weak points in the fat structure due to the low interfacial tension. For instance, the surface tension at an olive oil/water interface is 23.6 mN/m, lower than either of the two constituents[73]. Couzens and Trevena noted in previous studies of oil/water interfaces that the cavitation threshold is lower at the interface than in either of the bulk media[74]. Similarly, we suspect that fat is more susceptible to cavitation because of its inhomogeneous emulsion of oils and water. Although not reported in the results, we have also tested canine thigh muscle. The cavitation threshold was highly dependent on the focal position of the tissue, possibly due to the intramuscular fat throughout the structure. However, the pressure range for cavitation was bracketed by those for fat and water.

Numerical simulation of the bubble dynamics suggested that the threshold for a model bubble nucleus of 2.5 nm would have a pressure threshold of 28.2 MPa in water. For nuclei in this size range, surface tension is the dominant force controlling the threshold by the Laplace pressure. In this respect, it is similar to the Blake threshold[64]. In the frequency range of interest for therapy (0.1 – 10 MHz), the threshold was mostly independent of frequency in the range of elasticities and viscosities reported for tissues[49, 52-56], except for high viscosity (η =

0.1 Pa-s), where the threshold at 10 MHz was greater than in water. Note that while the threshold of an individual nucleus may not be a strong function of frequency, the probability of cavitation also depends on the number of nuclei within the focal volume. As such, if an equivalent transducer with a higher frequency were applied, one would expect an incremental increase in the predicted pressure threshold due to the smaller volume of the focus. This is supported by data from Arvengas et al.[67], who compared the cavitation statistics for 1 and 2 MHz transducers in distilled water and found an incremental increase in threshold at 2 MHz. Additionally, the true nuclei population in water appears to be better represented as a distribution of radii ≤ 2.5 nm rather than a single value with a set threshold. This is evident by the significantly greater number of cavitation bubbles activated in Figure 2.7 compared with say Figure 3.6 within a volume. Theoretically, shock scattering can produce tensile pressure waves as great as the peak-peak values of the incident wave, which gives $p_- > 100$ MPa. It appears that a greater negative pressure excursion will activate additional smaller nuclei coexisting with those which cavitate near this 28 MPa threshold.

In histotripsy, it is known that specific tissues are more resistant cavitation and mechanical tissue damage, such as major blood vessels or collagenous and fibrous structures[75]. Rather than their intrinsic threshold for cavitation being different, the results here suggest that bubble growth during inertial cavitation is suppressed. As shown in Figure 3.6, cavitation in the gelatin with higher concentration had a similar threshold to water, but the individual bubbles did not growth to as large of radii as those in water. Thus, while the macroscopic properties appeared to have minimal effect on the threshold, they did alter the bubble expansion and collapse. Such confinement of bubble behavior may increase the number of pulses required to completely fractionate tissue. Not only might this reduced activity result in minimal tissue damage directly, but it may

also suppress the shock-scattering mechanism of forming cavitation clouds. Smaller bubbles will not cause sufficient scattering to initiate this action, and no cavitation cloud or ensuing damage will be formed in the tissue. However, as suggested by Freund[76], cavitation dynamics may change over several thousand acoustic pulses as cyclic growth and collapse of the same cavitation bubbles damage the surrounding tissue, reducing the local effective viscosity and elasticity of the tissue. This could ultimately lead to enhanced bubble growth and initiation of the cloud after this initial exposure.

With knowledge of the cavitation dynamics, the pressure thresholds, and the beam pressure profiles for the transducer, it may be possible to create a more predictive mechanical ultrasound ablative therapy with cavitation. The shock-scattering mechanism for forming clouds, which uses multi-cycle pulses depends on the locations of inhomogeneities or 'weak nuclei' in the medium to act as the initial single bubble scatterers prior to growing the dense cloud which causes the majority of tissue disruption. As the location of heterogeneous nuclei cannot be controlled before treatment, this often results in clouds forming in distinct locations in the focal zone while other locations remain completely uncavitated[35]. By using a single-cycle pressure pulse exceeding the intrinsic threshold of the medium, cavitation can be generated more uniformly within the focal zone in a controllable and predictable manner. Furthermore, the location and extent of the cavitation bubble expansion can be predicted with a stochastic model of this cavitation activity based on the experimental pressure thresholds, as shown by this study that cavitation observed on high speed camera was in good agreement with the simulation results of the stochastic model. A more sophisticated estimate of the number of nucleation sites per unit volume or the full nuclei distribution would significantly enhance such a model. While cavitation has generally been regarded as unpredictable in ultrasound therapy,

this pulsing regime could create a very controllable situation for planning therapy, assuming such cavitation can cause the necessary mechanical tissue ablation efficiently. By adjusting the pressure to that near the cavitation threshold, a single bubble can be generated in one pulse, and the total region where cavitation is observed can be considerably smaller than the -6dB pressure profile of the focus. As such, cavitational lesions significantly smaller than the focal zone can be achieved. In thermal ultrasound therapy, applying too great of an acoustic dose can cause deleterious necrosis to collateral tissue by diffusion of heat. In contrast, the damage with cavitation would be limited to the focal region and overtreating may have minimal side effects, as the spatial boundary between very high probability and low probability is very narrow because of the intrinsically small value for the probability transition zone σ.

3.5 References

1. Yang X, Church CC. A model for the dynamics of gas bubbles in soft tissue. J. Acoust. Soc. Am. 2005;118:3595-3606

2. Allen JS, Roy RA, Church CC. On the role of shear viscosity in mediating inertial cavitation from short-pulse, megahertz-frequency ultrasound. IEEE Trans Ultrason Ferroelec Freq Control. 1997;44:743-751

3. Sponer J. Dependence of the cavitation threshold on the ultrasonic frequency. Czech. J. Phys. 1990;40:1123-1132

4. Deng CX, Xu Q, Apfel RE, Holland CK. In vitro measurements of inertial cavitation thresholds in human blood. Ultrasound Med. Biol. 1996;22:939-948

5. Holland CK, Deng CX, Apfel RE, Alderman JL, Fernandez LA, Taylor KJW. Direct evidence of cavitation in vivo from diagnostic ultrasound. Ultrasound Med. Biol. 1996;22:917-925

6. Fowlkes JB, Crum LA. Cavitation threshold measurements for microsecond length pulses of ultrasound. J. Acoust. Soc. Am. 1988;83:2190-2201

7. Atchley A. The crevice model of bubble nucleation. J. Acoust. Soc. Am. 1989;86:1065

8. Harvey EN, Barnes DK, McElroy WD, Whiteley AH, Pease DC, Cooper KW. Bubble formation in animals. I. Physical factors. J. Cell. Comp. Physiol. 1944;24:1-22

9. Yount D. Skins of varying permeability: A stabilization mechanism for gas cavitation nuclei. J. Acoust. Soc. Am. 1979;65:1429

10. Johnson BD, Cooke RC. Generation of stabilized microbubbles in seawater. Science. 1981;213:209-211

11. Morch KA. Cavitation nuclei and bubble formation---a dynamic liquid-solid interface problem. J. Fluids Eng. 2000;122:494-498

12. Crum LA. Tensile strength of water. Nature. 1979;278:148-149

13. Vinogradova OI, Bunkin NF, Churaev NV, Kiseleva OA, Lobeyev AV, Ninham BW. Submicrocavity structure of water between hydrophobic and hydrophilic walls as revealed by optical cavitation. J. Colloid Interf. Sci. 1995;173:443-447

14. Apfel RE, Holland CK. Gauging the likelihood of cavitation from short-pulse, low-duty cycle diagnostic ultrasound. Ultrasound Med. Biol. 1991;17:179-185

15. Atchley AA, Frizzell LA, Apfel RE, Holland CK, Madanshetty S, Roy RA. Thresholds for cavitation produced in water by pulsed ultrasound. Ultrasonics. 1988;26:280-285

16. Crum LA. Nucleation and stabilization of microbubbles in liquids. Appl. Sci. Res. 1982;38:101-115

17. Frizzell LA, Chen E, Lee C. Effects of pulsed ultrasound on the mouse neonate: Hind limb paralysis and lung hemorrhage. Ultrasound Med. Biol. 1994;20:53-63

18. Carstensen EL, Gracewski S, Dalecki D. The search for cavitation in vivo. Ultrasound Med. Biol. 2000;26:1377-1385

19. Charles C C. Spontaneous homogeneous nucleation, inertial cavitation and the safety of diagnostic ultrasound. Ultrasound Med. Biol. 2002;28:1349-1364

20. Briggs LJ. Limiting negative pressure of water. J. Appl. Phys. 1950;21:721-722

21. Fisher J. The fracture of liquids. J. Appl. Phys. 1948;19:1062

22. Ho-Young K, Panton RL. Tensile strength of simple liquids predicted by a model of molecular interactions. J. Phys. D: Appl. Phys. 1985;18:647

23. Temperley HNV. The behaviour of water under hydrostatic tension: III. Proc Phys Soc. 1947;59:199

24. Greenspan M, Tscheigg CH. Radiation-induced acoustic cavitation; apparatus and some results. J. Res. Nat. Bureau of Stand. Sect. C. 1967;71:299-311

25. Herbert E, Balibar S, eacute, bastien, Caupin F, ric. Cavitation pressure in water. Phys. Rev. E. 2006;74:041603

26. Sankin G, Teslenko V. Two-threshold cavitation regime. Dokl. Phys. 2003;48:665-668

27. Wurster C, Köhler M, Pecha R, Eisenmenger W, Suhr D, Irmer U, Brümmer F, Hülser D. Negative pressure measurements of water using the glass fiber optic hydrophone. Proceedings of the 1st World Congress on Ultrasonics. 1995:635

28. Zheng Q, Durben DJ, Wolf GH, CA. A. Liquids at large negative pressures: Water at the homogeneous nucleation limit. Science. 1991;254:829-832

29. Parsons JE, Cain CA, Abrams GD, Fowlkes JB. Pulsed cavitational ultrasound therapy for controlled tissue homogenization. Ultrasound Med. Biol. 2006;32:115-129

30. Xu Z, Ludomirsky A, Eun LY, Hall TL, Tran BC, Fowlkes JB, Cain CA. Controlled ultrasound tissue erosion. IEEE Trans Ultrason Ferroelectr Freq Control. 2004;51:726-736

31. Bigelow TA, Northagen T, Hill TM, Sailer FC. The destruction of escherichia coli biofilms using high-intensity focused ultrasound. Ultrasound Med. Biol. 2009;35:1026-1031

32. Maxwell AD, Cain CA, Duryea AP, Yuan L, Gurm HS, Xu Z. Noninvasive thrombolysis using pulsed ultrasound cavitation therapy - histotripsy. Ultrasound Med. Biol. 2009;35:1982-1994

33. Xu Z, Fowlkes JB, Ludomirsky A, Cain CA. Investigation of intensity thresholds for ultrasound tissue erosion. Ultrasound Med. Biol. 2005;31:1673-1682

34. Xu Z, Raghavan M, Hall TL, Chang C-W, Mycek M-A, Fowlkes JB, Cain CA. High speed imaging of bubble clouds generated in pulsed ultrasound cavitational therapy -histotripsy. IEEE Trans Ultrason Ferroelectr Freq Control. 2007;54:2091-2101

35. Maxwell AD, Wang T-Y, Cain CA, Fowlkes JB, Sapozhnikov OA, Bailey MR, Xu Z. Cavitation clouds created by shock scattering from bubbles during histotripsy J Acoust Soc Am. 2011;130: 1888-1898

36. Church CC. Prediction of rectified diffusion during nonlinear bubble pulsations at biomedical frequencies. J. Acoust. Soc. Am. 1988;83:2210-2217

37. Xu Z, Hall TL, Fowlkes JB, Cain CA. Optical and acoustic monitoring of bubble cloud dynamics at a tissue-fluid interface in ultrasound tissue erosion. J. Acoust. Soc. Am. 2007;121:2421-2430

38. Hall T, Cain C. A low cost compact 512 channel therapeutic ultrasound system for transcutaneous ultrasound surgery. AIP Conf. Proc. 2006;829:445-449

39. Parsons JE, Cain CA, Fowlkes JB. Cost-effective assembly of a basic fiber-optic hydrophone for measurement of high-amplitude therapeutic ultrasound fields. J. Acoust. Soc. Am. 2006;119:1432-1440

40. Howard D, Sturtevant B. In vitro study of the mechanical effects of shock-wave lithotripsy. Ultrasound Med. Biol. 1997;23:1107-1122

41. Roy R. An acoustic backscattering technique for the detection of transient cavitation produced by microsecond pulses of ultrasound. J. Acoust. Soc. Am. 1990;87:2451

42. Bailey MR, Pishchalnikov YA, Sapozhnikov OA, Cleveland RO, McAteer JA, Miller NA, Pishchalnikova IV, Connors BA, Crum LA, Evan AP. Cavitation

detection during shock-wave lithotripsy. Ultrasound Med. Biol. 2005;31:1245-1256

43. Brujan EA, et al. Jet formation and shock wave emission during collapse of ultrasound-induced cavitation bubbles and their role in the therapeutic applications of high-intensity focused ultrasound. Phys. Med. Biol. 2005;50:4797

44. Chen W-S, Brayman AA, Matula TJ, Crum LA. Inertial cavitation dose and hemolysis produced in vitro with or without optison®. Ultrasound Med. Biol. 2003;29:725-737

45. Rabkin BA, Zderic V, Vaezy S. Hyperecho in ultrasound images of hifu therapy: Involvement of cavitation. Ultrasound Med. Biol. 2005;31:947-956

46. Chitnis PV. Quantitative measurements of acoustic emissions from cavitation at the surface of a stone in response to a lithotripter shock wave. J. Acoust. Soc. Am. 2006;119:1929

47. Bot A, van Amerongen IA, Groot RD, Hoekstra NL, Agterof WGM. Large deformation rheology of gelatin gels. Polymer Gels Net. 1996;4:189-227

48. Hiroki K, Keiji S, Kenshiro T. Surface tension wave on gelatin gel. Jap. J. Appl. Phys. Pt. 2, Letters. 1991;30:L1668-L1670.

49. Wells RE, Merrill EW. Influence of flow properties of blood upon viscosity-hematocrit relationships. J. Clin. Invest. 1962;41:1591-1598

50. Mast T. Empirical relationships between acoustic parameters in human soft tissues. ARLO. 2000;1:37

51. Rosina J KE, Suta D, Kolárová H, Málek J, Krajci L. Temperature dependence of blood surface tension. Physiol. Res. 2007;56 Suppl 1:S93-S98

52. Diamond SL. Engineering design of optimal strategies for blood clot dissolution. Annu. Rev. Biomed. Eng. 1999;1:427-461

53. Kodama T, Tomita Y. Cavitation bubble behavior and bubble-shock wave interaction near a gelatin surface as a study of in vivo bubble dynamics. Appl. Phys. B. 2000;70:139-149

54. Nasseri S, Bilston LE, Phan-Thien N. Viscoelastic properties of pig kidney in shear, experimental results and modelling. Rheologica Acta. 2002;41:180-192

55. Abbas S, Bishop J, Luginbuhl C, Plewes DB. Measuring the elastic modulus of ex vivo small tissue samples. Phys. Med. Biol. 2003;48:2183

56. Geerligs M, Peters GWM, Ackermans PAJ, Oomens CWJ, Baaijens FPT. Linear viscoelastic behavior of subcutaneous adipose tissue. Biorheol. 2008;45:677-688

57. George J, Sastry NV. Densities, dynamic viscosities, speeds of sound, and relative permittivities for water + alkanediols (propane-1,2- and -1,3-diol and butane-1,2-, -1,3-, -1,4-, and -2,3-diol) at different temperatures. J. Chem. Eng. Data. 2003;48:1529-1539

58. Chavrier F. Determination of the nonlinear parameter by propagating and modeling finite amplitude plane waves. J. Acoust. Soc. Am. 2006;119:2639

59. Treeby BE, Cox BT, Zhang EZ, Patch SK, Beard PC. Measurement of broadband temperature-dependent ultrasonic attenuation and dispersion using photoacoustics. IEEE Trans Ultrason Ferroelectr Freq Control. 2009;56:1666-1676

60. Halpern A. The surface tension of oils. J. Phys. Colloid Chem. 1948;53:895-897

61. Hosmer DW, Lemeshow S. Confidence interval estimation of interaction. Epidemiol. 1992;3:452-456

62. Keller J. Bubble oscillations of large amplitude. J. Acoust. Soc. Am. 1980;68:628

63. Ayme EJ, Carstensen EL. Cavitation induced by asymmetric distorted pulses of ultrasound: Theoretical predictions. IEEE Trans Ultrason Ferroelectr Freq Control. 1989;36:32-40

64. Leighton TG. The acoustic bubble. San Diego: Academic Press; 1994.

65. Maxwell AD, Wang T-Y, Yuan L, Duryea AP, Xu Z, Cain CA. A tissue phantom for visualization and measurement of ultrasound-induced cavitation damage. Ultrasound Med. Biol. 2010;36:2132-2143

66. Canney MS, Bailey MR, Crum LA, Khokhlova VA, Sapozhnikov OA. Acoustic characterization of high intensity focused ultrasound fields: A combined measurement and modeling approach. J. Acoust. Soc. Am. 2008;124:2406-2420

67. Arvengas A. Fiber optic probe hydrophone for the study of acoustic cavitation in water. Rev. Sci. Instrum. 2011;82:034904

68. Keitel HG, Berman H, Jones H, Maclachlan E. The chemical composition of normal human red blood cells, including variability among centrifuged cells. Blood. 1955;10:370-376

69. Forbes RM, Cooper AR, Mitchell HH. The composition of the adult human body as determined by chemical analysis. J. Biol. Chem. 1953;203:359-366

70. Kiricuta I-C, Simplaceanu V. Tissue water content and nuclear magnetic resonance in normal and tumor tissues. Cancer Res. 1975;35:1164-1167

71. Granz B. Measurement of shock wave properties after the passage through a tissue mimicking material. IEEE Ultrasonics Symposium, 1994. 1994;3:1847-1851 vol.1843

72. Malcom GT, Bhattacharyya AK, Velez-Duran M, Guzman MA, Oalmann MC, Strong JP. Fatty acid composition of adipose tissue in humans: Differences between subcutaneous sites. Am. J. Clin. Nutr. 1989;50:288-291

73. Fisher LR, Mitchell EE, Parker NS. Interfacial tensions of commercial vegetable oils with water. J. Food Sci. 1985;50:1201-1202

74. Couzens DCF, Trevena DH. Tensile failure of liquids under dynamic stressing. J. Phys. D. 1974;7:2277

75. Cooper M, Zhen X, Rothman ED, Levin AM, Advincula AP, Fowlkes JB, Cain CA. Controlled ultrasound tissue erosion: The effects of tissue type, exposure parameters and the role of dynamic microbubble activity. IEEE Ultrasonics Symposium, 2004. 2004;3:1808-1811 Vol.1803

76. Freund JB. Suppression of shocked-bubble expansion due to tissue confinement with application to shock-wave lithotripsy. J. Acoust. Soc. Am. 2008;123:2867

CHAPTER 4

Measurement of Cavitation-Induced Tissue Damage

The previous two chapters described how short, high-amplitude ultrasound pulses initiate a cloud of cavitation in histotripsy. In this chapter, the relation between this cavitation and damage to cells and tissue structures is investigated. A tissue phantom is developed to observe cavitation and the resulting damaged region in histotripsy. A model for cavitation-induced strain is used to predict the region of destruction of red blood cells and tissues based on the bubble behavior, and correlated with observations in the phantom.

There are a number of ways in which cavitation can mediate damage to tissues and cells. Inertial cavitation, such as that observed in histotripsy, is thought to be particularly detrimental to tissue structures in the body. Besides histotripsy, the most notable examples of mechanical tissue damage caused by ultrasound are in lithotripsy, where the focal zone extends outside the region of treatment into the soft kidney tissue[1-3]. Damage to soft tissue is cumulative, occurring over treatments of ~2000 shocks[4]. Cavitation has been implicated as the primary cause of tissue damage in these treatments, with several potential mechanistic behaviors playing a role[5-7], including bubble-induced strain upon

expansion[8], bubble jetting[4, 9], bubble motion-induced shear stress[10], and bubble collapse shock waves[11]. One or more of these effects may play a role in the destruction of blood clots in histotripsy.

4.1 A Tissue Phantom for Cavitation Damage

Tissue-mimicking phantoms are commonly used in therapeutic ultrasound for dosimetry[12, 13], in-vitro research [14], transducer characterization [15], and quality assurance. A number of phantoms have been used to simulate thermal lesion formation caused by ultrasound-induced heating in high-intensity focused ultrasound (HIFU) [16-18]. While these can accurately mimic the response of soft tissues to heating, they are unable to visualize or quantify mechanical damage due to acoustic cavitation caused by high-intensity ultrasound. The lysis of cells due to cavitation has been known for some time. Hughes and Nyborg[19] demonstrated disruption of cells was specifically caused by the presence of cavitation from gas-filled holes in a brass plate driven at 20 kHz. Other in-vitro tests are often performed with cells in suspension [20, 21], cell layers [19, 22, 23], and immobilized in tissue mimicking materials for study of lithotripsy [24] and HIFU gene activation [25]. Cavitation-enhanced heating has also been studied in gel phantoms [26, 27], but the mechanical effects of cavitation were not measured.

A tissue phantom for measurement of mechanical cavitation damage would be valuable in both ultrasound imaging and therapy. Guidelines for limiting the output of diagnostic transducers are based on acoustic parameters which indicate the likelihood of generating cavitation, such as peak rarefactional pressure, transducer frequency, and pulse length. A phantom could verify whether a given transducer and set of acoustic parameters are capable of causing such effects. For ultrasound therapy, it may be useful for providing a

quantitative metric for the extent and pattern of unintended tissue damage (as in the case of lithotripsy and extracorporeal shock-wave therapy) surrounding the focus. Finally, it is beneficial for studying intentionally-induced cavitation damage, as such with histotripsy, which relies on cavitation to cause mechanical disintegration of tissue structures. Previously, studies of histotripsy have been performed in ex-vivo tissue [28, 29] or in-vivo [30]. However, a tissue phantom is capable of providing instant visual feedback, observation of cavitation-cell interaction, and a record of the accumulated damage immediately, while tissue samples require preparation and expensive histology to properly examine the morphology of lesions induced.

A tissue phantom for measuring cavitation induced damage should contain a visual marker to show the location and extent of mechanical damage. Therefore, it is important that the phantom is as optically transparent as possible, so that the markers indicating damage can be located by either gross examination or microscopy. Additionally, this property also allows for direct observation of cavitation-induced damage by high-speed imaging during insonation, which cannot be performed in ex-vivo tissue. In this study, we used red blood cells embedded within an agarose hydrogel to act as the visual indicator. If an appropriate cell density is chosen, the phantom will scatter and absorb light, making it appear translucent red. Upon rupturing the membranes of the red blood cells, the area will become uniform, no longer scattering light, and the phantom will locally appear more transparent. Previous work has demonstrated the sensitivity of red blood cells to even modest cavitation activity [31]. Nyborg and Miller [32], showed that red blood cells specifically in the vicinity of cavitation bubbles on a membrane were subjected to high shear stress due to microstreaming, a cause of lysis. Similarly, we found that the lysis of red cells in

the phantom is only induced when and where cavitation is generated by ultrasound.

In addition to being sensitive to cavitation damage, the phantom should ideally possess mechanical and acoustic properties similar to the tissue being treated (e.g. thrombus). The density, sound speed, and ultrasonic attenuation must be similar to tissue to appropriately simulate ultrasound imaging used for therapy guidance. Mechanical properties, such as elastic (Young's) modulus, must also be in the range of soft tissues. Cavitation models suggest that inertial cavitation can be suppressed with increasing elastic modulus [33]. Cavitation activity will in turn determine whether there is sufficient cell deformation to rupture cell membranes and incite irreversible tissue damage [7]. Finally, the gel should be relatively simple and inexpensive to prepare, as one purpose is to avoid the costs associated with using ex-vivo tissue and histology.

4.1.1 Methods: Phantom Preparation

The protocols described in this paper have been approved by the University Committee on Use and Care of Animals (UCUCA). Agarose gel phantoms were prepared using a mixture of Type VII agarose powder (Sigma-Aldrich Co., St. Louis, Missouri, USA) and canine red blood cells in 0.9% isotonic saline. Fresh canine blood was obtained from adult research subjects in an unrelated study and added to an anticoagulant solution of citrate-phosphate-dextrose (CPD) (C1765, Sigma-Aldrich Co., St. Louis, Missouri, USA) with a ratio of 1 mL CPD to 9 mL blood. Whole blood was separated in a centrifuge at 3000 rpm for 10 minutes. The plasma and white buffy coat were removed, and the red blood cells (RBCs) were saved for addition to the phantom. Agarose was slowly combined with saline while stirring at 20°C (1.5% w/v agarose/saline), forming a translucent solution. The solution was heated in a microwave oven for 30 seconds and then

stirred. Heating in 30 second intervals and stirring was repeated until the solution turned entirely transparent. The solution was placed under a partial vacuum of 20.5 psi for 30 minutes to degas the mixture. After removing the mixture from vacuum, a layer of agarose was poured into a rectangular polycarbonate housing to fill half of it with agarose. The housing was placed in a refrigerator at 4°C to allow the agarose to cool and solidify. The remaining agarose solution was kept at 45°C for 1 hour. A small amount of agarose solution was mixed with the RBCs (5% RBCs v/v). The frame with solidified agarose was removed from refrigeration and a thin layer of the RBC-agarose solution was poured onto the gel surface to allow the entire surface to coat in a layer ~500 μm thickness. After 5 minutes, the RBC/agarose layer was solidified, and the remaining agarose solution without RBCs was poured to completely fill the frame. This procedure created a thin layer of red blood cells suspended in the center of the agarose phantom. A solid RBC-agarose phantom can also be prepared with the tradeoff being loss of optical transparency. However, only results from the layered RBC phantom are reported herein.

4.1.2 Methods: Measurement of Phantom Properties

Measurements of tissue phantom properties including density, sound speed, attenuation, and elastic (Young's) modulus were performed. Ten agarose phantom samples were prepared as described above for measurement of properties. All experiments were performed at room temperature.

The density of each sample was characterized by direct measurement of volume and mass on a laboratory balance. Next, the sound speed and attenuation were measured using a broadband pulse technique. A 13 mm aperture 3.5 MHz unfocused transducer (Aerotech Laboratories, Lewistown, PA, USA) was placed in a degassed water tank, and a hydrophone (HGL-0085,

ONDA Corporation, Sunnyvale, CA, USA) was positioned facing the transducer approximately 7 cm from the source. Care was taken during experiment not to disturb the source and hydrophone in order to maintain fixed distance measurement. An insertion method such as that used here produces smaller errors due to diffraction than variable distance measurements, and diffraction can generally be neglected when the media have approximately the same speed of sound[34]. A broadband pulse with center frequency of 3.5 MHz was first transmitted through water. Next, the tissue phantom thickness was measured and placed in the path of the source, and the same pulse was transmitted. The attenuation coefficient was measured by calculated using the method outlined in [35]. The sound speed was determined by a time lag of the peak in cross-correlation of the acoustic signals with and without the sample in the path. The acoustic impedance was calculated directly from the product of density and sound speed.

Elastic modulus was measured using an elastometer constructed using the same method outlined in a paper by Egorov et al[36]. A motorized positioner was used to hold a 6.2 mm diameter aluminum rod with a hemispherical end on the sample placed on a laboratory balance. The rod was brought into contact with the gel, and pressed by the positioner into the gel a known distance. The scale reading was recorded to determine the force on the phantom. Several positions and force readings were recorded to obtain a plot of stress vs. strain. The Young's modulus of the phantom was determined by a linear regression fit to the stress-strain curve.

4.1.3 Methods: Generation and Imaging of Lesions

Histotripsy lesions were generated in the RBC phantom and ex-vivo porcine kidney to compare the morphology and progression of lesion formation in each sample. Fresh tissue was obtained from a local abattoir and placed in 0.9% saline

solution at room temperature. All experiments were conducted within 6 hours of harvest.

A spherically-focused piezocomposite transducer (Imasonic, Besançon, France) with a 10 cm diameter and 9 cm focal length was used as a therapy transducer. The transducer operates at 1 MHz, and is driven by a class D amplifier with matching network developed in our lab. The transducer was positioned in a tank of degassed, filtered water, and the focus was aligned to the cortex of the kidney sample in a plastic bag filled with saline submerged in the tank. Ultrasound was fired at a 3x3 grid of points sequentially, with 2 mm spacing between points. The total exposure at each point was 1500 pulses. The parameters used were 100 Hz pulse repetition frequency and 15 cycles pulse length. This pattern was chosen over single spot treatments so that lesions were more easily located in tissue for histological sectioning. After treatment, the tissue was removed from the bag and rinsed with fresh saline, then placed in a 10% phosphate-buffered formaldehyde solution (Fisher Scientific, Pittsburgh, PA, USA). After 7 days, the kidney was sectioned and Hematoxylin and Eosin-stained histology slides were made for each spot treated in the kidneys. The RBC phantom was immediately removed after treatment and the RBC layer was photographed.

To visualize the cross-sectional profile of tissue damage in the phantom, the transducer was used to deliver the same acoustic parameters to single focal spots in the phantom. In this case, the RBC layer was aligned perpendicular to the focal zone. After sonication of a spot, the focus was moved to a new location 1 cm away, and the exposure was repeated.

Images of lesions in tissue and the phantom were analyzed in MATLAB to determine the dimensions of the focal lesions from photographs of the phantom and histology slides for the kidneys.

B-Mode ultrasound images of the lesions in the phantom and tissue were recorded before and after treatment of kidneys and phantoms. An ultrasound imager with a 10 MHz linear probe (10L probe, Logiq 9, General Electric, Fairfield, CT, USA) was used to acquire images by placing the probe in contact with the tissue or phantom. For the phantom, the linear probe was oriented to acquire an image parallel with the RBC layer in the gel and the B-Mode gain was adjusted to observe the speckle pattern in the gel or tissue. Axial profiles of the lesions made by the therapy transducer were also obtained.

High-speed imaging of the phantom was performed while applying single histotripsy pulses to the phantom in a tank of degassed, filtered water. The therapy transducer described above was used to generate cavitation clouds in the phantom. A high speed camera (SIM02, Specialised Imaging Ltd., Hertfordshire, UK) was used to obtain high speed images of the cavitation cloud in the phantom placed in the water tank at the focus of the transducer (Figure 4.1). The field of view was chosen such that the entire extent of the bubble cloud at the focus could be observed. The end of a fiber optic bundle coupled to a flash lamp was positioned behind the RBC phantom to provide backlighting of the phantom during image exposure.

The gel phantom was positioned such that the camera was imaging through the plane of RBCs in the phantom, and the ultrasound propagated parallel to this plane and focused within the RBC layer. Prior to ultrasound exposure, an image of the phantom was recorded using a separate digital SLR camera (Nikon D200, Nikon USA, Melville, NY, USA) attached to the optical port of SIM 02 high-speed camera. After the initial image capture, a single, 10-cycle pulse with peak negative pressure of 19 MPa was generated by the therapy transducer, and images were recorded using the high speed camera in a time sequence 160 μs in length starting at the time the first cycle of the ultrasound pulse reached the

focus. Another image was recorded 30 seconds after exposure using the digital SLR camera to observe the final phantom appearance. The reason for use of the SLR camera for pictures before and after sonication was to minimize noise so that the two images could be subtracted to obtain a profile of the lesion. While this could also be done with the high-speed camera, the noise due to the camera's internal image intensifiers was much greater. A new location in the phantom was targeted for each pulse applied.

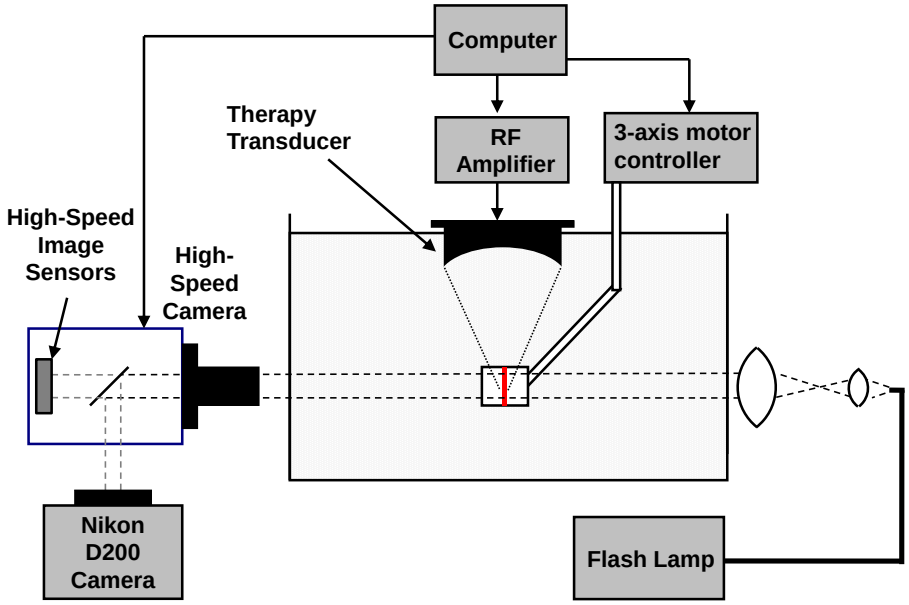

Figure 4.1. High speed imaging apparatus used to acquire images prior to, during, and after phantom insonation. The RBC layer (red line) of the phantom was positioned within the ultrasound focus. The high speed camera was positioned imaging the plane of RBCs, and a flash lamp was used to backlight the phantom. A digital camera was also used to take high-quality images before and after insonation.

Images were analyzed using MATLAB software (Mathworks, Natick, MA, USA). The damage profile in the phantom was assessed using the images before and after ultrasound exposure captured by the digital SLR camera. First, the images were cropped to obtain the same field of view as the high-speed camera.

Images were converted from color to grayscale, and image intensity in both before and after pictures was normalized such that the background intensity was the same for both pictures. A 3x3 pixel smoothing kernel was applied to reduce noise in the image. Next, the two images were subtracted to obtain the difference between the before and after pictures. Image contrast was then normalized such that the subtracted image spanned the entire 8-bit dynamic range. The image was converted to a binary image using the *graythresh* function in MATLAB to obtain the threshold level. Each lesion area was identified separately, and areas smaller than 10 pixels were removed as noise.

High speed images of the cavitation cloud were also processed to produce a binary image. A 3x3 pixel smoothing kernel was applied, and then the image was converted to binary using the same technique. Areas of the lesion were identified in the same manner as the lesion images. The overall dimensions and area of the lesions, as well as their locations were compared to the locations and size of the bubble cloud.

4.1.4 Results: Tissue Phantom Properties

A photograph of an untreated RBC phantom is shown in Figure 4.2. The phantom is transparent, except for the thin RBC layer in between the two layers of plain agarose. Although several agarose types were tested, Sigma Type VII was chosen because of its low gelling temperature and high clarity. The low gelling temperature allowed the agarose to cool to a temperature where red blood cells would not be lysed while adding to the mixture during preparation. The agarose layers are transparent, while the RBC-agarose mixture appears as a red, translucent layer. Layer thickness or % hematocrit within the RBC layer could be adjusted to achieve sufficient contrast between treated and untreated zones. 5% hematocrit was used for the purpose of these tests. We found the RBCs

are not lysed when the phantom is placed in pure water, even for several hours. However, the phantom cannot be left in tap water indefinitely during experiments, as diffusion of water into the agarose will eventually cause hypotonicity of the agarose and cell lysis. Red cell phantoms could be stored in refrigeration at 4^0C covered in plastic wrap for 2 weeks without change in appearance.

A total of 10 samples were prepared separately for measurement of the phantom properties. The mean density measured was 1.02 ± 0.016 g/cm^3 at 21^{o}C. The sound speed in the samples was 1501 ± 2 m/s, giving an acoustic impedance of 1.53 MRayl. Attenuation measured relative to water in the 8 samples was 0.11 ± 0.017 dB/cm at 1 MHz, and was found to increase nearly linearly with frequency in the range of 1-5 MHz. The mean value for Young's modulus measured was 62.0 ± 12.1 kPa. The values for Young's modulus varied significantly from sample to sample. However, the values were within the range measured by others for agarose gels [37], and soft tissues [38]. A summary of the properties for the phantom, as well as standard values for water at 20^0C and soft tissues is shown in Table 4.1.

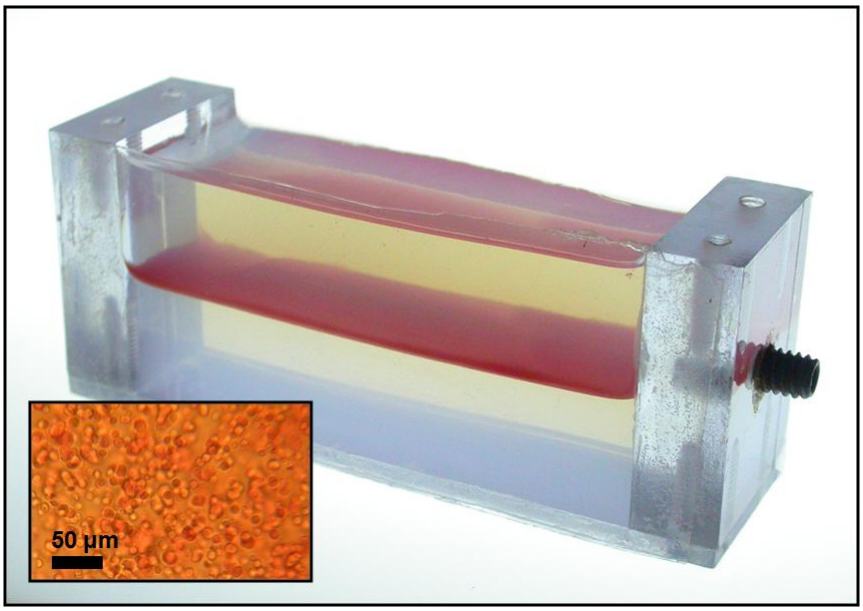

Figure 4.2. A photograph of the cell phantom in a polycarbonate holder. The phantom consists of 3 layers of agarose, with the middle layer containing 5% red blood cells. The insert shows the visual appearance of the red blood cell layer during examination under a microscope.

Table 4.1. Acoustic and mechanical properties of the tissue phantom measured in this study at 20°C. Reference values for properties from water and soft tissues are also provided.

	Water	Tissue Phantom	Soft Tissues
Density (kg/m^3)	998	1020	1050
Sound Speed (m/s)	1484	1501	1480-1560
Acoustic Impedance (MRayl)	1.48	1.53	1.61
Attenuation (dB/cm/MHz)	0.0022	0.11 (1-5 MHz)	0.4-0.7
Elasticity (kPa)	-	62	10-30

4.1.5 Results: Comparison with Lesions in Tissue

Lesions were generated using identical parameters in both the phantom and ex-vivo kidney and liver tissues. Lesions were induced by scanning a 3 x 3 grid of points with 2 mm spacing and 1500 pulses per point. Therefore, lesions

observed in the phantom and tissue histology are an accumulation of damage caused in 9 adjacent focal regions, although only 3 of the foci are in the plane of the RBC layer. The grid scan was used to create larger lesions which would be easily distinguished in tissue. Figure 4.3 shows photographs of lesions in the phantom and kidney tissue histology.

A total of 9 lesions were created in the phantom and 8 in the kidney cortex. The average lesion dimensions in the phantom were 18.5 ± 2.0 mm axially and 7.6 ± 0.4 mm laterally. The average dimensions in the kidney tissue were 13.3 ± 3.9 mm axially and 6.8 ± 0.8 mm laterally. In kidney tissue, the axial dimension of the lesion was often limited due to the overlap of the focal volume with parts of the medulla of the kidney. In this area, no tissue disruption was apparent. Therefore, the axial length of the lesion was often shorter than the full focus. Additionally, damage was more difficult to visualize in the tissue than the phantom, in part because of the lack of contrast between the homogenized and intact tissue. The boundaries of the lesion were well defined, with a width of only a few red blood cells between completely disrupted area of the phantom containing no intact cells and the area with similar appearance to untreated phantom (Figure 4.3). This result is consistent with previous studies of histotripsy lesions, where the lesion boundaries were found to be thin enough to bisect individual myocytes [39].

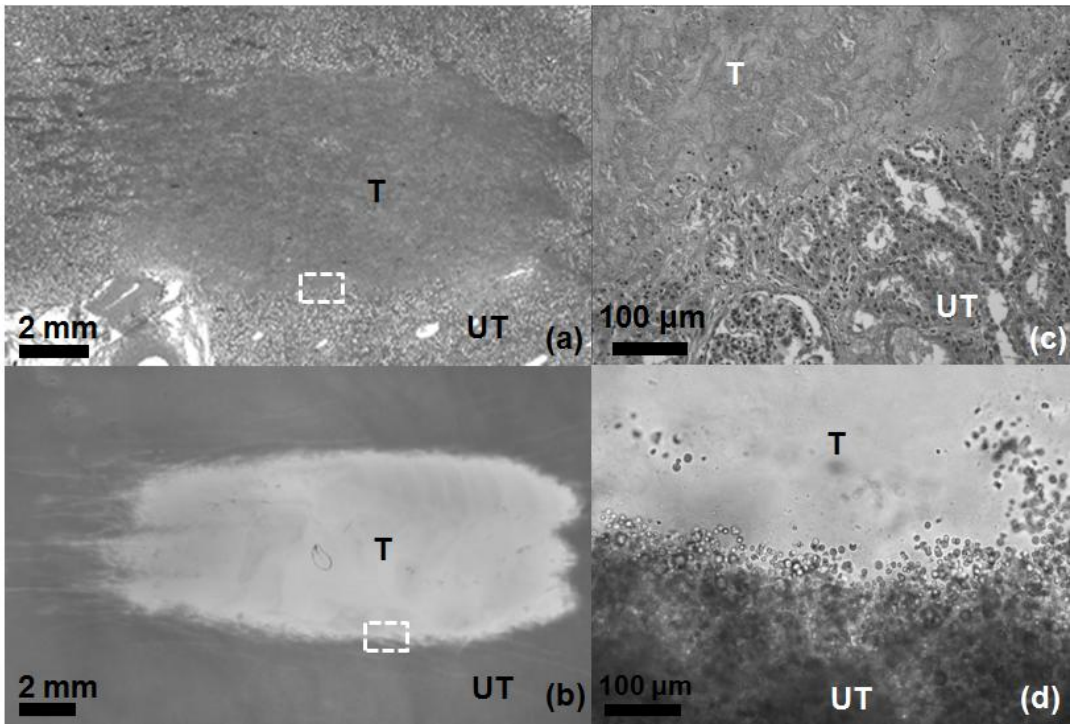

Figure 4.3. Images of (a) histology of a lesion generated in ex-vivo kidney using 1500 pulses in 3 adjacent focal spots with 2 mm spacing and (b) a lesion generated in the cell phantom using identical parameters. Ultrasound (US) propagation is from left to right. Lesions in kidney appear as a more homogeneous region due to cell structure disruption, while lesions in the phantom show increased transparency. Magnified images of the boundary between treated (T) and untreated (UT) regions of the lesions in Figure 4.3a and Figure 4.3b are also shown in Figure 4.3c and 4.3d, respectively. The disrupted zone of the phantom shows virtually no red blood cells remaining, while the region only 50µm from the lesions shows similar appearance to untreated phantom.

Images of the phantom treated were recorded using a B-Mode ultrasound imaging probe before and after treatment. The RBC layer appeared as a uniform area with increased speckle vs. the agarose without red blood cells or water. Although the speckle was apparent, higher gain settings on the machine were necessary to achieve equivalent contrast to that in real tissue. Lesions appeared as hypoechoic regions in the RBC layer of the phantom, as is common for

histotripsy lesions generated in tissue. Tissue and phantom lesion photographs and their corresponding B-Mode images are shown in Figure 4.4 for comparison. The size and shape of hypoechoic regions match well with the actual lesion size. The three tails of the treated zone are apparent with a higher degree of echogenicity on the B-Mode image than the upper part of the lesion. Under microscope, some cells are still intact within the lower tails of the lesion. This behavior is also apparent in tissue, where the degree of echogenicity and backscatter can be used as an indicator for treatment progression[40].

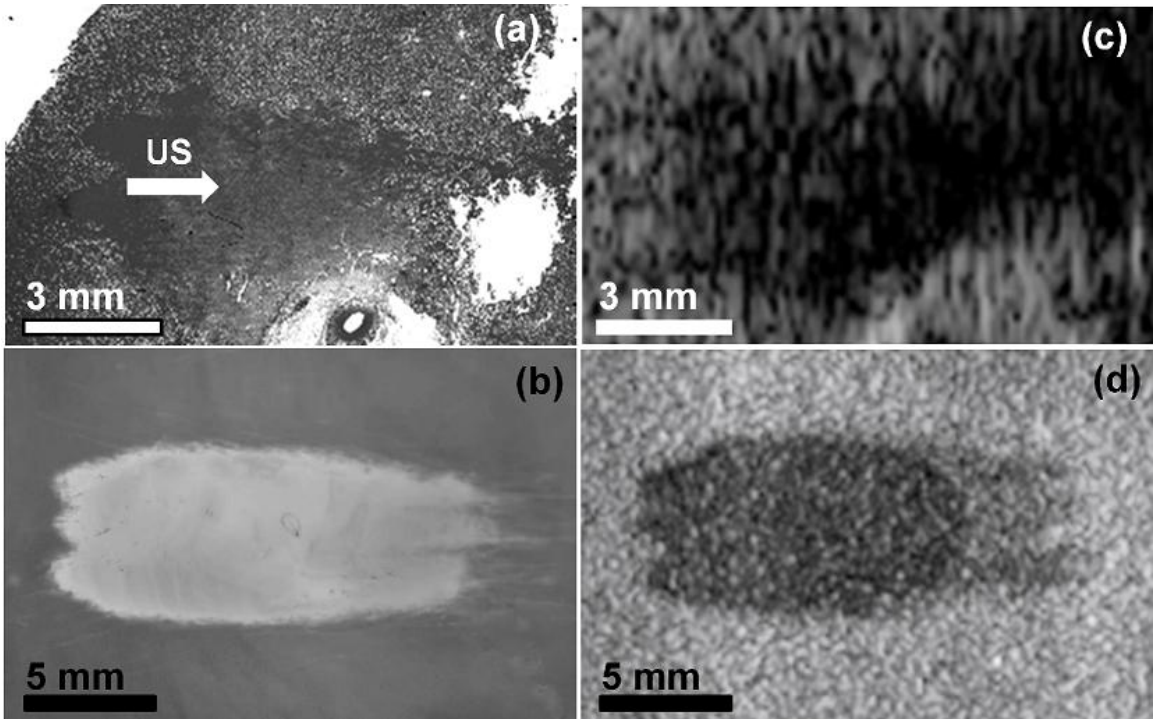

Figure 4.4. Comparison of photographs and B-Mode images of lesions. (a) shows a photograph of kidney lesion histology and (b) is a lesion in the cell phantom. Histotripsy ultrasound (US) propagation is from left to right. The B-Mode image has a hypoechoic appearance similar to that seen for histotripsy lesions in ex-vivo kidney tissue (c). A B-Mode image of the phantom lesion is shown in (d).

4.2 Investigation of the Mechanism of Damage to Red Blood Cells

4.2.1 Correlation of RBC Lesions with Cavitation Cloud

Cavitation clouds and individual cavitation bubbles were observed in the gel phantom during a single ultrasound pulse with the setup described in Figure 4.1. Clouds always formed at the center of the transducer focus laterally, with between 1-4 distinct clouds forming during the pulse along the axis of propagation. Smaller single cavitation bubbles were observed in a larger region surrounding the focus during the pulse and for 10-20 μs after the pulse. Clouds formed during ultrasound exposure and then collapsed over a time course of 70-140 μs after the ultrasound pulse had passed. Figure 4.5 shows a sequence of photos captured during a single histotripsy pulse using the high speed camera.

Lesions were not apparent immediately after cavitation collapse, but became visible within 1 second after ultrasound exposure. Undisrupted phantom appeared as a uniform translucent red plane within the phantom, while lesions in the gel showed increased light transmission and transparency, with a slight red or pink color. Therefore, lesions were identified and characterized based on the increased local light intensity observed while backlighting the phantom. From the profiles of the cavitation activity and resulting damage, it appears that the cloud at the center of the focal region is responsible for the large main lesion, while individual cavitation bubbles or small clusters in outlying regions of the phantom cause small areas of collateral damage (microlesions).

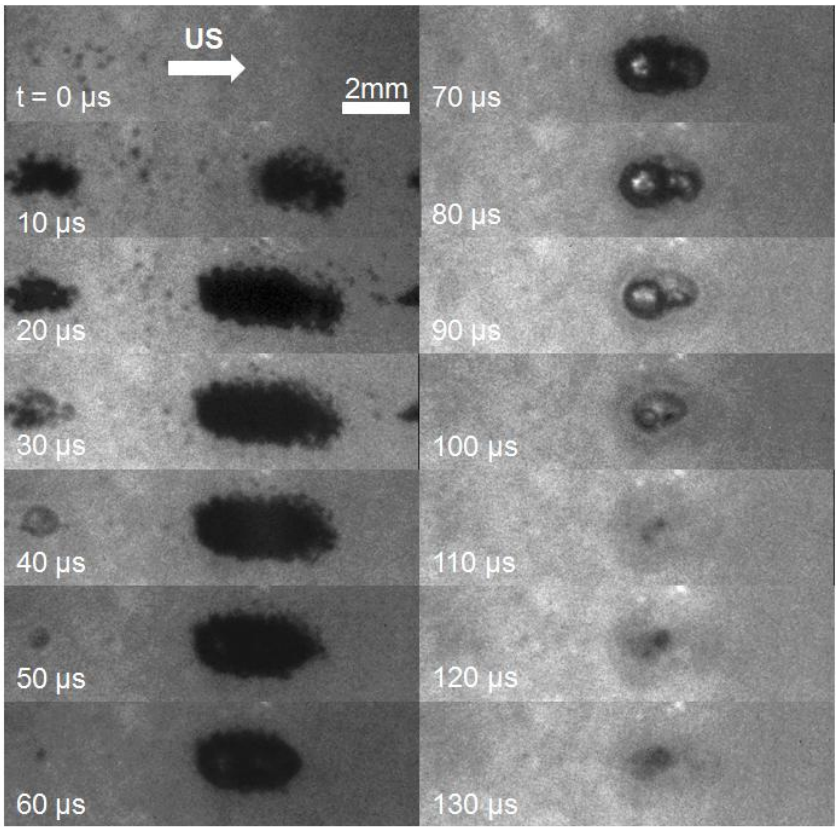

Figure 4.5. Images captured by the high-speed camera during a single ultrasound pulse. Ultrasound propagation is from left to right. The pulse arrives on the left at 0 µs and passes through the focus between 0-20 µs. The bubble cloud generated during the pulse then collapses 110 µs after ultrasound exposure.

High-speed images were analyzed to compare the size and shape of lesions to that of the cavitation clouds. Overall, 15 clouds and corresponding lesions were compared for location, dimensions, and overlapping area between cavitation and lesions. The 3rd high-speed frame (corresponding to 20 µsec after the initial incidence of ultrasound) was used for comparison, as this showed the full bubble cloud as well as surrounding cavitation bubbles. It was found the location of lesions coincided well with the location of bubble clouds. Figure 4.6 shows a photograph captured by the high-speed camera of the bubble cloud in the phantom, as well as the subtraction image of the damage induced to the

phantom during the single pulse. All lesions had similar morphology and dimensions to their corresponding bubble clouds. The overall area of the lesions (mean 1.7 mm^2 ±1.2 mm^2) was smaller than the area of the bubble clouds (mean 3.5 mm^2 ± 1.9 mm^2), although their locations coincided. Individual bubbles surrounding the main lesion had diameters of 171 ± 55 μm. The percentage of image area of the lesion overlapping the area of the bubble cloud was also computed, and it was found that between 94.6% - 100% of the damage for a given lesion occurred within the areas where bubbles were observed during the pulse (mean 98.4 %). These results suggest that the lesions appear in the phantom only where cavitation occurs. Without cavitation, lesions were not observed in the phantom. Some single bubbles also coincided with microlesions in the phantom in both size and shape. However, because the sensitive area of the phantom is two-dimensional, bubbles which were not in the plane of the RBC layer did not induce damage.

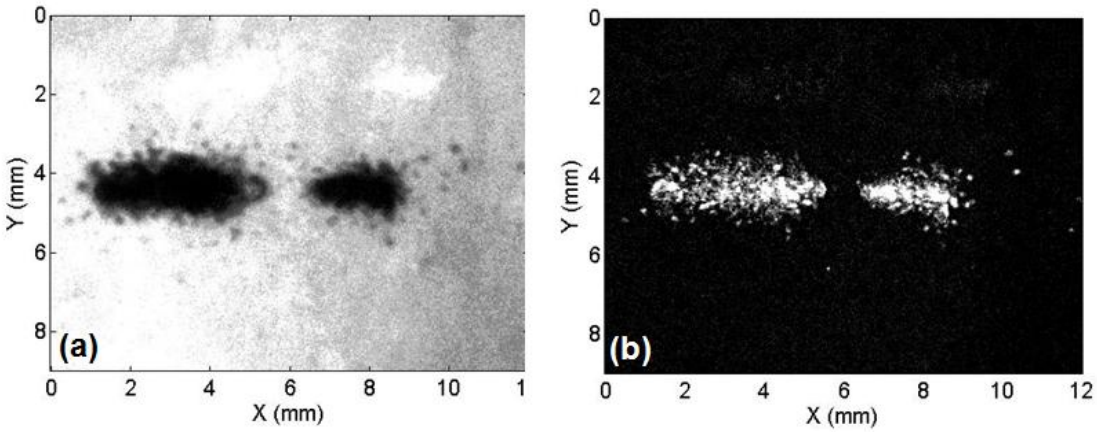

Figure 4.6. Examples of a bubble cloud and the corresponding lesion generated after ultrasound exposure. Ultrasound (US) propagation is from left to right. (a) High speed image of the bubble cloud 5 μs after ultrasound pulse. (b) Subtraction image of the lesion generated by the single pulse. All lesions matched well in shape and dimensions with the corresponding bubble clouds. Lesions due to individual bubbles surrounding the focus are also evident.

4.2.2 Analysis of Damage by Single Bubbles

Lesions were also made by applying ultrasound to a single spot through the tissue phantom RBC layer, producing a lateral profile of the cavitation damage. The 8 lesions generated in the phantom were very consistent, with a totally disrupted area at the center surrounded by small circular 'microlesions' extending approximately 5 mm from the lesion center (Figure 4.7). The mean diameter of the main lesion was 3.01 ± 0.15 mm, which is also consistent with the lateral dimension of bubble clouds observed in the gel. The microlesions had a size distribution from 20-440 μm diameter, with a peak in the range from 140-160 μm. Figure 4.8 shows a histogram for the size distribution of 710 microlesions in the phantom, excluding the main central lesions in 8 separate samples.

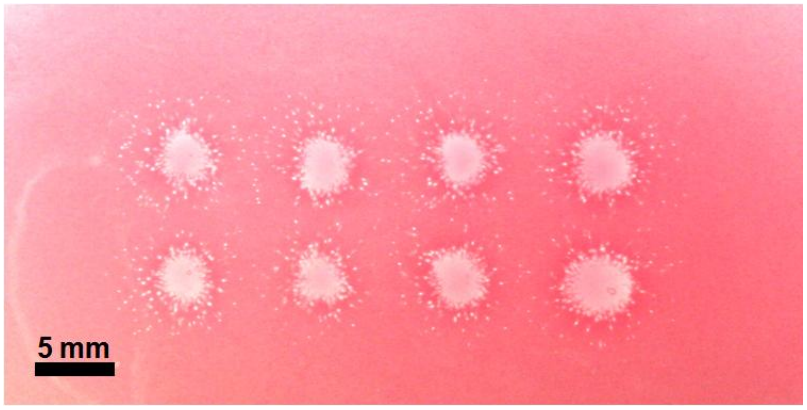

Figure 4.7. Eight lesions generated in a cell phantom by applying ultrasound perpendicular to the RBC layer. Each lesion is an accumulation of cavitation damage caused by applying 1500 pulses to a single focal spot. The phantom shows a completely disrupted region within the center of the focal zone, and small microlesions surrounding this area.

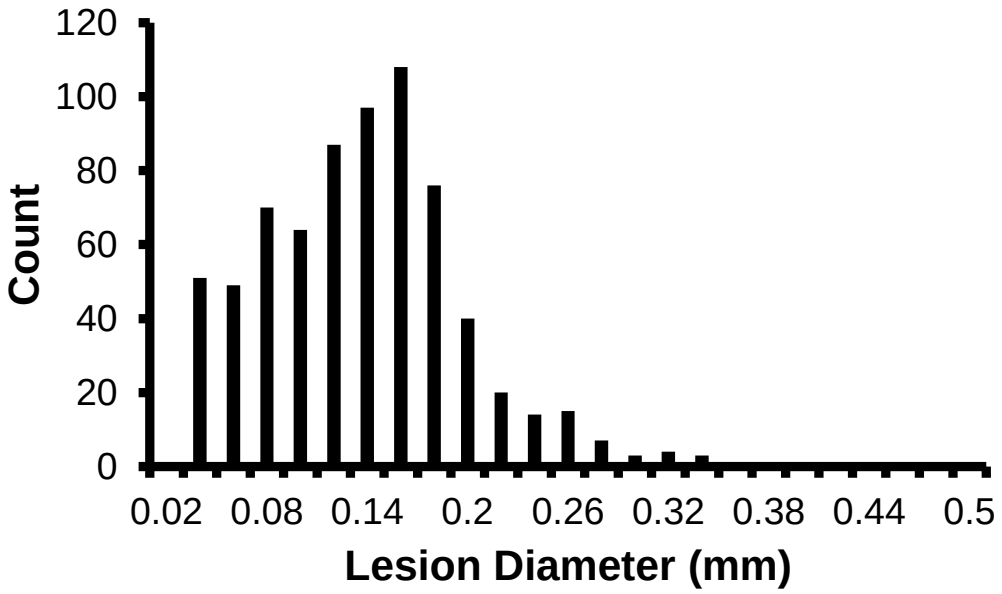

Figure 4.8. Histogram of collateral microlesions' diameters recorded in the 8 focal spots shown in Figure 4.7 (not including the central lesion). A local peak is observed at about 150 μm diameter, which corresponds well with single bubbles observed on high speed images of the phantom.

Images of cavitation occurring in an agarose phantom with the same concentration but without RBCS were taken to compare with the distribution of microlesion diameters. The same parameters were applied as those used to generate the lesions and images were captured for pulse numbers 100,200,300, and 400. Bubbles with the same range of diameters as those for the microlesions, with the peak number for diameter occurring at 120 μm and spanning the range 20 μm – 260 μm for n = 113 bubbles. Figure 4.9 shows example images of the peripheral bubbles captured by high-speed photography and microlesions in the phantom.

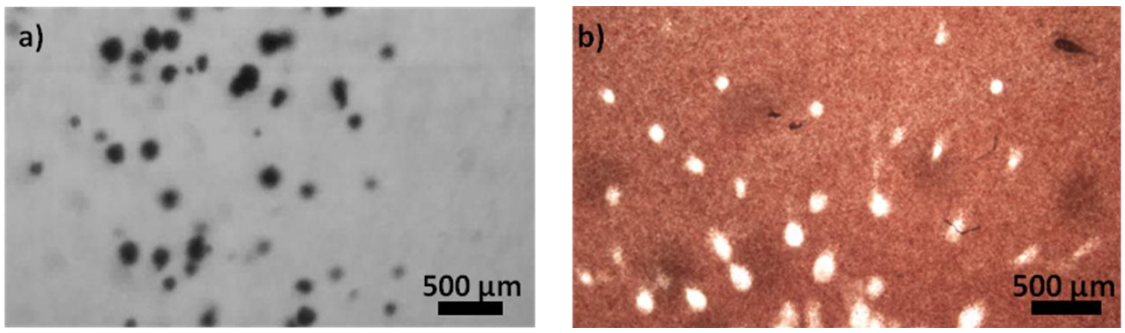

Figure 4.9. (a) Image of cavitation bubbles in the peripheral focus at the end of a histotripsy pulse captured in an agarose gel phantom without RBCs, using PRF = 100 Hz and pulse length = 15 cycles. (b) Small circular lesions near the edge of a primary lesion in the RBC phantom after exposure of the same parameters for 1500 pulses.

4.2.3 Model of Cavitation-Induced Damage

Based on the results above, a hypothesis was proposed that the disruption of the red blood cells occurs as a result of bubble-induced strain on the cell walls during inertial expansion. This mechanism has been previously discussed in light of hemolysis caused by lithotripter shock-induced expansion[7], and investigated for the possibility of hemolysis caused by ultrasound contrast agents in response to pressure pulses < 1 MPa *p*.[41].

One advantage of modeling RBCs is that their mechanical properties are well-characterized compared with other cell and tissue types[42, 43]. RBCs are a simple structure of a lipid bilayer membrane supported by a weak cytoskeleton. Lipid bilayers in general have a distinct mode of mechanical failure which results in cell death. Small pores in bilayers naturally form spontaneously through a stochastic process, but are transient and self-healing. Upon mechanical strain, however, pore formation becomes more frequent, and the distribution of pores' sizes shifts upward[44]. Above a certain strain of the area of the membrane, about 2-3%[7, 45], the cell bilayer becomes metastable and ultimately irreparable, and pore

formation is permanent. Thus, if the strain of red blood cells in the vicinity of an expanding bubble is calculated, one may estimate the zone in which the RBCs would be likely destroyed by a pulse.

To model this interaction, the modified Keller-Miksis model for a single bubble[33], introduced in Chapter 3, is expanded upon. A bubble displaces a fluid particle, initially at position r_0 relative to the distance of the particle from the initial bubble wall, R_0:

$$r = \sqrt[3]{r_0^{\,3} + \left(R^3 - R_0^{\,3}\right)} \tag{1}$$

A spherical section of the fluid environment can be considered for the cell if the cell elasticity is weak. Assuming inertial motion i.e. the displacement of the cell is similar to that of the surrounding medium, then the overall deformation of the cell perimeter can be calculated. Next, the surface area and areal strain are easily derived if the cell is axisymmetric (i.e. the bubble and cell are centered in the same plane). Since the cell is considered spherical, any change in shape due to deformation necessarily causes an increase in surface area and a tensile strain to the membrane.

For the bubble dynamics simulation, the properties of the medium were chosen to mimic the 1.5% agarose, with G = 20 kPa, η = 0.015 Pa-s, σ = 50 mN/m. The waveform used was a 15 cycle pulse with p_- = 15 MPa and f = 1 MHz using the same model from Chapter 3. The choice of initial bubble size is relatively unimportant for estimating the bubble expansion at such high pressure amplitudes[8, 46], and thus initial bubble radius is chosen as 1 μm for all cases tested.

Figure 4.10 shows the initial field of uniformly spaced points around the bubble at the initial radius and at maximum expansion. Also shown is the deformation of a 10 μm spherical cell (similar to an RBC diameter) at an initial

distance of 40 μm from the bubble. The maximum bubble size in the simulation R_{max} = 61 μm, in good agreement with the average size of bubbles observed during experiment near the peripheral focus close to the main lesion. Because the strain falls off with r_0^3, only cells in the vicinity of the bubble are severely distorted. Figure 4.11 shows the areal strain experienced by a cell vs. bubble-cell distance. The normalized distance d/R_{max} which causes an areal strain of 0.03 is 1.25 and 0.02 is 1.35. As 0.02-0.03 is the areal strain for RBC lysis, the results indicate that cell lysis is expected in an area slightly larger than the diameter of the bubble. For larger cells, a small difference in the threshold strain area was observed, with a 40 μm cell receiving a 0.03 strain at d/R_{max} = 1.31 and 0.02 strain at 1.40. Thus, the results here appear fairly insensitive to cell diameter.

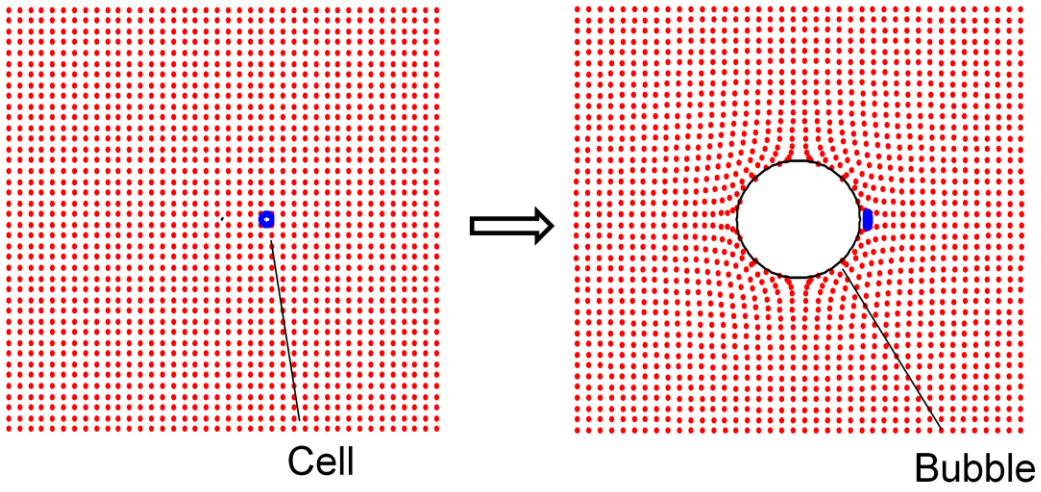

Figure 4.10. Cavitation model for strain induced in a solid matrix on a 10 μm RBC (blue line) by a bubble (black line). The bubble causes circumferential tension in the matrix around it, and tension to the cell membrane.

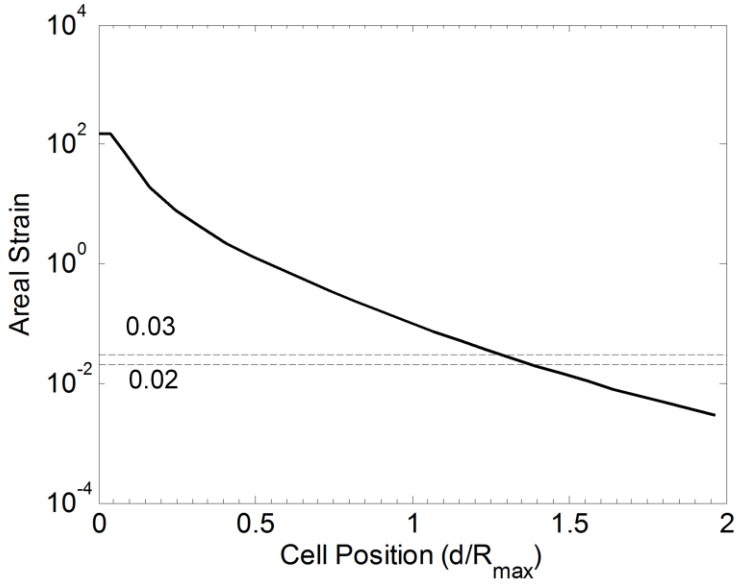

Figure 4.11. Areal strain to a 10 μm diameter cell membrane vs. cell distance from the bubble. The dashed lines are the 0.02 and 0.03 areal strain thresholds for damage, the typical values in literature for rupture of RBCs.

4.3 Discussion

Cavitation has been investigated extensively as a primary cause of ultrasound-induced tissue injury. However, it is difficult to observe the effects of cavitation in tissue in real time, and many mechanisms have been proposed for the cause of tissue-induced damage. Previous researchers have directly observed the interaction of cavitation with cells, either with liquid and gel cell suspensions [19-21, 24], cell monolayers[22], and vessel-mimicking phantoms[8]. We found that the tissue phantom described in this study can be used to directly observe cavitation and the resulting damage as it would occur in solid soft tissues, or at a soft tissue-liquid interface (such as the collecting ducts of kidneys or blood vessels)[47]. The phantom was found to be a very sensitive indicator of cavitation damage, with cell disruption visible even after a single, 10-cycle ultrasound pulse. Lesions

generated by histotripsy in the tissue phantom matched those found in ex-vivo tissue in morphology, and were more visible than those in kidney tissue. Furthermore, the phantom provides a more controllable method to study the effects of different ultrasound parameters and transducers than ex-vivo tissue, which will inherently contain significant sample-to-sample variation.

The indicator of cavitation-induced lesions in the phantom is a change in transparency due to disruption of red blood cells, which are known to be susceptible to cavitation damage [32]. The primary contents of red blood cells are water and hemoglobin, in a ratio of approximately 2:1 by weight [48]. Using a long-distance microscope attached to the SIM 02 high-speed camera, we have also observed individual cells within the phantom during histotripsy exposure. When cavitation occurs in the phantom the cells are locally disrupted. However, the change in appearance at the cellular level only occurs some time after the cavitation. In Figure 4.12, the cells still appear intact directly after cavitation cloud collapse. Within 1 second after ultrasound incidence the lesion becomes fully developed. Although cavitation temporarily displaces cells with respect to their equilibrium position within the agarose, they return to this position after cavitation collapse. Afterwards, the field becomes uniform, indicating diffusion of red cell contents into the agarose. Based on these observations, it is hypothesized that no hemoglobin or other products of the red blood cells have been destroyed, but diffusion of cell contents into the agarose after membrane disruption creates a homogeneous agarose-hemoglobin mixture. Since the entire area of agarose-hemoglobin will be the same index of refraction, minimal scattering occurs compared with the areas containing intact red blood cells.

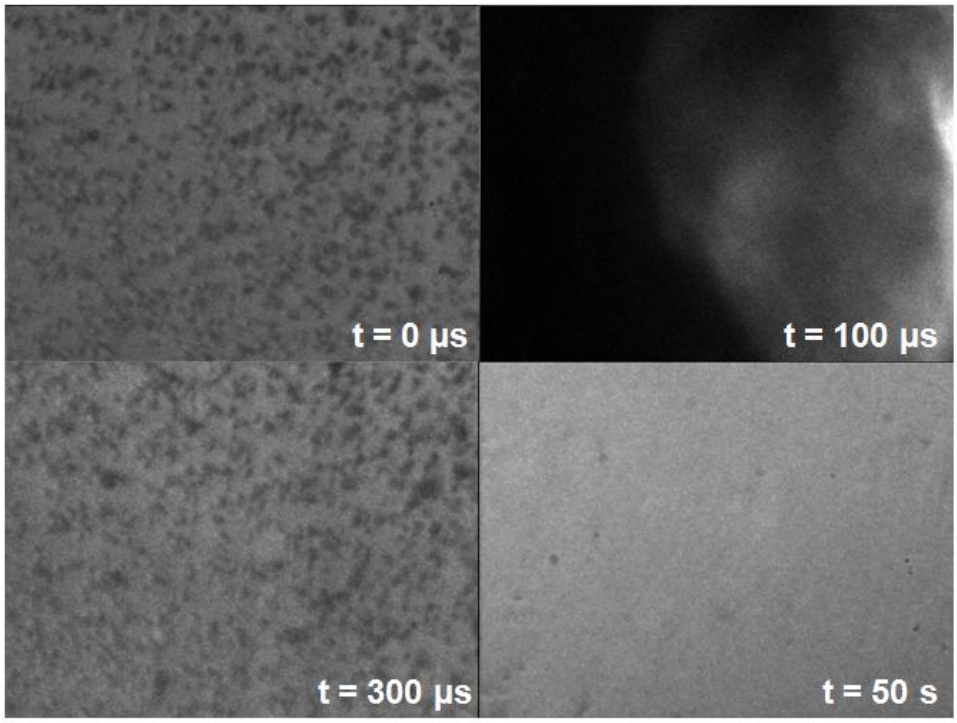

Figure 4.12. High speed images of the cell phantom under 20x magnification. Prior to insonation (t = 0), individual cells are observed in the agarose. After cavitation, the red blood cells are still visible as inhomogeneous regions (t = 300 µs). When another image is captured after 50 seconds, no cells are apparent in the area.

The disruption of cells by cavitation in the phantom caused lesions of similar morphology and lateral dimension as those formed in kidney. The axial length of several lesions in the kidneys extended to the distal surface of the kidney or into the medulla. In these instances, the lesions were only observed in the kidney cortex, limiting the length measured. However, the maximum length of lesions in phantom (19.8 mm) was similar to the maximum measured in kidney for lesions (19.4 mm). Therefore, the phantom appears to form lesions similar to ex-vivo soft tissue. The boundaries of the lesion in the phantom were also very distinct, similar to tissue damage caused by histotripsy. The smaller areas of damage surrounding the central lesion, as seen in Figure 4.9, show no intermediate layer

with reduced cell concentration, only total lack of cells or concentration similar to that of untreated phantom. This behavior suggests that damage to the phantom is a threshold phenomenon, and that red blood cells are either totally disrupted or remain completely intact.

The response of the phantom to cavitation damage on a B-Mode image was indicated as a local hypoechoic zone. This feature of histotripsy is commonly observed in tissue, as is a useful feedback metric to indicate when significant disruption has occurred [29]. Although flowing red blood cells typically have a hypoechoic appearance, static blood shows a speckle pattern, although at a reduced intensity from soft tissues [51-54]. The backscatter from red blood cells has been studied previously and the backscatter coefficient (BSC) can be determined as a function of hematocrit and medium properties[55]. Figure 4.13 shows our simulation of relative backscatter intensity vs. hematocrit of porcine red blood cells in agarose with an ultrasound frequency of 10 MHz using a Percus-Yevick packing theory for 3-D Rayleigh scattering as derived by Mo et al. At 5% hematocrit, the backscatter is a factor of 0.7 compared with the peak at 13%. However, high concentrations of RBCs will reduce light transmission, thus making high-speed imaging difficult. A hematocrit of 5% appears to be an acceptable compromise which allows both ultrasound and optical imaging simultaneously.

The demarcated lesions in the phantom were only found to occur at the location that cavitation clouds or individual cavitation bubbles were generated. Interestingly, the lesions formed were of similar extent and shape as the size of the bubble cloud shortly after the end of ultrasound exposure (within 10 μs), indicating that the bubble dimensions observed can provide an estimate of the damage. In this respect, if images of the bubble cloud are captured from each pulse over multiple pulses, the extent of damage may be estimated from an

overlay of the images. We have demonstrated this by subjecting a phantom to 3 pulses of ultrasound, capturing and image of each bubble cloud and lesion formed. Figure 4.14 shows an overlay of the bubble clouds from all 3 pulses and the resulting lesion of damage produced from the 3 pulses. This result, combined with the results at the end of Chapter 3 for bubble cloud simulation, provide a method to predict and experimentally validate the range of damage caused by a specific transducer and pulse sequence.

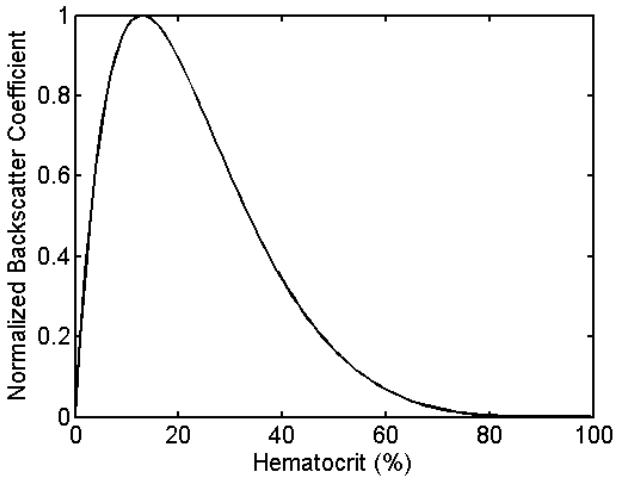

Figure 4.13. Ultrasound backscatter coefficient (BSC) vs. blood hematocrit in agarose at 10 MHz. The peak occurs at 13% in this case. A 5% phantom yields has a BSC of 0.7 compared with the peak.

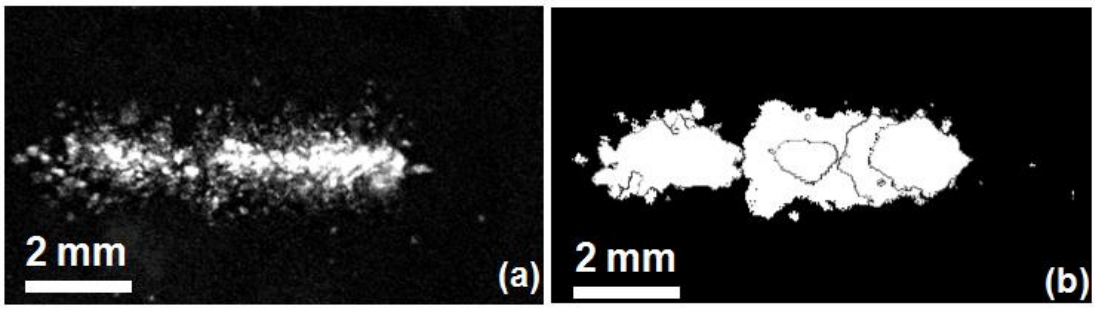

Figure 4.14. Image of a lesion generated from 3 single ultrasound pulses (a) and overlapping images of 3 bubble clouds taken from binary images (b). Ultrasound propagation was from left to right. Lesion damage matches the shape and location of the bubble clouds, although appears darker near the edges of the cloud.

A model of cavitation-induced strain by bubble expansion was also employed to try and predict the region in which cells would be ablated around a single bubble. The model estimated that the lesions should be somewhat larger than maximum bubble radius, assuming the strain induced by bubble expansion on adjacent cells is the primary mechanism of histotripsy cell disruption. While the peak bubble diameter was ~120 μm, the peak diameter of the lesions was 150 μm. It has also been observed that the formation of static bubbles in the RBC phantom causes surrounding cell lysis without any sonication. These data provide good evidence that bubble-induced strain can cause cell disruption, and possibly tissue disruption. However, additional mechanisms may contribute when multiple bubbles are present in a cloud. Using the RBC phantom with more controlled bubble nuclei placement, such as with laser-generated bubbles or microbubble contrast agents, future studies of the damage mechanism will be able to more precisely correlate bubble behavior and damage.

The phantoms containing axially-oriented lesions did not show circular spots of cavitation damage outside of the main lesion, but streaks through the RBC layer of the phantom parallel to the direction of propagation (Figure 4.3). This was not observed during single ultrasound pulses, suggesting the streaks are the cumulative effect of many pulses. The width of the streaks is similar to the diameter of the small lesions observed in the phantom. These show similar appearance to gel tunnels seen previously in agarose gels [49, 50]. Caskey et al. suggested that bubble jets played a role in tunnel progression. The tunnels indicate that histotripsy damage may progress by translational movement of individual bubbles in the cloud, which each form a linear lesion. With a high enough density of bubbles, the tunnels will overlap and completely ablate the targeted zone over several hundred pulses.

The cell phantom in this form has several limitations to be addressed. The most prominent is that it is 2-dimensional, and thus the entire lesion cannot be visualized optically, only a cross section. 3-dimensional phantoms of RBC-agarose can also be made, but the lesion formation cannot be observed in real time. Alternately, the full lesion volume can be estimated from the axial-lateral profile in the 2-dimensional phantom. However, alignment of the focus with the cell layer is critical to avoid obtaining an off-center cross-section and underestimating the focal dimensions. Multiple thin layers of red blood cells can be used to obtain the cross section at different planes in the phantom. The phantoms are also limited by temperature. The agarose mixture used in these experiments has a melting point of 70^0C, limiting its potential use as a thermal indicator. For combined thermal/mechanical lesion visualization, another optically-transparent tissue-mimicking material with higher melting point must be used. The addition of bovine serum albumin (BSA) [16] can provide indication of thermal lesions in both the blood layer and transparent layers. Finally, the acoustic properties of the phantom were intermediate between water and soft tissue. The sound speed can be increased from ~1500 m/s to the expected soft tissue value of 1540 m/s by addition of a small quantity of glycerol [56]. Attenuation can also be increased with BSA. Finally, scatters such as graphite are often used to increase the backscatter to accurately mimic specific tissues.

While accuracy of the acoustic characteristics undoubtedly plays an important role in imaging, the most important effects will be from properties that affect cavitation behavior. Models of cavitation response to ultrasound in a viscoelastic medium[33] predict that the bubble response varies significantly with tissue viscosity and elasticity, a result found in the observations in Chapter 3 as well. In the RBC phantom, the measured elasticity of the gel was 62 kPa, which matches well compared with literature values for 1.5% concentration agarose [57].

This value is somewhat higher than most soft tissues, which are on the order of 10 kPa [36]. Depending on composition, blood clots can have a wide range of elasticities. The elasticity of the gel can be predictably modified by agarose concentration to more accurately mimic these specific clot types [37].

4.4 References

1. Coleman AJ, Kodama T, Choi MJ, Adams T, Saunders JE. The cavitation threshold of human tissue exposed to 0.2-MHz pulsed ultrasound: Preliminary measurements based on a study of clinical lithotripsy. Ultrasound Med Biol. 1995;21:405-417

2. Delius M, Enders G, Xuan ZR, Liebich HG, Brendel W. Biological effects of shock waves: Kidney damage by shock waves in dogs--dose dependence. Ultrasound Med Biol. 1988;14:117-122

3. Matlaga BR, McAteer JA, Connors BA, Handa RK, Evan AP, Williams JC, Lingeman JE, Willis LR. Potential for cavitation-mediated tissue damage in shockwave lithotripsy. J Endourol. 2008;22:121-126

4. Freund JB, Shukla RK, Evan AP. Shock-induced bubble jetting into a viscous fluid with application to tissue injury in shock-wave lithotripsy. J. Acoust. Soc. Am. 2009;126:2746-2756

5. Bailey MR, Couret LN, Sapozhnikov OA, Khokhlova VA, ter Haar G, Vaezy S, Shi X, Martin R, Crum LA. Use of overpressure to assess the role of bubbles in focused ultrasound lesion shape in vitro. Ultrasound Med. Biol. 2001;27:695-708

6. Evan AP, Willis LR, McAteer JA, Bailey MR, Connors BA, Shao Y, Lingeman JE, Williams JRJC, Fineberg NS, Crum LA. Kidney damage and renal functional changes are minimized by waveform control that suppresses cavitation in shock wave lithotripsy. J. Urol. 2002;168:1556-1562

7. Lokhandwalla M, Sturtevant B. Mechanical haemolysis in shock wave lithotripsy (SWL): I. Analysis of cell deformation due to swl flow-fields. Phys. Med. Biol. 2001;46:413-437

8. Zhong P, Zhou Y, Zhu S. Dynamics of bubble oscillation in constrained media and mechanisms of vessel rupture in swl. Ultrasound Med. Biol. 2001;27:119-134

9. Lauterborn W, Hentschel W. Cavitation bubble dynamics studied by high speed photography and holography: Part one. Ultrason. 1985;23:260-268

10. Rau KR, Quinto-Su PA, Hellman AN, Venugopalan V. Pulsed laser microbeam-induced cell lysis: Time-resolved imaging and analysis of hydrodynamic effects. Biophys. J. 2006;91:317-329

11. Prokop AF, Soltani A, Roy RA. Cavitational mechanisms in ultrasound-accelerated fibrinolysis. Ultrasound Med. Biol. 2007;33:924-933

12. Arora D, Cooley D, Perry T, Skliar M, Roemer RB. Direct thermal dose control of constrained focused ultrasound treatments: Phantom and in vivo evaluation. Phys. Med. Biol. 2005;50:1919-1935

13. Canney MS, Bailey MR, Crum LA, Khokhlova VA, Sapozhnikov OA. Acoustic characterization of high intensity focused ultrasound fields: A combined measurement and modeling approach. J. Acoust. Soc. Am. 2008;124:2406-2420

14. Tu J, Matula TJ, Bailey MR, Crum LA. Evaluation of a shock wave induced cavitation activity both in vitro and in vivo. Phys. Med. Biol. 2007;52:5933-5944

15. Lierke EG, Hemsel T. Focusing cross-fire applicator for ultrasonic hyperthermia of tumors. Ultrason. 2006;44:e341-e344

16. Lafon C, Zderic V, Noble ML, Yuen JC, Kaczkowski PJ, Sapozhnikov OA, Chavrier F, Crum LA, Vaezy S. Gel phantom for use in high-intensity focused ultrasound dosimetry. Ultrasound Med. Biol. 2005;31:1383-1389

17. Lafon C, Khokhlova VA, Kaczkowski PJ, Bailey MR, Sapozhnikov OA, Crum LA. Use of a bovine eye lens for observation of hifu-induced lesions in real-time. Ultrasound Med. Biol. 2006;32:1731-1741

18. Divkovic GW, Liebler M, Braun K, Dreyer T, Huber PE, Jenne JW. Thermal properties and changes of acoustic parameters in an egg white phantom during heating and coagulation by high intensity focused ultrasound. Ultrasound Med. Biol. 2007;33:981-986

19. Hughes DE, Nyborg WL. Cell disruption by ultrasound. Science. 1962;138:108-114

20. Miller DL, Thomas RM, Williams AR. Mechanisms for hemolysis by ultrasonic cavitation in the rotating exposure system. Ultrasound Med. Biol. 1991;17:171-178

21. Williams JC, Woodward JF, Stonehill MA, Evan AP, McAteer JA. Cell damage by lithotripter shock waves at high pressure to preclude cavitation. Ultrasound Med. Biol. 1999;25:1445-1449

22. Brayman AA, Lizotte LM, Miller MW. Erosion of artificial endothelia in vitro by pulsed ultrasound: Acoustic pressure, frequency, membrane orientation and microbubble contrast agent dependence. Ultrasound Med. Biol. 1999;25:1305-1320

23. Sondén A, Svensson B, Roman N, Brismar B, Palmblad J, Kjellström BT. Mechanisms of shock wave induced endothelial cell injury. Lasers Surg. and Med. 2002;31:233-241

24. Brümmer F, Brenner J, Bräuner T, Hülser DF. Effect of shock waves on suspended and immobilized L1210 cells. Ultrasound Med. Biol. 1989;15:229-239

25. Liu Y, Zhong P. High intensity focused ultrasound induced transgene activation in a cell-embedded tissue mimicking phantom. IEEE Ultrasonics Symposium, 2006. 2006:1746-1749

26. Holt RG, Roy RA. Measurements of bubble-enhanced heating from focused, mhz-frequency ultrasound in a tissue-mimicking material. Ultrasound Med. Biol. 2001;27:1399-1412

27. Liu H-L, Chen W-S, Chen J-S, Shih T-C, Chen Y-Y, Lin W-L. Cavitation-enhanced ultrasound thermal therapy by combined low- and high-frequency ultrasound exposure. Ultrasound Med. Biol. 2006;32:759-767

28. Kieran K, Hall TL, Parsons JE, Wolf Jr JS, Fowlkes JB, Cain CA, Roberts WW. Refining histotripsy: Defining the parameter space for the creation of nonthermal lesions with high intensity, pulsed focused ultrasound of the in vitro kidney. J. Urol. 2007;178:672-676

29. Wang T-Y, Xu Z, Winterroth F, Hall TL, Fowlkes JB, Rothman ED, Roberts WW, Cain CS. Quantitative ultrasound backscatter for pulsed cavitational ultrasound therapy-histotripsy. IEEE Trans Ultrason Ferroelectr Freq Control. 2009;56:995-1005

30. Hall TL, Hempel CR, Lake AM, Kieran K, Ives K, Fowlkes JB, Cain CA, Roberts WW. Histotripsy for the treatment of bph: Evaluation in a chronic canine model. IEEE Ultrasonics Symposium, 2008. 2008:765-767

31. Williams AR, Miller DL. Photometric detection of atp release from human erythrocytes exposed to ultrasonically activated gas-filled pores. Ultrasound Med. Biol. 1980;6:251-256

32. Nyborg WL, Miller DL. Biophysical implications of bubble dynamics. Appl. Sci. Res. 1982;38:17-24

33. Yang X, Church CC. A model for the dynamics of gas bubbles in soft tissue. J. Acoust. Soc. Am. 2005;118:3595-3606

34. Xu W, Kaufman JJ. Diffraction correction methods for insertion ultrasound attenuation estimation. IEEE Trans. Biomed. Eng. 1993;40:563-570

35. He P. Direct measurement of ultrasonic dispersion using a broadband transmission technique. Ultrason. 1999;37:67-70

36. Egorov V, Tsyuryupa S, Kanilo S, Kogit M, Sarvazyan A. Soft tissue elastometer. Med. Eng. Phys. 2008;30:206-212

37. Normand V, Lootens DL, Amici E, Plucknett KP, Aymard P. New insight into agarose gel mechanical properties. Biomacromolecules. 2000;1:730-738

38. Ophir J, Alam S, Garra B, Kallel F, Konofagou E, Krouskop T, Merritt C, Righetti R, Souchon R, Srinivasan S, Varghese T. Elastography: Imaging the elastic properties of soft tissues with ultrasound. J.Med. Ultrason. 2002;29:155-171

39. Xu Z, Fan Z, Hall TL, Winterroth F, Fowlkes JB, Cain CA. Size measurement of tissue debris particles generated from pulsed ultrasound cavitational therapy - histotripsy. Ultrasound Med. Biol. 2009;35:245-255

40. Hall TL, Fowlkes B, Cain CA. A real-time measure of cavitation induced tissue disruption by ultrasound imaging backscatter reduction. IEEE Trans Ultrason Ferroelectr Freq Control. 2007;54:569-575

41. Gracewski SM, Miao H, Dalecki D. Ultrasonic excitation of a bubble near a rigid or deformable sphere: Implications for ultrasonically induced hemolysis. J. Acoust. Soc. Am. 2005;117:1440-1447

42. Rand RP, Burton AC. Mechanical properties of the red cell membrane: I. Membrane stiffness and intracellular pressure. Biophys. J. 1964;4:115-135

43. Alfred W.L J. Viscoelastic properties of the human red blood cell membrane: I. Deformation, volume loss, and rupture of red cells in micropipettes. Biophys. J. 1973;13:1166-1182

44. Kashchiev D, Exerowa D. Bilayer lipid membrane permeation and rupture due to hole formation. Biochimica et Biophysica Acta. 1983;732:133-145

45. Needham D, Nunn RS. Elastic deformation and failure of lipid bilayer membranes containing cholesterol. Biophys. J. 1990;58:997-1009

46. Zhong P, Cioanta I, Zhu S, Cocks FH, Preminger GM. Effects of tissue constraint on shock wave-induced bubble expansion in vivo. J. Acoust. Soc. Am. 1998;104:3126-3129

47. Xu Z, Fowlkes JB, Ludomirsky A, Cain CA. Investigation of intensity thresholds for ultrasound tissue erosion. Ultrasound Med. Biol. 2005;31:1673-1682

48. Keitel HG, Berman H, Jones H, Maclachlan E. The chemical composition of normal human red blood cells, including variability among centrifuged cells. Blood. 1955;10:370-376

49. Caskey CF, Qin, Shengping, Dayton, Paul A., and Ferrera, Katherine A. Microbubble tunneling in gel phantoms. J Acoust Soc Am. 2009;125:EL183

50. Williams AR, Miller DL. The use of transparent aqueous gels for observing and recording cavitation activity produced by high intensity focused ultrasound. IEEE Ultrasonics Symposium, 2003. 2003;2:1455-1458

51. Hoskins PR. Physical properties of tissues relevant to arterial ultrasound imaging and blood velocity measurement. Ultrasound Med. Biol. 2007;33:1527-1539

52. Nicholas D. Evaluation of backscattering coefficients for excised human tissues: Results, interpretation and associated measurements. Ultrasound Med. Biol. 1982;8:17-28

53. Raju BI, Srinivasan MA. High-frequency ultrasonic attenuation and backscatter coefficients of in vivo normal human dermis and subcutaneous fat. Ultrasound Med. Biol. 2001;27:1543-1556

54. Turnbull DH, Wilson SR, Hine AL, Foster FS. Ultrasonic characterization of selected renal tissues. Ultrasound Med. Biol. 1989;15:241-253

55. Mo LYL, Kuo IY, Shung KK, Ceresne L, Cobbold RSC. Ultrasound scattering from blood with hematocrits up to 100%. IEEE Trans. Biomed. Eng. 1994;41:91-95

56. Inglis S, Ramnarine KV, Plevris JN, McDicken WN. An anthropomorphic tissue-mimicking phantom of the oesophagus for endoscopic ultrasound. Ultrasound Med. Biol. 2006;32:249-259

57. Hall TL, Hempel CR, Wojno K, Xu Z, Cain CA, Roberts WW. Histotripsy of the prostate: Dose effects in a chronic canine model. Urol. In Press.

CHAPTER 5

Histotripsy Thrombolysis *In-Vitro*

This chapter describes *in-vitro* experiments evaluating histotripsy as a method of thrombolysis. Clots are treated under conditions with and without flow to determine the rate of thrombolysis. To confirm thrombolysis occurs as a result of histotripsy, its onset is correlated with the initiation of a bubble cloud. In addition to characterizing the efficacy of histotripsy thrombolysis, initial studies investigating potential side effects of the treatment are described. In particular, debris generated by histotripsy is analyzed for its potential to cause embolism. Vessel wall damage is also evaluated. These studies provide support for further testing of histotripsy thrombolysis and will guide future studies in determining what aspects are necessary for detailed exploration.

5.1 Methods

5.1.1 Clot Formation

Canine blood, which has similar values for hematocrit, total protein, fibrinogen and platelets compared with human blood[1, 2], was used to form clots *in-vitro*. Fresh whole canine blood was obtained from research subjects in an unrelated study and a citrate-phosphate-dextrose (CPD) solution (#C1765,

Sigma-Aldrich Co., St. Louis, Missouri, USA) was immediately added as an anti-coagulant at a ratio of 1 mL CPD per 9 mL blood. The blood was stored at 4°C for up to three days prior to use in a polypropylene container. To induce clotting, a 0.5 M $CaCl_2$ standard solution (#21107, Sigma-Aldrich Co., St. Louis, Missouri, USA) was mixed with the blood, using 0.05 mL $CaCl_2$ per 1 mL blood. The blood was drawn in 0.4 mL volumes into 1 mL syringes to form cylindrical clots with approximate dimensions of 4 mm (diameter) × 20 mm (length). Syringes were transferred to a water bath with temperature 37°C for 2 hours prior to the experiment to incubate the clots. All clots were then carefully removed from syringes, weighed, and transferred to a 0.9% room temperature (21°C), air-saturated saline solution. All clots were treated between 2 - 6 hours after addition of $CaCl_2$. The resulting clots prior to treatment had a mean mass of 331 +/- 39.8 mg for those used in the static vessel model. Clots for the flow model were formed on a loose string by mounting the string longitudinally in the syringe. The string with the attached thrombus was removed from the syringe after clotting, and the ends of the string were fixed to the 6 mm tube. This technique was used to hold the clot in place under flow during the experiment.

5.1.2 Vessel Model

A stationary vessel model with no background fluid flow was employed for assessment of thrombolysis (Figure 5.1). The model used a 6-mm diameter, 60-mm length low-density polyethylene (LDPE) tube with wall thickness of 500 μm to act as a vessel holding the clot. The LPDE plastic has an acoustic impedance similar to that of a vessel wall. The tube was filled with 0.9% saline and the clot was carefully transferred to the tube. Tapered silicone rubber stoppers were used

to plug the ends of the tube to contain the saline and clot debris from the treatment.

To test the effect of high flow rates on histotripsy thrombolysis, clots were treated in a circulatory model with filtered water (Figure 5.1). Filtered water has the potential to lyse red blood cells due to hypotonicity of the environment. The effects of flow and osmotic gradient on cell lysis were accounted for by a control group of clots which were submerged under the same conditions in the flow system for the same amount of time but were not exposed to histotripsy. The flow model used a pulsatile flow pump (Pulsatile Blood Pump, Harvard Apparatus, Holliston, Massachusetts, USA) with settings to control the pulses per minute and stroke volume. The pump was attached with vinyl tubing to one end of the vessel-mimicking LPDE tube in a water bath to allow flow into the tube. 1-mm and 100-μm rated filter paper was placed downstream from the tube to capture large clot debris and fragments. The pulsatile pump was set to operate at 70 beats per minute (bpm) with a stroke volume of 15 mL and a systolic to diastolic ratio of 35:65. These values were chosen to produce a mean flow velocity of 50 cm/sec in the 6 mm diameter LPDE tube, which is an upper limit for mean blood flow velocities typically found in major vessels [3].

Clots were formed on a string based on a technique developed previously[4, 5]. Both ends of the string were secured to hold the clot in position under flow. The transducer focus was scanned along the clot in the direction opposite of flow at a rate of 0.1 mm/s. After treatment, any remaining clot was removed from the tube and weighed to calculate the thrombolysis rate.

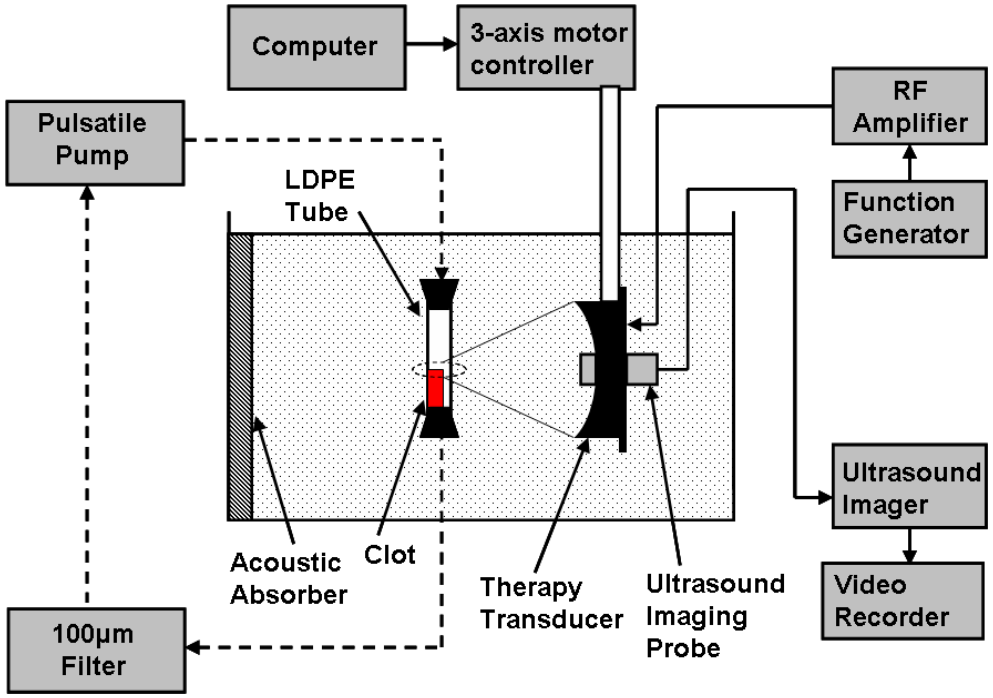

Figure 5.1. Experimental apparatus for in-vitro thrombolysis. A blood clot is placed in an LDPE tube and the therapy transducer aligned with the focus at one end of the clot using a 3-axis positioning system. An ultrasound imager is located concentric with the therapy transducer for image-guidance during treatment. A 5 MHz single-element transducer to record a scattered signal was mounted perpendicular to the therapy transducer with their foci overlapping (not shown). The dashed lines show the connection of the circulatory flow system, when present. In static saline, the ends of the tube are plugged with rubber stoppers.

5.1.3 Ultrasound Generation

The histotripsy treatment was performed using a piezocomposite 1-MHz focused transducer (Imasonic, S.A., Besançon, France) with a 15-cm focal length and 15-cm diameter. The focal volume is cigar-shaped, with dimensions 15 mm along the axis of propagation and 2.0 mm laterally at -3dB peak negative pressure of 12 MPa. The therapy transducer has a 4-cm diameter hole in the middle for inserting an imaging probe. A class D amplifier developed in our lab

was used to drive the transducer. Ultrasound was pulsed using 5-cycle bursts at a pulse repetition frequency (PRF) of 1 kHz. Ultrasound was applied to clots at different peak negative pressures of 2, 4, 6, 8, 10, and 12 MPa with corresponding spatial peak pulse average intensities (I_{SPPA}) of 150, 600, 2000, 3600, 5900, and 7000 W/cm^2. Pressure values for the ultrasound were obtained from waveforms recorded using a fiber optic probe hydrophone built in house[6]. The probe was mounted with the fiber end facing perpendicular to the ultrasound propagation to prevent cavitation from corrupting measurements or damaging the tip [7]. The signal was averaged over 200 pulses to reduce noise. Recorded pressure waveforms are shown in Figure 5.2. No deconvolution was applied to the recorded waveforms, thus the peak positive pressure is slightly underestimated for these measurements.

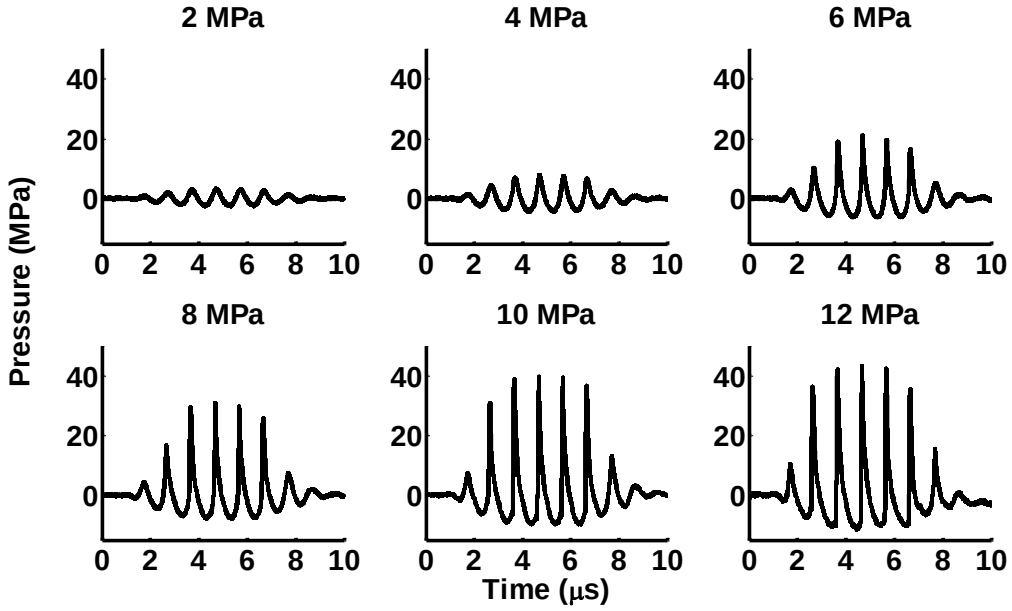

Figure 5.2. Pressure waveforms of therapy pulses at the focus of the transducer. The signals shown are averages of 200 pulses. The peak negative pressure is listed above each waveform. Measurements were recorded using a fiber optic probe hydrophone.

All treatments were performed at room temperature (21°C), in a degassed water tank with dimensions 100 cm × 75 cm × 67.5 cm. The transducer was mounted to a 3-axis motorized positioning system (Velmex, Inc., Bloomfield, NY, USA) controlled by a personal computer. The positioning system was used to position the clot in the transducer focus. Ultrasound was applied until the entire clot was dissolved or 300 seconds of treatment had occurred. The transducer focus was fixed throughout the treatment and the clot spontaneously moved into the focus until it was completely dissolved. The thrombolysis rate was calculated as the difference in initial mass and final mass of the clot divided by the amount of time ultrasound was applied (total treatment time).

5.2 Histotripsy Thrombolysis Efficacy

5.2.1 Erosion Rates without Flow

A total of 56 clots were treated in the stationary model. At peak negative pressures (p_-) of 2 and 4 MPa, no visible clot disruption was observed. At p_- of 6 and 8 MPa, the clot was partially fractionated into tiny debris after 300 seconds of histotripsy treatment. At p_- of 10 and 12 MPa, the entire clot was always completely fractionated within 300 seconds of treatment. Clot disruption was only observed visually when a bubble cloud was initiated at the focus of the transducer. If the bubble cloud was generated adjacent to the clot (within 10 mm), the clot would spontaneously move towards the bubble cloud until the center of the clot was aligned with the bubble cloud. During thrombolysis, the color of the clot changed from red to white at the surface where it was eroded, and then further dissolved until no visible fragments remained. This suggests

red blood cells were destroyed prior to breakdown of the extracellular clot matrix. The progression of a treatment is shown in Figure 5.3.

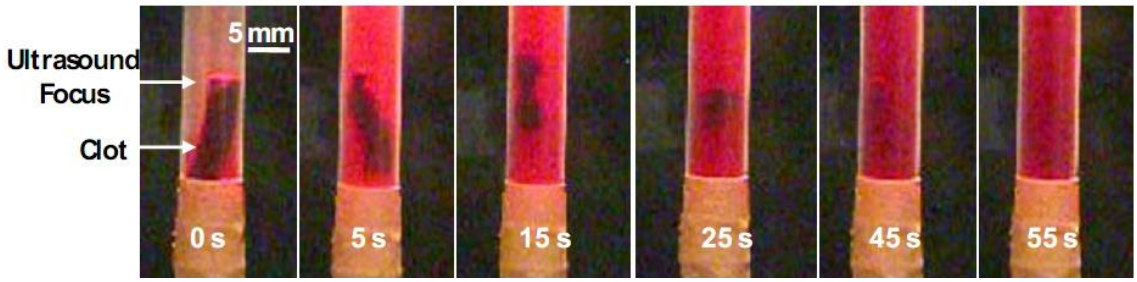

Figure 5.3. Progression of treatment in static saline. Ultrasound propagation is from right to left in the image. The clot moves into the focus of the transducer almost immediately after ultrasound exposure is started generated. The clot quickly loses mass and is bisected at the focus. Each of the two larger pieces is then dissolved over 45 seconds until no visible particles remain.

The thrombolysis rate was plotted as a function of peak negative pressure (p_- = 0 to 12 MPa) in Figure 5.4 (mean and standard deviation, n = 8). The corresponding peak positive pressure and I_{SPPA} are listed in Table 5.1. In the control group (p_- = 0 MPa), clots were placed in saline for 5 minutes without ultrasound exposure, and visible clot disruption was never observed. Similarly, at p_- = 2 and 4 MPa, no visible changes we observed during treatment and the thrombolysis rate was not statistically different from that of the control group. The thrombolysis rate was 0.13 +/- 0.038 mg/sec for the control group and 0.12 +/- 0.047 mg/sec at pressure of 4 MPa (t-test, P = 0.22). It is possible that most of the weight reduction for each of these three groups was due to handling of the clot to transfer it into and out of the tube or dissolution of clot serum into the saline.

At p_- = 6 MPa, 4 of 8 clots treated had rates similar to the control group (0.066 +/- 0.047 mg/sec). The other 4 clots had significantly higher thrombolysis rates (0.366 +/- 0.087 mg/sec) than control. At $p_- \geq 8$ MPa, a significant increase in thrombolysis rate was observed for all clots in comparison to the control group

(paired t-test, $P < 0.0001$). At the highest pressures (p_- of 10 and 12 MPa), all clots were completely fractionated in times between 80 – 260 seconds. There was an increase in thrombolysis rate with peak negative pressure between 6-12 MPa (t-test, $P < 0.05$). The mean rate was 0.21 +/- 0.17 mg/sec at p_- of 6 MPa and 2.20 +/- 0.85 mg/sec at p_- of 12 MPa.

Table 5.1. Number of treatments with bubble cloud initiation and significant thrombolysis at each pressure level. (n = 8 at each pressure)

P- (MPa)	P+ (MPa)	I_{sppa} (W/cm^2)	I_{spta} (W/cm^2)	Clot Weight (Pre) (mg)	Clot Weight (Post) (mg)	Number of treatments with thrombolysis*	Number of treatments with initiation
0	0	0	0	340 ± 38	300 ± 40	0	0
2	3	150	1	320 ± 54	285 ± 54	0	0
4	8	600	4	342 ± 34	296 ± 27	0	0
6	20	2000	14	316 ± 39	251± 73	4	7
8	32	3600	25.2	354 ± 25	64 ± 52	8	8
10	39	5900	41	310 ± 41	1.2 ± 3.5	8	8
12	43	7000	49	332 ± 32	1.2 ± 3.5	8	8

*The occurrence of thrombolysis is defined in this paper as any treatment where the thrombolysis rate is greater than twice the mean thrombolysis rate of the control group.

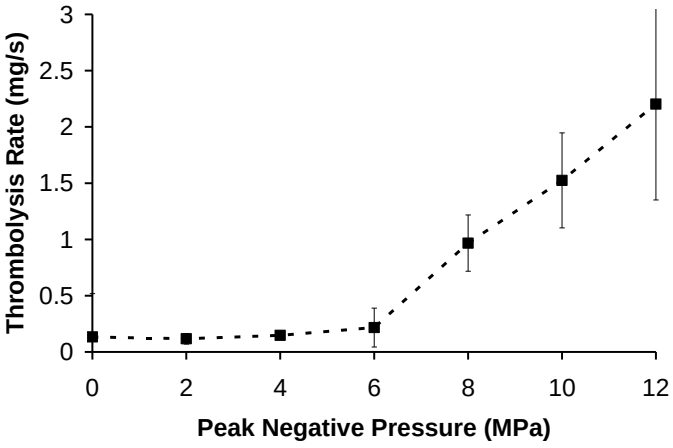

Figure 5.4. Thrombolysis rate as a function of peak negative pressure at the therapy focus (mean +/- standard deviation, n = 8). Pressures below 6 MPa had no observable effect on the clot after 5 minutes of treatment. At 6 MPa or greater, an increase in rate is observed, and the clot is quickly dissolved in times ranging between 80 - 300 seconds.

5.2.2 Erosion Rate with Flow

Since cavitation may be influenced by the presence of flow, (e.g. cavitation nuclei may be swept away), the feasibility of histotripsy thrombolysis was also tested in a fast flow environment. Clots were treated under a mean flow velocity of 50 cm/s. This value is the upper limit of mean flow velocities in major vessels. Clots formed for this experiment were smaller (150 +/- 26 mg) than those used in the stationary clot model due to difficulty forming large clots on the string. Eight clots were treated at p_- = 12 MPa, and clot weight was reduced by 72% +/- 21% (mean and standard deviation) in the fast flow in 100 seconds. During this time, the therapy focus was scanned to cover the entire clot at a scanning rate of 0.1 mm/sec. The thrombolysis rate was 1.07 +/- 0.34 mg/s, significantly higher than the control rate of 0.27 +/- 0.12 mg/s (t-test, $P < 0.0002$). However, the rate at p_- = 12 MPa here was lower than those in static saline at the same pressure level.

Serial filters of 1 mm and 100 μm were used to capture any large clot debris or fragments generated by histotripsy treatment. No measurable debris was captured by the 1 mm filter. In two of the eight treated clots, 5% and 12% of the initial clot weight was captured by the 100 μm filter paper. In one of eight control clots, 17% of the clot weight was captured by the 100 μm filter. All other filters showed less than 3% variance in weight before and after the experiment. The possibility that large clot fragments were separated from the string by the flow due to weak adhesion could not be excluded.

5.3 Cavitation Detection and Image Feedback

5.3.1 Ultrasound Imaging

A 5-MHz ultrasound imager (System FiVe, General Electric, Fairfield, Connecticut, USA) was used for targeting the clot and monitoring treatment progress. The imager was positioned through the central hole in the therapy transducer such that it always imaged the therapy plane. For targeting prior to treatment, a bubble cloud was generated at the focus of the transducer in the empty water bath and appeared as a hyperechoic zone on an ultrasound image. The position of the hyperechoic zone was marked on the image as the focus. Once the tube containing the clot was added to the water bath, the therapy transducer was positioned so that the focus marker was aligned at one end of the clot. Once the targeting is achieved, histotripsy treatment was applied to the clot. The treatment progress and completion was monitored through reduced echogenicity on the B-Mode image resulting from breakup of the clot.

The histotripsy thrombolysis treatment was monitored with B-mode ultrasound imaging in real-time. Prior to application of ultrasound, the clot appeared as a hyperechoic zone inside the tube walls on the B-mode ultrasound image (Figure 5.5a). During the treatment, a bubble cloud was generated in the tube adjacent to the clot, which appeared as a temporally changing hyperechoic zone at the therapy transducer focus (Figure 5.5b). Interference of the therapy acoustic pulses with the imager caused only minimal corruption of the image due to the low duty cycle used for treatment (0.5%). As the treatment progressed, the clot's hyperechoic zone reduced in size and echogenicity. The bubble cloud remained on the clot surface throughout the treatment. Once the clot was entirely

fractionated, its hyperechoic zone on the image disappeared and the inside of the tube became hypoechoic (Figure 5.5c).

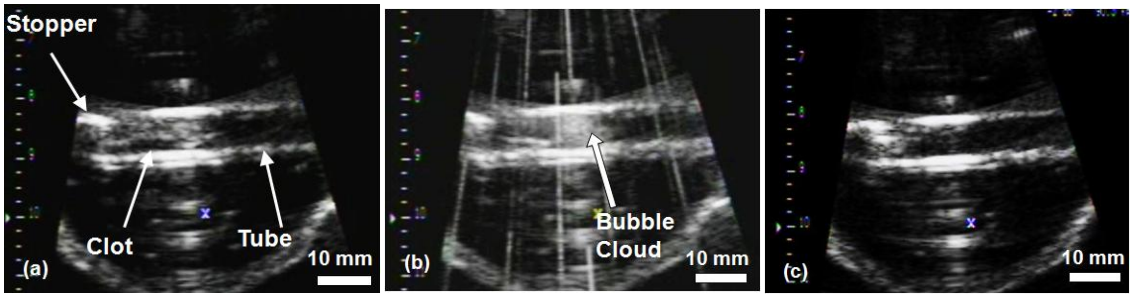

Figure 5.5. B-Mode images of the histotripsy thrombolysis treatment using a 5 MHz imaging probe. The imaging probe is approximately 8 cm from the ultrasound focus. The ultrasound propagation is from top to bottom of the image. The clot is visible in the tube as an echogenic region prior to insonation (a). The bubble cloud is visible during treatment in (b). The vertical lines in (b) are acoustic interference of the therapy transducer with the imager. However, most of the image remains uncorrupted. The echogenicity of the clot is greatly reduced after complete thrombolysis (c).

5.3.2 Cavitation Detection

Acoustic backscatter from the cavitating bubble cloud was passively received using a 2.5-cm aperture 5-MHz focused single-element transducer with a focal length of 10 cm (Valpey Fisher Corp., Hopkinton, Massachusetts, USA). It was connected directly to a digital storage oscilloscope (9354TM, Lecroy, Chestnut Ridge, New York, USA) for data collection. The backscatter signal was recorded by the oscilloscope every 300 ms in a 20 μs window timed to capture the scattered therapy pulse. Previously, it has been shown that tissue fractionation only occurs when initiation of a temporally changing acoustic backscatter is detected corresponding to formation of a cavitating bubble cloud[8-10]. Here, the initiation was detected by the temporally-changing scattered wave using the

method detailed in a previous study[8]. One difference in this experiment is that the backscatter receiver was positioned facing 90° from the therapy transducer instead of through the central hole of the therapy transducer, because the hole was occupied by the imaging probe. This technique measured the continuous dynamic change in scattering energy due to pulse-to-pulse changes in the bubble cloud. Briefly, the normalized energy for each backscatter waveform is calculated. A moving standard deviation over time of the normalized energy is then calculated. When this standard deviation (pulse-to-pulse variation in backscatter) is above a set threshold for 3 or more consecutive points, we define this as initiation of a bubble cloud. From this, the total amount of time a bubble cloud was present during treatment for each trial could be calculated. The initiation threshold for each pressure level was determined by linear extrapolation from measurements at the lowest pressure levels, where no initiation was observed.

Detection of temporally changing acoustic backscatter was used to monitor a cavitating bubble cloud. Without the initiation and maintenance of this temporally changing backscatter, no tissue fractionation was generated by histotripsy in our previous studies[8, 11]. It was found that without initiation, no thrombolysis was observed, i.e., the thrombolysis rate was similar to the control rate. In 28 of 31 treatments (90%) where initiation was detected, the thrombolysis rate was significantly higher than the control. Table 5.1 shows the number of events for each pressure where thrombolysis occurred, as well as the number of events where initiation occurred. Thrombolysis was considered to have occurred when the thrombolysis rate was greater than twice the control rate.

Percentage of time a bubble cloud was initiated throughout treatment was calculated. The percentage of initiated time was the amount of time that temporally changing acoustic backscatter was detected divided by the total

treatment time. The percentage of initiated time was plotted as a function of peak negative pressure (Figure 5.6). p- of 2-4 MPa had very low mean values for percentage of initiated time (< 0.5%) and thrombolysis was never observed at these pressure levels. p- of 6 MPa had an intermediate percentage of initiated time of 56%. At this value, 4 clots where thrombolysis occurred also had a high percentage of initiated time (mean 87%) vs. 4 with low thrombolysis rates (mean 25%). For 8-12 MPa, the mean percentage of initiated time was > 99.6% and thrombolysis always occurred. These data support the claim that the cavitation cloud is necessary for histotripsy thrombolysis.

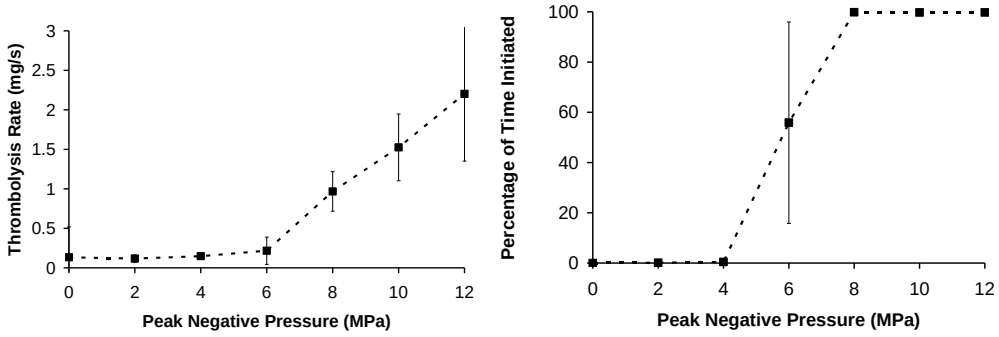

Figure 5.6. (a) Thrombolysis rate as a function of peak negative pressure at the therapy focus (mean +/- standard deviation, n = 8). Pressures below 6 MPa had no observable effect on the clot after 5 minutes of treatment. At 6 MPa or greater, an increase in rate is observed, and the clot is quickly dissolved in times ranging between 80 - 300 seconds. (b) Percentage of time initiated vs. peak negative pressure. The percentage of time initiated is defined as the initiated time divided by the total treatment time. Initiation here refers to the initiation of a temporally changing backscatter described in the text. For pressures < 6MPa, initiation was never detected. Above 6 MPa, initiation was always observed and the initiated state remained throughout the treatment.

The thrombolysis rate at $p_- = 6$ MPa was previously defined as the mass loss divided by the total treatment time. However, it was shown that during only 56% of the treatment time was a bubble cloud present. To obtain an estimate of

the thrombolysis rate only when a cloud is initiated, the total initiated time can be used to calculate rate instead of total treatment time. This calculation gives a thrombolysis rate of 0.58 +/- 0.17 mg/sec, which is significantly higher than the thrombolysis rate calculated using the treatment time. Since thrombolysis appears to only occur when the bubble cloud is initiated, this rate provides a better measure for the efficiency of the bubble cloud.

5.4 Safety of Histotripsy Thrombolysis

5.4.1 Debris Size Measurement

There is a concern that the clot fragments or debris generated by histotripsy may occlude downstream vessels and cause hazardous emboli. To address this issue, the suspended clot debris was serially filtered through 1 mm, 100 μm, 20 μm, and 5 μm filters after treatment to measure the total weight of particles in each size category. The dry weight of each filter was measured prior to treatment. After filtering, the samples were dried over 12 hours, and each filter was reweighed.

To obtain a more sensitive measurement of particle distribution, the suspended clot debris from the stationary vessel model was also measured using a particle sizing system, a Coulter Counter (Multisizer 3, Beckman Coulter, Fullerton, California, USA). After treatment, the clot debris saline suspension was collected from each of the treated clots and the debris size distribution was measured using the Coulter Counter. This device measures the impedance change due to the displacement by the particle volume of a conducting liquid in which the particles are suspended. The impedance change is proportional to the particle volume. Volume of debris particle is calculated and diameter is

estimated assuming a spherical shape for each particle. The measurement size range is 2-60% of the size of aperture tube which is part of the Coulter Counter. A 100-μm diameter aperture tube was use to achieve a dynamic range of 2 – 60 μm in diameter. Debris larger than 60 μm which blocked the aperture tube caused interruption of the measurement, and was noted. The sizing resolution is approximately 1% of the particle diameter. Two measurements were taken for each sample.

To obtain the size distribution of clot debris generated by histotripsy, samples were measured using filter papers rated to 5 μm, 20 μm, 100 μm and 1 mm. The wet and dry weights of several whole clots were recorded. Whole clots with a wet weight of 350 mg were reduced to 100 mg weight once dried. We then measured the change in dry weight of the filter to estimate the debris size distribution. All four filters' dry weights changed by ≤ 1 mg. No significant difference was found between control and any of the treated samples. These results suggest that at least 96% (96 mg of 100 mg) of the clot was broken down to particles smaller than 5 μm.

Additionally, saline samples containing suspended clot debris were removed from the tube after each treatment and measured by the Coulter Counter. The mean debris distributions between 2 – 60 μm particle diameter are shown in Figure 5.7. For control clots, a mean of 95% +/- 4% of the debris volume was between 2-10 μm, 3% between 10-30 μm, and 2% between 30 - 60 μm. In treatment samples where thrombolysis was detected, 72-94% of the debris was 2-10 μm, and 3-12% was between 30-60 μm. The mean number of particles counted in the treatment samples was similar to the controls. Samples treated at the highest pressures (10 and 12 MPa) had a higher percentage of larger particles (30-60 μm) than lower pressures. Debris distributions also showed a large increase in

particles smaller than 6 μm for those treated at high pressures, suggesting the disruption of individual cells.

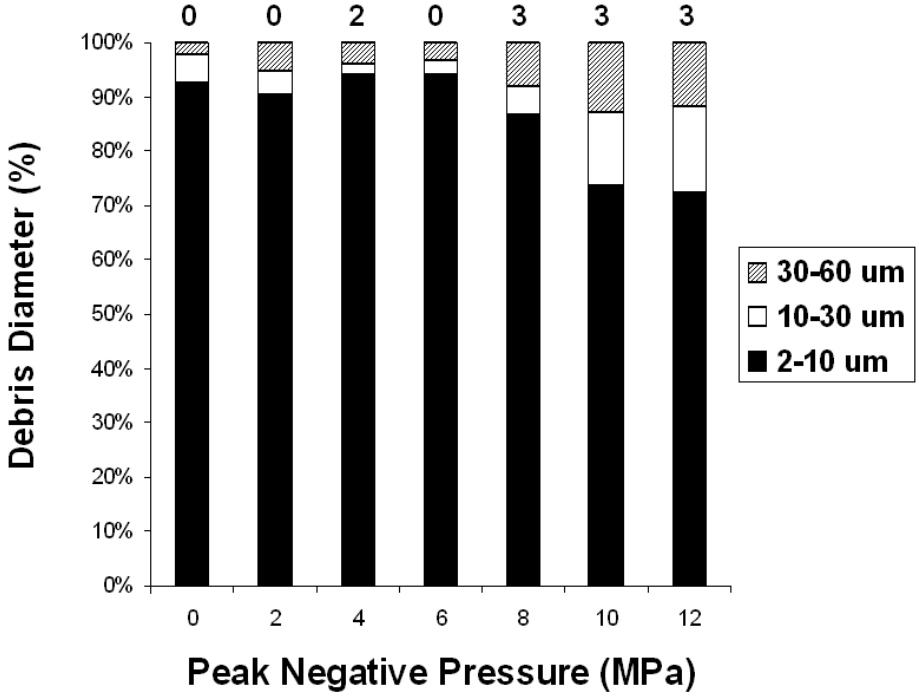

Figure 5.7. Debris volume distribution by particle diameter as measured by the Coulter Counter. A majority of the debris volume is smaller than 10 μm diameter for samples at all pressure levels. However, an increase in larger particles (30-60 μm) is apparent at 10 and 12 MPa. The number of measurements where the tube was blocked (number of particles > 60 um) is listed above each bar in the figure. There were 16 measurements taken at each pressure level.

In 2 of 56 measurements (two measurements per treatment) where thrombolysis was not detected, the 100 μm tube was blocked. In 9 of 56 measurements where thrombolysis was detected, the 100 μm tube was blocked. The blockage of the tube suggested the presence of one or more particles larger than 60 μm. These results suggest that particles larger than 60 μm are generated during the treatment, although some of them may result from process other than histotripsy thrombolysis.

5.4.2 Vessel Damage Histology

Aside from embolism, there are other concerns that must be addressed regarding the safety of histotripsy thrombolysis. As histotripsy mechanically fractionates a clot, there is a possibility that the bubble cloud generated for thrombolysis might also damage the surrounding blood vessel. Clots in canine aorta and vena cava segments were treated using the same acoustic parameters as in this study at a pressure level of p- = 12 MPa. Figure 5.8 shows the histology of control and treated segments after 300 seconds of exposure. Histotripsy-treated aorta and vena cava walls remained intact in this initial histological study. Small areas of endothelial disruption were found on both control and treated vessels. However, no damage was apparent to the underlying smooth muscle or adventitia.

Vessels without clots (3 treatments in canine aorta and 3 in canine IVC) were also directly exposed to histotripsy, targeting the inner vessel wall specifically. The vessel was cut and unfolded along the long axis and pinned to a gelatin tissue phantom to form a sheet with the inner wall facing the transducer. Figure 5.9 shows the two vessels treated with the same parameters for 600 seconds without moving the focus. In this case, smooth muscle (medial layer) disruption was observed and visible erosion of the layer occurred in the arterial segment. In the vein segment, some damage to the surface is also apparent, although no visible indentation occurred. No penetration through the adventitia was apparent in any sample. The vessel's higher resistance to histotripsy-induced damage compared to thrombi is likely due to its mechanical strength being higher than that of soft tissues we have treated previously.

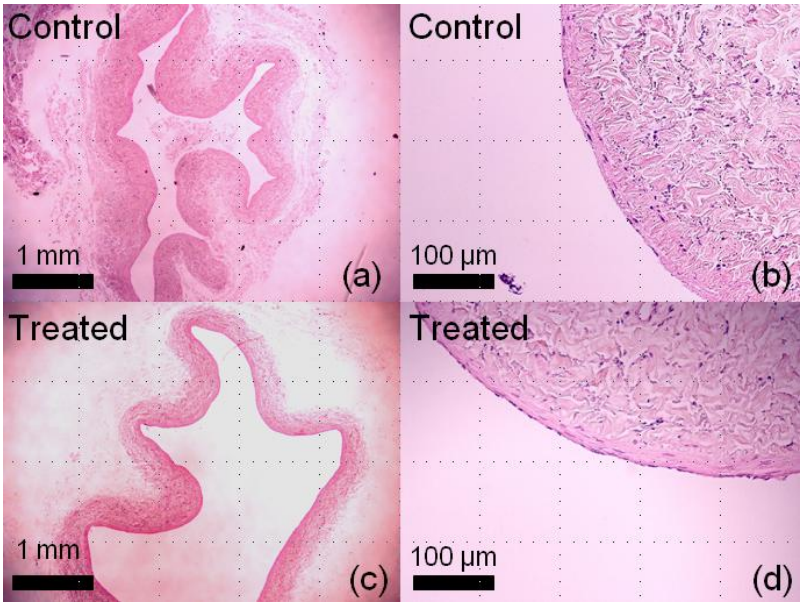

Figure 5.8. Histological slides (H&E stain) from treatment of clots in canine inferior vena cava segments. A control sample is shown in (a) and a magnified view in (b). A treated sample exposed to 300 seconds of ultrasound at p- of 12 MPa is shown in (c) and a magnified view (d). Both samples were intact, and no discernable damage was observed to the treated vein wall.

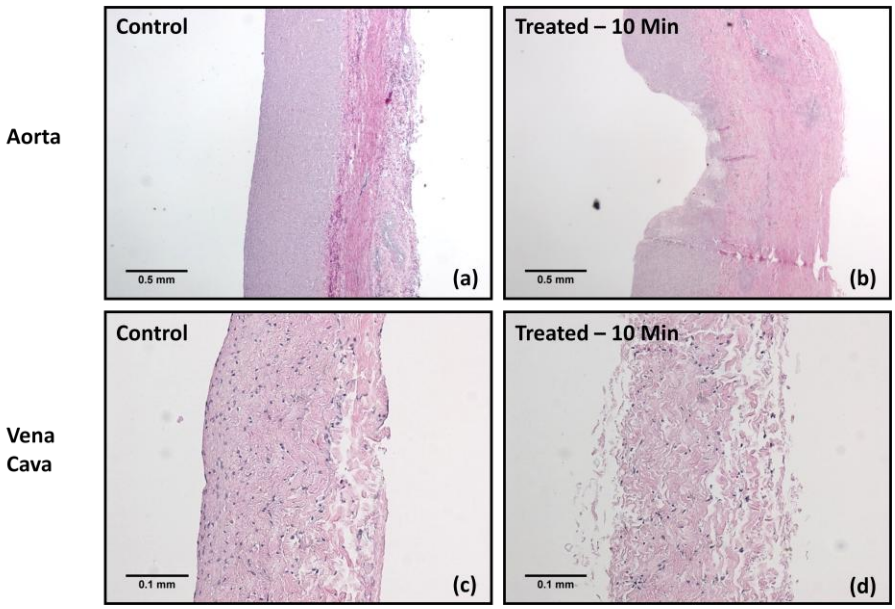

Figure 5.9. Histological slides (H&E stain) from treatment of the wall of canine aorta (top) and inferior vena cava (bottom) segments. A control sample of an aorta is shown in (a) and a treated section of the wall in (b). (c) and (d) show the same for a vena cava segment.

In addition to mechanical damage, the vessel may also be damaged by ultrasound-induced heating. However, histotripsy uses a very low duty cycle and the time-averaged intensity at the focus is low. In the experiments reported here, the maximum I_{spta} was 49 W/cm^2. The histotripsy group has previously investigated the acoustic parameter space of histotripsy[12] and have used parameters which primarily cause mechanical ablation without significant heating. The temperature rise during the treatment of clots in static saline was measured by thermocouple. The maximum temperature rise recorded over 5 minutes was 7^0C, which is unlikely to cause thermal damage to the vessel wall. With the presence of flow, the temperature rise is expected to be lower due to heat convection. However, possible vessel damage is an important safety issue, and must be further studied in acute and chronic in vivo animal studies.

5.5 Discussion

In this chapter, histotripsy was applied to cause thrombolysis *in-vitro* without the use of thrombolytic agents. Previous researchers explored the use of high-intensity focused ultrasound alone to break down blood clots[13, 14]. It was suggested that cavitation collapses were the underlying cause of damage. Similarly, the results here indicated cavitation was the primary factor responsible for thrombolysis, specifically the bubble cloud characteristic of histotripsy.

Our understanding of histotripsy is consistent with the results from this study. It was found that thrombolysis only occurs when the cavitating bubble cloud was detected by acoustic backscatter. The acoustic parameters effective for thrombolysis were also consistent with the parameters determined to be effective for other soft tissue fractionation: short pulses, a low duty cycle, and a peak negative pressure > 6MPa. It is possible that the actual threshold value for bubble

cloud initiation and thrombolysis will be different *in-vivo* than in the environments in this work, due to the difference in cavitation environment such as the availability of pre-existing nuclei and the properties of the fluid and tissue surrounding the clot.

One major advantage of histotripsy is that it can be easily guided by real-time ultrasound imaging for targeting and treatment monitoring. Such guidance is a primary challenge for any non-invasive technique and essential to ensure the treatment accuracy and efficiency. The results suggest that histotripsy thrombolysis can be also guided using real-time ultrasound imaging. The bubble cloud was highly echogenic and dynamic on a B-mode image, and blood clots could be readily identified and aligned to the therapy focus. The progression of thrombolysis could also be monitored by observing clot echogenicity. Doppler color flow mapping of the occluded vessel will also be beneficial in future studies[16]. Using these techniques, histotripsy thrombolysis can be visualized and guided by real-time ultrasound imaging feedback.

As bubble dynamics are highly dependent on their environment, there is a possibility that the effects of histotripsy may be hindered by high blood flow velocities. The maintenance of a bubble cloud likely depends on previously initiated nuclei, and those nuclei may be swept out of the focus by background flow. We studied the feasibility of histotripsy thrombolysis at the highest natural flow velocity in-vivo (50 cm/sec). When clots were subjected to a high-velocity pulsatile flow, histotripsy was still capable of fractionating the clot. This result shows that a cavitation cloud can be initiated and maintained in the fast flow. In this situation, the thrombolysis rate was lower than those treated without flow. This could be because the clot is held in a fixed position in the flow model, and the transducer focus must scan along the clot to completely fractionate it. Since

we did not optimize the scanning velocity, some of the clot remained intact after treatment in several cases.

When histotripsy is used to treat soft tissues (e.g. kidney, myocardium, and prostate), it fractionates tissue to a sub-cellular level with debris of a few microns or smaller. Similarly, histotripsy can fractionate a blood clot into small debris. The filter measurements suggest >96% of the debris weight was smaller than 5 μm. The Coulter Counter method also showed that small particles (2-10 μm) were a majority (74-94%) of debris in the range of 2-60 μm. The fact that the number of particles counted in both control and treated samples was similar suggests that a majority of debris generated by histotripsy is outside of the Coulter Counter range (i.e. likely smaller than 2 μm). Both the filter and Coulter Counter measurements indicated that histotripsy breaks the clot into particles below the size of individual red blood cells (6-8 μm). 100-μm mechanical filters have been used to successfully prevent embolism, and only particles larger than this may be considered potentially unsafe emboli. The Coulter Counter measurement indicated occasional debris particles larger than 100 μm. Debris generated at lower pressures (6 and 8 MPa) also contained fewer large fragments than higher pressures. It is possible that the acoustic parameters could be adjusted to minimize the number of large particles. However, it is not clear that whether particles >100 μm can be avoided completely during treatment.

Vessel wall damage varied depending on the proximity of the focus to the vessel wall. Targeting of clots for 5 minutes in the vessel led to apparent focal denudation of the vessels but complete destruction of the clots. Meanwhile, specific targeting of the vessel wall caused significant damage to the intima and media of the artery in a region similar to the focal zone. Vein walls seemed more resistant to macroscopic damage, although it was still apparent in the 10-minute treatment of the wall. Damage ranging from focal endothelial denudation all the

way to obvious vessel perforation has been observed even with currently-used percutaneous mechanical thrombectomy devices[17], with several consistently showing partial or complete medial disruption [18, 19]. Minor vessel wall injury can lead to acute rethrombosis, and in the long-term intimal hyperplasia and fistulas[17]. Significant vessel damage can also lead to aneurism and significant bleeding[17]. To reduce the risk of rethrombosis, anticoagulation therapy may be required during and after histotripsy thrombolysis[17]. Because of the apparent consequences of mistargeting, future work should evaluate the long-term complications with vessel wall damage and precision.

Hemolysis may also be an adverse effect of histotripsy thrombolysis. Red blood cells are easily damaged by shear forces, and have been previously shown to be susceptible to cavitation[20, 21]. The debris measurements suggest that histotripsy breaks down red blood cells within the clot to subcellular fragments. Therefore, it is also likely that free erythrocytes in blood will also be lysed. When hemolysis occurs in a significant volume of blood, it can cause hemolytic anemia and hyperkalemia[22]. As the treatment is only localized to the small focal volume and the flow rates in occluded vessels are generally low, it is unlikely that large volumes of blood will be lysed during the treatment. Ultrasound (and cavitation in particular) has also been observed to cause platelet aggregation and activation, which facilitates clotting[23]. There is a possibility that histotripsy may similarly cause clot reformation by activating platelets. We plan to study all these possible side effects of histotripsy thrombolysis in our future *in-vitro* and *in-vivo* experiments.

5.6 References

1. Robbins SL. Pathologic basis of disease. Philadelphia: Saunders; 1974.

2. Day MJ, Mackin A, Littlewood J, British Small Animal Veterinary A. Bsava manual of canine and feline haematology and transfusion medicine. Quedgeley, Gloucester, UK: British Small Animal Veterinary Association; 2000.

3. Vennemann P, Lindken R, Westerweel J. In vivo whole-field blood velocity measurement techniques. Exp.Fluids. 2007;42:495-511

4. Winter PM, Shukla HP, Caruthers SD, Scott MJ, Fuhrhop RW, Robertson JD, Gaffney PJ, Wickline SA, Lanza GM. Molecular imaging of human thrombus with computed tomography. Academ. Radiol. 2005;12:S9-S13

5. Yu X, Song S-K, Chen J, Scott MJ, Fuhrhop RJ, Hall CS, Gaffney PJ, Wickline SA, Lanza GM. High-resolution mri characterization of human thrombus using a novel fibrin-targeted paramagnetic nanoparticle contrast agent. Magn. Reson. Med. 2000;44:867-872

6. Parsons JE, Cain CA, Fowlkes JB. Cost-effective assembly of a basic fiber-optic hydrophone for measurement of high-amplitude therapeutic ultrasound fields. J. Acoust. Soc. Am. 2006;119:1432-1440

7. Pishchalnikov YA, McAteer JA, VonDerHaar RJ, Pishchalnikova IV, Williams Jr JC, Evan AP. Detection of significant variation in acoustic output of an electromagnetic lithotriptor. J. Urol. 2006;176:2294-2298

8. Xu Z, Fowlkes JB, Rothman ED, Levin AM, Cain CA. Controlled ultrasound tissue erosion: The role of dynamic interaction between insonation and microbubble activity. J. Acoust. Soc. Am. 2005;117:424-435

9. Xu Z, Fowlkes JB, Cain CA. A new strategy to enhance cavitational tissue erosion by using a high intensity initiating sequence. IEEE Trans Ultrasonics Ferroelectr Freq Control. 2006;53:1412-1424

10. Xu Z, Raghavan M, Hall TL, Mycek M-A, Fowlkes JB, Cain CA. Evolution of bubble clouds produced in pulsed cavitational ultrasound therapy - histotripsy. IEEE Trans Ultrason Ferroelectr Freq Control. 2008;55:1122-1132

11. Parsons JE, Cain CA, Fowlkes JB. Spatial variability in acoustic backscatter as an indicator of tissue homogenate production in pulsed cavitational ultrasound therapy. IEEE Trans Ultrason Ferroelectr Freq Control.2007;54:576-590

12. Kieran K, Hall TL, Parsons JE, Wolf Jr JS, Fowlkes JB, Cain CA, Roberts WW. Refining histotripsy: Defining the parameter space for the creation of nonthermal lesions with high intensity, pulsed focused ultrasound of the in vitro kidney. J. Urol. 2007;178:672-676

13. Rosenschein U, Furman V, Kerner E, Fabian I, Bernheim J, Eshel Y. Ultrasound imaging-guided noninvasive ultrasound thrombolysis : Preclinical results. Circulation. 2000;102:238-245

14. Westermark S, Wiksell H, Elmqvist H, Hultenby K, Berglund H. Effect of externally applied focused acoustic energy on clot disruption in vitro. Clin. Sci. 1999;97:67-71

15. Parsons JE, Cain CA, Abrams GD, Fowlkes JB. Pulsed cavitational ultrasound therapy for controlled tissue homogenization. Ultrasound Med. Biol. 2006;32:115-129

16. Zierler BK. Ultrasonography and diagnosis of venous thromboembolism. Circulation. 2004;109:I-9-I-14

17. Sharafuddin MJ, Hicks ME. Current status of percutaneous mechanical thrombectomy. Part I. General principles. J Vasc Interv Radiol. 1997;8:911-921

18. Lin P, Mussa F, Hedayati N, Naoum JJ, Zhou W, Yao Q, Kougias P, El Sayed H, Chen C. Comparison of angiojet rheolytic pharmacomechanical thrombectomy versus angiojet rheolytic thrombectomy in a porcine peripheral arterial model. World J. Surg. 2007;31:715-722

19. Castaneda F, Li R, Patel J, DeBord JR, Swischuk JL. Comparison of three mechanical thrombus removal devices in thrombosed canine iliac arteries. Radiol. 2001;219:153-156

20. Danckwerts H-J, Juergens K-D. Ultrasonic investigations of hemolysis. Ultrasound Med. Biol. 1977;2:339-341

21. Poliachik SLb, Chandler WL, Mourad PD, Bailey MR, Bloch S, Cleveland RO, Kaczkowski P, Keilman G, Porter T, Crum LA. Effect of high-intensity

focused ultrasound on whole blood with and without microbubble contrast agent. Ultrasound Med. Biol. 1999;25:991-998

22. Sweet SJ, McCarthy S, Steingart R, Callahan T. Hemolytic reactions mechanically induced by kinked hemodialysis lines. Am. J. Kidney Dis. 1996;27:262-266

23. Poliachik SL, Chandler WL, Ollos RJ, Bailey MR, Crum LA. The relation between cavitation and platelet aggregation during exposure to high-intensity focused ultrasound. Ultrasound Med. Biol. 2004;30:261-269

CHAPTER 6

The Noninvasive Embolus Trap (NET)

In this chapter, an adjunct technique to histotripsy thrombolysis is explored which may minimize or prevent embolism during thrombolysis and other cardiovascular procedures. In the last chapter, most of the debris from histotripsy thrombolysis was found to be small particles unlikely to occlude substantial vessels. However, a few particles in the 100 μm – 1 mm range were generated with flow, and the variable conditions *in-vivo* may also produce larger fragments. In this chapter, it is demonstrated that the bubble cloud can simultaneously attract, trap, and erode clot particles, even against blood flow. The mechanism of this trapping is explored and the potential for bubble clouds to trap and erode emboli is investigated. This phenomenon may be useful as a method to prevent embolism in histotripsy and other cardiovascular surgeries.

6.1 Embolic Protection

Emboli are detached clots or other particles which may flow through the vasculature and occlude a vessel. Emboli consisting of blood clots or arterial plaque can result in stroke[1, 2], pulmonary embolism[3], and renal damage[4]. During

many cardiovascular interventions, such as mechanical thrombectomy, embolic protection devices (EPDs) are utilized to prevent clot fragments from causing damage to downstream organs. The most common versions of these are catheter-based deployable mesh filters or distal occlusion balloons[5]. EPDs are becoming commonly used during angioplasty and stenting of carotid arteries, as previous research has demonstrated that microemboli are generated by these procedures[6]. It has also been noted that clots can be generated during heart surgeries and similarly travel to the cerebral vasculature[7, 8]. Certain EPDs can be left in position long-term, such as an inferior vena cava filter, which prevents DVTs that can unexpectedly dislodge from reaching the lungs[9].

Researchers have recently demonstrated that the application of acoustic radiation pressure generated by an ultrasound transducer can divert solid emboli from the ascending aorta during surgery as an alternative to perioperative filters[10]. While this has been shown to successfully prevent particle migration towards the brain, the particles instead are redirected to other organs which may cause damage to them. Another novel approach to remove emboli during open chest surgery also uses acoustic radiation force to separate lipid particles from the blood in a small fluidic device[11].

Acoustic trapping of solid particles can also be accomplished using standing and traveling wave techniques for cell and particle manipulation and separation[12-16]. These methods commonly involve the use of acoustic radiation pressure to create a net force on small particles, drawing them to a fixed location. Further specificity for manipulating individual particles has been achieved by focused ultrasound. Wu[17] demonstrated a form of 'acoustic tweezers' using two opposing 3.5 MHz transducers to create a negative potential in their confocal region, trapping particles as large as frog eggs. A single-beam focused acoustic trap has been developed by Lee and Shung[18], which uses the transverse intensity

gradient generated by strong focusing to create a force up to hundreds of nN on micron-sized particles[19]. This approach is similar to more commonly employed optical tweezers[20], but generates significantly greater force.

In Chapter 5, acoustic trapping and manipulation of clots was observed. It was mentioned that the clots were spontaneously drawn to the focus when a bubble cloud was generated. We propose to apply this phenomenon to develop a non-invasive embolus trap (NET). A NET would be a cavitation cloud generated in a blood vessel downstream from a site for treatment of the blood clot or surgical site with the purpose of capturing and destroying clot fragments or other potential emboli. The NET would ideally capture large fragments and simultaneously erode them to a size which would not block major vessels downstream. In this way, the NET acts like a filter, capturing large particles while allowing blood flow through the vessel.

6.2 Capture of Clot Particles in a Vessel

We tested the use of a secondary cavitating bubble cloud as a non-invasive embolus trap. Our preliminary results show that when a clot fragment flows into the cavitating bubble cloud generated by histotripsy in a vessel tube, it can be stopped (and trapped) near the cloud and further fractionated into small debris. The same therapy transducer system and acoustic parameters as those used for studying histotripsy thrombolysis *in-vitro* were used here. Clot fragments of diameter 3 mm were cut from clots formed as described in Chapter 5, and injected into a circulatory model with a background flow of ~5 cm/s, upstream from the transducer focus. The apparatus is shown in Figure 6.1. A bubble cloud was generated in the tube center using p_- of 12 MPa. The bubble cloud was about 2 mm width, occupying approximately 1/3 of the tube diameter. The 3 mm clot

fragment drifted into the bubble cloud and became trapped near the transducer focus. While trapped in the cloud, the clot was further fractionated. Within one minute from when the clot fragment entered the bubble cloud, it was completely broken down with no visible fragments remaining.

This experiment was repeated 13 times to test the ability of histotripsy to capture clot fragments that would potentially be hazardous emboli. Of the 13 trials, all clots were stopped as they drifted into the bubble cloud. The clot fragments were further fractionated to smaller particles which were then ejected from the cloud. The largest particles ejected from the cloud were sub-millimeter. When the clot fragments were captured, 7 of the 13 clots were completely fractionated in a time of 142 +/- 99 seconds. 5 of 13 clots were partially fractionated before being swept out of the tube. They were held near the bubble cloud for a mean time of 132 +/- 66 seconds. 1 of 13 clots was held near the bubble cloud for 5 seconds, but was then swept downstream by background flow and remained unfragmented.

While this erosion rate was significantly lower than that for treating large clots with the same parameters, the captured particles were often not within the focus, but adjacent to it. Figure 6.2 shows another example of a particle trapped with the cavitation cloud illuminated next to it. The erosion rate may be lower because of the small fraction of time the clot is in contact with the cavitation cloud. Smaller particles were also observed to be ejected as far as 1 cm from the focus, only to be drawn back into it against the circulating flow. For this transducer, the focal transverse -6dB pressure beamwidth is only ~ 2 mm. These observations suggest that the trapping mechanism, studied in the following section, is related not directly to the cavitation or acoustic pressure, but rather by fluidic streaming in the vessel caused by ultrasound.

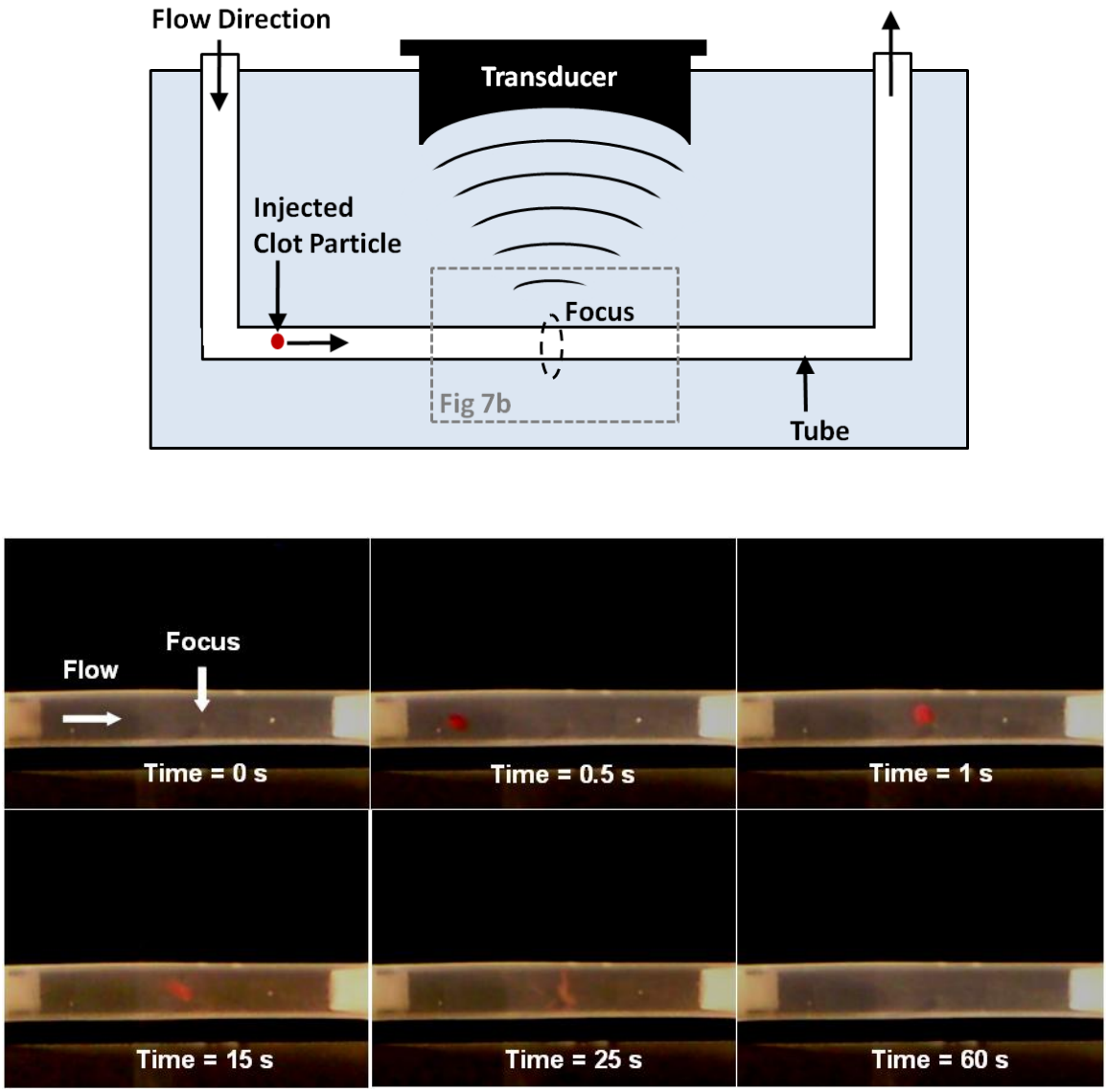

Figure 6.1. (top) Schematic of the experiment demonstrating the ability of histotripsy to trap clot fragments. A transducer is focused in a tube with flow. A clot particle is injected into the tube which is swept into the focus of the ultrasound. (bottom) A clot fragment flows from the left side of the tube into the bubble cloud at the focus of the transducer generated prior to arrival of the fragment, with p- of 12 MPa. The clot fragment remains near the cloud at the transducer focus, and is further broken down over the course of 60 seconds. The bubble cloud is transparent and not visible in the images. The mean background flow rate is ~5 cm/s from left to right.

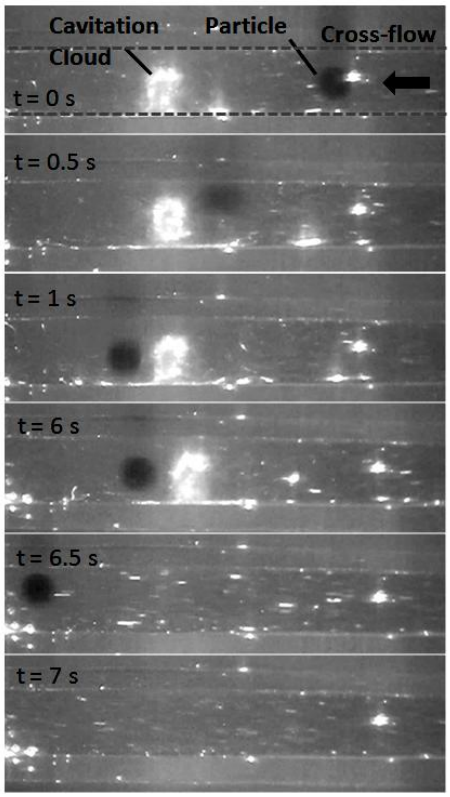

Figure 6.2. Photograph sequence showing the capture of a particle in a cavitation cloud against a crossflow in a 6-mm diameter tube. The particle enters the cloud at t = 0.5 s and is trapped downstream between t = 1 - 6 s. The ultrasound is stopped between t = 6 – 6.5 s, and the particle is released, continuing migration downstream.

6.3 Mechanism of Particle Trapping by NET

An investigation into the mechanism of the trapping may provide indications for how to improve it, such that it can be implemented in cases of high flow velocity, for example, major arteries. In this section, more realistic tissue phantoms are developed to accurately mimic the mechanical and fluidic environment in the vessel. Particle image velocimetry (PIV) is the main tool used to study the hydrodynamic interactions of cavitation with the fluid and with solid particles trapped near the focus.

6.3.1 Tissue Phantoms

A blood vessel phantom was developed to mimic the flow environment and properties of the vessel wall and soft tissue surrounding the vessel. The phantom was composed of two parts: a 1.5-mm thickness vessel wall mimic composed of 30% cross-linked gelatin and the surrounding tissue mimic composed of 10% gelatin which was not cross-linked. The protocol to create the vessel wall is similar to that of Ryan and Foster[21]. Gelatin Type A (Sigma Aldrich, St. Louis, MO, USA) was added to distilled water with concentration of 30% wt/vol. The mixture was stirred and heated on a hot plate continuously for 1 hour to ensure complete dissolution of the gelatin into the water. This mixture was poured into a 9-mm inner-diameter polycarbonate tube with 15 cm length to fill it approximately half way. A glass rod 6 mm diameter was inserted into the center of the tube to displace the gelatin. Care was taken to prevent air bubbles in the mixture, which could alter transmission of ultrasound through the phantom. This mold was placed in refrigeration for 1 hour to solidify. The solid gelatin tube was carefully extracted and placed into a 10% formalin solution for 15 minutes, then removed and rinsed. The ends of the gelatin vessel were cut to create a 13-cm length tube. A polycarbonate box (5 x 5 x 13 cm) with acoustic windows made from 25-μm thickness polyester was constructed to house the phantom. A flow inlet and outlet were attached to the box such that a steady flow could be generated through the phantom. The vessel was held in position by placing a glass rod through the inlet, center of the vessel wall, and outlet. A 10% gelatin mixture was created using the same gelatin type. This mixture was degassed in a vacuum jar at a partial vacuum of 76 kPa for 30 minutes after the solution was completely mixed. The solution was then poured to fill the polycarbonate housing, embedding the vessel phantom in the box. The entire

housing was placed in refrigeration for 2 hours at 4° C to solidify. The phantom was returned to room temperature prior to the experiment.

A circulatory flow system was constructed to simulate steady blood flow through the vessel phantom. A peristaltic pump (Masterflex, Cole-Parmer, Vernon Hills, IL, USA) was used to provide a controllable mean flow rate through the phantom. The pump was modified for control by an external voltage source (V2000, Hewlett-Packard, Palo Alto, CA, USA). The pump inlet was connected to a reservoir of fluid containing PIV tracer particles. The particles consisted of 10 μm hollow glass beads (TSI, Shoreview, MN, USA), and the fluid was a degassed 30/70 mixture of glycerol and water. This mixture was chosen to provide a fluid with a similar viscosity to blood, which has a viscosity of about 3 x 10^{-3} Pa·s under physiologic conditions[22]. The pump outlet was connected to the phantom through a pulse dampener to provide a steady flow. The opposing end of the phantom was connected back to the fluid reservoir.

A phantom was also created to mimic embolic particles in the blood stream. The particles were made from 4% wt/vol agarose gel (Type VII, Sigma-Aldrich, St. Louis, MO, USA) and were formed as spheres with diameters between 1-4 mm. The purpose of using agarose as opposed to real blood clots was that the agarose spheres were resilient to cavitation erosion, and therefore maintained their diameter throughout the entire experiment. Blood clots would be broken down quickly during exposure to the ultrasound and cavitation. Agarose beads were made by mixing 4% wt/vol agarose with a 30/70 vol/vol mixture of glycerol/deionized water. The mixture was heated above 70° C until it appeared fully transparent and then degassed for 30 minutes. A pipette was used to draw a small amount of agarose solution, which was then dropped into a test tube containing mineral oil at -4° C. Because of the hydrophilic nature of the agarose solution, the droplet formed a spherical shape which solidified quickly in the

cold oil. After a number of particles were produced, they were kept in the mineral oil at room temperature until the experiment. These particles were nearly transparent, which allowed penetration of the light sheet beyond the particle for complete PIV measurements of the surrounding fluid flow. The resulting particles were nearly neutrally buoyant (ρ_P = 1.08 g/cm^3).

6.3.2 Ultrasound System

A spherically-focused, 10-cm diameter, 10-cm focal length lead-zirconate-titanate (PZT) transducer was used to generate a cavitation cloud within the vessel phantom during the experiments. The transducer was positioned in a tank of degassed water along with the vessel phantom housing. The tank dimensions were 60 x 30 x 36 cm. A 3-axis manual positioning stage was used to control the position of the transducer. The focus of the transducer was aligned such that the acoustic axis was perpendicular to the vessel long axis and centered along the cross-section of the phantom. The transducer was electrically driven with a multi-cycle sinusoidal pulse using a class-D amplifier developed in our lab, which was controlled by a field-programmable gate array (FPGA) logic board (DE1, Altera, San Jose, CA, USA). The transducer was driven with a center frequency of 1.162 MHz to apply acoustic pulses with pulse durations (PDs) of 5-20 cycles at pulse repetition frequencies (PRFs) between 200 Hz – 2 kHz. Pressure waveforms of acoustic pulses at the transducer focus were measured using a calibrated fiber-optic hydrophone developed in-house. In all experiments except those for varying acoustic pressure, the peak negative pressure of the each pulse was 12 MPa and the peak positive pressure was 53 MPa (Figure 6.3). The focal region is ellipsoidal, with the -6dB peak negative pressure beamwidth of the focal region 1.8 mm transverse to the beam axis, and 13 mm along the beam axis.

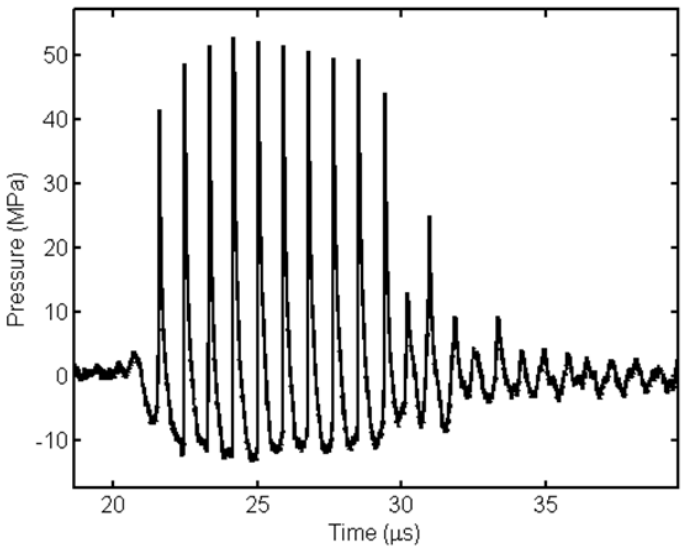

Figure 6.3. Focal pressure waveform of an ultrasound pulse with p_-= 12 MPa, the amplitude used for most of this study.

6.3.3 PIV System

A high speed camera (Phantom V210, Vision Research, Wayne, NJ, USA) was used to capture PIV images for flow analysis. The camera has a maximum resolution of 1280 x 800, and can capture 2200 frames per second at this resolution, up to approximately 5000 frames. A 532nm Nd:YAG continuous wave laser was used for illumination (JenLas D2.17, Jenoptik AG, Jena, Germany). The laser beam was passed through a series of cylindrical lens to create a light sheet with controllable thickness and width at the region of interest within the vessel phantom. The light sheet thickness in this study was about 500 μm, positioned in the center plane of the vessel phantom. The laser was triggered by a separate function generator to control the pulse length of the light, which was in turn triggered by the FPGA board. This setup allowed time-resolved imaging of the fluid flow within the vessel phantom, which could be used to determine whether or not the flow pattern was steady. The PIV system is shown

in Figure 6.4**.** The images collected were analyzed using an open-source PIV analysis software (PIVLAB, W.Thielicke and E. Stamhuis, Univ. Applied Sciences, Bremen, Germany) in MATLAB (The Mathworks, Natick, MA).

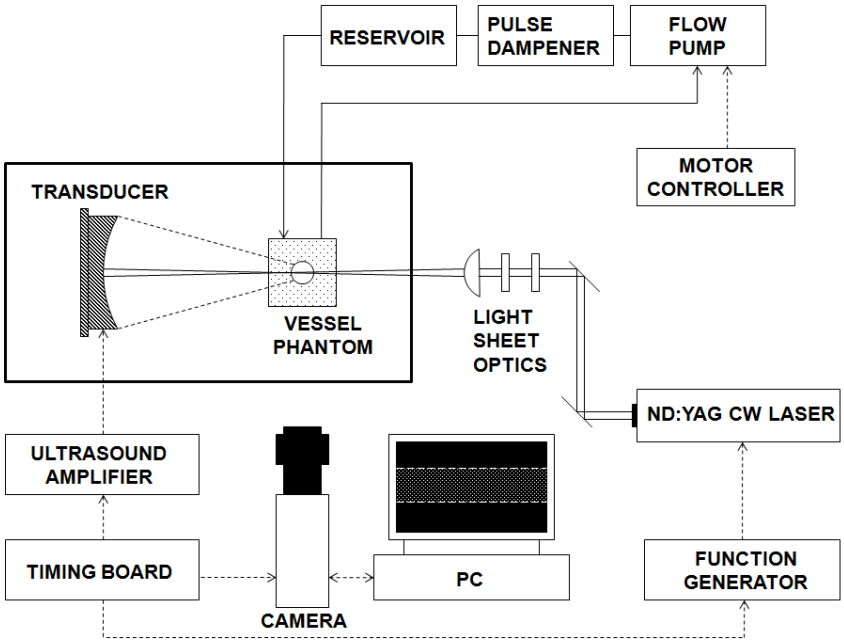

Figure 6.4. A schematic of the experimental setup used for PIV of the vessel phantom during application of ultrasound. A circulatory flow is generated by a pump to continuously cycle a glycerol/water solution containing PIV particles through the phantom. The ultrasound transducer is focused into the vessel phantom transverse to the circulatory flow, driven by a class D amplifier. A high-speed camera is used to capture a sequence of images in the vessel phantom during ultrasound application. Lighting is provided by a light sheet produced by a Nd:YAG 532 nm laser.

6.3.4 Acoustic Streaming During Histotripsy

A cloud of cavitation was generated during ultrasound application at the transducer focus, contained within the fluid of the vessel phantom. This cavitation cloud was visible only on select frames of the PIV images, because the camera frame rate was faster than the ultrasound pulse rate. Cavitation clouds in

histotripsy are formed and expand during the ultrasound pulse and collapse in 100 - 200 μs[23, 24]. With this in mind, the results presented here ignore the fast-time oscillatory motion of the fluid caused by the cavitation and instead focus on the slow-time steady flow pattern created by acoustic streaming[25, 26].

In the vessel phantom, the fluid accelerates through the ultrasound focus in the direction of acoustic propagation. PIV measurements show that vortices are created laterally to either side of the focus due in the presence of the cylindrical boundary (Figure 6.5). These arise because of the necessity of a fluid return path near the top of the vessel to satisfy continuity of the fluid volume. The velocity is highest in the focus and along the distal vessel wall, which receives the impinging focal flow. The flow pattern and velocity are steady, particularly at lower flow velocities. However, there is some variance in flow velocity at the focus when cavitation is present between measurements.

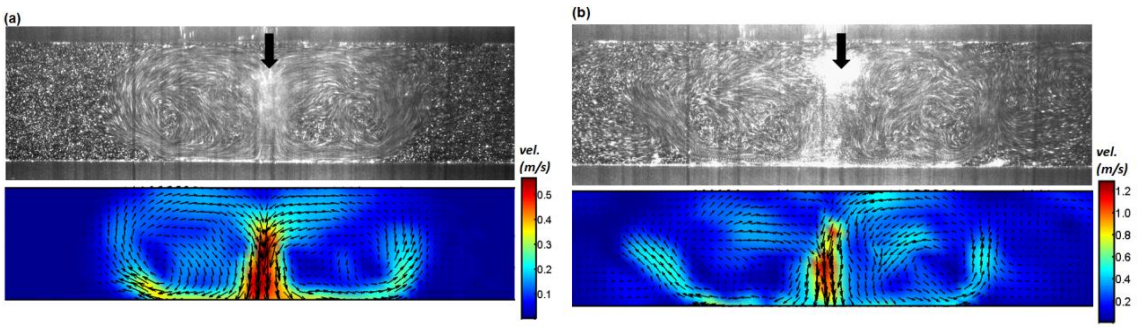

Figure 6.5. (a) Time-averaged photograph (top) and PIV velocity map (bottom) of fluid flow pattern created by cavitation-induced streaming in the vessel phantom. The vessel phantom is 6 mm diameter. The black arrow in the top frame shows the direction of acoustic propagation and position of the beam axis. The vectors in the PIV frame indicate the direction and magnitude of flow, and the color map in the PIV frame shows fluid velocity magnitude normalized to the peak value. The ultrasound PRF was 400 Hz and PD was 10 cycles during this exposure. The flow pattern shows the highest velocity is generated at the focus towards the distal wall of the tube, with vortices forming on either side. (b) The same as (a) but ultrasound PRF was 1000 Hz and PD was 20 cycles during exposure.

The magnitude of the focal streaming velocity, u_f, shows a marked threshold dependence on acoustic pressure. Figure 6.6 provides measured peak flow velocities through the focus vs. acoustic focal pressure at a PRF of 1 kHz and PD of 10 cycles. A distinct pressure threshold is observed between peak negative pressure p_- = 7.6 and 7.9 MPa, and u_f increases by more than an order of magnitude between these values. At $p_- \geq 7.9$ MPa, cavitation is also observed on PIV images. At the threshold, cavitation formed in the liquid only near the distal boundary in the vessel. As the pressure is increased, the cavitation cloud grows towards the center of the tube. These data suggest that cavitation is responsible for the high streaming velocities observed at relatively low time-average acoustic focal intensity. The maximum focal flow velocity increases almost linearly with pressure above the cavitation threshold (least-squares linear regression, $u_f = 0.18p_- - 1.4$ m/s, $R^2 = 0.97$).

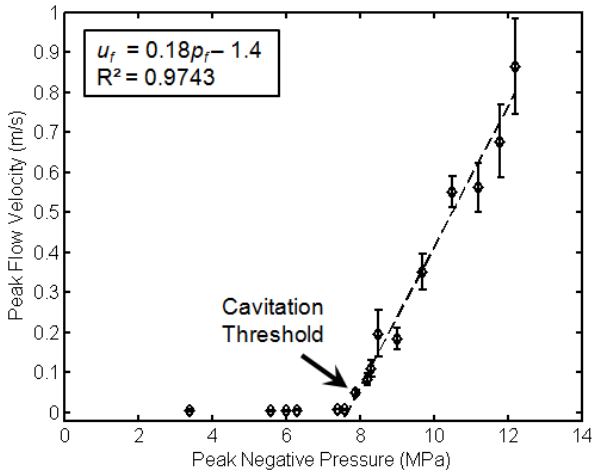

Figure 6.6. Peak streaming flow velocity at the focus within the vessel phantom vs. pulse focal pressure. A threshold for high flow velocities appears between p_- = 7.6 MPa and p_- = 7.9 MPa. The black arrow indicates the lowest pressure at which cavitation was visualized during PIV. Above the threshold, the flow velocity is approximately linear with peak negative pressure. The dashed black line is a least-squares linear fit to the data between p_- = 7.9 to 12.2. Each data point shows the mean value from 10 measurements and the error bars are one standard deviation.

The flow velocity was also measured vs. focal position relative to the vessel walls. The position of the focus was shifted along the direction of acoustic propagation over a range of +/- 6.6 mm from the center of the vessel. This range corresponds with the -6dB pressure beamwidth of the focal region for p_-. Figure 6.7 shows the peak focal flow velocity vs. focal position using PRF = 1000 Hz, PD = 10 cycles, and p_- = 12 MPa. When the focal center is positioned in the fluid (position between -3 to 3 mm), the flow velocity is highest, ranging from 0.62 to 1.02 m/s.

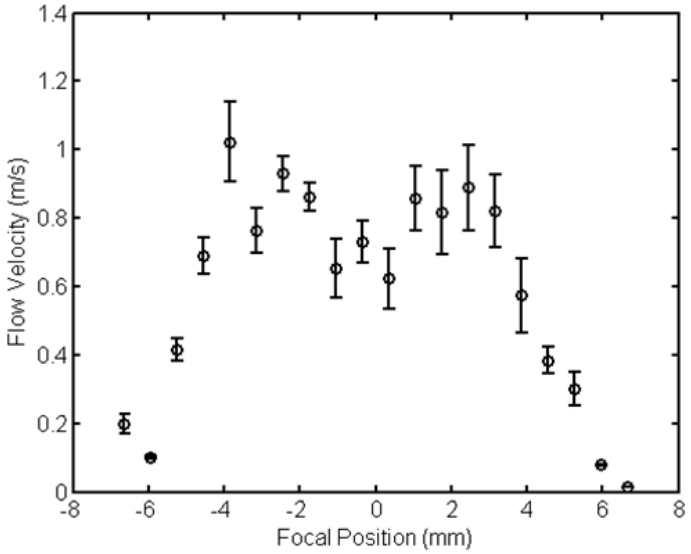

Figure 6.7. Peak focal flow velocity vs. position of the focus relative to the vessel center. The positive direction is away from the transducer. Error bars indicate the standard deviation in n = 10 measurements.

The fluid flow velocities were found to increase as either the PRF or PD was increased while maintaining the same peak negative pressure. For instance, the fluid velocity with 10 cycle pulses applied at 200 Hz PRF results in u_f = 28 cm/s, while the same pulse length applied at a rate of 1000 Hz results in u_f = 95 cm/s (see Figure 6.8). However, a saturation of u_f was observed for PRF = 2000 Hz, where the flow velocities were similar to those at PRF = 1000 Hz. Higher focal

flow in turn increased the flow velocity in the vortices. The flow velocity of the vortex, u_v, was measured as the maximum velocity in the region diametrically opposed to the focus around the vortex. The ratio u_v / u_f varied between 0.2 to 0.3 over the range of parameters tested, but no trend was observed vs. PRF or PD. The flow in the outer vortices showed lower variance in velocity than the focal measurements. The wider variance in measurements at the focus is probably caused by unpredictable positions and transient activity of cavitation bubbles within the focus during each pulse. As the position of the cavitation bubbles change each pulse, the flow in this region is somewhat unsteady. The vortices' dimensions remain relatively constant in the absence of cross-flow across the range of parameters tested in this study. At higher focal velocities (> 50 cm/s), the vortices are less uniform, and counter-vortices are generated further down the length of the tube **(**Figure 6.5**)**.

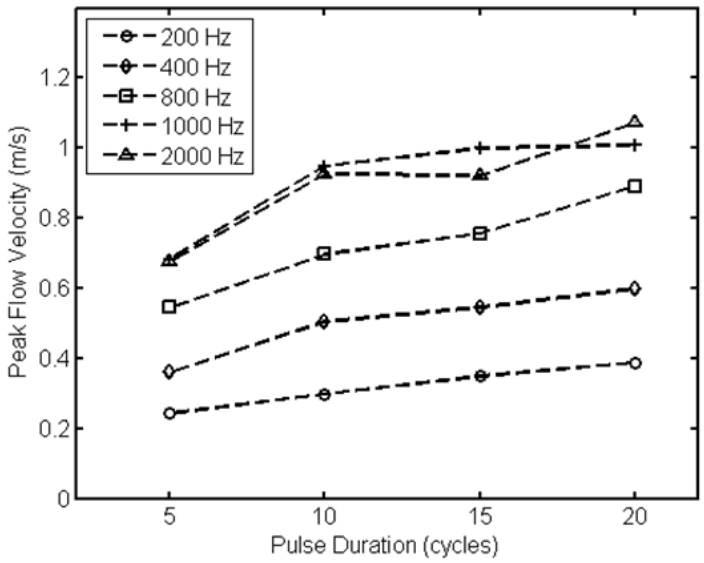

Figure 6.8. Focal flow velocities vs. PD for 5 different sets of PRF between 200 – 2000 Hz. Increasing either PD or PRF results in an increase in flow velocity at the focus, although some limitation of the peak flow velocity is seen between PRF = 1000 and PRF = 2000. Each point represents the mean value of n = 30 measurements.

The flow pattern within the vessel is modified under a steady crossflow. Flow patterns were measured under mean crossflow velocities between u_c = 0 - 14 cm/s. In the cylindrical vessel phantom, this corresponds with peak crossflow velocities up to 28 cm/s. The Reynolds numbers for these flow rates in the 6 mm diameter vessel varies from Re = 0 – 280. A subset of the parameters measured in stationary conditions in the previous section was measured with crossflow. As the cross-flow velocity was increased, the vortices became strained, with the downstream vortex elongating, and the upstream vortex compressing in the direction of flow (Figure 6.9). At higher flow rates, the downstream vortex would vanish entirely, leaving an area of quiescence in the upper region of the tube, while a smaller, high velocity jet formed along the lower surface of the tube in the direction of the crossflow. In this way, the crossflow was diverted to a small, high velocity stream during passage through the ultrasound focus. The upstream vortex core grew smaller in diameter as the flow rate was increased. Finally, at the highest crossflow velocities, the narrow jet in the downstream region expanded to occupy the diameter of the tube (similar to flow observed in the absence of ultrasound) and the upstream vortex vanished altogether.

The flow patterns followed the same transitions with increasing crossflow under all sets of acoustic parameters. However, the flow velocities at which the transitions were observed were higher for parameters which produced higher focal flow velocities. Figure 6.10 displays the measured upstream vortex lateral diameter (diameter along the vessel long axis) for 4 sets of acoustic parameters tested vs. crossflow velocity. Vortex center and diameter are identified and measured using the method of cross-sectional lines[27]. It is apparent that the reduction of this vortex is delayed to higher crossflow as the overall acoustic power is increased by increasing PD or PRF.

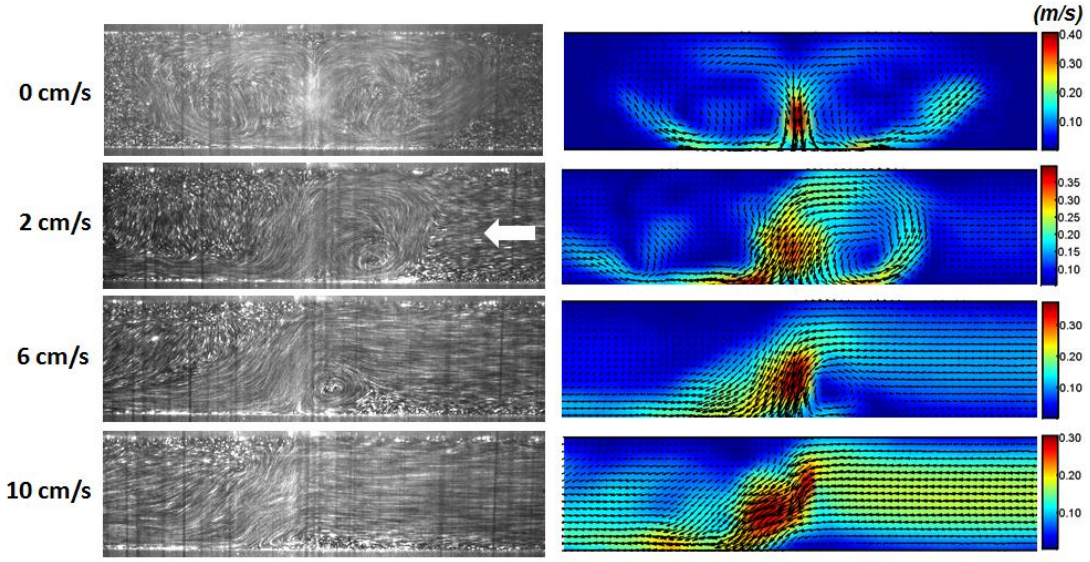

Figure 6.9. Time-averaged photographs (left) and velocity fields (right) around the focus under increasing crossflow velocity. The mean crossflow velocity is shown on the left. For this experiment, PD = 5 cycles and PRF = 400 Hz. The white arrow in the left frame at u_c = 2 cm/s shows the direction of crossflow. The colorbar on the right gives the velocity magnitude scale in m/s.

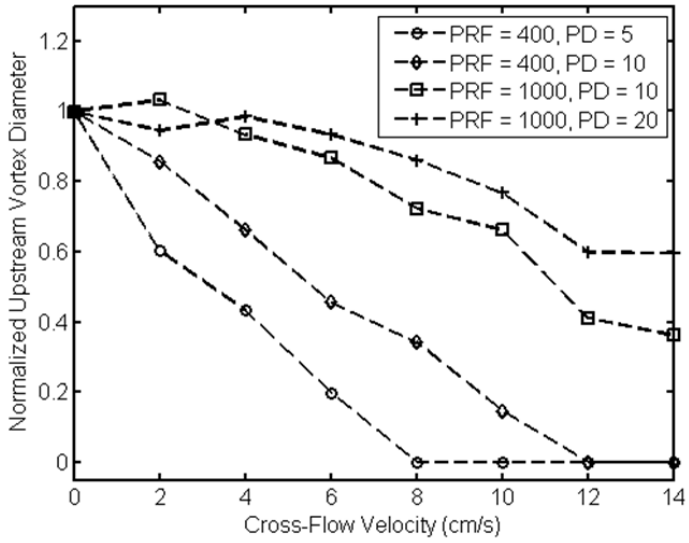

Figure 6.10. Lateral diameter of upstream vortex core vs. crossflow velocity for 4 sets of acoustic parameters. Vortex diameter is normalized to the measurement with no crossflow. The vortex diameter is reduced at higher crossflow velocities for higher-power parameter sets.

6.3.5 Particle Trapping

Solid spherical particles of agarose were injected into the vessel phantom to observe their trajectory relative to the fluid flow patterns observed under sonication. Particle diameters varied from 1 mm to 4 mm. Particles < 1 mm could not be used imaged because their trajectory was occasionally out of the plane of the laser sheet. A program was written in MATLAB to calculate the position of the particle centroid with each image frame. Since the particles used in this study were much larger than the PIV tracers, the particle could be isolated in each frame by low-pass filtration of the image. The image was then converted to binary and the centroid of the sphere was calculated. In the absence of crossflow, particles were drawn into either vortex, from as far as 1 cm outside the vortex core. Larger particles (3.5-4 mm) obtained an equilibrium position with their centroid near the center of the vortex core. Smaller particles (1.5-2 mm) did not obtain a steady equilibrium position, but migrated in circular fashion along the streamlines of the vortex, up to the outer limits of the vortex diameter. Thus, while their position was not stable, they remained within the confines of the vortex. Figure 6.11 shows the trajectory of a 3.5 mm particle over a period of 1.5 seconds.

Under crossflow, particles could be trapped either upstream or downstream from the focus. In the case where the particles are trapped upstream, they remain centralized in the vortex, similar to the conditions in the absence of crossflow (Figure 6.12a). In this position, the particle experiences no net translational drag force (although the particle may rotate about the vortex center). Particles trapped downstream from the focus remained near the focus in the center of the tube, in the region where the flow velocity is low (Figure 6.12b). At lower crossflow velocities, the downstream vortex is strained but not entirely absent, and some

return flow is present in the tube. However, at higher crossflow near the particle escape velocity, the particle was trapped in a position such that flow over the particle surface was entirely directed downstream. This observation suggests that the drag force from the fluid flow on the particle is not the sole force determining the trajectory of the particle.

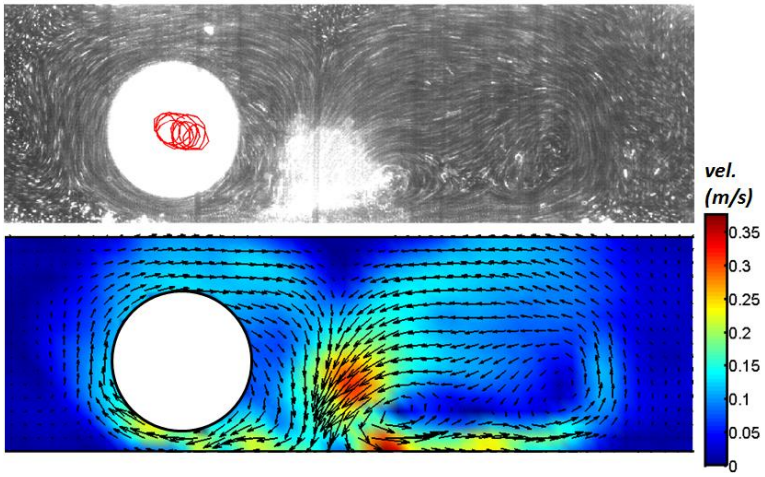

Figure 6.11. Time-averaged image of a particle trapped in the fluid vortex next to the acoustic focus. The red trace in the upper frame shows the trajectory of the particle centroid over 1.5 seconds. The trajectory consists of small circular motions about the center of the vortex.

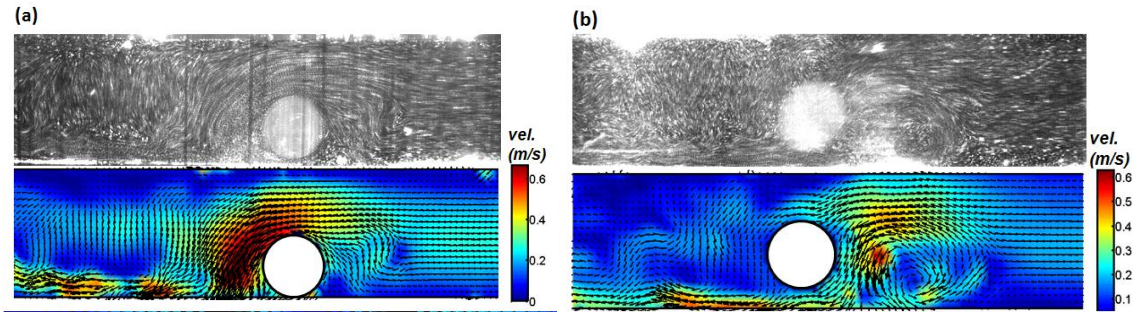

Figure 6.12. (a) Photograph and flow velocity map of a particle trapped upstream from the focus. Mean crossflow velocity is 6 cm/s and the particle diameter is 3 mm. (b) Photograph and flow velocity map of a particle trapped downstream from the focus. The mean crossflow velocity is 10 cm/s and the particle diameter is 3 mm. In both (a) and (b), the applied PRF = 1000 Hz and PD = 10 cycles.

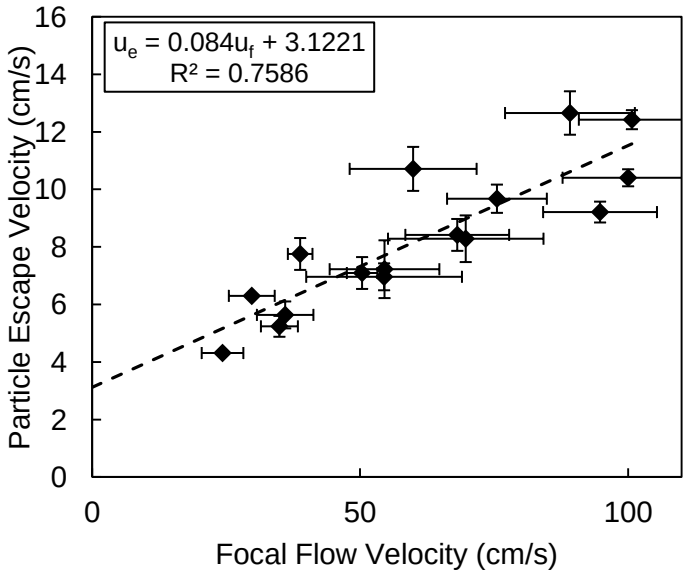

Figure 6.13. Escape velocity of 3-4 mm particles vs. focal flow velocities measured at different acoustic parameter sets. As either PRF or PD is increased, the particles can be trapped against a higher crossflow velocity. The black dashed line shows a linear least-squares fit to the data. The horizontal error bars are standard deviation in measurement for focal velocities while vertical error bars are standard deviation in particle escape velocity.

6.3.6 Pressure Gradient Forces on an Embolus

The particle motion is dictated by fluid-particle momentum transfer by different forces. These forces include drag, fluid pressure gradient, Basset history force, added mass, and lift force due to particle rotation[28]. The influence of the body force (gravity) in this situation is minimized due to the near-neutral buoyancy of the particles in this study. For very small particles with insignificant inertial effects, drag is the primary deterministic force on the particle's motion. This knowledge is exploited in PIV, where it is assumed that the tracer particles will move along the fluid steamlines at the velocity of the fluid[29, 30]. However, for

larger particles of low density, the fluid pressure gradient becomes significant and can be dominant in determining the particle trajectory[28, 31]. The pressure gradient in a steady flow due to the fluid acceleration may be estimated from PIV measurements. In this case, the pressure Poisson equation is used, obtained by applying the divergence operator on the Navier-Stokes equation. The continuity equation for incompressible, steady flow, is then applied to eliminate the viscous terms, leading to:

$$\nabla^2 p = -\rho \nabla \cdot (u \cdot \nabla u) \tag{6.1}$$

where u is the flow velocity vector, p is pressure, and ρ is the fluid density. Since PIV only obtains the in-plane components of flow, it is assumed the out-of-plane component can be neglected. Under this assumption, Eq. 6.1 is reduced to a two-dimensional version:

$$\frac{\partial^2 p}{\partial x^2} + \frac{\partial^2 p}{\partial y^2} = -\rho \frac{\partial}{\partial x}\left(u \frac{\partial u}{\partial x} + v \frac{\partial u}{\partial y} \right) - \rho \frac{\partial}{\partial y}\left(u \frac{\partial v}{\partial x} + v \frac{\partial v}{\partial y} \right) \tag{6.2}$$

Eq. 6.2 is an elliptic-type partial differential equation and can be solved by an iterative relaxation method. First, the derivatives are discretized by central difference on the interior points and forward difference on the edges. Eq. 6.2 is then solved by a successive over-relaxation (SOR) method to find the pressure field[32]. Since Eq. 6.2 only provides the second derivative of pressure, the boundary conditions on each edge of the PIV field must be stipulated prior to calculation. A Dirichlet boundary condition $p = 0$ was applied to the inlet and outlet edges of the PIV frame. A Neumann boundary condition was applied to the vessel wall boundaries of the frame. This boundary condition was determined from the Navier-Stokes equation for steady,incompressible flow:

$$\frac{\partial p}{\partial n} = \frac{\partial p}{\partial y} = -\rho\left(u\frac{\partial v}{\partial x} + v\frac{\partial v}{\partial y}\right) + \mu\left(\frac{\partial^2 v}{\partial x^2} + \frac{\partial^2 v}{\partial y^2}\right) \qquad 6.3$$

Note that only the y-component of flow gradient is used, since it is normal to the boundary. The derivatives for Eq. 6.3 are discretized by forward difference method, and the pressure gradient is calculated for the boundary.

The coefficient of pressure, C_p, given as[33]

$$C_p = \frac{p_0 - p}{1/2\,\rho u_0^{\,2}}, \qquad 6.4$$

is used as an indicator of pressure, where the inlet and outlet pressure pressure $p_0 = 0$ and u_0 is the measured peak crossflow velocity. C_p provides a measure of the relative forces due to drag from the crossflow to the force generated by the pressure gradient. At $u_c = 0$, the velocity is set at $u_0 = 0.1$ cm/s for reference. Figure 6.14 shows the pressure maps associated with the different crossflow conditions displayed in Figure 6.9**.** Most notably, region of low pressure exists near the focus within the lower half of the tube. As the crossflow velocity is increased, this region of low pressure remains, but the value C_p, which is relative to the crossflow velocity, is reduced. Figure 6.14 shows that with a crossflow velocity u_c = 2 cm/s, a minimum C_p = -28.9 is observed. At u_c = 10 cm/s, the minimum C_p = -0.8. As shown in Figure 6.14, the pressure gradient exists downstream even in the absence of the vortex. Thus, a particle could be trapped within this region of low drag and substantial pressure gradient directed towards the focus, which coincides with our observations of the particle location during trapping. Figure 6.15 shows C_p for 4 different sets of parameters vs. crossflow velocity. The corresponding values of C_p at the particle escape velocity were found by interpolation on Figure 6.15. The mean value was $C_{p,escape}$ = 4.5 +/- 0.7 for particles of 3-4 mm diameter. Given the consistency of this parameter with

respect to escape velocity, the minimum value of C_p appears to be a good indicator of trapping ability for a given parameter set measured in the absence of particles.

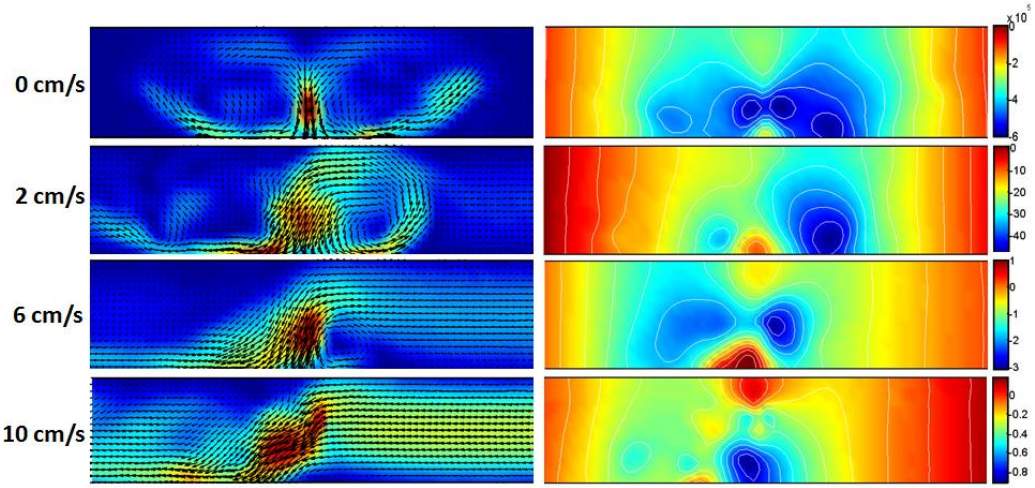

Figure 6.14. Velocity (left) and coefficient of pressure (right) maps of the corresponding fluid flow patterns displayed in Fig. 8. The color bar on the right indicates the pressure coefficient, C_p, for the pressure map. Pressure maps show a negative pressure gradient towards the focus. As crossflow velocity is increased, the pressure gradient is maintained, but the value of the pressure coefficient is reduced.

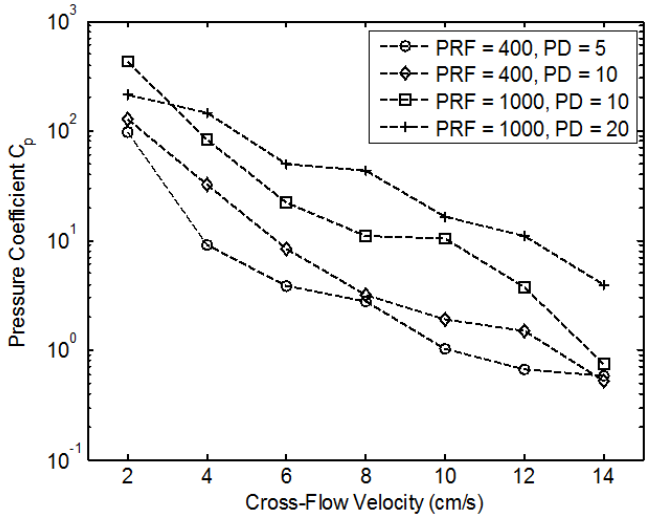

Figure 6.15. Pressure coefficient C_p vs. crossflow velocity for four sets of data using different PD and PRF. In general, pressure coefficient decreases with increasing crossflow velocity. 3 - 4 mm particles were found to escape near C_p = 4.5.

6.4 Discussion

A method to reduce the risk of embolism was proposed, using a bubble cloud to capture and fractionate the emboli. In the preliminary test, we demonstrated that the bubble cloud can trap a large clot particle, even in a flow field, near the focus and further fragment it. The acoustic trapping property of histotripsy, we plan may be developed into a **Non-invasive Embolus Trap (NET)**, which is a secondary cavitating bubble cloud set downstream of the primary treatment cloud to capture and further fractionate any escaping clot fragments. The NET could be created by a separate transducer and effectively act as a filter for large emboli. Our preliminary test indicated that clot fragments can be trapped and further broken down into smaller fragments. The NET, if successful, would add an additionally degree of safety to histotripsy thrombolysis. Such particle attraction and trapping is inherent to the primary therapy bubble cloud as well, depending on the acoustic parameters. This technique may also be an effective means to prevent embolism in other vascular surgeries.

In this chapter, fluid flow patterns generated by a cavitation cloud at the focus of an ultrasound transducer were measured experimentally to understand how solid particles such as emboli may be trapped during ultrasound exposure. The results indicate that focused ultrasound produces high-velocity streaming of the liquid through the focus in the presence of cavitation. Without cavitation, such flow velocities were not observed. This acoustic trapping ability appears to be caused by cavitation-induced fluid flow. Microstreaming can generate a flow pattern pulling particles towards a single bubble even in the presence of an overall directional flow. This phenomenon is also applicable (and may be magnified) when bubbles act collectively as a cloud. The peak velocity in the experiments was as high as 1.2 m/s. The behavior of cavitating bubble clouds

using short, finite-amplitude, focused ultrasound pulses has been studied in the context of histotripsy for ultrasound tissue erosion[24, 34]. While the acoustic pulse drives the formation and growth of the cavitation bubbles, the bubbles simultaneously act to scatter a significant portion of the wave. This imparts a radiation force on the bubbles, causing their translation through the focus and streaming of the liquid surrounding the bubbles. While acoustic streaming with focused transducers has been investigated previously for purposes such as diagnostic ultrasound imaging, the flow velocities are usually only a few cm/s[35]. In higher power applications, such as acoustic hemostasis[36], focal flow velocities could reach similar values to those observed here in large vessels. However, it may require far greater acoustic power to achieve the same flow, since the streaming would rely on attenuation of ultrasound in the blood rather than cavitation.

The flow velocity through the focus was found to correspond nearly linearly with the peak negative pressure of the pulse. For acoustic streaming at low *Re* and small pressure gradients, the streaming velocity increases with the square of the acoustic pressure amplitude p_a, or linearly with the acoustic power P[37, 38]. However, the introduction of hydrodynamic nonlinearity associated with the advection term in the Navier-Stokes equation at higher *Re* is predicted to shift the relation of streaming velocity and driving pressure to first order[37]. For PRF and pulse duration, the flow velocities increase at lower order. This is because a doubling of PRF or pulse duration doubles the time-averaged acoustic intensity, while a doubling of pressure would correspond to a four-fold increase. Thus, it is expected that a change in acoustic intensity I_a should change the focal streaming velocity $u_f \propto \sqrt{I_a}$. This appears to be the case for PRF but the pulse duration was less effective in increasing the flow velocity for equivalent power. This is possibly a result of the bubble dynamics in response to varying the pulse length.

Previous observation of cavitation bubble behavior by high-speed imaging revealed that bubbles oscillate primarily at the beginning of a pulse but will oscillate minimally after several acoustic cycles, remaining expanded well above resonant radius until the end of the pulse[39, 40]. In theoretical treatments of radiation force on cavitating bubbles, it has been shown that maximum force on the bubble occurs around resonance[41]. Thus, the majority of momentum transferred to the liquid may occur during bubble collapse, only during the initial cycles of the pulse. If this is the case, it would be most beneficial to use very short pulses at a higher rate to maximize streaming.

In the absence of crossflow, the streaming generated fluid vortices to either side of the focus. However, it should be noted that the true 3-dimensional flow around the focus is a vortex ring with the focus at the center. One limitation of this study was that only the central plane of the vessel was imaged, based on the assumption that the out-of-plane flow was minimal. This plane was chosen because particles motion is observed to be mainly confined to these dimensions. Particles are occasionally observed to switch for the upstream to downstream vortex or vice-versa. Knowledge of the 3-dimensional field could provide additional understanding of the particulate motion, as well as provide more accurate pressure calculations in the flow.

The streaming pattern is altered with the introduction of a cross-flow, breaking the symmetry of the vortex ring structure. In the region upstream from the focus, the vortex flow persisted but the diameter grew smaller with increasing crossflow. Particles which are trapped at the center of the vortex experience no net translational drag force (although rotational drag may be present), and the fluid pressure reaches a local minimum near the vortex center. However, the likelihood of a particle becoming trapped in the position has some dependence on the size of the vortex. As the vortex diameter becomes smaller, it

becomes increasingly probable that the particle will follow the open streamlines near the top of the vessel and the drag force will cause it to flow past through the focus and downstream. The fact that the upstream vortex remains larger at higher crossflow velocities for higher PRF or PD explains the increased ability to trap in this position.

Despite the stability of the particle position in the upstream vortex, it is just as common to observe the particle trapped downstream from the focus, particularly at higher crossflow velocities. In the region downstream from the focus, the vortex is absent, yet the particle remains trapped near the focus. This is evidence that an additional force - a pressure gradient - also exists in the direction of the focus laterally, against the cross-flow direction. As the crossflow is increased further, the drag force on the particle which opposing the pressure gradient is increased, allowing the particle to escape.

Above certain dose limits, platelet activation[42], significant hemolysis[43, 44], or vascular trauma[45] are observed in ultrasound under certain conditions. This study did not explore the potential side effects of the NET, and further examination of the clinical applicability is necessary to determine if the benefits of such a device would outweigh the risks. In particular, cavitation bubbles are known to cause hemolysis through various mechanisms[46]. Since the blood volume exposed to the focus is much greater with a normal vessel compared with an occluded vessel as in thrombolysis, hemolysis in particular could be problematic. These effects may present a tradeoff between the maximum trapping abilities of the NET and tolerable side-effects.

Currently, the highest mean crossflow velocity at which we have observed particles trapped is 25 cm/s using a transducer with a larger aperture and a higher curvature than that used in this study. Mean blood flow velocities in large arteries such as the carotid can reach more than 50 cm/s, peak systolic flow

velocity can reach higher than 1 m/s[47, 48]. If the NET was implemented during histotripsy thrombolysis, however, blood flow through the afflicted vessel would be reduced, improving the likelihood of trapping free clot thrombus fragments. Based on this study, there are several strategies which could improve this trapping effect for these higher velocities. We observed that higher focal streaming velocities correlate with trapping at higher crossflow velocities. Increasing the acoustic PRF while maintaining a low PD appears the most efficient method for generating streaming. Alternately, the focus could be extended against the direction of crossflow. As the crossflow is increased, each fluid particle would remain in the focal region for a longer time, thus experiencing a larger change in momentum. By increasing the width of the focus, a fluid particle could also remain in the focus for a longer period.

6.5 References

1. Donnan GA, Fisher M, Macleod M, Davis SM. Stroke. Lancet. 2008;371:1612-1623

2. Reimers B, Corvaja N, Moshiri S, Sacca S, Albiero R, Di Mario C, Pascotto P, Colombo A. Cerebral protection with filter devices during carotid artery stenting. Circulation. 2001;104:12-15

3. Monreal M, Ruiz J, Olazabal A, Arias A, Roca J. Deep venous thrombosis and the risk of pulmonary embolism. A systematic study. Chest. 1992;102:677-681

4. Scolari F, Tardanico R, Zani R, Pola A, Viola BF, Movilli E, Maiorca R. Cholesterol crystal embolism: A recognizable cause of renal disease. Am. J. Kidney Dis. 2000;36:1089-1109

5. Zahn R, Ischinger T, Mark B, Gass S, Zeymer U, Schmalz W, Haerten K, Hauptmann KE, von Leitner E-Rd, Kasper W, Tebbe U, Senges J. Embolic

protection devices for carotid artery stenting: Is there a difference between filter and distal occlusive devices? J. Am. Coll. Cardiol. 2005;45:1769-1774

6. Markus HS, Clifton A, Buckenham T, Brown MM. Carotid angioplasty. Detection of embolic signals during and after the procedure. Stroke. 1994;25:2403-2406

7. Sotaniemi KA. Brain damage and neurological outcome after open-heart surgery. J. Neurol. Neurosurg. Psychiatry. 1980;43:127-135

8. Barbut D, Hinton RB, Szatrowski TP, Hartman GS, Bruefach M, Williams-Russo P, Charlson ME, Gold JP. Cerebral emboli detected during bypass surgery are associated with clamp removal. Stroke. 1994;25:2398-2402

9. Streiff MB. Vena caval filters: A comprehensive review. Blood. 2000;95:3669-3677

10. Sauren LDC, la Meir M, Palmen M, Severdija E, van der Veen FH, Mess WH, Maessen JG. New ultrasonic radiation reduces cerebral emboli during extracorporeal circulation. Euro. J. Cardio-Thoracic Surg. 2007;32:274-280

11. Jönsson H, Holm C, Nilsson A, Petersson F, Johnsson P, Laurell T. Particle separation using ultrasound can radically reduce embolic load to brain after cardiac surgery. Ann. Thoracic Surg. 2004;78:1572-1577

12. Coakley WT, Bardsley DW, Grundy MA, Zamani F, Clarke DJ. Cell manipulation in ultrasonic standing wave fields. J. Chem. Technol. Biotechnol. 1989;44:43-62

13. Oberti S, Möller D, Neild A, Dual J, Beyeler F, Nelson BJ, Gutmann S. Strategies for single particle manipulation using acoustic and flow fields. Ultrasonics. 2010;50:247-257

14. Nilsson A, Petersson F, Jonsson H, Laurell T. Acoustic control of suspended particles in micro fluidic chips. Lab chip. 2004;4:131-135

15. Evander M, Johansson L, Lilliehorn T, Piskur J, Lindvall M, Johansson S, Almqvist M, Laurell T, Nilsson J. Noninvasive acoustic cell trapping in a microfluidic perfusion system for online bioassays. Anal. Chem. 2007;79:2984-2991

16. Yamakoshi Y, Noguchi Y. Micro particle trapping by opposite phases ultrasonic travelling waves. Ultrasonics. 1998;36:873-878

17. Wu J. Acoustical tweezers. J. Acoust. Soc. Am. 1991;89:2140-2143

18. Lee J, Shung KK. Radiation forces exerted on arbitrarily located sphere by acoustic tweezer. J. Acoust. Soc. Am. 2006;120:1084-1094

19. Lee J, Teh S-Y, Lee A, Kim HH, Lee C, Shung KK. Single beam acoustic trapping. Appl. Phys. Lett. 2009;95:073701-073703

20. Ashkin A, Dziedzic JM, Bjorkholm JE, Chu S. Observation of a single-beam gradient force optical trap for dielectric particles. Opt. Lett. 1986;11:288-290

21. Ryan LK, Foster FS. Tissue equivalent vessel phantoms for intravascular ultrasound. Ultrasound Med. Biol. 1997;23:261-273

22. Wells RE, Merrill EW. Influence of flow properties of blood upon viscosity-hematocrit relationships. J. Clin. Invest. 1962;41:1591-1598

23. Xu Z, Hall TL, Fowlkes JB, Cain CA. Optical and acoustic monitoring of bubble cloud dynamics at a tissue-fluid interface in ultrasound tissue erosion. J. Acoust. Soc. Am. 2007;121:2421-2430

24. Xu Z, Raghavan M, Hall TL, Mycek M-A, Fowlkes JB, Cain CA. Evolution of bubble clouds produced in pulsed cavitational ultrasound therapy - histotripsy. IEEE Trans Ultrason Ferroelectr Freq Control. 2008;55:1122-1132

25. Lighthill SJ. Acoustic streaming. J. Sound Vibrat. 1978;61:391-418

26. Nyborg WL. Acoustic streaming due to attenuated plane waves. J. Acoust. Soc. Am. 1953;25:68-75

27. Heinrich V. Detection of vortices and quantitative evaluation of their main parameters from experimental velocity data. Meas. Sci. Tech. 2001;12:1199

28. Crowe C, Sommerfeld M, Tsuji Y. Multiphase flows with droplets and particles. Boca Raton: CRC Press; 1998.

29. Mei R. Velocity fidelity of flow tracer particles. Exp. Fluids. 1996;22:1-13-13

30. Melling A. Tracer particles and seeding for particle image velocimetry. Meas. Sci. Tech. 1997;8:1406

31. Meng H, Geld vdCWM. Particle trajectory computations in steady non-uniform liquid flows. Liquid-solid flows : 1st ASME-JSME fluids engineering conference, 1991 New York: ASME; 1991:183.

32. Ames WF. Numerical methods for partial differential equations. San Diego: Academic Press; 1992.

33. Massey B, Ward-Smith J. Mechanics of fluids. New York: Taylor & Francis; 2006.

34. Xu Z, Hall TL, Fowlkes JB, Cain CA. Effects of acoustic parameters on bubble cloud dynamics in ultrasound tissue erosion (histotripsy). J. Acoust. Soc. Am. 2007;122:229-236

35. Zauhar G, Starritt HC, Duck FA. Studies of acoustic streaming in biological fluids with an ultrasound doppler technique. Brit, J. Radiol. 1998;71:297-302

36. Vaezy S, Martin R, Mourad P, Crum L. Hemostasis using high intensity focused ultrasound. Euro. J. Ultrasound. 1999;9:79-87

37. Mitome H, Kozuka T, Tuziuti T. Effects of nonlinearity in development of acoustic streaming. Jap. J. Appl. Phys.34:2584

38. Kamakura T, Matsuda K, Kumamoto Y, Breazeale MA. Acoustic streaming induced in focused gaussian beams. J. Acoust. Soc. Am. 1995;97:2740-2746

39. Kreider W, Bailey MR, Sapozhnikov OA, Khokhlova VA, Crum LA. The dynamics of histotripsy bubbles. ISTU 2010.

40. Wang T-Y, Maxwell AD, Park S, Xu Z, Fowlkes JB, Cain CA. Why are short pulses more efficient in tissue erosion using pulsed cavitational ultrasound therapy (histotripsy)? ISTU2009.1215:40-43

41. Dayton PA, Allen JS, Ferrara KW. The magnitude of radiation force on ultrasound contrast agents. J. Acoust. Soc. Am. 2002;112:2183-2192

42. Poliachik SL, Chandler WL, Ollos RJ, Bailey MR, Crum LA. The relation between cavitation and platelet aggregation during exposure to high-intensity focused ultrasound. Ultrasound Med. Biol. 2004;30:261-269

43. Chen W-S, Brayman AA, Matula TJ, Crum LA, Miller MW. The pulse length-dependence of inertial cavitation dose and hemolysis. Ultrasound Med. Biol. 2003;29:739-748

44. Miller DL. A review of the ultrasonic bioeffects of microsonation, gas-body activation, and related cavitation-like phenomena. Ultrasound Med. Biol. 1987;13:443-470

45. Miller DL, Gies RA. The interaction of ultrasonic heating and cavitation in vascular bioeffects on mouse intestine. Ultrasound Med. Biol. 1998;24:123-128

46. Miller DL, Thomas RM, Williams AR. Mechanisms for hemolysis by ultrasonic cavitation in the rotating exposure system. Ultrasound Med. Biol. 1991;17:171-178

47. Jiang Z-L, Yamaguchi H, Takahashi A, Tanabe S, Utsuyama N, Ikehara T, Hosokawa K, Tanaka H, Kinouchi Y, Miyamoto H. Blood flow velocity in the common carotid artery in humans during graded exercise on a treadmill. Eur. J. Appl. Physiol. 1995;70:234-239-239

48. Holdsworth DW, et al. Characterization of common carotid artery blood-flow waveforms in normal human subjects. Physiol. Meas. 1999;20:219

CHAPTER 7

Therapy Transducers for Histotripsy Thrombolysis

In this chapter, transducers are designed specifically for histotripsy thrombolysis *in-vivo.* A method to inexpensively iterate transducer designs is developed using rapid prototyping. The acoustic properties for transducer elements, matching layers, and lens are characterized to optimally implement high-bandwidth, high-peak power focused transducers. These transducers are demonstrated to produce similar output pressure levels and tissue fractionation to commercially manufactured devices. These transducers will allow customization for specific applications in histotripsy thrombolysis.

7.1 Transducer Fabrication by Rapid Prototyping

7.1.1 Ultrasound Therapy Transducers

Focused ablative ultrasound therapies, such as high-intensity focused ultrasound (HIFU) thermal therapy and histotripsy, have demonstrated precise surgical destruction of pathological tissues noninvasively[1-4]. These therapies rely on focused transducers to deliver high acoustic intensity or pressure to a localized region to ablate the tissue of interest. HIFU requires that a sufficient

acoustic intensity be delivered to the focal region for a sufficient time to cause tissue necrosis through heating. For histotripsy, high-pressure, short duration acoustic pulses are applied to cause mechanical breakdown of tissue in the focal volume by inciting cavitation clouds or bubbles through boiling [5, 6]. Histotripsy requires focal pressure levels of 10 to > 25 MPa peak negative pressure, and the peak positive pressure can exceed 100 MPa.

In order to generate such pressure levels, careful consideration is required for design of the therapy transducers. Transducers are most commonly constructed from piezoceramic or piezocomposite materials, using spherically curved segments which produce ideal focusing. Typical resonant frequencies vary from 500 kHz to 4 MHz depending on the application. Therapy transducers can range from simple single element construction [7], to phased arrays of several hundred individual elements to facilitate focal steering [8-10]. Histotripsy transducers used in previous work have been constructed by industry (Etalon and Imasonic), made from piezoceramic of piezocomposite elements which are air-backed and contain a single quarter-wavelength matching layer. These transducers must be large compared to the wavelength to have considerable focal pressure gain. This stipulation can cause significant difficulty when constructing very large, curved transducers which must necessarily maintain high accuracy along the curvature of the surface. While these transducers have been fairly reliable, they have limited geometric specifications, cost $5000-20000, and require between 1.5-6 months for construction. This turnaround makes it difficult to iterate designs and make small changes to optimize the transducers. It is often desirable to form complex geometries for therapy transducers, for integration and alignment of imaging feedback probes[11], alignment of multiple therapy elements[12], generation of complex focal patterns[13], or maximal utilization of an available acoustic window in the body[14]. Iteration of such transducer designs can be costly and

time consuming at the research level due to the associated cost and lead time for producing focused piezoelectric elements and machining required for suitable transducer housings.

7.1.2 Rapid Prototyping

In order to minimize the cost and time of designing transducers, we have used rapid prototyping additive manufacturing for construction of focused, high-pressure therapy transducers with arbitrary complexity. Rapid prototyping is gaining acceptance in engineering practice as a method to evaluate functional and nonfunctional components in research as an alternative to machining[15, 16]. Rapid prototyping has advantage over subtractive (e.g. machining) or formative (e.g. injection molding) processes in that it is cost-effective, fast, and can produce items of nearly limitless complexity. Common methods of rapid prototyping include stereolithography[17], selective laser sintering, fused deposition modeling (FDM), and 3D printing (Figure 7.1). Materials used in such machines can be conventional and proprietary polymers, elastomers, plaster, ceramic composites, and metals. One disadvantage of rapid prototyping methods is that the materials are generally not equivalent of solid conventional engineering materials, and have not been characterized to the same extent. Thus, further research is needed to determine if such materials are suitable for functional prototypes. In particular, very little data exists on the acoustic properties of these materials, although some mechanical and ultrasonic analysis has been performed[18]. The accuracy and resolution of the machines is dictated by their technology. For instance, a stereolithography apparatus (SLA) system can produce resolution in all dimensions between 10-100 μm. This accuracy has been found to be precise enough to align ultrasound elements in the low MHz range.

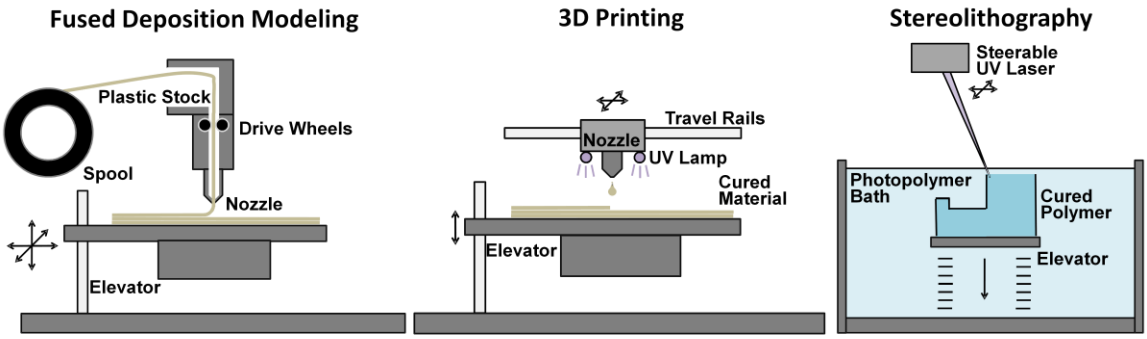

Figure 7.1. Methods of rapid prototyping utilized for transducer manufacture. Fused deposition modeling (left) melts stock from a thermoplastic spool and dispenses it onto a movable table, where it solidifies. 3D printing (center) works similar to an inkjet printer, dispensing drops of photopolymer which is cured by UV lamps attached to the print head. Stereolithography apparatus (right) uses a focused, steerable UV laser to cure select regions of photopolymer on the surface of a liquid bath. After each layer is constructed, an elevator can drop the cured material into the bath so the next layer can be formed.

7.1.3 Methods of Transducer Fabrication with Rapid Prototyping

Histotripsy transducers can be produced in several forms with rapid prototyping:

1. Construction of a transducer using a **single, solid, spherical segment of piezoceramic material**. The element is sealed into a **housing constructed on a rapid-prototyping machine**, with the concave side of the transducer in contact with the load medium. This is the simplest and most time-efficient method of construction. An example is shown in Figure 7.2.

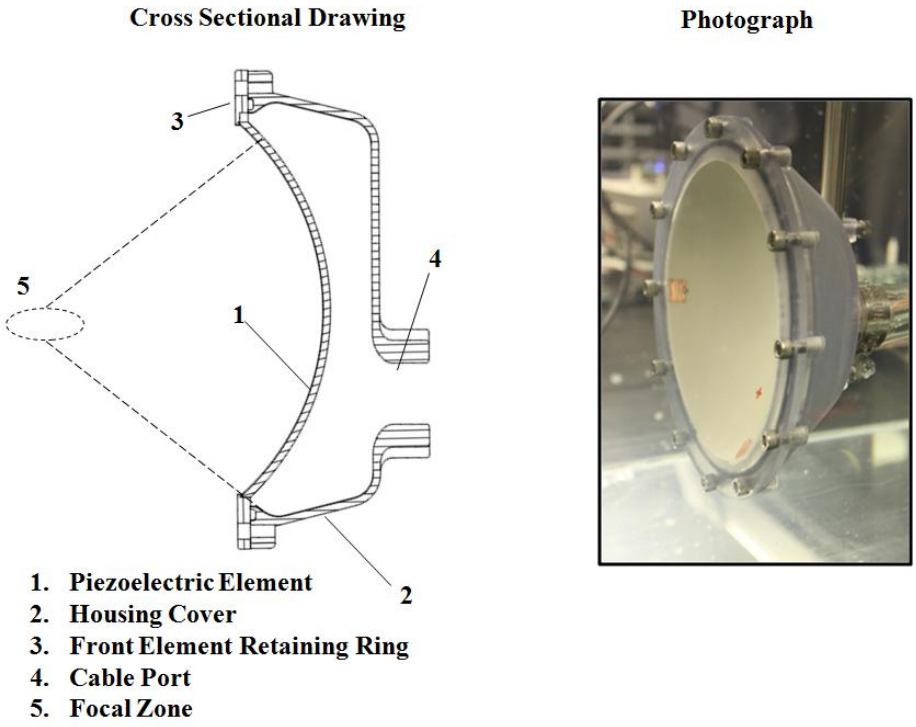

Figure 7.2. A cross-sectional drawing (left) and photograph (right) of a completed single-element transducer. The 750 kHz transducer has a 15-cm aperture with 10 cm focal length. The housing provides waterproofing for internal connections and mounting hardware.

2. Construction of a transducer using a **single, solid, spherical segment of piezoceramic material** which has been **electrically separated on one electrode into multiple sub-elements**. The ceramic is sealed into a **housing constructed on a rapid-prototyping machine**, with the concave side of the transducer in contact with the load medium. This method is more time-consuming than the previous, because each element requires cabling and driving individually. However, small elements have a higher impedance than one equivalent large element, and can be driven to higher voltage for a given amplifier system with appropriate electrical networks.

3. Construction of a transducer using **multiple spherical segments of piezoceramic material, all of them aligned confocally by a rapid-prototyped housing**. The elements are each sealed into the housing, with the concave side in contact with the load medium. One of the most difficult aspects of making multi-element focused transducers or arrays is ensuring alignment of elements. This can be done by computer numerically controlled (CNC) machining of a housing, but is easily performed with by rapid prototyping. This method is more time-consuming than the previous two, because individual sealing of each element is necessary. However, smaller ceramics are more available than large single ceramics commercially. An example is shown in Figure 7.3.

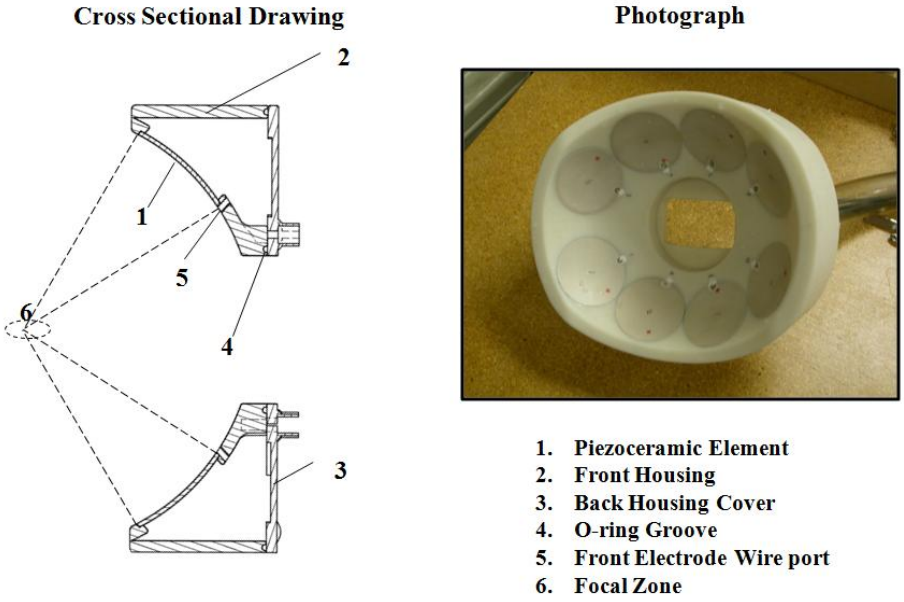

Figure 7.3. A cross-sectional drawing (left) and photograph (right) of a completed transducer with multiple spherical segments. The 1 MHz transducer has a 18 x 16 cm aperture and 10 cm focal length. A central hole in the transducer allows an ultrasound imager to be placed for targeting and feedback during treatment.

4. Construction of a transducer using **multiple spherical segments of piezoceramic material, all of them aligned confocally by placement on a rapid-prototyped mold face**, and back-filling the elements with a solidifying material and constructing a housing around the material. The mold face is removed after solidification of the back-fill, leaving the elements in contact with the load medium. This method allows use of non-rapid-prototyping materials for the housing, but has the benefit of using rapid-prototyping for alignment of elements. An example is shown in Figure 7.4.

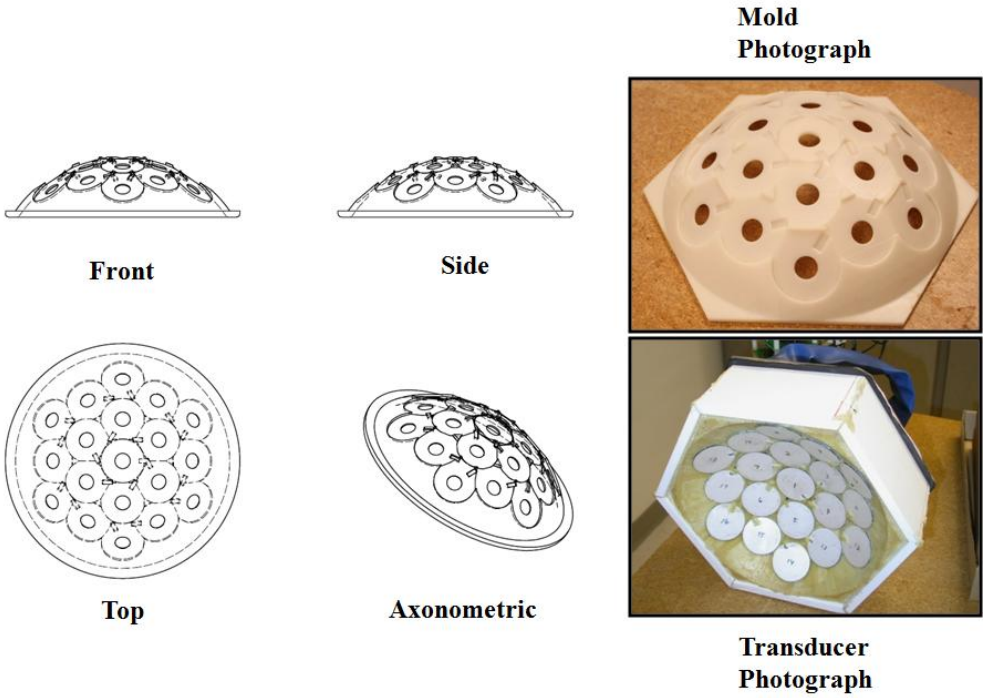

Figure 7.4. A drawing of a mold (left) and images of the mold and completed transducer (right) created by a prototyped mold. A mold holds 19 200 kHz elements 200, aligned for an 11-cm focal length and 18 cm aperture. The elements are set with a rigid polyurethane foam.

5. Construction of a transducer using a **single or multiple flat disks or plates of piezoceramic material**, all of them positioned with the element face normal to

the direction of the transducer focus, and **acoustic lenses applied to focus their output to the transducer focus** (Figure 7.5). In this design, a rapid prototyping machine generates a housing including the acoustic lenses for the individual focused elements. This requires specific rapid-prototyped materials which permit ultrasound transmission. A matching layer may or may not be applied between the element and acoustic lens. If a matching layer is not applied, the element is directly adhered to the back of the lens. If a matching layer is applied, standoffs are either included in the rapid prototyped construct or added secondarily into the element space to create a gap between the element and lens to be filled with the matching layer material. The matching layer then acts as the adhering compound between the element and the lens. An example is shown in Figure 7.5.

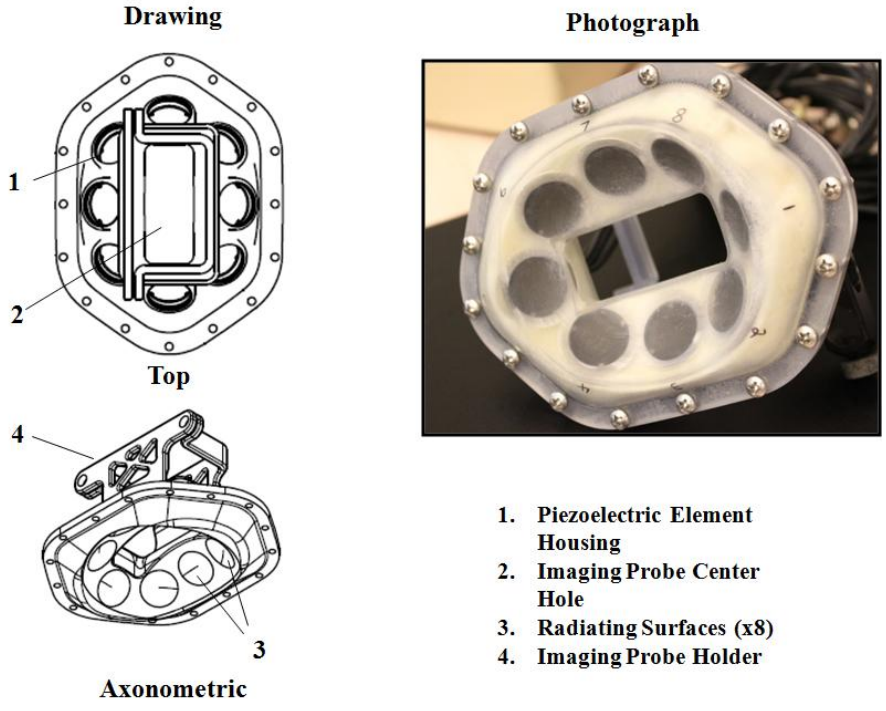

Figure 7.5. Drawings (Left) and a photograph (Right) of a completed histotripsy thrombolysis transducer which uses prototyped lens and built-in matching layers to increase bandwidth. The transducer has a 1-MHz center frequency, an 8.6 x 7.3 cm aperture, and 5.5 cm focal length.

7.1.4 Fabrication of Focused Transducers with Acoustic Lens

The advantages of design method 5 over the others are: (1) flat ceramics that are more readily available than curved ceramics can be used, reducing the cost and time of transducer construct, (2) matching layers can be applied easily, allowing much higher surface pressure output, (3) element alignment is facilitated because lens alignment is built into the housing, and (4) no electrodes contact the load medium, meaning the transducer is well isolated from the patient. The disadvantages of this design are (1) lower heat dissipation and achievable average power output and (2) there is some attenuation due to matching layer/lens. This design has been demonstrated increase pulsed pressure output, extending the size range of transducers which can perform histotripsy.

When using acoustic lens, the focusing of sound requires that the lens geometry is shaped differently than from a spherical curvature. For a plane wave propagating in the lens medium, the surface must be concave for $c_{lens} > c_{load}$. In this case, it is ideal that the surface is elliptical. This shape is difficult to produce in subtractive machining without the use of CNC, but can be accomplished with the same time and difficulty as a spherical curvature in rapid prototyping. However, it is necessary that the material is sufficiently low attenuation and high sound speed that the lens can be made thin and transmit most of the sound energy to the load.

Matching layers are applied to maximize bandwidth imaging transducers and maximize power transfer in HIFU transducers. The matching layer impedance is often chosen to be near the geometric mean between the element and load medium. While this does optimize the bandwidth, theoretical treatment

shows, in fact, that the power transfer at a particular frequency in the bandwidth is lowered compared to the unmatched case[19]. The matching layer acts to dampen the resonance of the transducer, but at the same time, attenuates some of the energy transferred. For histotripsy, efficiency is not the key parameter, but rather, maximum pressure output with short pulse duration. Broadband matching facilitates this by providing several advantages over unmatched elements:

1. Matching layers allow a greater percentage transfer of energy per cycle from the element into the medium. For instance, the peak pressure in water relative to the peak pressure in a resonant PZT ceramic is about 0.08. In a matched element, this ratio is about 0.22. This means that the same pressure in water can be achieved with lower stress on the element. Since PZT has an ultimate stress limit prior to fracture, the pressure output into the water below this ultimate limit is higher with matching.
2. Matching layers increase the bandwidth of the transducer. This is important in histotripsy where short duration pulses (3-10 cycles) are required to prevent heating the medium and to maximize cavitation activity. Higher bandwidth can alternatively be achieved by electrical tuning of the elements. This bandwidth provides a method for testing variation of transducer driving frequency and its effect on histotripsy as well.
3. Matching layers increase the electrical impedance of a transducer element. This means a lower current draw is needed from the amplifier for a given voltage, and less 'electric stress' is placed on the driving system. However, this usually comes at the cost of a reduced output to some extent. Thus, a voltage gain network is applied to generate a greater voltage across the elements.

4. In the case where the matching layer is not a conductive material, the matching layer provides a means of electrical isolation from the load medium and the patient. When acoustic lens are made from rapid prototyping material, this is usually not an issue, as the elements are already isolated.

7.1.5 Design and Fabrication Process

First, the transducer specifications are obtained for the transducer based on application. For example, the transducer aperture size is determined by the available acoustic window size. The focal distance of the transducer depends on the thickness of the intervening tissue. The focal zone size, which primarily depends on the transducer frequency and f-number, is selected by the requisite treatment accuracy.

Second, based on these design requirements, the individual elements are determined by iterative simulation with piezoelectric and propagation models to find appropriate element geometry, quantity, and arrangement. If a voltage transformation network (matching network) is to be applied, the element electrical impedance should be sufficiently high so that the equivalent impedance with the network will not be beyond the amplifier's current output capabilities. One can determine if voltage transformation is necessary by the maximum voltage a transducer element can withstand. If the amplifier can output the calculated V_{max} without a voltage transformation network (400 V for the class D driver[8]), no network is necessary. The class D driver in these studies can generally handle loads of about 10-20 Ω, and the final impedance of the elements (with or without a matching network) should be determined based on the amplifier capabilities. Once the network is designed, a full single-element system

is simulated with the piezoelectric model to estimate the maximum achievable surface pressure for the design.

Element quantity and arrangement are chosen according to the transducer specifications. The propagation model is employed at this point to evaluate the transducer focal gain and focal dimensions. Using the output from the piezoelectric model as the input for this simulation, some idea of the focal pressure can be obtained. However, the designer should be aware that any pressure numbers estimated at the focus will likely be inaccurate, as nonlinear propagation will greatly affect this value for the pressure range used in histotripsy. In future work, a nonlinear propagation model or other pressure estimation scheme could be used to more accurately estimate focal pressure.

After the element geometric configuration is chosen within the transducer specifications, the transducer housing can be designed in a CAD program for fabrication in the rapid-prototyping system. After the ceramic elements and cabling are sealed into the housing, the constructed transducer can then be characterized for focal pressure, beam profile, and cavitation activity.

An example of the design and construction of a transducer using the rapid prototyping method for application to treating deep-vein thrombosis in the femoral veins with histotripsy is described in section 7.3 of this chapter [20, 21]. The transducer incorporated a linear array ultrasound imager to optimize the therapy feedback imaging. The focal volume of the transducer was specified such that cavitation would be generated solely within the target vessel lumen to minimize collateral damage. The transducers are tested in Chapter 8 for *in-vivo* evaluation of histotripsy thrombolysis.

7.2 Characterization of Materials for Transducer Fabrication

Materials to be used in the transducer for the piezoceramic elements, matching layer, and acoustic lens were characterized. The sound speed and attenuation of rapid-prototyped polymers was evaluated for acoustic lens. A suitable material for the matching layer was also determined. Finally, the mechanical strength of several piezoceramic materials was considered to determine the maximum voltage which could be applied to the elements. The methods and results for testing these materials are included in this section.

7.2.1 Rapid Prototyping Materials

Several methods of rapid prototyping were tested for acoustic properties, including fused-deposition modeling (FDM), 3D printing, and stereolithography apparatus (SLA). A 3-mm thickness sample of material was generated by each system as a test piece. The FDM machine operates by applying a melted thermoplastic through a nozzle, which is fed by a solid spool of material. This plastic is dispensed onto a CNC platform and solidifies in place. The step resolution of the system used in this study was 178 μm. The pieces produced by an FDM machine (Stratasys, Eden Prarie, MN, USA) were made with the highest material density settings on the machine to ensure low porosity. The 3D printer (Objet, Billerica, MA, USA) dispenses photopolymer drops and cures them immediately after application onto the previous solid part layer. The lateral print resolution is 100 μm and the vertical build layer step resolution is 16 μm. Different photopolymers can be placed to form a composite material with the rigidity varying between soft rubber to hard plastic. For the purposes of generating specified acoustic parts, only the hard plastic material was tested

because softer materials would not maintain precisely formed shapes. The SLA system (Viper SLA, 3d Systems, Rock Hill, SC, USA) uses a steerable focused UV laser to cure selected regions in a bath of a liquid photopolymer. This system has a lateral resolution of about 75 μm and vertical step size of 100 μm. Several material types were tested from the SLA machine.

Density of a material was calculated directly from the known volume of the part and the measured mass. A transmission method was used to measure the sound speed and attenuation. Two flat, circular PZT transducers with 1 cm diameter were positioned 8 cm apart, and the material was positioned within 5 mm of the receiver. One transducer was connected to a function generator (Berkeley Nucleonics, San Rafael, CA, USA), driven with a short burst at 1 MHz. The other transducer was used as a received, attached to a digital storage oscilloscope (Lecroy, Chestnut Ridge, NY, USA). This method allowed near plane wave propagation through the material. The sound speed was determined from the cross-correlation of two waveforms: one received in open water and the other with the material in the acoustic path. The sound speed could be found from the time lag Δt between the signals from:

$$c_t = \frac{c_w x_t}{c_w \Delta t + x_t}, \tag{7.1}$$

where x_t is the material thickness and c_w is the sound speed in water. With this information, the acoustic impedance is calculated from the product of the sound speed and density. Finally, the attenuation is calculated from the relative amplitude with and without the material in the path, adjusting for the reflections caused by the material/water interfaces calculated with the measured acoustic impedance.

The results are summarized in Table 7.1. ABS plastic printed by an FDM machine displayed slightly lower sound speed and density to molded ABS [22], but

higher attenuation [23]. The density of the printed ABS material with the highest density setting on the system was 93% of that of cast ABS material. While this difference is small, it suggests that air is introduced in the plastic structure during the fabrication process, making the part slightly porous. The result of this added porosity is increased attenuation, which is desirable to avoid for transmission of sound. Similarly, the material printed by the Objet 3D printer (Vero White) had attenuation of 3 dB/cm at 1 MHz, but a higher sound speed compared with the ABS from the FDM machine.

Table 7.1. Acoustic properties of rapid prototyped materials and typical plastics.

	Material	Density (kg/m^3)	Sound Speed (m/s)	Acoustic impedance (MRayl)	Attenuation (dB/cm at 1 MHz)
FDM	ABS	990	2040	2.02	3.5
3D Printer	Vero White	1170	2370	2.77	3.0
SLA	Accura 25	1200	2300	2.76	3.6
	Accura 48HTR	1200	2550	3.06	
	Accura 60 (Blue)	1210	2570	3.11	4.1
	Accura 60 (Red)	1210	2540	3.07	
	Accura PEAK	1360	2860	3.89	
	Accura Extreme	1200	2390	2.87	
	Accura Bluestone	1780	3090	5.50	
Plastics*	ABS	1070	2170	2.32	2.3
	Acrylic	1190	2750	3.27	1.3
	Delrin	1420	2430	3.45	6.0
	HDPE	945	2221	2.10	3.0
	LDPE	920	1950	1.79	0.5
	Polypropylene	890	2660	2.37	3.6
	Polycarbonate	1180	2270	2.68	5.0
	Polystyrene	1050	2400	2.52	0.4
	PVC	1380	2380	3.28	2.2

*All plastics values are taken from ref 23.

*All plastics attenuation values were recorded at 5 MHz. The values listed for 1 MHz are calculated assuming a linear trend of attenuation vs. frequency.

The SLA materials had acoustic properties consistent with extruded or cast engineering plastics. The sound speed of various samples ranged from 2300 – 3090 m/s, with a consistent density around 1200 kg/m^3 among most samples. While it is desirable to use a material with high sound speed for the acoustic lens to minimize its thickness and attenuation, finish quality and limited availability of the materials with highest sound speed precluded their use for transducer construction. The Accura 60 material was chosen to produce most transducer prototypes. Accura 60 is also semi-transparent, which allows identification of printing defects and water infiltration into the housing.

7.2.2 Matching Layer Materials

For a piezoceramic element of acoustic impedance Z_e and load impedance Z_l, the criteria for a single quarter-wavelength matching layer impedance has been derived by several others. The simplest argument is for transmission of a wave through a simple quarter-wavelength thickness sheet with infinite media on either side [24]. In this case, maximum power transfer is obtained when the matching layer impedance is the geometric mean of the element and load impedances:

$$Z_m = \sqrt{Z_e Z_l} \tag{7.2}$$

This equation does not account, however, for the finite thickness of the element. Desilets [25] instead formulates the ideal matching layer as if the desired impedance should be achieved at the center-tap of the piezoelectric transmission line within the KLM model, and thus, the front half of the element should be treated as a second matching layer, in addition to the actual matching layer. This results in an alternate formula:

$$Z_m = \sqrt[3]{Z_e Z_l^{\,2}} \tag{7.3}$$

Souquet [26] derived a third equation for the impedance based on the solution that for maximum bandwidth, the transducer mechanical and electrical Q should be equivalent. This leads to a slightly different value for Z_m:

$$Z_m = \sqrt[3]{2 Z_e Z_l^{\,2}} \tag{7.4}$$

Note that the goal of the matching layer for the therapy transducers is not necessarily to generate the highest bandwidth, but to increase the element electrical impedance, provide high output at the center frequency, and decrease the stress internal to the element for a given surface pressure. Eq. 7.4 appears to fulfill these criteria the best, supplying the largest output at the center frequency [27]. However, it has been demonstrated that the addition of a polymer acoustic lens increases the optimal impedance closer to Eq. 7.2 [28]. Thus, for the purposes of design, Eq. 7.4 is utilized when a matching layer is applied directly between the load and element, while Eq. 7.2 is applied when an acoustic lens is included.

These experimental results were compared with a theoretical model which predicts sound speed and density of a 0-3 composite material, based on the individual sound speeds and density of components. The modified Reuss model [29] has been shown to be an accurate, simple method for such calculations, where the density is simply defined by the weighted sum of component densities (ρ):

$$\rho_c = V_e \rho_e + V_p \rho_p \tag{7.5}$$

And the sound speed is found from the elastic moduli (M) and volume fractions (V) of the individual components:

$$\frac{1}{M_c} = \frac{V_e}{M_e} + \frac{V_p}{M_p} \tag{7.6}$$

$$c_c = \sqrt{\frac{M_c}{\rho_c}} \tag{7.7}$$

These equations were used to determine the matching layer impedance for the experimental mixtures, and compared with the results.

These equations can help determine if such a model can be used in place of experimental tests to find the appropriate formulation for a given piezoceramic type. Matching layer materials were made from epoxy-powder composites. Different formulations of matching layers we created with the chosen types of epoxy and three types of powders. Matching layer test pieces were created by mixing epoxy and powder together, hand stirring the mixture until no dry powder remained in the liquid epoxy. Two epoxies were chosen based on their adhesive capabilities: Hysol E-120HP (Henkel, Rocky Hill, CT, USA) and TAP Super Hard Epoxy (Rhino Linings, San Diego, CA, USA). Powders consisted of either silicon carbide (SiC), cerium oxide (CeO_2), or tungsten (W), and were mixed in different weight ratios with epoxy. Each mixture was degassed in a vacuum chamber for 10 minutes, then poured into a cylindrical mold to make a cylindrical sample with 2.5 cm diameter and 1 cm thickness. The samples were allowed to cure for 24 hours and then removed from the mold. Each sample's properties were then measured by the same method as the rapid prototyping materials.

A total of 18 mixtures using cerium (IV) oxide (CeO_2), silicon carbide (SiC), or tungsten (W) were used to evaluate the acoustic impedance of the materials as ideal matching layers for transducers with and without lens. Using Eq. 7.4 for the ideal matching layer without lens, the impedance should be Z_{ML} = 5.4 MRayl. Using Eq. 7.2 for the ideal matching layer with lens, the impedance should be Z_{ML} = 7.0 MRayl.

Table 7.2 shows the properties of the 18 materials tested with various powders. In general, the sound speed of mixtures first decreases as low fractions of powder are mixed, then rises to the sound speed of the bulk powder material

as the fraction approaches 1. However, SiC, which has a very high bulk sound speed of approximately 13000 m/s, showed an increasing trend of the sound speed with powder fraction. This behavior was inconsistent with the model trend, which showed a decrease in apparent sound speed (Figure 7.6). However, all three materials were in good agreement with the calculated acoustic impedance.

Table 7.2. Measured acoustic properties of matching layer mixtures.

Epoxy Type	Powder Type	Epoxy Fraction (w/w)	Powder Fraction (w/w)	Density (kg/m^3)	Sound Speed (m/s)	Acoustic Impedance (MRayl)
TAP	SiC	0.80	0.20	1313	2608	3.42
TAP	SiC	0.60	0.40	1483	2666	3.95
TAP	SiC	0.40	0.60	1766	2956	5.22
TAP	CeO_2	0.80	0.20	1335	2430	3.24
TAP	CeO_2	0.60	0.40	1699	2356	4.00
TAP	CeO_2	0.40	0.60	2036	2255	4.59
TAP	W	0.60	0.40	1792	1950	3.49
TAP	W	0.40	0.60	2662	1710	4.55
TAP	W	0.15	0.85	4973	1490	7.41
Hysol	SiC	0.80	0.20	1226	2240	2.75
Hysol	SiC	0.60	0.40	1430	2293	3.28
Hysol	SiC	0.40	0.60	1690	2504	4.23
Hysol	CeO_2	0.80	0.20	1244	2081	2.59
Hysol	CeO_2	0.60	0.40	1519	2040	3.10
Hysol	CeO_2	0.40	0.60	1763	1973	3.48
Hysol	W	0.26	0.74	3462	1441	4.99
Hysol	W	0.15	0.85	4974	1253	6.23
Hysol	W	0.15	0.85	4921	1232	6.06
Hysol	W	0.13	0.87	5527	1239	6.85

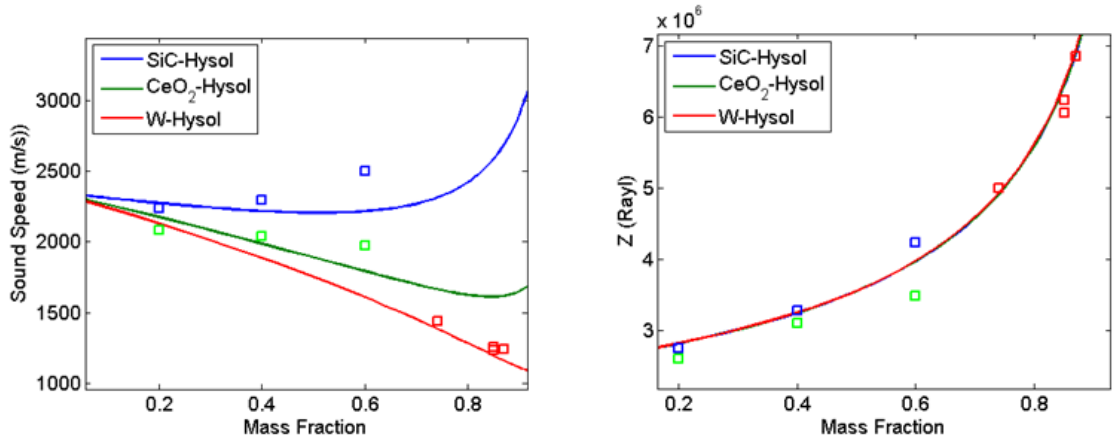

Figure 7.6. Sound speed (left) and acoustic impedance (right) predicted by the model (solid lines) and experimental measurements (squares), all as functions of mass fraction of powder in epoxy. Powders with lower bulk sound speed produced materials with lower sound speed, but impedance vs. fraction was consistent between the three materials, as predicted by the model.

Tungsten proved the most ideal material for use as a matching layer. Due to its high density, a small volume of tungsten was required compared with the other powders, which means the combined mixture was of lower viscosity and more easily degassed. Mixtures of CeO_2 and SiC were difficult to mix beyond 60% powder. A mixture of 87% tungsten to Hysol w/w was found to be near the ideal value for a transducer with lens. Mixtures of 78% tungsten to Hysol or 71% tungsten to TAP epoxy were found by the model to produce an appropriate impedance without lens. Attenuation was not recorded for most samples, but for the 87% w/Hysol mixture, the attenuation was 10.5 dB/cm at 1 MHz. For matching layers of quarter-wavelength thickness, the attenuation due to the matching layer would be ~0.4 dB, which gives > 95% transmission.

7.2.3 Piezoelectric Element Materials

Different compositions of piezoceramic material were evaluated to determine their ultimate pressure output limits prior to failure. Elements were positioned in a water bath with the front surface in contact with the water and enclosed in a small housing to ensure air backing of elements. A capsule hydrophone was positioned facing the transducer with 10 cm distance from the transducer surface. The element was attached to a voltage gain network and class D amplifier to apply up to 2400 V_{pp} on the element. The amplifier is controlled by a field-programmable gate array logic board (Altera, San Jose, CA, USA). Each element was first driven with a base signal of 10 V_{pp} to measure the output under low amplitude conditions. The element was then driven for 10 seconds with a high amplitude signal of 10 cycles at a PRF of 1 kHz. The base signal was then reapplied to ensure the pressure output was the same. This was repeated, incrementing the test voltage each time until the base pressure output from the element was reduced. This process was also repeated to test the elements with acoustic lens with and without matching layers to compare with the bare elements in direct contact with the water.

For each type of transducer element, n = 3 elements were tested to determine the voltage at which the pressure output was irreversibly degraded. Element damage appeared as small chips in the back surface of the element, most often occurring near the center (Figure 7.7). This pattern suggests damage by lateral or radial resonances in the PZT material. This damage was evident in PZT, PZ26, and PZT with lens at similar drive voltages around 1000 V_{pp} and an estimated surface pressure of 1.3 – 1.8 MPa (Figure 7.8). In PZ36 material, which has a lower lateral coupling coefficient and lower impedance, no visible signs of failure were observed. However, element output decreased drastically at a similar drive

voltage and pressure to the aforementioned materials. The application of a lens to the PZT4 disk also did not significantly alter the failure pressure.

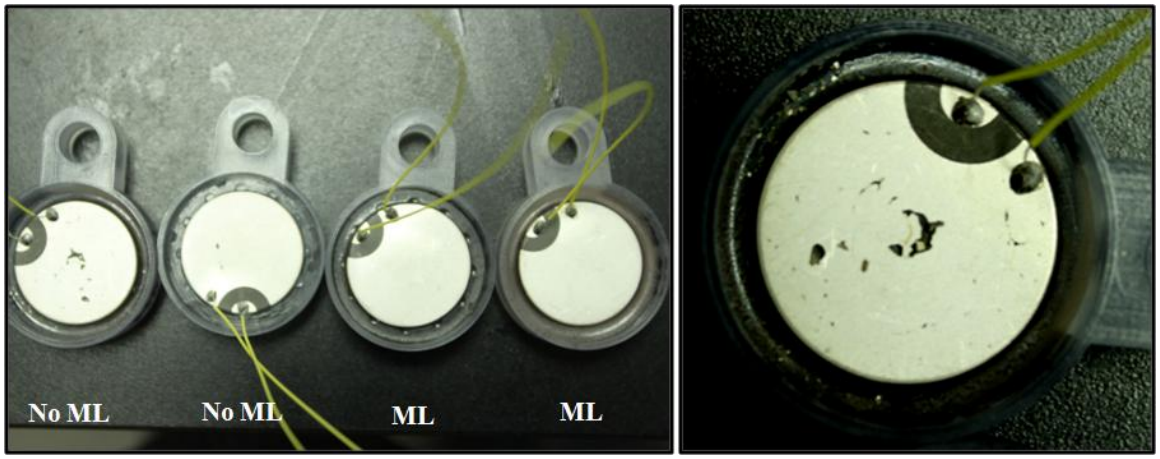

Figure 7.7. (Left) Photograph of four test elements in housings. The back surfaces of two elements without matching layers and two with matching layers are shown. (Right) Close up view of the leftmost element without matching layer. Note the small chips along the element surface. This mechanical failure coincided with irreversibly decreased element output. ML: matching layer.

The PZT + matching layer + lens configuration did not incur irreversible damage at 2000 V_{pp}, even when driven at this voltage for 300 seconds. Some decrease in the voltage input and pressure output was observed vs. time, possibly because of self-heating and detuning of the element [30]. The lens unfortunately provides excellent thermal insulation from the water bath, and thus active cooling might be necessary in applications were high average power output is a requisite. Average power density for tests with the elements with matching layer/lens during maximum driving conditions was 7.8 W/cm^2, although it decreased to 5.9 W/cm^2 after 300 seconds driving due to this detuning. The element pressure output and impedance recovered to their original values after the ceramic returned to ambient temperature.

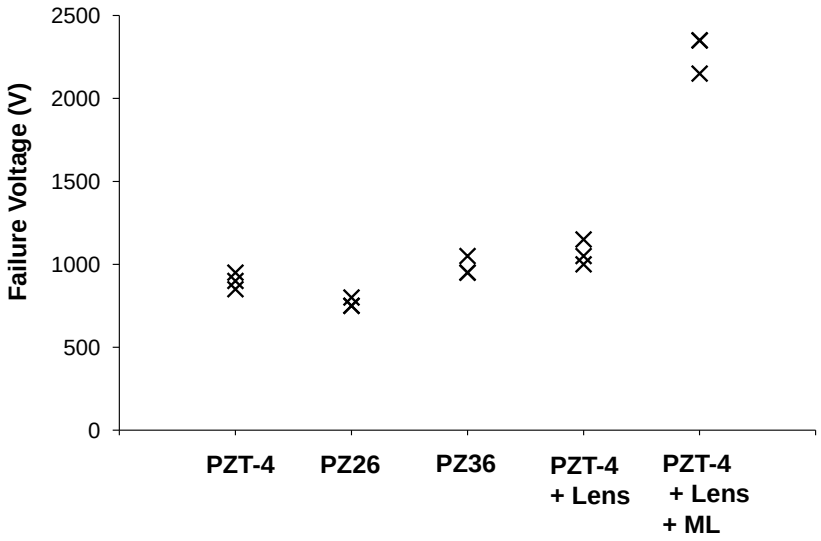

Figure 7.8. Maximum element surface pressure prior to failure with 10 cycle pulses applied at a 1% duty cycle. All types of PZT tested had similar failure points without matching layer. Each measurement (n=3 for each type) is shown as an 'x'. A consistent failure pressure for the elements with matching layer was not determined; two values tested at 2350V are the limit for the amplifier and did not fail. Thus, 2000 V_{pp} was considered a safe limit to drive 1 MHz elements with matching layer.

7.3 Characterization of Thrombolysis Prototypes

7.3.1 Transducer Specifications for Thrombolysis

One specific transducer is demonstrated here as an example for the therapy transducer design using rapid prototyping. The transducer is designed for treatment of deep-vein thrombosis (DVT) in the femoral veins. This transducer is meant to be coupled to the leg by a water bath and controlled by a 3-axis motorized positioner. The therapy probe must be integrated with an ultrasound imaging probe that is used to guide and monitor treatment progression.

In order to obtain adequate images of vessels, it is necessary to position the ultrasound imaging probe as close as possible to the target. The probe footprint

is 50 mm x 8 mm, thus the elements must fit around this geometry. For the *in-vivo* testing performed in Chapter 8, the vessel depth is 1.5 cm, which provides a lower bound for the transducer working distance. The focal dimensions of the transducer are determined based on the target size. The target vessel is about 6 mm diameter. For focused transducers, the axial dimension defines the longest dimension of the focus, which should at most 6 mm to ensure cavitation occurs solely in the vessel lumen. Furthermore, based on previous histotripsy studies, the focal gain should be > 30 to generate enough pressure to generate a cavitation cloud. The minimum transducer gain which has previously generated a cavitation cloud in histotripsy *in-vivo* is 26.

7.3.2 Transducer Modeling

Several equivalent circuit models exist for piezoelectric ceramics operating in thickness mode. An extended form of the KLM model is applied here[31]. For detailed derivation of the model, see the Appendix of the dissertation. Only the results of the model are given below. Note that although surface pressure measurements are provided, these are not directly applicable to the experimental results or propagation model, as the diffraction from the element edges generally creates a spatially-dependant pressure across the element surface. More applicable is the element surface velocity, u_s, which is used as the actual input to the Rayleigh integral. However, surface pressure is given here to give an idea of the pressure gain afforded by focusing as $p_s = u_s \rho_l c_l$.

Each element in the transducer was made from a modified PZT-4 (Steiner & Martin's, Miami, FL, USA). Given the specification that the transducer fit around the imaging transducer, and that the transducer focal length was 5 cm, 2-cm diameter disk-shaped elements were chosen with a thickness resonance of 1 MHz. The properties for different PZT formulations are shown in Table 7.3. For

the modeled results, properties for PZT-4 are used. For an element of the specified geometry and parameters, the element electrical impedance for an element coupled to water directly as a load and air as a backing is shown in Figure 7.9.

Table 7.3. Material properties of the piezoelectric materials in this study, as well as the matching layer and lens parameters for this transducer.

	PZT-4	PZT-8	Pz36	Matching Layer	Lens
ε_s	650	600	300	N/A	N/A
k_T	0.45	0.45	0.5	N/A	N/A
P (kg/m^3)	7550	7500	5500	5500	1200
c_0 (m/s)	4590	4590	2600	1240	2560
Z_0 (MRayl)	34.6	34.4	14.3	6.8	3.1

Figure 7.9 also shows equivalent plots of the impedance with a matching layer with Z_m = 6.8 MRayl, close to the geometric mean of 7.2 MRayl, and a lens layer Z_l = 3.1 MRayl. The element impedance at 1 MHz with 2 meter BNC RG-174 cable is simulated to be 61 – 107 j Ω. A voltage gain of 4 is desired to transform the maximum voltage on the element from 400 V to 1600 V_{pp}. The voltage network C and L values given in the appendix are C = 1.3 nF and L = 9.7 μH. Available values of 1 nF and 11 μH give gain G = 3.5. Applying this to the simulation, the impedance as seen by the amplifier for one element becomes 20.5 Ω, within the limits of the amplifier.

Note that with addition of the voltage network to the element, the impedance remains fairly constant across the bandwidth of 0.8 – 1.3 MHz for the element with matching layer and lens (Figure 7.10). Without the matching layer or lens, the impedance varies with small changes in frequency from only 4 Ω at 0.86

MHz up to a peak of nearly 200 ohms at 1.06 MHz and back down to about 4 ohms at 1.16 MHz (Figure 7.10). This also means the bandwidth is narrow at the low-impedance positions (see Figure 7.11). The flattening of the impedance curve by the matching layer and lens leads to a more consistent output vs. frequency.

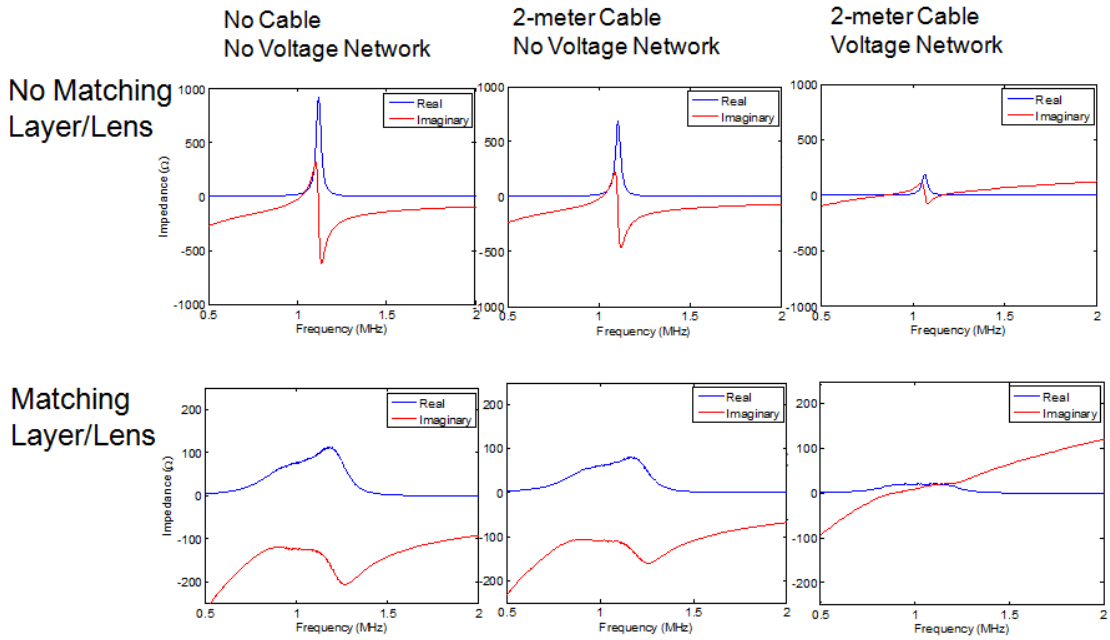

Figure 7.9. Impedance traces of elements without (top) and with (bottom) a matching layer/lens. The element impedance is shown directly connected to the element terminals (left), at the end of a 2-meter cable attached to the elements (center), and at the input to the voltage gain network (right).

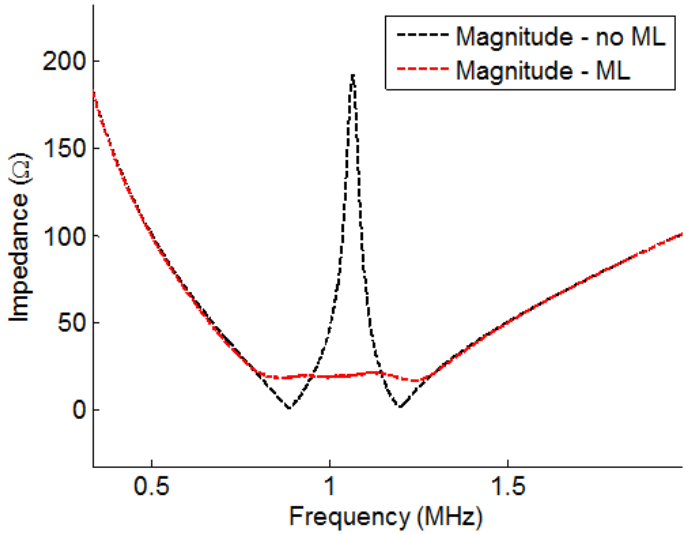

Figure 7.10. Impedance magnitude of a 1 MHz element with voltage network and cable with (red line) and without (black line) matching layer and lens.

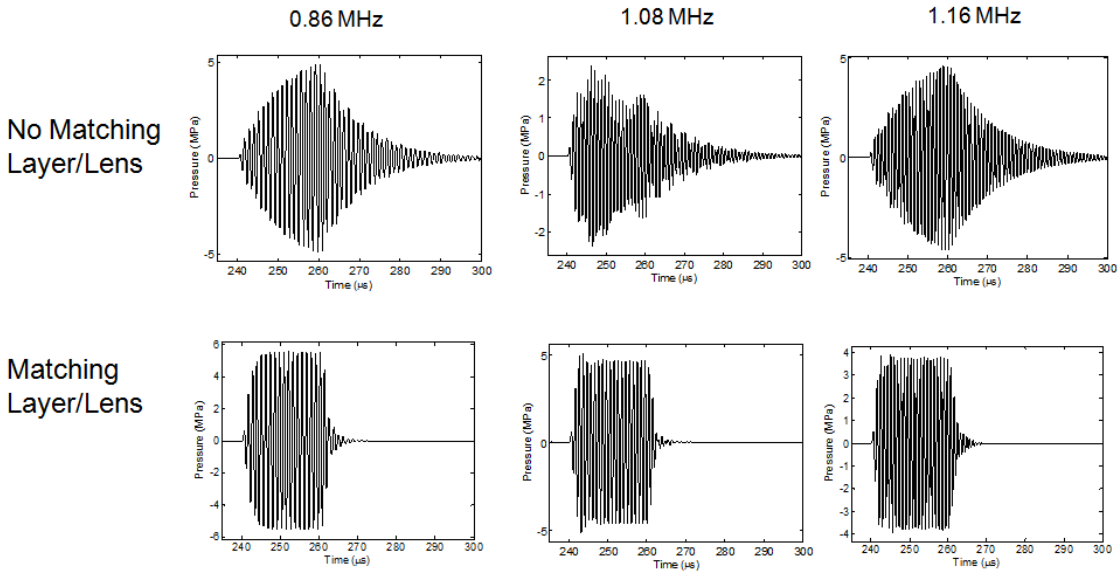

Figure 7.11. Equivalent surface pressure in the load medium for an element without (top) and with (bottom) matching layer and lens at 3 separate frequencies. The matching layer/lens element shows faster ringup time and more consistent pressure output across the bandwidth.

Similar surface pressures can be achieved by transducer elements with and without matching layers, but the element without matching has a ringup time of more than 20 cycles to reach the same steady state amplitude as the matched element reaches in 3-4 cycles. As only the largest amplitude cycles of the pulse will contribute to bubble cloud generation, the long ringup time for the unmatched transducer will consequentially increase the undesirable heating as a side-effect of the treatment and make it inefficient. Due to the increased bandwidth of the transducer with matching, very short pulses with high amplitude can be produced. The impulse responses of two equivalent transducers with and without matching layers are shown in Figure 7.12. Note that the peak voltage into each element is nearly identical, but the matched transducer peak pressure output is 2.9 times larger than the unmatched case. Thus, the voltage applied to the unmatched element is considerably higher for equivalent output. The peak-peak voltage with matching layer/lens is about 2.1 kV_{pp} to achieve 6 MPa surface pressure, while the unmatched element requires > 9 kV_{pp} to achieve the same (Figure 7.13). Another result of matching is reduced internal stress in the element for a given surface pressure in the load, as a greater percentage of the resonant wave each cycle is transmitted to the load medium. These factors all suggest that acoustic matching is important to obtain short, high-amplitude pulses with a controllable output, supporting the data in section 7.2.3.

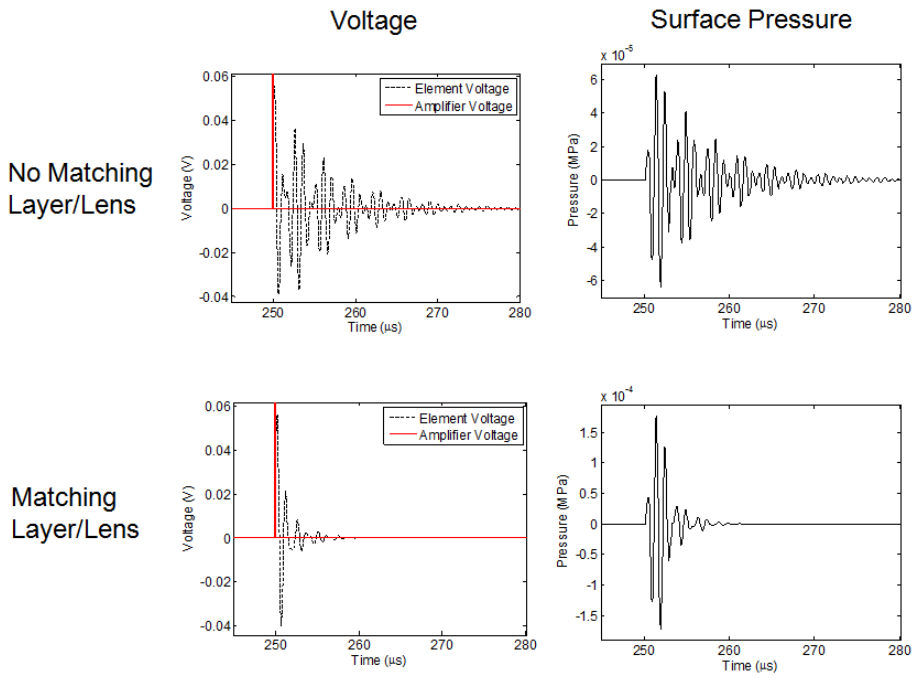

Figure 7.12. Impulse response of transducer elements without (top) and with (bottom) a matching layer. The voltage response (left) and pressure response (right) are shown. Note that approximately 3 times the peak pressure is achieved with a matching layer applied when the peak voltage is the same.

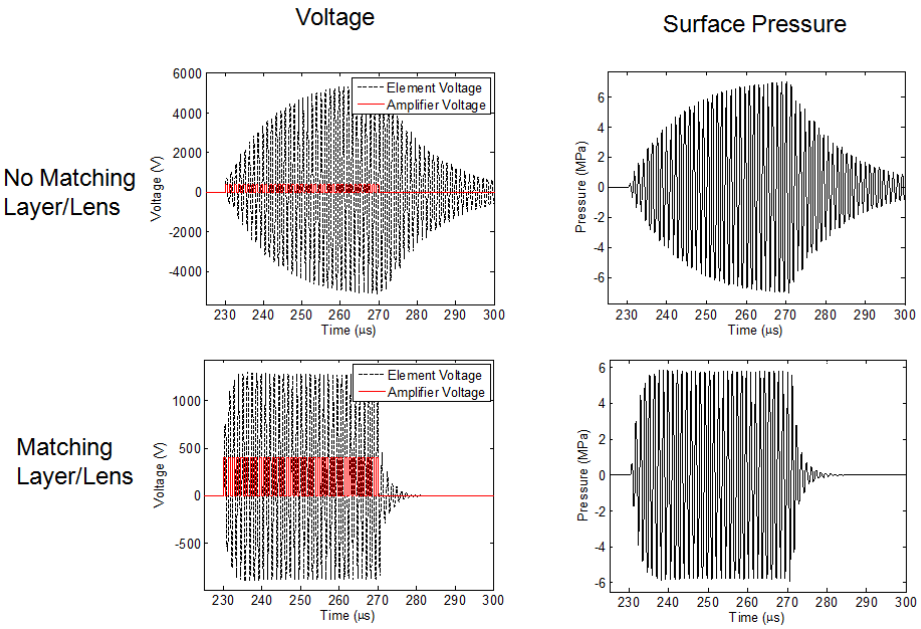

Figure 7.13. Voltage (left) and pressure (right) for matched and unmatched elements at their maximum output frequency (860 kHz). Note that the voltage gain at this frequency is higher than the calculated 3.7, closer to 5.

A propagation model based on the Rayleigh integral[24] was implemented to determine the focal characteristics of the transducer, including the focal dimensions and focal gain for transducers. This equation defines linear propagation with excellent accuracy. As discussed in Chapter 2, histotripsy can be highly dependent on nonlinear propagation, thus the linear propagation model is a simplification and does not accurately predict the waveforms developed at the focus. However, the cavitation cloud and peak negative pressure of the focal waveform occur over a similar region to that predicated by linear theory. The linear focal gain can also be calculated which provides an indication based on previous histotripsy transducers whether sufficient pressure can be generated. Previous histotripsy transducers used for *in-vitro* and *in-vivo* studies have focal gains ranging from 40-90 [21, 34, 35].

Propagation models were developed for point sources, rings, disks, rectangular plates, and spherical segments with circular and rectangular aperture with arbitrary cutouts such as central holes. If a single element is being modeled, its dimensions are established and then the geometry is constructed of individual point sources with no greater than $\lambda/2$ spacing to ensure accuracy throughout the entire pressure field. If multiple elements are to be simulated, the center position of each element is also input, and the model then produces copies of the transducer element at each location. This allows accurate simulation of transducer geometries with F# = *total aperture* / *focal length* > 0.55. The simulation is performed at the transducer center frequency, meaning it is accurate for CW or long bursts. Short burst simulation requires a diffractive transient model such as that described in Chapter 2 for the hemisphere geometry.

Each element in the transducer is focused to a common focal point. The focal gain of a single, spherically-focused transducer element can be estimated by the ratio of Rayleigh distance to focal distance:

$$G_f = \frac{z_r}{z_f} = \frac{A}{\lambda z_f}, \qquad 7.8$$

where A is the active area of the transducer element. The histotripsy transducer used in preliminary studies of thrombolysis had G_f = 42. However, this transducer had a focal dimensions which exceeded the target vessel diameter and had too great of a focal length, causing difficulty placing an imaging guidance probe in the vicinity of the vessel. Thus, a transducer with similar focal gain but with smaller focal dimensions was required to improve the imaging and therapy outcome. Additionally, the transducer was required to house an available linear array imaging probe which is suitable for vascular imaging. This probe had a footprint of 50 mm x 8 mm. As such, the 2-cm therapy elements for the new thrombolysis transducer were positioned around a central hole (see Figure 7.5) as closely as possible. Figure 7.14 shows the simulated pressure field output by designed transducer. At 1 MHz, the transducer has G_f = 33, meeting the specification. The previous design was capable of much greater pressure output than was necessary to achieve cavitation in-vivo, and as such, this gain should be sufficient to treat vessels through 1-2 cm overlying tissue. Additionally, the focal dimensions at 1 MHz are small enough to target the 6-7 mm diameter vessels. While greater gain can be obtained at higher frequencies (Table 7.4), the smaller focal dimensions will increase acoustic attenuation, extend the treatment time, and make transducer construction more difficult. Thus, 1 MHz was chosen as the frequency for the final design.

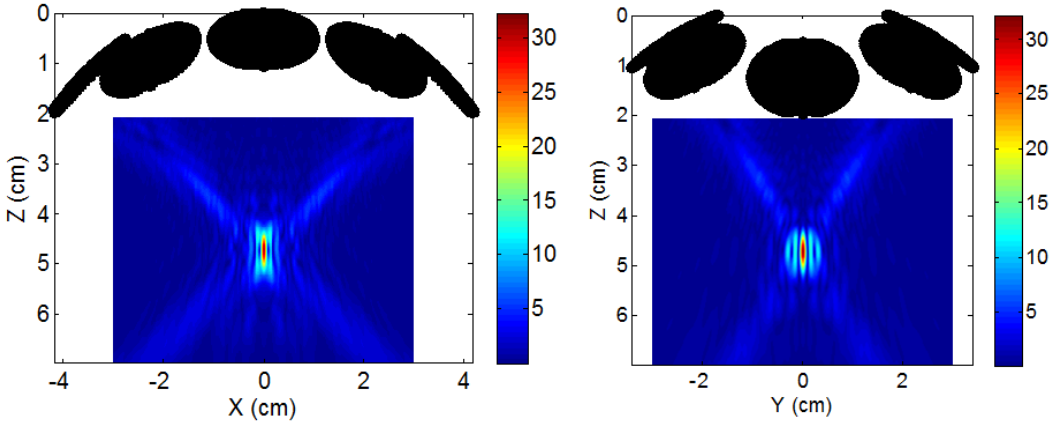

Figure 7.14. Two-dimensional pressure beam patterns for a 1 MHz transducer shown in Figure 7.5. (Left) X-Z profile of the focal plane. (Right) Y-Z profile of the focal plane.

The large spacing between the elements along the Y-axis due to the imager port cause substantial grating lobes around the focus (Figure 7.15). These grating lobes have amplitude around 1/3 the peak pressure amplitude. However, it has been shown that lesions can be accurately created only within the main focus, even in the presence of grating lobes which are greater than ½ the amplitude of the main beam[36]. Thus, it is expected that cavitation will be confined to the main beam dimensions.

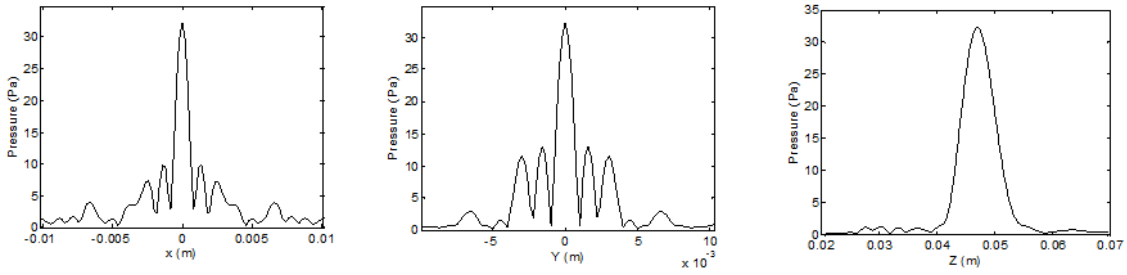

Figure 7.15. One-dimensional beam profiles corresponding to Figure 7.14. (Left) X transverse pressure profile. (Center) Y transverse pressure profile. (Right) Z axial pressure profile.

Table 7.4. Comparison of focal dimensions and gain between 3 transducers of the same geometry but different frequency.

	-6dB X (mm)	-6dB Y (mm)	-6dB Z (mm)	Focal Gain
1 MHz	1	1.2	6.6	33
1.5 MHz	0.7	0.8	4.2	49
2 MHz	0.5	0.6	3.3	66

7.3.3 Transducer Fabrication

Several iterations of the thrombolysis transducer were constructed (Figure 7.16). In the first designs, 8 spherical segments of PZ26 material were used without matching layer in 8 subhousings. While this minimized the size of the device, difficulties in preventing electrical problems at voltages > 800V required a larger design. The second generation device consisted of one larger housing in which all the elements could be properly seated and isolated electrically. This device was initially successful in generating cavitation *in vivo,* but the driving voltages necessary were near the mechanical failure limit for the ceramics as determined in section 7.2.3, and fragmentation was evident in the back face of multiple elements after about 600 seconds of operation. Thus, the final design was constructed using the matching layer/lens methodology. This design is described in detail in the remainder of this chapter.

The overall aperture of the final transducer was 7.3 cm x 8.6 cm. The radius of curvature for the transducer was chosen to be 5 cm to position the imaging probe in the center as close to the target as possible. The central port for the ultrasound imager was designed to hold a 10 MHz linear array (10L, GE Healthcare, Fairfield, CT) or a 12 MHz phased array probe (S12, Philips Healthcare, Andover, MA) for high frequency imaging of the vasculature. All 3 prototypes were printed on a Viper SLA system with Accura 60, which was chosen because the

material had low attenuation, adequate printing resolution and high sound speed compared materials on other systems.

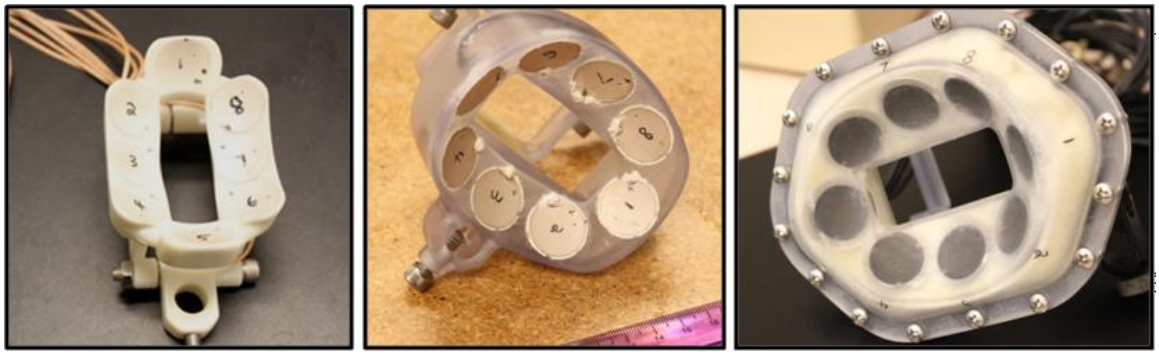

Figure 7.16. First (left), second (center), and third (right) generations of the thrombolysis transducer. The first two generations used spherically curved PZ26 segments directly in contact with a water bath, while the third generation used flat, circular PZT-4 disks with a matching layer and lens applied for focusing.

Transducers were constructed with piezoelectric elements made from the PZT4 material. On the surface of the lens facing the element, three small standoffs were printed to create a gap with the thickness of the matching layer. Details of each element assembly are shown in Figure 7.17. A small volume of matching layer material was mixed as described in Section 7.2.2, and dispensed as a droplet in the center of the back lens surface. The element was then pressed onto the standoffs. Excess material runs into adjacent wells to prevent the material from overflowing onto the back of the element and causing electrical breakdown around the element at high driving voltage. The pressure may be applied by hand, or pressed by a compression cap which screws into the element housing behind the element and applies continuous pressure on the element back surface. All elements were populated into the housing in this manner, and

allowed to cure for at least 24 hours before any measurements were made. Two wires were soldered onto the element front and back silver electrodes. A silver-bearing solder (96/4 Sn/Ag) was used to prevent dissolution of the electrode during soldering. Soldering was performed at 250 °C for no greater than 3 seconds per electrode. This minimized the possibility of oxidation of the joint and depolarization of the element. The wires were soldered to either RG-58, RG-174, or RG-316 coaxial cable terminated by Bayonet Neill-Concelman (BNC) connector. The cables were run through ports in the housing, and sealed with flexible polyurethane (Double Bubble, Hardman, Kansas City, KS).

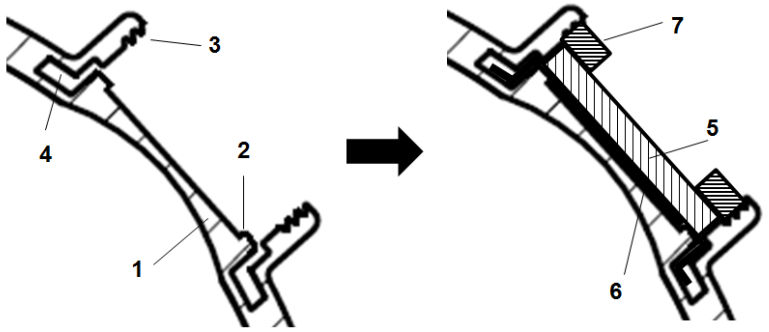

1. Acoustic Lens
2. Matching Layer Standoff
3. Compression Ring Threads
4. Matching Layer Overflow Well
5. Piezoelectric element
6. Matching Layer
7. Compression Ring

Figure 7.17. Cross-sectional detail of a piezoelectric element housing with lens corresponding to the transducer in Figure 7.5. The left image shows the housing prior to placement of the element and matching layer, and the right image shows the final state once the element is in place.

7.3.4 Comparison with Model

For modeling of the third generation transducer, a 2-cm diameter disc made from PZT-4, the same as in section 7.2.3 with a matching layer. The modeled and

measured electrical impedance curves of a single element with matching layer and lens are provided in Figure 7.18. Good agreement is observed between measurement and the model near resonance when the matching layer thickness is chosen appropriately. For this transducer, the model indicated that the matching layer was 45 μm thicker than $\lambda/4$, causing the higher impedance curve at frequencies > 1 MHz. The error in matching layer thickness is likely due to the printer resolution limit, which prints the transducer housing in 100 μm increments. However, the impedance curves were remarkably consistent between elements. For n = 8 elements, the impedance at 1.0 MHz was 48.3 +/- 1.5 Ω for the real part and -94.6 +/- 3.3 jΩ for the imaginary part (mean +/- standard deviation). For comparison, the impedance given by the model is 44 – 102j Ω at 1 MHz with the matching layer thickness = $\lambda/4$ + 45 μm. At low frequency, there is some deviation of the model from the measurements, caused by radial (lateral) modes in the element, which are not considered in the 1-D KLM model.

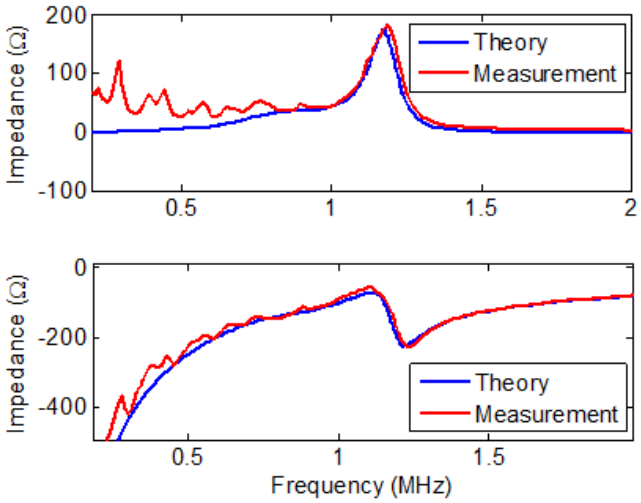

Figure 7.18. Comparison of simulated (blue) and measured (red) electrical end-of-cable impedance for an element of the thrombolysis transducer. The real impedance is shown on the top and imaginary part is on the bottom. Note there is some deviation from theory at lower frequencies due to radial modes in the transducer element, which are not accounted for in the model.

A two-dimensional pressure map was acquired by scanning the field with a capsule hydrophone (HGL-0085, Onda Corp, Sunnyvale, CA). The peak positive pressure values from a 10-cycle burst were used to record the pressure amplitude at each point in the field. Figure 7.19 shows the normalized pressure amplitude as predicted by the propagation model and as measured by the hydrophone. The lateral -6dB beamwidth at z = 50 mm from the transducer face was 5.1 mm in the simulation and 5.3 mm measured. Near the transducer surface (z = 7.5 mm), the beam width was 17 mm when simulated and 15.9 mm when measured. These measurements suggest that the acoustic lens provides nearly ideal focusing similar to a spherical transducer segment.

The beam profiles of the full transducer (all 8 elements driven) was also measured and compared with simulation. The X x Y x Z -6 dB pressure beam width for the simulation was 1.0 x 1.2 x 6.6 mm for the 1 MHz transducer. When measured with the capsule hydrophone, the beam width at the focal plane was 1.0 x 1.3 x 6.9 mm. These measurements are also in agreement with the simulated values.

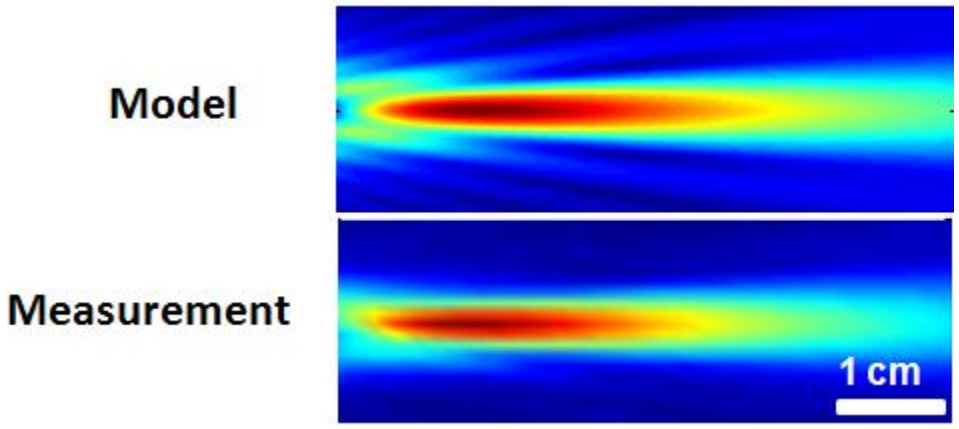

Figure 7.19. Axial-Lateral pressure amplitude distribution around the focus simulated for a single, 2 cm element at 1.1 MHz. Sound propagation is from left to right in the simulation. The color indicates normalized pressure amplitude, with red being the highest and blue being close to zero.

7.3.5 Output Focal Pressure

A fiber-optic probe hydrophone (FOPH) constructed in our lab was used to measure focal pressure waveforms of the completed transducer[37]. The hydrophone had a bandwidth a 50 MHz, an active element of 100 μm diameter, and a low-frequency sensitivity of 0.35 mV/MPa. The capsule hydrophone with known frequency response was used to find the frequency response of the hydrophone. A deconvolution procedure was written to correct for the hydrophone frequency response to obtain accurate pressure waveforms. The transducer focal pressure was measured in degassed water up to the point where cavitation occurred. Beyond this pressure level, measurements were recorded in a cavitation-resistant liquid (1,3, butanediol), as described in Chapter 3.

Ideally, all lenses are constructed such that each lens surface is equidistant from the transducer focus. If this is not the case, a phase delay will exist between elements. Depending on the phase delay, the pressure wave from each element may constructively or destructively interfere at the focal point. One criteria for the acceptable phase shift between elements for focusing is $< \lambda/8$ [38]. To determine the phase error between multiple elements in the transducer, a capsule hydrophone was positioned at the transducer focus, and each element was driven individually. The eight waveforms received are shown in Figure 7.20. The time delay difference between the most leading and lagging elements is 80 ns, or $\lambda/12$. This phase error corresponds with a decrease of 10% in the focal peak-peak pressure under linear conditions compared to ideal element alignment.

Figure 7.21 shows the pressure waveform at 80% drive voltage to the transducer measured in butanediol, with the peak negative pressure reaching 31 MPa and the peak positive pressure reaching 83 MPa. These results compared well with measurements in water up to 50% drive voltage. Due to cavitation on

the hydrophone tip, pressure waveforms greater than 2 cycles could not be acquired at large pressure amplitudes.

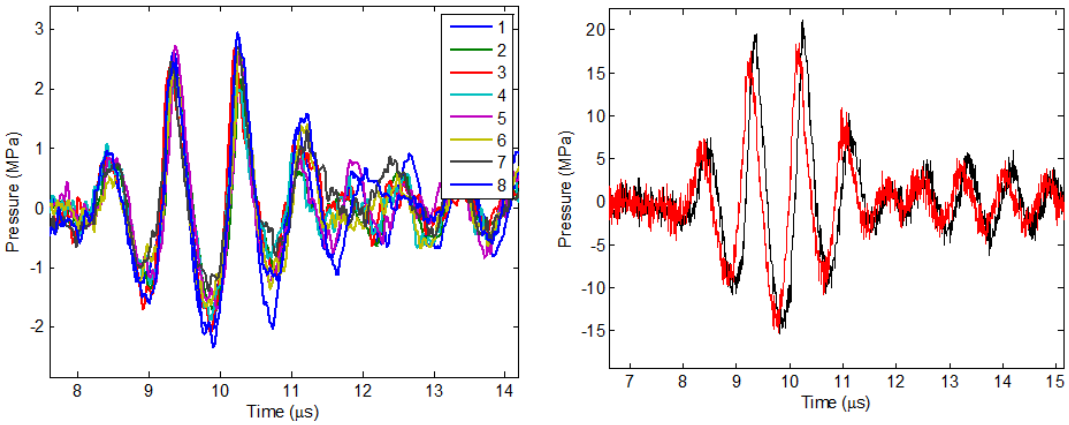

Figure 7.20. (Left) Waveforms received at the transducer focus by each of the eight elements in the therapy transducer. (Right) Focal pressure estimated by summing all eight waveforms recorded without (red) and with (black) phase error correction. Correction of phase error leads to approximately 10% increase in pressure output.

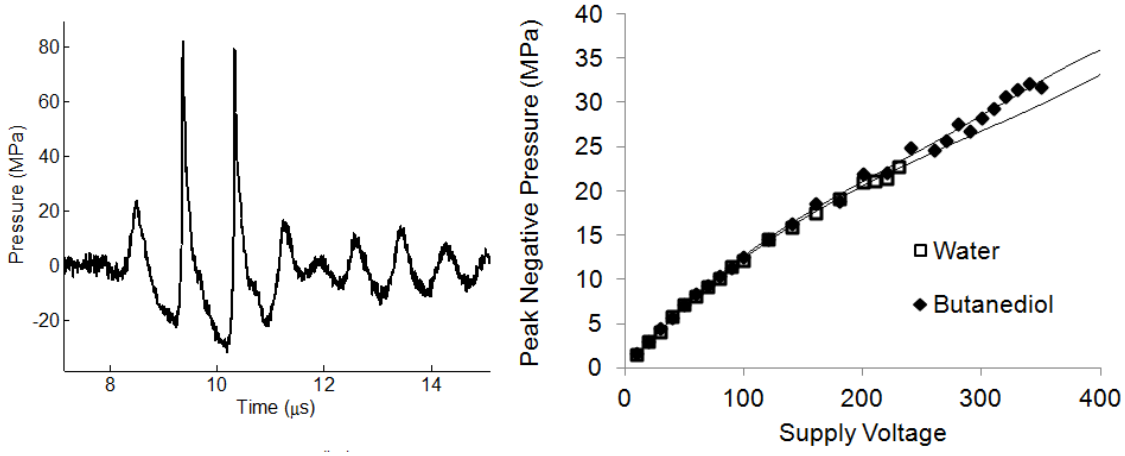

Figure 7.21. (Left) Focal pressure waveform recorded by FOPH at 80% drive voltage. (Right) Peak negative focal pressure vs. DC supply voltage. The amplifier can operate at supply voltages up to 400 V. The focal pressure was measured in water up to 220 V and in butanediol up to 350V. The lines give least-squares 5th-order polynomial fit curves to each data set.

7.3.6 Transducer Testing for Histotripsy Thrombolysis

In order to determine the cavitation potential of the constructed transducer, bubble clouds were imaged by high speed photography under different pulse length and pulse repetition frequencies (Figure 7.22). The lowest peak-negative pressure values at which cavitation is observed each pulse was defined as the cavitation cloud threshold for a specific set of acoustic parameters in degassed water. The pressure levels are given in Table 7.5. As either pulse repetition frequency (PRF) or pulse length (PL) are increased, the bubble cloud can be sustained each pulse at a lower pressure level. At the highest power setting, a cavitation cloud is generated at 19.5 MPa peak negative pressure. While this is somewhat higher than other histotripsy transducers, it is expected based on results in Chapter 2 that transducers with high curvature similar to this design will have a greater negative pressure threshold than those with lower curvature because of nonlinear propagation. At the lowest PRF and pulse length, cavitation clouds do not appear consistently until p_- = -30.7 MPa. This is consistent with data from Chapter 3 using this transducer, which indicates that cavitation is generated each pulse only when p_- < -28 MPa.

Thrombolysis was performed with this transducer using the same protocol from Chapter 5 to form and treat blood clots. A PRF of 1 kHz and pulse duration of 5 cycles were used at p_- of 26 MPa. Similar clot fractionation was observed, with a mean erosion rate of 1.22 +/- 0.35 mg/s for n = 10 clots. This rate is comparable to the transducer used in Chapter 5, indicating similar performance for thrombolysis. It is difficult to directly compare the transducers since they have different focal dimensions and require different pressures to achieve cloud cavitation. Further evaluation of the transducer is provided in Chapter 8, where it is tested in an *in-vivo* porcine model.

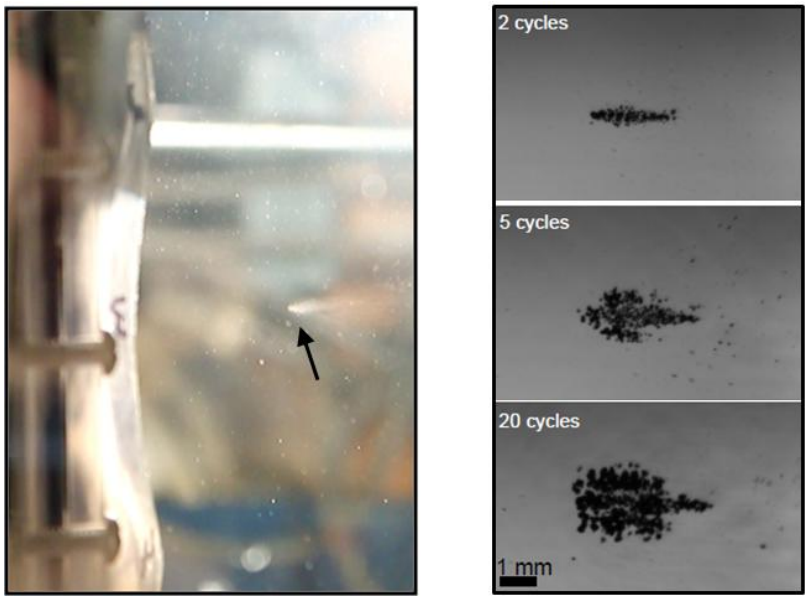

Figure 7.22. A photograph of a bubble cloud (left) indicated by the black arrow as it appears in water. (Right) Three examples of cavitation clouds imaged by high speed backlit photography with different pulse lengths. Note that short pulses produce cavitation in a region similar to the transducer focal pattern, while longer pulse durations produce lesions even outside of the main focus due to shock scattering and grating lobes. These effects are discussed in Chapters 2 and 3.

Table 7.5. Pressure (MPa) above which a cavitation cloud occurs each pulse at different pulse lengths (PL) and pulse repetition frequency (PRF).

		PRF (Hz)			
		1	**10**	**100**	**1000**
PL (cycles)	**2**	30.7	30.7	30.7	24.6
	3	30.7	30.7	26.2	23.9
	5	29.3	29.3	23.2	21.6
	10	29.3	28.5	22.4	20.3
	20	29.3	28.5	22.4	19.5

7.4 Discussion

A methodology for designing and constructing therapy transducers capable of performing histotripsy thrombolysis was developed in this study using additive manufacturing. Several techniques have been explored to construct transducers of single- and multiple-element configurations. At the time of this publication, the histotripsy lab has designed and prototyped more than 30 transducers for various applications in histotripsy including thrombolysis. The most effective strategy was found to use several small elements with matching layers and lens. This design made it possible for the amplifier to drive at high voltage through a voltage transforming network, and prevented mechanical failure of the transducer under high pressure output.

Rapid prototyping of transducers holds several key advantages for developing transducers in a research setting. First, the overall cost and time to produce a prototype is greatly reduced compared with a conventional machining process. Although materials for a rapid prototyping system can be expensive per unit weight, since they are built additively, no material is lost during manufacture. There is also no penalty for introducing additional complexity into the design. For instance, to reduce cost of material, a hollow frame can be adopted with a strut pattern for rigidity. Whereas in machining it is often prudent to reduce cost by requiring as few cuts as possible to finish the piece, in rapid prototyping, complexity has no tradeoff. While this can be to the benefit of the designer, it can also be a pitfall. If such a part is to be mass produced, it may require injection molding or other techniques with more significant geometric limitations. In such a case, some features of the parts may have to be redesigned for these production modes. However, for the purposes of research, where only a few units are typically developed, this is generally not a concern.

The materials in such designs are generally not equivalent in mechanical nature to their cast or extruded counterparts. While some machines, such as FDM, utilize ABS or polycarbonate to produce prototypes, the layering of the materials does not produce parts with the same strength as a solid piece. Furthermore, other machine types, particularly those which use photopolymers, require proprietary formulations which do not particularly match the properties of any conventional material, but they encompass the same range as plastics. Some machines, such as the 3D printer used in this study, can in fact produce composites with continuously variable elastic moduli. Several of these materials were characterized in this study for the purpose of identifying those which would be suitable as acoustic parts. Several materials were found to be suitable, but the material produced by the SLA machine provided the proper combination of low attenuation and high sound speed to produce lens with low loss. The 3D printing system tested in this study, had a step resolution of 16 μm, which could have provided more precise fabrication of matching layers, and will perhaps be utilized for future transducer construction. Further work is needed to accurately characterize materials from other systems which may provide more precise and lower loss acoustic materials for transducers. As the range of materials which can be used by the machines grows, it may become possible to print the ceramic elements, matching layers, and electrodes of the transducer, simplifying the process even further.

In focused ultrasound thermal therapy, the ceramics are generally capable of operating within the required pressure output range needed to cause tissue ablation. However, histotripsy requires focal pressures significantly higher than thermal therapy, and the ceramics in early therapy transducers were stressed to their mechanical limits. Additionally, the necessity of short pulses meant significantly greater bandwidth was needed. The matching layer/lens

combination allowed the transducer to be made with a small aperture and focal gain and still provide sufficient focal pressure. The model demonstrated that the matching layer prevents the buildup of stress due to a strong resonance within the ceramic element when highly mismatched to the load. This allowed the transducers to be driven to nearly 3 times the surface pressure prior to failure. Although this method extended the mechanical limits of the transducer elements, the insulation provided by the lens prevented dissipation of heat in the element at higher driving powers. Even with a duty cycle of 1% at 2000 V_{pp} input, the elements reached nearly 70 ^{o}C after driving for 300 seconds. This causes a change in the sound speed in the ceramic material and a shift in the resonant frequency. As a result, the output is lowered, and the total power into the element is limited until it returns to ambient temperature.

It is worth noting that rapid prototyping technologies have proven invaluable in producing other mechanical components in the lab. Molds for vascular and other tissue phantoms have been produced with the rapid prototyping systems, which can create parts imitating the complex geometry of human anatomy. One adjunct technology is 3D scanning, which allow solid body digital models of physical objects to be recorded. This has been used, for instance, to scan the complex ergonomic shapes of ultrasound imaging probes. The model of the probe can then be used by a rapid prototyping machine to print a holder for the imaging probe which conforms to its surface perfectly. As the technology progresses and a wider number of materials become available for additive manufacturing, the applications for the technology in ultrasound research will also likely grow.

7.5 References

1. Kennedy JE, ter Haar GR, Cranston D. High intensity focused ultrasound: Surgery of the future? Brit. J. Radiol. 2003;76:590-599

2. Rosenschein U, Furman V, Kerner E, Fabian I, Bernheim J, Eshel Y. Ultrasound imaging-guided noninvasive ultrasound thrombolysis : Preclinical results. Circulation. 2000;102:238-245

3. Parsons JE, Cain CA, Abrams GD, Fowlkes JB. Pulsed cavitational ultrasound therapy for controlled tissue homogenization. Ultrasound Med. Biol. 2006;32:115-129

4. Lake AM, Hall TL, Kieran K, Fowlkes JB, Cain CA, Roberts WW. Histotripsy: Minimally invasive technology for prostatic tissue ablation in an in vivo canine model. Urol. 2008;72:682-686

5. Xu Z, Fowlkes JB, Ludomirsky A, Cain CA. Investigation of intensity thresholds for ultrasound tissue erosion. Ultrasound Med. Biol. 2005;31:1673-1682

6. Canney MS, Khokhlova VA, Bessonova OV, Bailey MR, Crum LA. Shock-induced heating and millisecond boiling in gels and tissue due to high intensity focused ultrasound. Ultrasound Med. Biol.2010;36:250-267

7. Arthur HC, Victor YF, Donald EM, Roy WM, Shahram V. An image-guided high intensity focused ultrasound device for uterine fibroids treatment. Med. Phys. 2002;29:2611-2620

8. Hall T, Cain C. A low cost compact 512 channel therapeutic ultrasound system for transcutaneous ultrasound surgery. AIP Conf. Proc. 2006;829:445-449

9. Junho S, Hynynen K. Feasibility of using lateral mode coupling method for a large scale ultrasound phased array for noninvasive transcranial therapy. IEEE Trans Biomed Eng. 2010;57:124-133

10. Clement GT, et al. A hemisphere array for non-invasive ultrasound brain therapy and surgery. Phys. Med. Biol. 2000;45:3707

11. Vaezy S, Shi X, Martin RW, Chi E, Nelson PI, Bailey MR, Crum LA. Real-time visualization of high-intensity focused ultrasound treatment using ultrasound imaging. Ultrasound in Med. Biol. 2001;27:33-42

12. Diederich CJ, Hynynen K. Ultrasound technology for hyperthermia. Ultrasound in Med. Biol. 1999;25:871-887

13. Cain CA, Umemura S. Concentric-ring and sector-vortex phased-array applicators for ultrasound hyperthermia. Microwave Theory and Techniques, IEEE Transactions on. 1986;34:542-551

14. Hall TL, Hempel CR, Sabb BJ, Roberts WW. Acoustic access to the prostate for extracorporeal ultrasound ablation. J. Endourol.;24:1875-1881

15. Yan X, Gu P. A review of rapid prototyping technologies and systems. Computer-Aided Design. 1996;28:307-318

16. Giannatsis J, Dedoussis V. Additive fabrication technologies applied to medicine and health care: A review. Int. J. Adv. Manuf. Tech. 2009;40:116-127

17. Hull CW. Apparatus for production of three-dimensional objects by stereolithography. 1986; US Patent 4575330:16

18. Simonin L, Zissi S, Gonnet JP, Hunsinger JJ, Corbel S, Lougnot DJ. Characterization of heterogeneous structure in a polymer object manufactured by stereolithography with low-frequency microechography. J. Mat. Chem. 1996;6:1595-1599

19. Toda M. Narrowband impedance matching layer for high efficiency thickness mode ultrasonic transducers. Ultrason. Ferroelec. and Freq. Cont., IEEE Trans. 2002;49:299-306

20. Lensing AWA, Prandoni P, Prins MH, Büller HR. Deep-vein thrombosis. *The* Lancet. 1999;353:479-485

21. Maxwell AD, Cain CA, Duryea AP, Yuan L, Gurm HS, Xu Z. Noninvasive thrombolysis using pulsed ultrasound cavitation therapy - histotripsy. Ultrasound Med. Biol. 2009;35:1982-1994

22. Hartmann B. Ultrasonic properties of poly(4-methyl pentene-1). J. Appl. Phys. 1980;51:310-314

23. Acoustic properties of materials: Plastics. 2003; Onda Corporation.

24. Blackstock DT. Fundamentals of physical acoustics. 2000; Wiley.

25. Desilets CS, Fraser JD, Kino GS. The design of efficient broad-band piezoelectric transducers. Sonics and Ultrasonics, IEEE Trans. 1978;25:115-125

26. Souquet J, Defranould P, Desbois J. Design of low-loss wide-band ultrasonic transducers for noninvasive medical application. Sonics and Ultrasonics, IEEE Trans. 1979;26:75-80

27. Gudra T, Opielinski KJ. Influence of acoustic impedance of multilayer acoustic systems on the transfer function of ultrasonic airborne transducers. Ultrasonics. 2002;40:457-463

28. Koivuniemi A, Kovanen PT, Hyvönen MT. Molecular dynamics simulations of a lipovitellin-derived amphiphilic [beta]-sheet homologous to apob-100 [beta]-sheets at a hydrophobic decane-water interface. Biochimica et Biophysica Acta 2008;1784:1668-1675

29. Kim KS, Lee KI, Kim HY, Yoon SW, Hong SH. Dependence of particle volume fraction on sound velocity and attenuation of epdm composites. Ultrasonics. 2007;46:177-183

30. Martin RW, Vaezy S, Proctor A, Myntti T, Lee JBJ, Crum LA. Water-cooled, high-intensity ultrasound surgical applicators with frequency tracking. Ultrason. Ferroelec. and Freq. Cont., IEEE Trans. 2003;50:1305-1317

31. Krimholtz R, Leedom DA, Matthaei GL. New equivalent circuits for elementary piezoelectric transducers. Electron. Lett. 1970;6:398-399

32. van Kervel SJH, Thijssen JM. A calculation scheme for the optimum design of ultrasonic transducers. Ultrasonics. 1983;21:134-140

33. Maréchal P, Levassort F, Tran-Huu-Hue L-P, Lethiecq M. Lens-focused transducer modeling using an extended klm model. Ultrasonics. 2007;46:155-167

34. Hall TL, Hempel CR, Wojno K, Xu Z, Cain CA, Roberts WW. Histotripsy of the prostate: Dose effects in a chronic canine model. Urol. In Press, Corrected Proof

35. Xu Z, Ludomirsky A, Eun LY, Hall TL, Tran BC, Fowlkes JB, Cain CA. Controlled ultrasound tissue erosion. IEEE Trans Ultrason Ferroelectr Freq Control. 2004;51:726-736

36. Kim Y, Wang T-Y, Xu Z, Cain CA. Lesion generation throguh ribs using histotripsy therapy without aberration correction. IEEE Trans Ultrason Ferroelectr Freq Control. 2011;58:2334-2343

37. Parsons JE, Cain CA, Fowlkes JB. Cost-effective assembly of a basic fiber-optic hydrophone for measurement of high-amplitude therapeutic ultrasound fields. J. Acoust. Soc. Am. 2006;119:1432-1440

38. Manes GF, Atzeni C, Susini C. Design of a simplified delay system for ultrasound phased array imaging. IEEE Trans. Sonics and Ultrasonics. 1983;30:350-354

CHAPTER 8

Histotripsy Thrombolysis *In-Vivo*

In this chapter, histotripsy thrombolysis is evaluated *in-vivo* specifically for treatment of deep-vein thrombosis (DVT). A porcine model of acute DVT was developed and treatment of thrombi using histotripsy was performed. The thrombus was visualized and targeted by ultrasound imaging and color Doppler. The histotripsy transducer focus was aligned with the vessel and scanned along the clot during sonication to cause breakdown of the thrombus. Preliminary evaluation of possible tissue and vessel damage was also performed. Finally, the transducers described in Chapter 7 were tested for their improved imaging feedback and ability to perform histotripsy.

8.1 Porcine Thrombosis Model

8.1.1 Animal Preparation

The protocols described in this article have been approved by the University Committee on Use and Care of Animals (UCUCA). Juvenile pigs (mixed breed) weighing between 30-40 kg were used as subjects for the study. The animal was first sedated with 5 mg/kg teletamine + zolazepam (Telazol, Fort Dodge Animal Health, Fort Dodge, IA, USA) and 2.5 mg/kg xylazine (Lloyd Laboratories,

Shenandoah, IA, USA). The subject was then intubated and placed in a supine position. 0.5%-3.5% isoflurane (Vet-One, Meridian, ID, USA) was used as an anesthetic. Subjects did not require mechanical respiration during any of the procedures or treatment. Pulse rate, SpO_2, temperature, and respiration rate were continuously monitored during the procedure. A chemical depilatory (Nair, Church & Dwight Co., Princeton, NJ, USA) was applied to the legs for 10 minutes to ensure complete removal of hair and provide better ultrasound coupling.

8.1.2 Thrombus Formation

Several models for DVT have been developed previously in pigs [1, 2], which have similar vascular anatomy to humans [3]. For this model, acute thrombi were induced by balloon catheter occlusion of a vessel segment and procoagulant infusion. Two 5F wedge occlusion balloon catheters (Arrow International, Reading, PA, USA) with 8 mm diameter balloons were introduced into the femoral vein by percutaneous venous puncture distal from the anticipated site of thrombus formation. Catheters were inserted at two adjacent access sites and positioned with balloon edges separated by 20 mm and the catheter of the proximal balloon within the formation site. Both balloons were inflated to occlude a 20 mm segment of the vessel, and 50 U (0.1 mL) thrombin (Thrombin JMI, King Pharmaceuticals, Bristol, Tennessee, USA) was infused through the distal catheter end-hole into the occluded region between the two balloons to induce thrombus formation. In general, pigs are considered hypercoagulative in comparison with humans and other species [4]. To prevent thrombus formation outside the occluded vessel segment, heparin was administered systemically as a 100 U/kg bolus through an ear-vein catheter immediately after thrombin infusion. This combination allowed clots to preferentially form only in the region

between the balloons. This method proved satisfactory in controlling thrombus length in the vein. Balloons were left inflated for 2 hours after thrombin injection, after which, the deflated catheters were pulled distal to the thrombus but left in the vessel to prevent bleeding. An additional bolus of heparin was delivered every hour during thrombus formation and throughout the remainder of the experiment. Anticoagulation was measured by activated clotting time (ACT) (Hemochron 400, International Technidyne Corporation, Edison, NJ, USA) or activated partial thromboplastin time (APTT). An APTT of > 70 s or ACT > 200 seconds was maintained throughout the procedure.

Ultrasound imaging of the femoral vessels was performed to collect two-dimensional (2D) and color Doppler images of the vessel transverse and long-axis views. Images were captured before and after clot formation using a 10 MHz linear array probe (10L, Logiq 9, GE Healthcare, Fairfield, CT, USA) coupled directly to the skin of the animal.

8.1.3 Thrombus Characterization

Consistent-length clots were formed using the method outlined above in 12 subjects. Without introduction of heparin, clot formation would continue beyond the intended site down the length of the vessel once the balloons were deflated. Additionally, some thrombus would also form on the catheters while balloons were inflated. Heparin was necessary to prevent this action. Using the combined thrombin/heparin approach, thrombi formed in the 12 subjects were 20.1 +/- 6 mm length (mean +/- standard dev.). The diameter of the vein was 5.5 +/- 1.0 mm along the formation site, at a depth of 13-17 mm. In 6 of 12 cases, the clots were occlusive, as indicated by lack of flow through the hyperechoic clotted region on color flow Doppler (Figure 8.1 a,b). In the other 6 cases, the clots were partially occlusive with flow indicated as a narrowed channel through the lumen after the

clot was formed (Figure 8.1 c,d). The vessel occlusion or partial occlusion and thrombus location were identified using ultrasound imaging with the 10 MHz linear array placed on the skin.

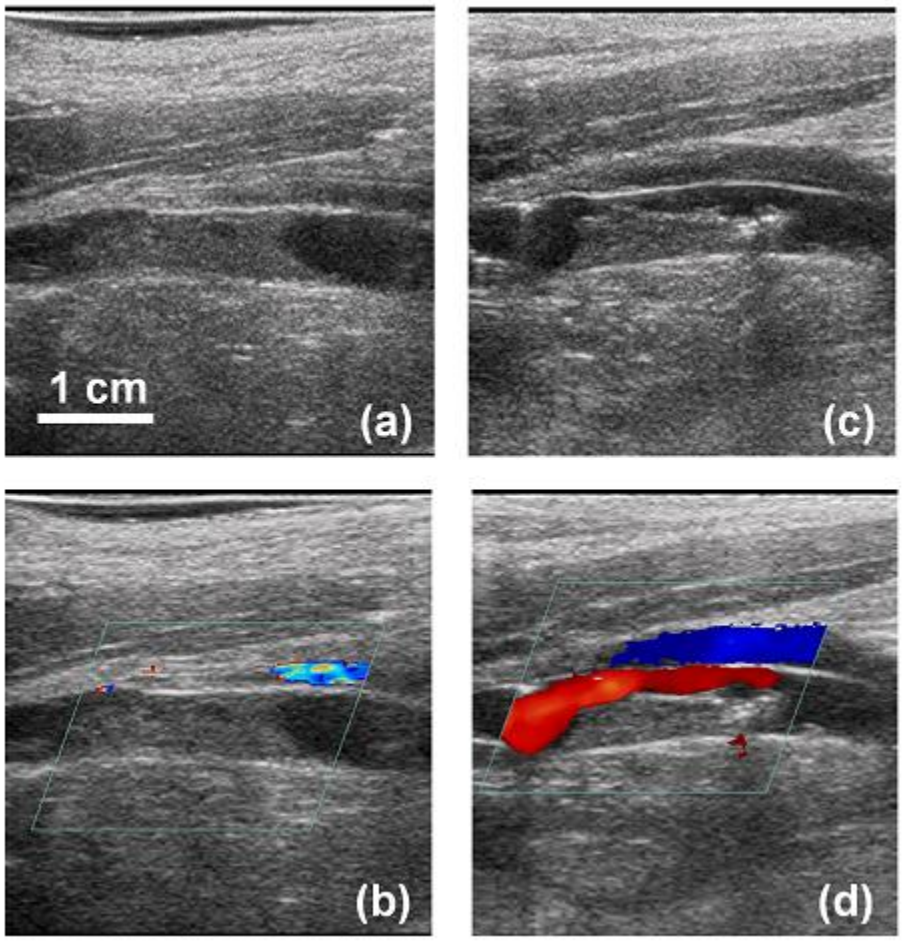

Figure 8.1. Example ultrasound images captured with a 10 MHz linear array probe of fully occlusive thrombus in 2D (a) and color Doppler (b). 2D and color Doppler images of a partially occlusive thrombus are shown in (c) and (d).

8.2 Feasibility Study of Histotripsy Thrombolysis

8.2.1 Therapy Apparatus

A 1-MHz 10-cm diameter spherically-focused transducer with 9 cm focal length (Imasonic, Besancon, France) was held in the water bowl and attached to a computer-controlled 3-axis motorized positioning stage (Parker Hannafin, Rohnert Park, CA, USA). The transducer had a 4 cm concentric hole, through which an 8 MHz phased array ultrasound imaging probe was placed (S8, SONOS 7500, Philips Healthcare, Andover, MA, USA). This imager was used to align the therapy focus with the clot. The transducer was driven by a custom class D amplifier developed in house connected with an FPGA timing board (Altera DE1, Terasic Technologies, Dover, Delaware, USA) to control ultrasound pulsing parameters [5]. The transducer pressure output was calibrated prior to the experiments by a fiber-optic probe hydrophone which recorded pressure level vs. input voltage at the focus in degassed water [6]. The focus is ellipsoidal, with dimensions at the -6dB pressure being 1.9 mm x 1.9 mm x 13.5 mm, the longer dimension being along the axis of ultrasound propagation. This volume defines the region over which the acoustic pressure is greater than half the pressure at the center of the focus.

After clots were formed, a bath of degassed water heated to 40^0C was placed over the legs of the subject. Degassed water (O_2 concentration 40% of saturation level) was used to minimize cavitation or bubble formation in the water, which can reduce ultrasound transmission into the subject. The bath consisted of a stainless steel bowl with a hole cut in the bottom and a transparent polyethylene sheet lining the bowl (Figure 8.2). The polyethylene was coupled to the legs using degassed ultrasound coupling gel (Lithoclear MV, Sonotech Inc.,

Bellingham, WA, USA). The plastic sheet was inspected to ensure that all air bubbles trapped in the gel were removed from the sonication area on the leg.

8.2.2 Pretreatment Planning

Alignment of the transducer focus with the thrombus was performed in three steps, guided by ultrasound imaging. First, the focus of the transducer was located on the ultrasound image by applying histotripsy pulses to an empty water bath. During this procedure, a cavitation cloud appeared at the focus as a bright (hyperechoic), percolating region on the 2D image. Since this cavitation is the primary mechanism of thrombolysis, the temporally changing hyper echoic zone on ultrasound image is used as the indication that histotripsy thrombolysis treatment is progressing normally. The center of the hyperechoic zone was marked as the focal position. Second, the focus was aligned within the vessel proximal to the end of the thrombus, with the therapy ultrasound propagation perpendicular to the vessel. A short (< 1 s) exposure was performed to confirm cavitation in the vessel lumen. Third, a scanning route to move the focal position along the entire length of the thrombus was determined prior to the treatment. The focus was scanned from the proximal end of the thrombus distally along the thrombus by movement of the entire transducer without rotation. At the new positions (spaced ~ 5 mm apart), cavitation was confirmed by short exposure to ensure the cloud position overlapped the thrombus and was contained to the vessel lumen. After confirmation, this position was recorded by the computer. This process of moving, confirming, and recording the target position was repeated until the distal end of the clot was reached. A program was then used to interpolate a path for the transducer through the alignment points (Figure 8.3).

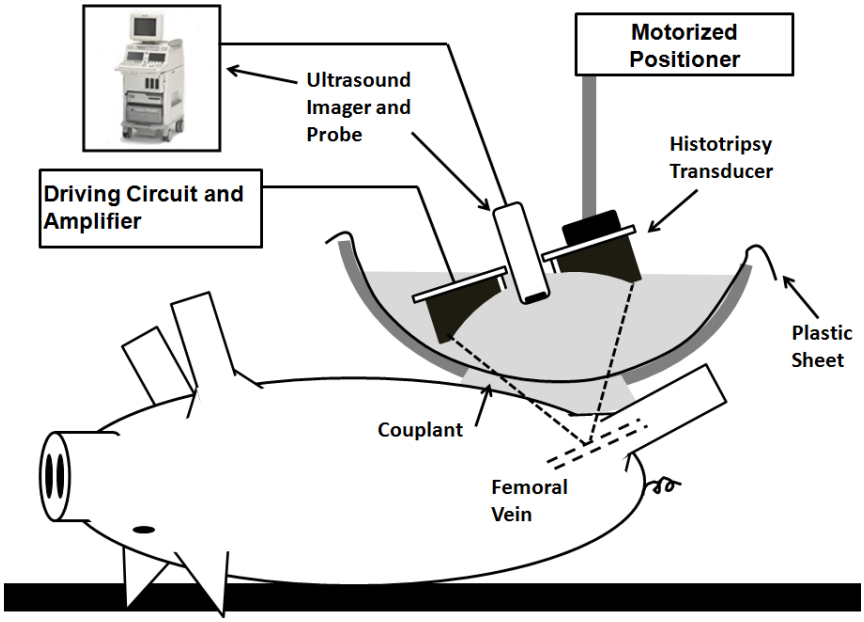

Figure 8.2. Experimental treatment apparatus used for histotripsy thrombolysis. A focused therapy transducer is coupled to the legs by a water bath with an acoustic window of polyethylene at the bottom. The transducer is focused on the femoral vein, guided by a phased array ultrasound imager. A motorized positioner is used to scan along the clot during treatment.

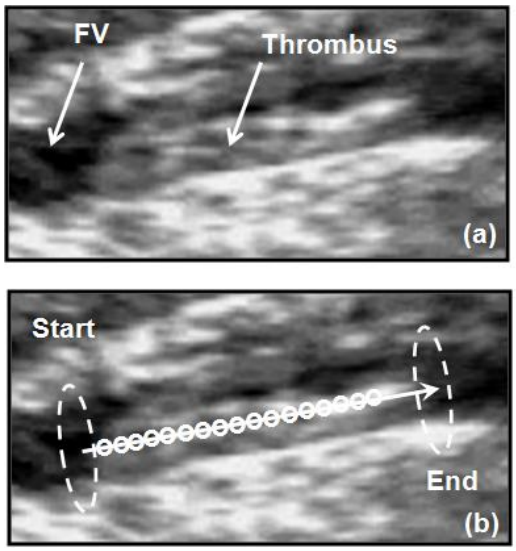

Figure 8.3. (a) Thrombus formed in the femoral vein (FV) of a subject, as visualized by the 8 MHz therapy guidance imager from a distance of approximately 8 cm. (b) A scanning route determined during pretreatment planning, with the approximate focus positions (dashed ellipses) at the start and end of treatment. Each small circle along the path indicates a position of the focus during the treatment.

Upon completion of targeting, therapy pulses were applied to the thrombus following the predetermined scanning route at a set velocity. A velocity of 0.1 mm/s was used, covering 1 cm of the thrombus in 100 seconds. The histotripsy transducer was driven to emit 5 cycle ultrasound pulses at a rate of 1 kHz. The peak negative pressure (the maximum tensile pressure at the focal maximum reached during a pulse) was between 14 - 19 MPa as measured in a water bath (free field). The transducer output necessary to generate a cavitation cloud varied between subjects, likely due to anatomical variation of the overlying tissue. In general, the lowest output level which induced a bubble cloud consistently in the vessel was used for each treatment. The measured range of pressure levels used corresponds with spatial peak pulse average intensity (I_{sppa}) = 9800-21000 W/cm^2 and spatial peak temporal average (I_{spta}) = 49-105 W/cm^2 in water at the focus. I_{sppa} is the average intensity over the duration of a pulse at the focal maximum (acoustic power per unit area), while I_{spta} is the average intensity at the focal maximum averaged over the time during and between pulses. Peak negative pressure and I_{sppa} can be considered measures of potential to generate cavitation, while I_{spta} is a measure of potential for thermal heating from the ultrasound. Because the pulses are only being applied 0.5% of the time, the I_{spta} is much lower than I_{sppa}, and thus heating is minimized. After completion of each scan, the therapy was terminated and the transducer was removed from the water bath. The 10 MHz linear array transducer was applied to image the vein and evaluate echogenicity and flow through the vessel as indications of thrombolysis. If a substantial portion of the thrombus was still visible after treatment, another treatment was applied. For each thrombus treatment, up to 3 additional scans were performed, with the spatial path of the focus modified to target the remaining thrombus in the vein each time.

8.2.3 Post-treatment Protocol

All animals were euthanized within 30 minutes from end of treatment by intravenous delivery of 150 mg/kg sodium thiopental. The femoral bundle and surrounding muscle tissue were extracted from each leg, and rinsed thrice with 0.9% saline. Afterwards, the tissue was placed in 10% formalin solution for fixation. H&E slides were then prepared as cross sections of the femoral bundle and examined by light microscopy for signs of injury. The lungs of several animals were grossly visualized within 5 minutes after euthanasia for indications of injury due to embolic events.

8.2.4 Treatment Outcome

The histotripsy treatment applied was guided by ultrasound imaging using the 8 MHz phased array inserted in the center hole of the therapy transducer, which was 8 cm distance from the thrombus. The thrombus was distinguished in the vessel lumen by an area of increased echogenicity on the therapy guidance imager (Figure 8.4a). The bubble cloud generated at the focus of the therapy transducer was confined to the vessel lumen as it appeared on a 2D image as a dynamic echogenic region on the surface of or within the thrombus (Figure 8.4b,c). As the focus was scanned over the clot following the predetermined route, the treated area underwent a reduction in echogenicity, indicating thrombolysis was occurring in that region[7]. After treatment, the 10 MHz linear array imager was used to confirm the treatment result with higher quality imaging. When echogenicity reduction was observed by the therapy guidance transducer, it was always confirmed by the linear array imager. Usually, the bubble cloud did not occupy the entire width of the vessel, and thus the entire thrombus was not lysed within a single scan of the vein. Under these

circumstances, another scan was performed adjusting the focus to a new position laterally within the vessel and scanning the same longitudinal section.

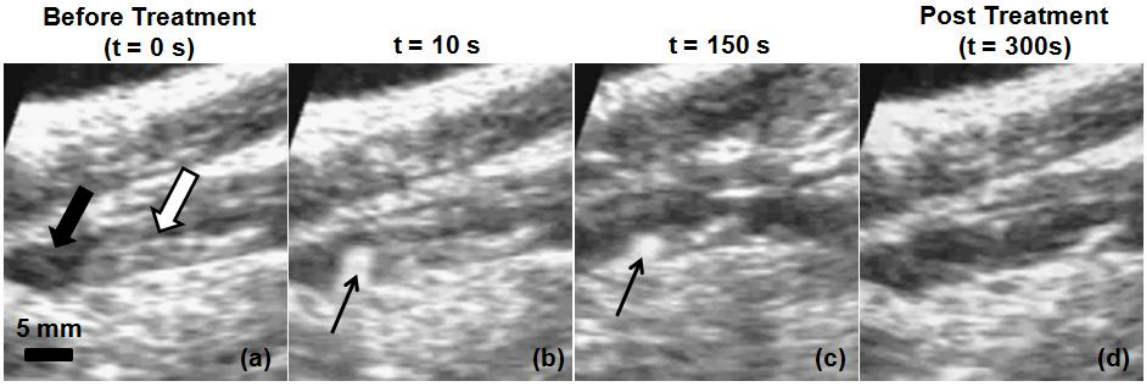

Figure 8.4. Progression of a single treatment scan. (a) The echogenic thrombus (white arrow) is differentiated from the darker empty lumen (black arrow) of the vein prior to treatment. During sonication (b,c), the bubble cloud (small arrows) appears as a dynamic hyperechoic zone on or in the thrombus, indicating the focal position of the transducer. After the 300-second treatment (d), the echogenicity of the thrombus is reduced compared with (a), indicating where the clot has been broken down. Treatment time from start of sonication is listed above each image.

In 10 of 12 cases, the treatment resulted in a reduction in thrombus volume as indicated on 2D ultrasound. In 7 of 12 instances, vessels showed improved signs of flow. For the 6 fully occlusive cases, 4 had flow at least partially restored through the vein according to color Doppler imaging, visualized as creation of a flow channel through the lumen (Figure 8.5). The average flow channel diameter (measured at the narrowest point with color Doppler) was 3.2 +/- 0.5 mm for these cases. For the 6 partially occlusive cases, 3 showed flow improvement as an increase in dimensions of the flow channel in the occluded region (Figure 8.6). The average increase in flow channel diameter was 2.6 +/- 1.0 mm for these treatments. In 2 of 12 cases, no apparent echogenicity reduction or flow improvement was observed. In these two experiments, a bubble cloud could not

be generated in the vessel or thrombus. For all treatments which a bubble cloud was generated in the vessel, at least partial breakdown was achieved. The mean ultrasound exposure time for a treatment was 10.5 +/- 5.5 minutes (range 2.6 to 18.0 minutes). The outcome of 12 treated thrombi is presented in Table 8.1.

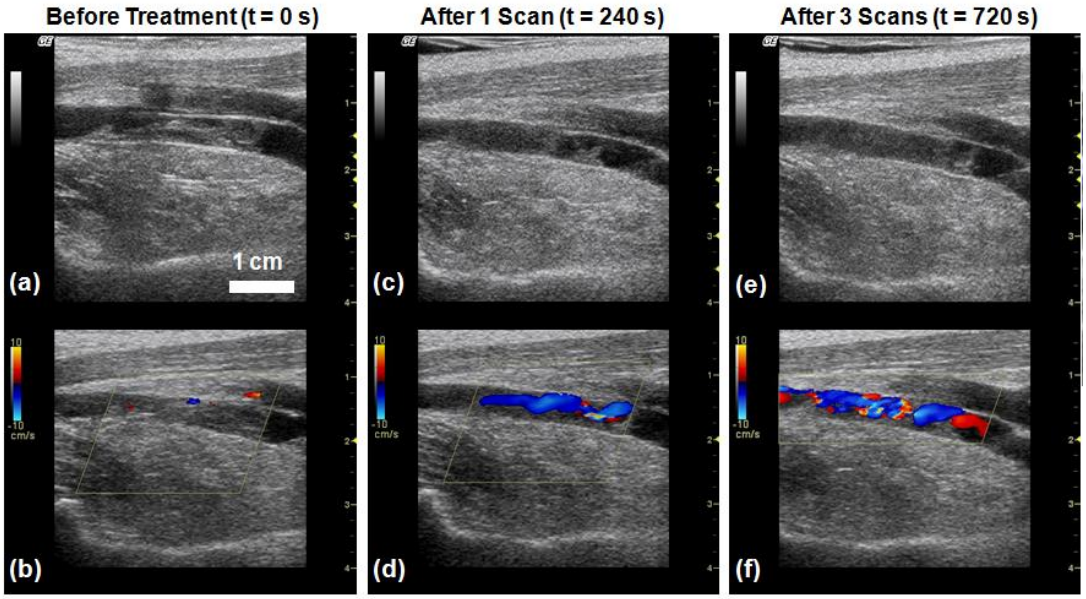

Figure 8.5. Ultrasound images of the femoral vein captured by a linear array imaging probe between treatments of a fully occlusive thrombus. (a) and (b) show the original appearance of the vessel on 2D imaging and with color Doppler. (c) and (d) show the thrombus after 240 seconds of treatment (one scan). (e) and (f) show the final condition of the clot after 720 seconds (three scans). Note the decreased echogenicity in the lumen on (c) and (e) compared with (a). Also, a flow channel is clearly visible on (d) and (f), while none was present before treatment in (b).

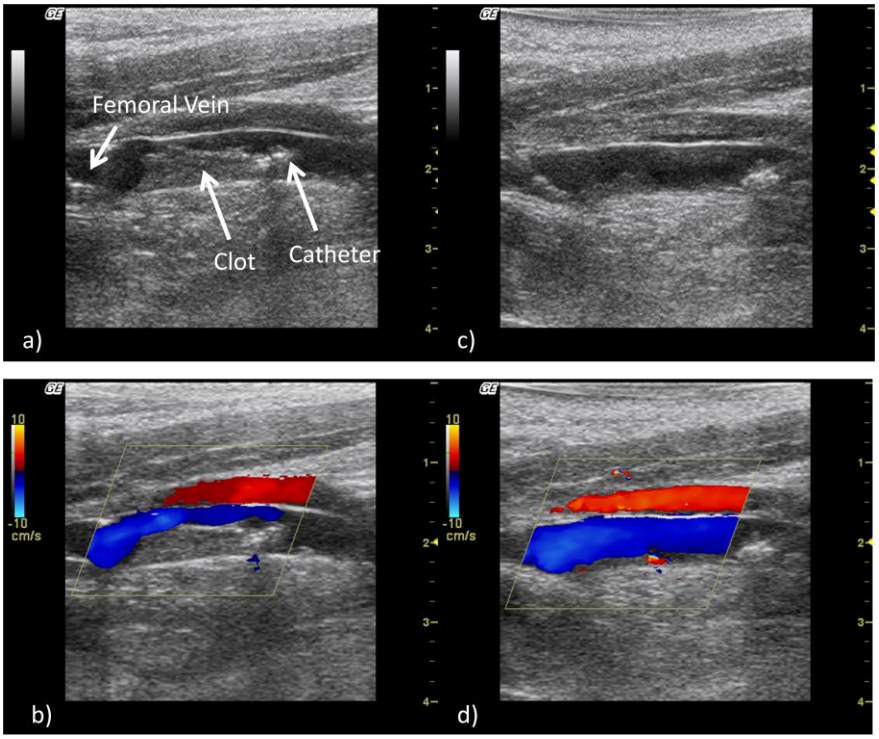

Figure 8.6. Ultrasound images of the femoral vein captured by a linear array imaging probe before and after treatment of a partially occlusive thrombus. (a) and (b) show the original appearance of the vessel on 2D imaging and with color Doppler prior to treatment. (c) and (d) show the appearance after 300 seconds of treatment with 2D imaging and color Doppler.

Table 8.1. Summary of histotripsy therapy outcomes.

	Partial	**Occlusive**	**All**
N	6	6	12
Clot Length (mm)	21.3 +/- 0.41	18.8 +/- 0.6	20.1 +/- 0.6
Vessel Diameter (mm)	5.3 +/- 0.6	5.7 +/- 0.6	5.5 +/- 0.6
Percent Occlusion[†]	75.1 +/- 14.2	100	87.6 +/- 16.2
Treatment Time (s)	615 +/- 283	636 +/- 414	625 +/- 334
Clot Echogencity Decreased	5	5	10
Flow Improved on Doppler	3	4	7
Increase in Channel Diameter (mm)[‡]	2.6 +/- 1.0	3.2 +/- 0.5	3.0 +/- 0.8

[*]Clot length, vessel diameter, percent occlusion, and treatment time are given as (mean +/- standard deviation)

[†] 'Percent Occlusion' is defined as the percentage of the vessel cross sectional area occupied by thrombus before treatment at the section of maximum occlusion.

[‡] Increase in channel diameter lists only the cases where flow improvement was detected on color Doppler.

As an acute study, assessment of vessel damage in the 12 vessels treated with clots was confounded by tissue injury from percutaneous catheter insertion and balloon dilation. Significant hemorrhage was apparent, likely attributed to the thrombus formation process. However, in these cases, no vessel perforations attributed to histotripsy were identified.

Histological samples where clots were formed but not treated showed that catheter insertion and balloon inflation caused damage to the vessel prior to treatment. To evaluate the vessel damage caused by histotripsy alone, vessels without clots were treated. Untreated vessels without clots formed were used as controls. A 15 mm segment of the femoral vessel was treated for 300 seconds using the same ultrasound parameters as those used to treat thrombi with peak negative pressure of 19 MPa, scanning the vessel twice at a rate of 0.1 mm/s.

To more accurately assess the damage incurred due to histotripsy alone, 4 femoral vein segments without formed thrombi were treated, eliminating the factor of catheter-induced damage. These vessels were all intact upon histological examination. In 3 of the 4 subjects, minor zones of hemorrhage were present in the venous adventitia and fat or muscle tissue below the femoral vein (the region overlapping the distal part of the ultrasound focus) (Figure 8.7 a,b,c). Regional denudation of endothelium lining the vein was observed as well. In one specimen, significant intramural hemorrhage was visible in part of the vessel wall and surrounding tissue, although no perforation of the vessel wall occurred (Figure 8.7 d,e,f). During this treatment, some small echogenicities indicating cavitation were observed beneath the vessel in addition to the cavitation cloud in the lumen. The femoral artery did not show signs of damage or endothelial disruption. Thus, damage was confined to the area near the focal zone of the transducer. Control samples (untreated vessels without clots) did not show any

signs of vessel injury or hemorrhage. No macroscopic indications of injury due to embolism were observed in the lungs of 4 of the subjects.

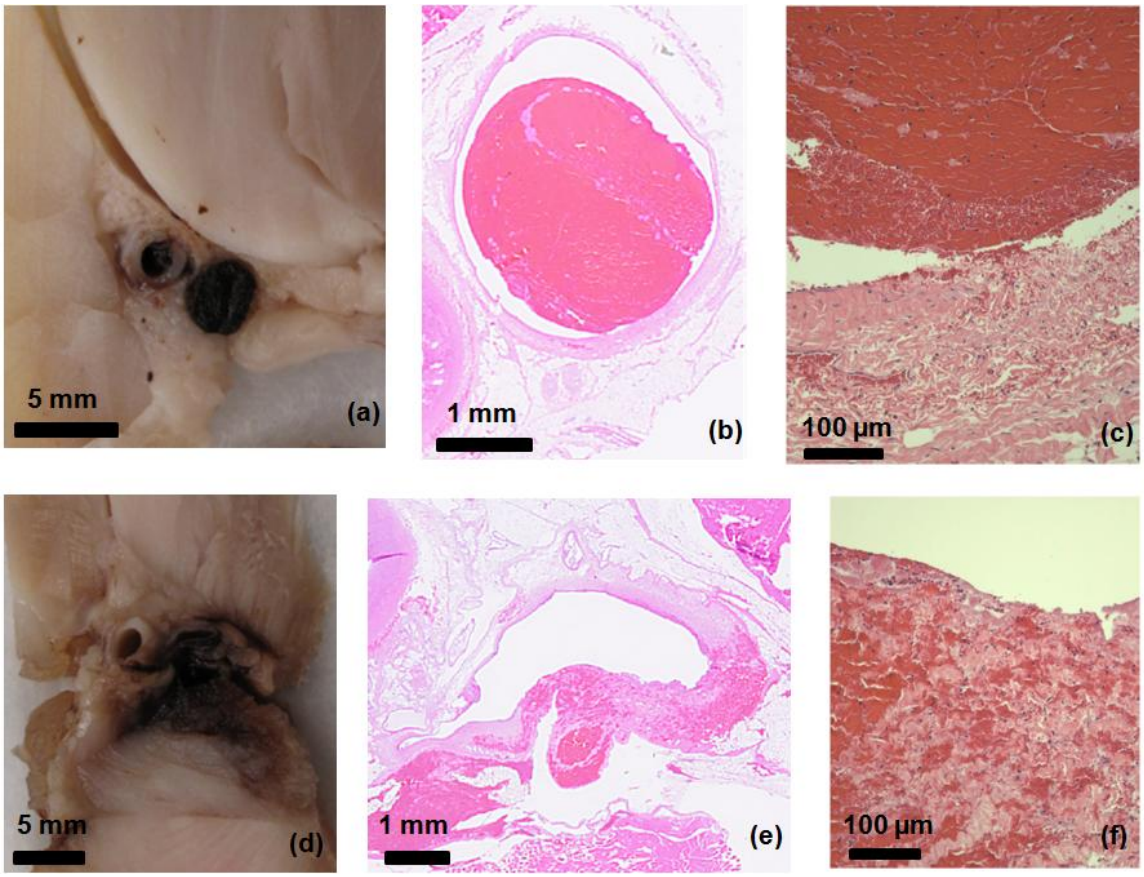

Figure 8.7. Gross images and vessel histology of veins treated by histotripsy. (a) Gross image of femoral bundle showing minimal damage, as seen in 3 of 4 treated vessels. Histology of the vein is shown in (b), with a higher magnification displayed in (c). Minor intramural hemorrhage can be seen within the adventitia. (d) Gross image of femoral bundle shown hemorrhage below the vessel treated by histotripsy. (e) shows histology of the vein, with higher magnification displayed in (f). Greater hemorrhage was present in this specimen and the underlying muscle tissue, although the vessel remained intact.

8.2.5 Discussion

These studies demonstrated the feasibility of employing histotripsy as a noninvasive thrombolytic therapy. The clots formed in the femoral vein could be targeted using a combination of 2D and Doppler ultrasonography. Furthermore, the bubble cloud generated during therapy provided feedback for where thrombolysis was occurring. In most cases, cavitation was confined to the vessel lumen, and the corresponding decrease in echogenicity of the thrombus only occurred in this region. However, the large therapy transducer used in this work placed the therapy guidance imager 8 cm from the target vessel, providing low resolution images of the clot for targeting. Although histotripsy has been previously performed using such large transducers (9 – 15 cm aperture and 9-10 cm focal length) [8, 9], this is unnecessary for treatment of DVT, as the typically afflicted veins lie only 1-3 cm beneath the skin surface [10]. An improved transducer with shorter focal distance would allow imaging to be directly at the skin surface, providing image quality similar to the linear array probe used in this study.

In over 50% of the treatments, histotripsy improved the flow through the vessel. In 83% of cases, a reduction in thrombus volume and burden was observed, indicating homogenization of the treatment zone. In the 2 instances where histotripsy could not successfully treat any part of the thrombus, a bubble cloud could not be generated within the vessel lumen. The likely cause of this phenomenon was air trapped either at the skin surface or within the vessel. During catheterization, air may have entered the insertion site. Air was visible in one of the cases within the vessel, which likely prevented transmission of ultrasound to the clot. In the other case, cavitation formed in the water bath on the plastic bag at the bottom of the bowl, suggesting poor coupling to the animal.

These problems are unrelated to the actual treatment but rather the experimental apparatus chosen here. In all cases where a bubble cloud was initiated in the vessel, at least partial breakdown of the thrombus was achieved. Flow restoration was not always achieved. This failure was in part because of limited resolution of the therapy guidance transducer. In several instances, the full extent of the clot was not clearly delineated, and thus could not be treated. This problem may also be addressed by improved imaging, which will allow high-resolution imaging of the entire clot extent and thus improved accuracy and targeting. This improvement is discussed in the following section.

Vessels which were treated without forming clots contained hemorrhage localized to the area around the treatment zone. While vessel perforation was not observed in any of the treatments, small areas of medial and adventitial damage were present in the part of the vessel where the bubble cloud was seen during imaging. Local pockets of hemorrhage have also been observed in soft tissues such as prostate or kidney treated by histotripsy [11, 12]. The collateral damage was inferred in these cases to be caused by cavitation bubbles. Injury to surrounding tissue during histotripsy thrombolysis may resolve as fibrous growth and scarring, while damage to the vessel wall can cause neointimal growth and reocclusion if severe [13]. In 3 of the 4 cases, the damage to the actual vessel was minimal, during which cavitation was confined to the vessel lumen. In the other case where cavitation was observed outside the vessel, significant damage to surrounding tissue was found. Unfortunately, the focal length of the therapy transducer (13 mm) was nearly double the mean vessel diameter (6 mm). Design of a transducer with smaller focal size is achievable using higher frequency or increasing transducer curvature. Ideally, the focal depth of field should be less than or equal to the vessel diameter. A design with focal depth of field of 6.9 mm is evaluated in Section 8.3. Additionally, choice of acoustic parameters in

histotripsy plays a large role in the size and extent of cavitation clouds generated, as well as the tissue erosion rate [14]. Smaller focal size and higher resolution imaging may improve the precision such that histotripsy could be extended to treat smaller and more tortuous vessels. Despite the range of observed effects, the vessels with minimal injury suggest that the procedure is possible without incurring significant damage.

Other side effects may occur during histotripsy which were not evaluated in this initial study, including risk of embolism and hemolysis. In Chapter 5, the debris generated by clot breakdown was measured [15]. In all cases, > 96% of the clot weight was reduced to particles smaller than 8 μm, with no particles larger than 100 μm found. Upon preliminary gross examination of the lungs in this study, no injury due to embolism was observed. While these results suggest that the debris generated by histotripsy consists of clinically insignificant fragments, a full evaluation of the clot particles generated by the procedure *in vivo* is needed to confirm this assertion. Hemolysis is another effect which warrants investigation, as acoustic cavitation is known to cause lysis of red blood cells in suspension [16, 17]. Elevated potassium levels due to hemolysis can lead to hyperkalemic cardiac arrhythmia [18]. While no signs of arrhythmia were observed during or after treatment in any subjects for the present study, the typical level of hemolysis which occurs during histotripsy should be evaluated.

Acute thrombi formed over 3 hours were treatable in this study, but DVT usually presents itself clinically over longer terms. While DVT begins as a red thrombus, it rapidly organizes to fibrous and then collagenous architecture over days or weeks, with small recanalized channels within the thrombus [19]. As the clot grows older and stiffer, it may be more difficult to induce thrombolysis by histotripsy. The relative proportions of materials that make up the clot (e.g. red blood cells, platelets, fibrous tissue) will also contribute to changes in mechanical

properties and the threshold for generating cavitation. Previous work in histotripsy has shown that materials with higher Young's modulus do not erode as readily as soft tissues normally treated[20]. As mentioned, DVT maturity can be determined through ultrasound 2D echogenicity or elastography [21, 22]. It may be important to identify thrombus age and modify acoustic treatment parameters of histotripsy to effectively treat acute vs. chronic DVTs. Future work will evaluate the ability of histotripsy to treat a range of DVT ages.

8.3 Evaluation of Histotripsy Thrombolysis Prototype Transducers

8.3.1 Methods

Two transducer prototypes were tested in porcine subjects for image feedback quality and therapy transducer efficacy. These transducers are shown in Figures 7.3 and 7.5 of Chapter 7. The first is a larger design, with 18x16 cm aperture, with a center hole for a linear array imager, which can be rotated independently of the therapy transducer 90^{o} to produce either long-axis or cross-sectional images of the vessel. The second transducer (characterized in Chapters 3 and 7) was 8.3 cm x 7.3 cm and contained a fixed central hole for a linear array imager. Pigs were prepared as described in Section 8.1.1, and clots were formed using the minimally invasive catheter-based technique developed during previous experiments. After 2 hours, the balloons were removed and the clot was imaged with ultrasound B-Mode and Doppler imaging (Logiq 9, General Electric Healthcare, Fairfield, CT, USA). A water bath was coupled to the pig's legs with ultrasound gel to provide acoustic coupling for the therapy. The transducer was attached to a 3-axis motorized positioning system. A linear array ultrasound probe was placed through the hole of the transducer to view the therapy plane

for targeting. The transducer was placed in the water bath and the focus was aligned with the vessel. Several points along the clot were chosen as a path for the focus to follow during treatment starting from the proximal end of the clot and ending at the distal end of the clot. Ultrasound pulses were then delivered at each point along the path at 1 kHz PRF and peak negative pressures between 18-30 MPa. The vessel containing the clot was imaged pre- and post- clot formation as well as pre and post treatment using B-mode and Doppler ultrasound.

8.3.2 Results

The larger transducer was tested first, and provided improved B-Mode imaging quality compared with the sector array transducer used in the feasibility study (Figure 8.8a,b). The original system imager had a standoff distance of 8 cm from the target, while the larger prototyped imager standoff was 4.5 cm, and the smaller transducer standoff was about 4 cm. The linear array transducer (10L, Logiq 9, GE Healthcare, Fairfield, CT) provided better image resolution and more distinction between the clot and blood vessel.

The larger transducer was able to generate a cavitation cloud reliably in the femoral vein in $n = 6$ experiments. In 3 of the experiments, clots were not formed in the vessels. In the other 3 experiments, similar clot ablation was observed to that in the preliminary study. However, the larger transducer proved to be cumbersome to maneuver and the range of motion with the focus was limited by its large size and limited aperture of the water bath. This prevented in one case treatment of the entire clot. Thus, while this transducer was capable of performing histotripsy thrombolysis reliably with good imaging quality, it was practically limited by the overall size.

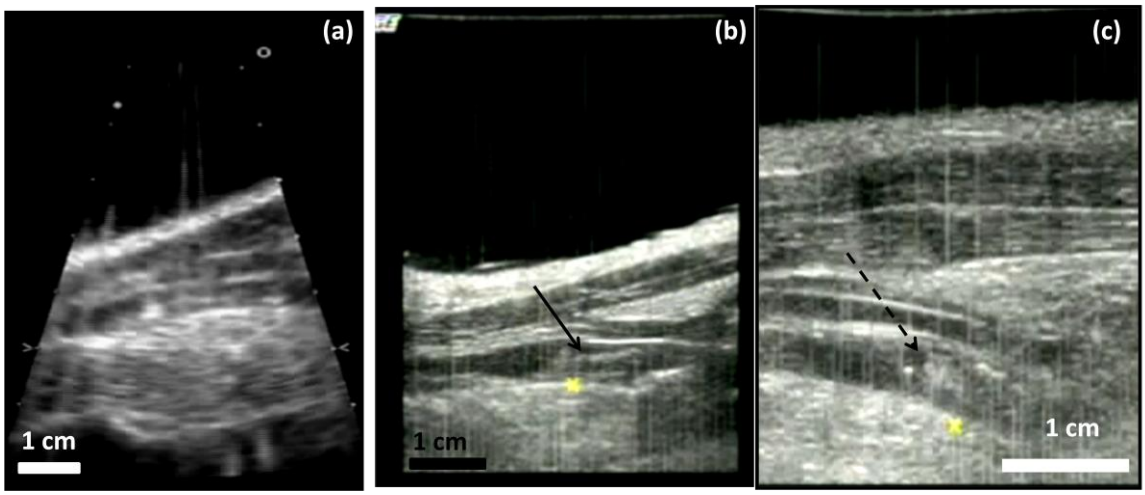

Figure 8.8. (a) Example image produced by the SONOS 7500 imager with S8 phased array probe on the original therapy system. (b) Example B-mode image of the femoral vein with the larger prototype transducer using a 10 MHz linear array for GE Logiq 9 imager. The black arrow indicates a clot formed in the vessel. (c) Image during treatment with the smaller therapy transducer captured with the same 10 MHz linear array. The dashed arrow indicates the bubble cloud in the vessel.

The smaller transducer was tested in 4 pigs, 1 with a clot and 3 without. In the pig with a clot and one without, a cavitation cloud could be generated in the vessel (Figure 8.8c). This transducer often required nearly maximum power output to reliably cavitate, and cavitation was spatially intermittent. Several additional parameter sets were tested in these subjects, but cavitation was often spatially dependant regardless of parameters. While this transducer was more easily maneuvered and allowed the smallest standoff of the imager to the target vessel, the inadequate pressure at the focus was not satisfactory for performing full treatments.

The pressure loss at the focus compared with in a water bath may be due to reflection from the skin surface, attenuation of the tissue, or shadowing of pulse by cavitation in the prefocal region. These effects are still being investigated to potentiate the use of a small footprint transducer for histotripsy thrombolysis.

Although neither transducer proved to be an ideal candidate for histotripsy thrombolysis, continual improvements are being made to the design using rapid prototyping. A future design for a more powerful transducer with the same aperture and focal length as the smaller transducer used in this study will be constructed to optimize its mobility, image quality, and therapeutic capabilities.

8.4 References

1. Lin PH, Chen C, Surowiec SM, Conklin B, Bush RL, Lumsden AB. Evaluation of thrombolysis in a porcine model of chronic deep venous thrombosis: an endovascular model. J Vasc Surg. 2001;33(3):621-627.

2. Katoh M, Haage P, Spuentrup E, Gunther RW, Tacke J. A Porcine Deep Vein Thrombosis Model for Magnetic Resonance-Guided Monitoring of Different Thrombectomy Procedures. Invest Radiol. 2007;42(11):727-731.

3. Hughes HC. Swine in cardiovascular research. Lab Anim Sci. 1986;36(4):348-350.

4. Palsgaard-Van Lue A, Strom H, Lee MH, Jensen AL, Birck MM, Wiinberg B, Kjelgaard-Hansen M, Martinussen T, Kristensen AT. Cellular, hemostatic, and inflammatory parameters of the surgical stress response in pigs undergoing partial pericardectomy via open thoracotomy or thoracoscopy. Surg Endosc. 2007;21(5):785-792.

5. Hall T, Cain C. A Low Cost Compact 512 Channel Therapeutic Ultrasound System For Transcutaneous Ultrasound Surgery. AIP Conf. Proc. 2006;829(1):445-449.

6. Parsons JE, Cain CA, Fowlkes JB. Cost-effective assembly of a basic fiber-optic hydrophone for measurement of high-amplitude therapeutic ultrasound fields. J. Acoust. Soc. Am. 2006;119(3):1432-1440.

7. Hall TL, Fowlkes B, Cain CA. A real-time measure of cavitation induced tissue disruption by ultrasound imaging backscatter reduction. IEEE Trans Ultrason Ferroelectr Freq Control. 2007;54(3):569-575.

8. Xu Z, Fowlkes JB, Rothman ED, Levin AM, Cain CA. Controlled ultrasound tissue erosion: The role of dynamic interaction between insonation and microbubble activity. J. Acoust. Soc. Am. 2005;117(1):424-435.

9. Roberts WW, Hall TL, Ives K, Wolf JJS, Fowlkes JB, Cain CA. Pulsed Cavitational Ultrasound: A Noninvasive Technology for Controlled Tissue Ablation (Histotripsy) in the Rabbit Kidney. J. Urol. 2006;175(2):734-738.

10. Seyahi N, Kahveci A, Altiparmak MR, Serdengecti K, Erek E. Ultrasound imaging findings of femoral veins in patients with renal failure and its impact on vascular access. Nephrol Dial Transplant. 2005;20(9):1864-1867.

11. Hempel CR, Hall TL, Cain CA, Fowlkes JB, Xu Z, Roberts WW. Histotripsy ablation of the prostate: evaluation of histopathology, safety, and tolerability in a chronic canine model. J. Urol. 2009;181(4, Supplement 1):704-704.

12. Hall TL, Kieran K, Ives K, Fowlkes JB, Cain CA, Roberts WW. Histotripsy of rabbit renal tissue in vivo: temporal histologic trends. J Endourol. 2007;21(10):1159-1166.

13. Brody WR, Angeli WW, Kosek JC. Histologic fate of the venous coronary artery bypass in dogs. Am J Pathol. 1972;66(1):111-130.

14. Xu Z, Hall TL, Fowlkes JB, Cain CA. Effects of acoustic parameters on bubble cloud dynamics in ultrasound tissue erosion (histotripsy). J. Acoust. Soc. Am. 2007;122(1):229-236.

15. Maxwell AD, Cain CA, Duryea AP, Yuan L, Gurm HS, Xu Z. Noninvasive Thrombolysis Using Pulsed Ultrasound Cavitation Therapy - Histotripsy. Ultrasound Med. Biol. 2009;35(12):1982-1994.

16. Miller DL, Thomas RM, Williams AR. Mechanisms for hemolysis by ultrasonic cavitation in the rotating exposure system. Ultrasound Med. Biol. 1991;17(2):171-178.

17. Poliachik SLb, Chandler WL, Mourad PD, Bailey MR, Bloch S, Cleveland RO, Kaczkowski P, Keilman G, Porter T, Crum LA. Effect of high-intensity focused ultrasound on whole blood with and without microbubble contrast agent. Ultrasound Med. Biol. 1999;25(6):991-998.

18. DeFronzo RA, Bia M, Smith D. Clinical disorders of hyperkalemia. Annu Rev Med. 1982;33:521-554.

19. Xie H, Kim K, Aglyamov SR, Emelianov SY, Chen X, O'Donnell M, Weitzel WF, Wrobleski SK, Myers DD, Wakefield TW, Rubin JM. Staging deep venous thrombosis using ultrasound elasticity imaging: animal model. Ultrasound Med Biol. 2004;30(10):1385-1396.

20. Cooper M, Zhen X, Rothman ED, Levin AM, Advincula AP, Fowlkes JB, Cain CA. Controlled ultrasound tissue erosion: the effects of tissue type, exposure parameters and the role of dynamic microbubble activity. Ultrasonics Symposium, 2004 IEEE, 2004.

21. Fowlkes JB, Strieter RM, Downing LJ, Brown SL, Saluja A, Salles-Cunha S, Kadell AM, Wrobleski SK, Wakefield TW. Ultrasound echogenicity in experimental venous thrombosis. Ultrasound Med Biol. 1998;24(8):1175-1182.

22. Emelianov SY, Chen X, O'Donnell M, Knipp B, Myers D, Wakefield TW, Rubin JM. Triplex ultrasound: elasticity imaging to age deep venous thrombosis. Ultrasound Med Biol. 2002;28(6):757-767.

CHAPTER 9

Conclusions and Future Work

This work has demonstrated the feasibility of histotripsy thrombolysis and elucidated aspects of the histotripsy mechanism. The described mechanisms of histotripsy will hopefully provide a more solid basis for decisions regarding future design of treatment protocols, therapy transducer systems, and imaging feedback. Future work in histotripsy thrombolysis will evaluate its clinical potential and different applications. This chapter attempts to summarize and connect the findings in the entirety of this work, and provide direction for future experiments which will move histotripsy thrombolysis towards clinical implementation.

9.1 Mechanisms of Histotripsy Thrombolysis

The mechanistic analyses performed in this work used a combined experiment/simulation approach. Observations were made to develop a hypothesis, which could then be tested through simple models, experiments, and additional observations. While cavitation is often a confounding variable in ultrasound therapies and has been considered unpredictable and uncontrollable, the results of the simplified models developed in this thesis and their good agreement with the observations indicates that prediction of cavitation-based

therapy is possible. For instance, the simulation at the end of Chapter 3 shows that one can start with the input voltage to the transducer and estimate the predicted zone of damage at the focus. These results are encouraging and hopefully will stimulate further research into controlling cavitation.

The process of histotripsy can be broken into multiple physical interactions:

1) The electrical system applies a voltage to the focused transducer, which converts this electrical energy into a mechanical wave. 2) This wave propagates from the transducer, through several media, including the couplant and tissue layers, to the focal zone. 3) The wave then interacts with the target tissue to form cavitation bubbles at the focus. 4) These cavitation bubbles cause stress/strain on the tissue which irreversibly break down its structure.

Each of these steps was addressed to some degree in this work. In Chapter 7, transducers and models were developed to predict and control the conversion of amplifier electrical pulses into mechanical waves through the layers of the transducer and into the medium. The modeling was able to accurately predict piezoelectric element behavior, which output short sinusoidal pulses. A linear propagation model was employed to estimate the focusing to the target location. This model did not account for the waveform distortion which is prominent in histotripsy and clearly an important factor of the process. While a full nonlinear acoustics model was beyond the scope of this dissertation, nonlinear models exist which can estimate the full waveform shape at the transducer focus and its geometric pressure distribution[1-3]. Thus, steps 1 and 2 of the process can be well modeled, and it is likely that the pressure field can be almost fully characterized based on knowledge of the transducer geometry and the applied voltage waveform.

Chapters 2 and 3 provided a fairly complete picture of the 3rd step, that is, the interaction of these nonlinear ultrasound pulses with the medium to form

cavitation. In Chapter 2, theory was developed which examined the process of cloud initiation. The pulse at the focus contains multicycle shocked pulses. The negative pressure swings of these pulses expand single cavitation bubbles in the focus, and the shocks scatter from them. This enhances the local negative pressure, exciting many nuclei not cavitated by the incident pulse. In Chapter 3, the actual threshold for these nuclei was determined. This characterization of the nucleation environment tells us how the medium will respond to these pressure pulses. The fundamental limitation here is that the positions of nuclei are stochastic, and we cannot know for sure where each of the weak and strong nuclei reside in the tissue. However, we can statistically estimate the probability of cavitation in different regions at least for very short pulses. Thus, over many pulses, one can estimate the volume in which nuclei will be likely to undergo cavitation. This model, coupled with the bubble dynamics simulation can provide the accumulated cavitated region over a treatment. Finally, Chapter 4 discussed a method for measuring the extent of damage caused to cells in response to this cavitation. By the relationship found that the cells are destroyed in an area similar to the maximum bubble size, the lesion may be similar to the total cavitation area in step 3.

Several additional interactions were not examined in this work. First, while bubble cloud initiation was investigated in detail, how bubble clouds are maintained over many pulses was not. Provided the PRF is sufficiently high, it appears that many of the same cavitation nuclei generated during initiation can be re-expanded with another pulse. If these bubbles dissolve into the medium prior to the next pulse, re-initiation of the cloud would be required. This is known as the memory effect of histotripsy.

Results from the tissue phantom indicate that significant cell death is apparent, even after a single pulse. Why does histotripsy generally require >

1000 pulses to completely fractionate tissue? This question has similarly appeared in lithotripsy research, where tissue damage occurs after a threshold dose (about 1000 shocks) and then increases greatly between 1000-2000 shocks[4]. While RBCs and other cells may be irreversibly destroying even by a single pulse, it is possible that the extracellular matrix remains mostly intact. Another possibility is that bubble expansion is confined in real tissue more severely in the phantom, damaging only sparse regions of the tissue, and that damage must progress by translation of bubbles through a stiff matrix as discussed in Chapter 4. In Chapter 3, it was noted that bubble expansion was suppressed in structures with high viscosity. Unfortunately, the viscoelastic characteristics of tissues at finite strain are nonlinear and not well-characterized. The properties of tissue may also change as damage occurs, with the tissue becoming more compliant and less viscous, allowing greater bubble growth and further propagating damage. Understanding the progression of the lesion formation in tougher tissues may suggest more efficient treatment methods.

9.2 Future Work in Histotripsy Thrombolysis

At this point in time, the feasibility of histotripsy thrombolysis has been established, both *in-vitro* and *in-vivo*. This technology is promising and given the potential implications for its successful development, further investigation is warranted. The following studies were not included in this work, but could provide improvements and more definite evaluation of the applicability of this treatment.

An *in-vitro* study is needed to evaluate if aged clots can be treated similar to fresh clots. Such a study would be particularly relevant to treating chronic DVT, where intimal hyperplasia causes fibrous ingrowth of material during vessel wall

remodeling. Since this material can be as hard or harder than vessel wall material, separate acoustic parameters from those for treating fresh clots may be useful. In these cases, preservation of the original vessel wall is less important, and simple creation of a flow channel is sufficient to relieve symptoms.

Imaging feedback in this work was limited to a combination of B-Mode and Doppler ultrasound, which have been shown to be useful in other histotripsy treatments[5]. While breakdown of the clot causes temporary hypoechogenicity, it was often difficult to distinguish the clot from free static blood, a problem common in other clinical scenarios such as identification of internal bleeding and hematoma[6, 7]. Color Doppler was effective at indicating restoration of flow, but only provides an 'all or nothing' indication of the treatment completion, and thus, it is difficult to determine progress until a flow channel is created. Doppler ultrasound could be used to greatly enhance the image feedback during thrombolysis, and histotripsy in general. First, we have been able to observe a strong color Doppler signal of the bubble cloud when using low PRFs, which provides significantly better contrast than B-Mode imaging, particularly *in-vivo* (Figure 9.1). The translational motion and scattering from bubbles makes them easily detectable by this method. This technique will require synchronization of the ultrasound imaging and therapy at higher PRFS, as the therapy pulses cause massive interference on the image otherwise. Second, in this dissertation it was observed that histotripsy causes high-velocity acoustic streaming in the vessel, and this flow would certainly be detectable by Doppler. By analyzing the regions where acoustic streaming is observed on a color Doppler map, one could differentiate between liquid blood and solid clot. Since liquefaction is the primary desirable treatment outcome, an ultrasonic method for sensing this phase change would be the most direct noninvasive measurement of efficacy of

the treatment. Shear wave imaging and elastography are additional techniques which may help differentiate clot and blood, as well.

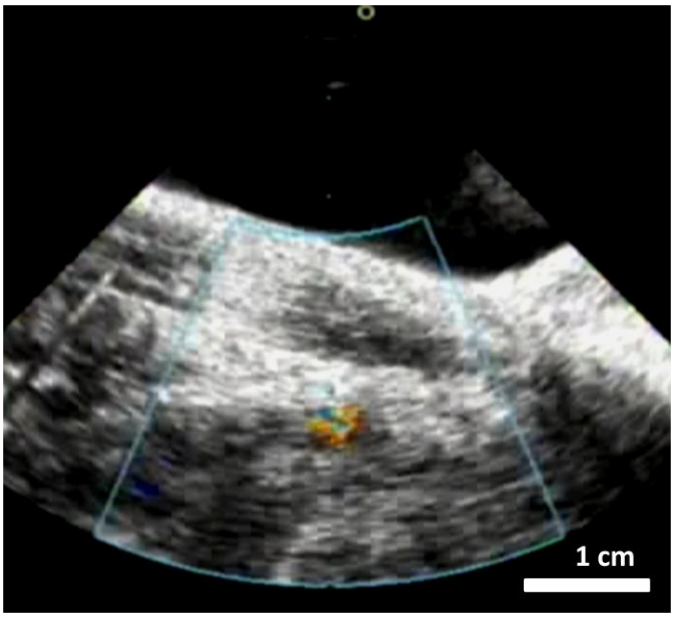

Figure 9.1. Color Doppler ultrasound image during application of therapy at low PRF, with a bubble cloud formed in an occluded femoral vein lumen. A strong Doppler signal is present in the lumen when a bubble cloud is generated, which may provide a more sensitive method of bubble cloud detection.

B-Mode and Doppler image feedback was greatly improved by the integration of ultrasound imaging probes specifically for vascular imaging and shortening the standoff distance to the target. This was accomplished by redesign of the therapy transducer for the thrombolysis application. The rapid prototyping method of transducer design has proved to be a flexible technology for iteratively improving transducers to shape them towards clinical application. While the most recent version of the smaller transducer provided the best imaging quality, it was unreliable in cavitating, possibly because of prefocal cavitation. A next iteration will likely be sufficient in both image quality and power to perform the next *in-vivo* studies of histotripsy thrombolysis, and thus,

further work in therapy transducer design will probably only be necessary for development of different thrombolysis applications. Different applications of thrombolysis will inherently present different acoustic windows between transducer and target, as well as greater motion of the target. The initial application treating DVT was partially chosen because of the open acoustic window and minimal motion of the target. However, histotripsy through the ribs and treatments of heart tissue have demonstrated a remarkable resistance of the procedure to aberration effects[8, 9]. Combined with ongoing research in motion tracking, treatment of portal vein thrombosis, renal artery thrombosis, and potentially myocardial infarction may be possible. Perhaps the application with the greatest challenge is stroke, as treatment through the skull has not been demonstrated, and a great amount of attenuation occurs in transmission into the skull at ultrasonic frequencies. A very high-gain transducer with a lower frequency could potentiate targeted transcranial treatment of stroke. Unfortunately, the tradeoff from use of low frequency is a loss of precision due to the diffraction limit. The results from Chapter 3 indicate that precise lesions may be producible which are much smaller than the -6 dB beamwidth of the transducer using very short pulses. Transcranial treatments will also necessitate exploration of new imaging modalities which could allow precise targeting of the cerebral vasculature. Determination of which treatments could benefit most from histotripsy thrombolysis will require careful evaluation of these potential challenges.

Finally, a chronic assessment of the side effects and long-term outcome of treatment for histotripsy thrombolysis *in-vivo* should be conducted once it is confirmed that the therapy transducer and imaging methods are satisfactory. *In-vivo* testing will provide an assessment of 1) acute and chronic side effects of the treatment, 2) long-term patency of the vessel, and 3) potential problems with the

therapy system, coupling, and imaging which do not arise *in-vitro*. Acute side effects include hemolysis, vascular and soft tissue damage, embolism, and promotion of thrombosis. It was found that histotripsy causes local denudation of the endothelium in almost all treatments, but vessel damage beyond this was generally localized to small regions of intramural hemorrhage but not dissection of the vessel wall or perforation. Hemolysis can lead to renal failure and in extreme cases, cause hyperkalemia which could be life-threatening. However, our acute study *in-vivo* indicated that exposures as long as 30 minutes to occluded vessels did not cause such an effect. Additionally, no significant symptoms associated with embolism have been found acutely, such as lung damage in treating the porcine thrombosis model.

9.3 Conclusions

Histotripsy thrombolysis can potentially treat several important cardiovascular diseases noninvasively. Further work in understanding the mechanisms for histotripsy thrombolysis could potentiate more predictable, controllable and efficient treatments. Exploring the limits of precision and efficacy of this technology will help determine cardiovascular applications where histotripsy will be most beneficial.

9.4 References

1. Kamakura T, Ishiwata T, Matsuda K. Model equation for strongly focused finite-amplitude sound beams. J. Acoust. Soc. Am. 2000;107:3035-3046

2. Tavakkoli J, Cathignol D, Souchon R, Sapozhnikov OA. Modeling of pulsed finite-amplitude focused sound beams in time domain. J. Acoust. Soc. Am. 1998;104:2061-2072

3. Jing Y, Clement GT. On the use of gegenbauer reconstructions for shock wave propagation modeling. J. Acoust. Soc. Am. 2011;130:1115-1124

4. Freund JB, Shukla RK, Evan AP. Shock-induced bubble jetting into a viscous fluid with application to tissue injury in shock-wave lithotripsy. J. Acoust. Soc. Am. 2009;126:2746-2756

5. Hall TL, Fowlkes B, Cain CA. A real-time measure of cavitation induced tissue disruption by ultrasound imaging backscatter reduction. IEEE Trans Ultrason Ferroelectr Freq Control. 2007;54:569-575

6. Zauhar G, Starritt HC, Duck FA. Studies of acoustic streaming in biological fluids with an ultrasound doppler technique. Brit. J. Radiol. 1998;71:297-302

7. Shi X, Martin RW, Vaezy S, Kaczkowski P, Crum LA. Color doppler detection of acoustic streaming in a hematoma model. Ultrasound Med. Biol. 2001;27:1255-1264

8. Owens G, Miller R, Owens S, Swanson S, Ives K, Ensing G, Gordon D, Xu Z. Intermediate-term effects of intracardiac communications created noninvasively by therapeutic ultrasound (histotripsy) in a porcine model. Pediat. Cardiol. 2011:1-7

9. Kim Y, Wang T-Y, Xu Z, Cain CA. Lesion generation throguh ribs using histotripsy therapy without aberration correction. IEEE Trans Ultrason Ferroelectr Freq Cont. 2011;58:2334-2343

APPENDIX

Transducer Element Electrical Model

This appendix pertains to Chapter 7, providing the theory and derivations for the full piezoelectric model utilized for transducer impedance and pressure output estimation. The Krimholtz-Leedom-Matthaei (KLM) model applied here is considered intuitive from a time-domain standpoint, representing the mechanical thickness of the transducer by transmission lines [1]. This formulation is amenable to a transfer matrix approach, where several matrices, each describing an electrical or mechanical part of the transducer, can be multiplied to determine the pressure-voltage transfer function. This method was developed by Van Kervel and Thijssen [2], and has been further developed by Marechal et al. [3] for calculations with a spherically-curved acoustic lens. These works were followed to develop the basic theory for the KLM model. Additionally, models of the amplifier, transducer cable and matching networks were included on the electrical side of the network, and for the acoustic side, equations for elliptical lens were developed to determine the impedance and surface pressure profile.

A.1 Piezoelectric Equivalent Circuit

The electrical circuit equivalent for a piezoelectric element operating in thickness mode is given in Figure A.1. The electrical side consists of a capacitance

equal to the clamped capacitance (C_0) of the element, a reactive element with impedance $-jX_0$, and an electro-mechanical transformer with turn ratio φ:1. The mechanical side is a transmission line with intrinsic sound speed (c_0) and impedance (Z_0) defined by the properties of the piezoelectric material. The transmission line connects to the transformer at its center point. Two terminations are present at the transmission line ends, corresponding to the backing acoustic impedance (Z_1) and load impedance (Z_2). Note that in the case of matching layers or other materials attached to the load face of the transducer, the value of Z_2 is not simply that of the final load medium, but rather is calculated iteratively to include all material layers.

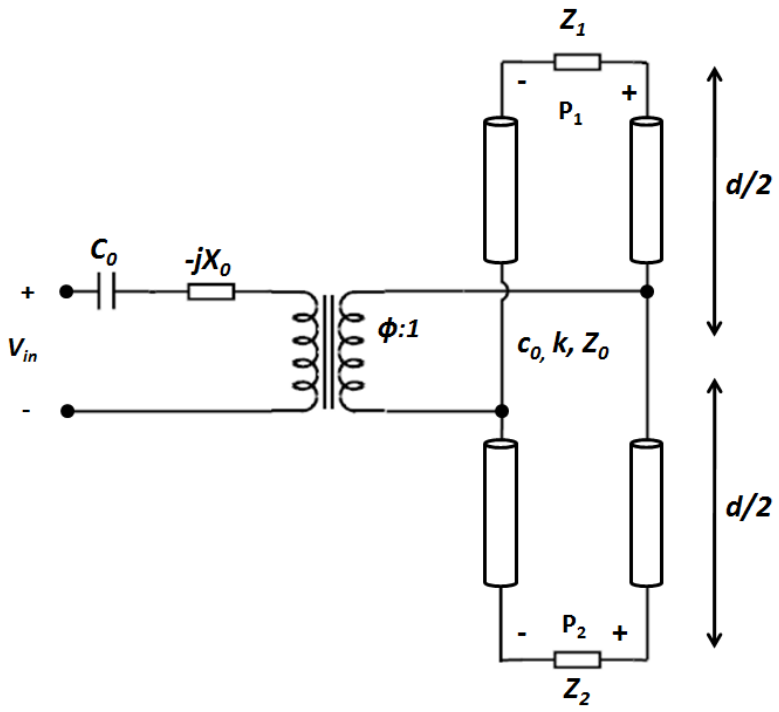

Figure A.1. Piezoelectric model developed by Krimholtz, Leedom, and Matthaei. Voltage is input at the electrical terminal which contains series impedance of a capacitance, transformer, and reactive element. The voltage and current in the transformer are converted to mechanical quantities velocity and force, which are input at the center point of a mechanical transmission line with length equal to the element thickness. Each end of the transmission line is terminated by the acoustic load and backing impedances.

The element capacitance, C_0, is given by $C_0 = \varepsilon_s A/d$, where ε_s is the clamped dielectric constant, A is the element surface area on one side and d is the element thickness. The other electrical components are given by:

$$-jX_0 = \frac{{k_T}^2}{\omega C_0 \mathrm{sinc}(\omega/\omega_0)} \tag{A.1}$$

$$\phi = k_T \sqrt{\frac{\pi}{\omega_0 C_0 Z_0}} \mathrm{sinc}\left(\frac{\omega}{2\omega_0}\right) \tag{A.2}$$

where k_T is the material coupling coefficient, ω is the input frequency, $\omega_0 = \pi c_0/d$ is the characteristic frequency of the element. Van Kerval[2] derives the transfer function for the surface pressure as a function of applied voltage to the electric input with a transfer-matrix method as:

$$\frac{P_2}{V_{in}} = \frac{Z_2}{Z_e N_{11} + N_{12} + (Z_e N_{21} + N_{22}) Z_2} \tag{A.3}$$

where N_{ij} are the matrix elements, and Z_e is the driver impedance attached to the input of the element. To derive the values N_{ij}, the impedance at the back face is first defined as seen by the front face by standard transmission line theory:

$$Z_b = \frac{Z_0 + jZ_1 \tan\left(\frac{\omega d}{2c_0}\right)}{Z_1 + jZ_0 \tan\left(\frac{\omega d}{2c_0}\right)} \tag{A.4}$$

This value is then incorporated to solve the individual transmission coefficients [3]:

$$N_{11} = \frac{1}{\phi}\left(\cos\left(\frac{\omega d}{2c_0}\right) + j \sin\left(\frac{\omega d}{2c_0}\right) Z_b\right) \tag{A.5}$$

$$N_{12} = \frac{1}{\phi Z_0}\left(j\sin\left(\frac{\omega d}{2c_0}\right) + \cos\left(\frac{\omega d}{2c_0}\right) Z_b \right) \quad \text{A.6}$$

$$N_{21} = N_{11} Z_0 \left(1 - {k_T}^2 \operatorname{sinc}\left(\frac{\omega d}{\pi c_0}\right)\right) + j\sin\left(\operatorname{sinc}\left(\frac{\omega d}{2c_0}\right)\right)\phi A Z_0 \quad \text{A.7}$$

$$N_{22} = N_{21} Z_0 \left(1 - {k_T}^2 \operatorname{sinc}\left(\frac{\omega d}{\pi c_0}\right)\right) + \cos\left(\operatorname{sinc}\left(\frac{\omega d}{2c_0}\right)\right)\phi A \quad \text{A.8}$$

At this point, all terms in Eq. A.3 are determined except the load impedance, Z_2 and the electric input impedance, Z_e. However, the problem is simplified by directly calculating the electrical transfer functions between the amplifier and piezoelectric material. Thus, V_{in} is calculated independently from these equations, and $Z_e \rightarrow 0$. This simplifies Eq. A.3 to:

$$\frac{P_2}{V_{in}} = \frac{Z_2}{N_{12} + N_{22} Z_2}, \quad \text{A.9}$$

and the electrical impedance looking into the electrical terminals of the piezoelectric element is [3]:

$$Z_{in} = \frac{Z_2 N_{22} + N_{12}}{N_{11} + Z_2 N_{21}} \quad \text{A.10}$$

To find the load impedance Z_2, an iterative approach is adopted. Starting with the final load impedance, in this case water or tissue, the impedance looking into a layer with thickness t_n and impedance Z_n, by the same transmission line theory as Eq. A.4 [4]:

$$Z_{in,n} = \frac{Z_{in,n+1} + jZ_n \tan\left(\frac{\omega t_n}{c_n}\right)}{Z_n + jZ_{in,n+1} \tan\left(\frac{\omega t_n}{c_n}\right)} \quad \text{A.11}$$

Thus, each layer can be terminated by the layer in front of it, with an equivalent impedance given by Eq. A.11. Each layer is calculated up to the front

face of the piezoelectric material. This allows an arbitrary number of layers to be integrated into the model. Finally, the transfer function from the piezoelectric front face to the final load medium is given by [3]:

$$\frac{P_{load}}{P_2} = \sum_n \frac{Z_{in,n+1}}{Z_{in,n+1}\cos\left(\frac{\omega t_n}{c_n}\right) + jZ_n \sin\left(\frac{\omega t_n}{c_n}\right)} \qquad \text{A.12}$$

Sections A.2 and A.3 are devoted to defining the appropriate electrical values for the voltage gain network, cable, and amplifier. This allows one to calculate V_{in}. Finally, in section A.4, a model for the elliptical acoustic lens and matching layers are developed to calculate the value Z_2 for this variable-thickness layer.

A.2 Cable Equivalent Circuit

The equations for an electrical transmission line (cable) and additional electrical networks were included in the KLM model. Since the frequencies of interest (0.1 – 10 MHz) are low, their wavelengths in the cable (~10 – 1000 m) are long compared with the length of the cable (1-2 m), and the transmission time is therefore negligible. However, the inductance, capacitance, and resistance can contribute significantly to the transducer impedance under certain circumstances. Thus, a short transmission line model is appropriate for these frequencies as a simple RLC circuit, shown in Figure A.2. This circuit is directly coupled to the element input through a solder-joint resistance R_s (incorporated into Z_t) on one side, and connected to the amplifier through an electrical gain network.

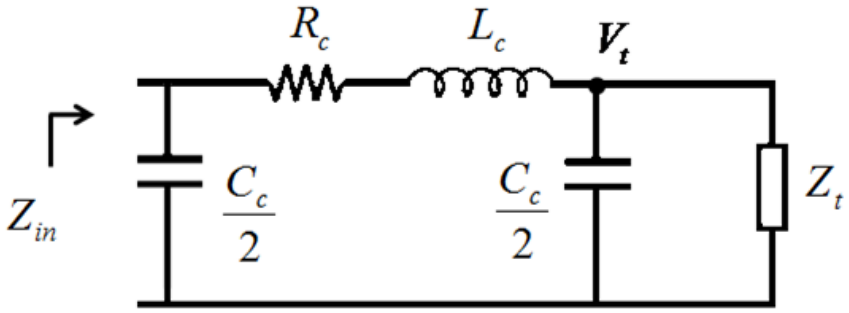

Figure A.2. Lumped parameter model for a short length of cable attached to a transducer element with impedance Z_t. The cable has a capacitance C_c, inductance L_c, and resistance R_c.

The cable half-capacitance $C = C_c/2$ is used for convenience in derivation. To find the input impedance into the transducer from the cable end, the following equations are solved:

$$Z_s = R_c + j\omega L_c + \frac{Z_t}{1 + j\omega C Z_t} \qquad \text{A.13}$$

$$Z_{in} = \frac{Z_s}{1 + j\omega C Z_s} \qquad \text{A.14}$$

Input of Eq. A.13 into Eq. A.14 and solving yields an expression for Z_{in} in terms of R_c, L_c, C_c and Z_t:

$$Z_{in} = \frac{-\omega^2 C L_c Z_t + j\omega\left(C R_c Z_t + L_c\right) + R_c + Z_t}{-j\omega^3 C^2 L_c Z_t - \omega^2 C\left(C R_c Z_t + L_c\right) + j\omega C\left(2Z_t + R_c\right) + 1} \qquad \text{A.15}$$

Assuming the cable resistance is very low, this expression can be reduced to a simplified version:

$$Z_{in} = \frac{-\omega^2 C L_c Z_t + j\omega C + Z_t}{-j\omega^3 C^2 L_c Z_t - \omega^2 C L_c + 2j\omega C Z_t + 1} \qquad \text{A.16}$$

This gives the impedance as seen by the input of the voltage gain network. This electrical network on the input side of the cable consists of an L-bridge inductance and capacitance. This is traditionally called a 'matching network', where the network transforms the load impedance to match the source

impedance. This network is applied in this case instead to transform the voltage to a desired quantity to be applied across the transducer elements.

A.3 Amplifier and Voltage Network

The electrical driving system for applying high voltage to the transducer elements is perhaps the single most important component of the histotripsy apparatus. Without proper design of the electronic driving system, the high instantaneous power necessary to generate extreme focal pressures used in histotripsy would be difficult. Ultrasound thermal therapy transducers are typically driven with RF amplifiers which have a set output impedance of 50 ohms and are meant for continuous output up to a couple thousand watts power. Such a high average power is not required for histotripsy. However, it is necessary to use a very low output impedance driver which can source high instantaneous power. A typical histotripsy transducer may draw 10-20 W of power time-averaged, but with a duty cycle of 0.1 %, 10- 20 kW of power is required during a pulse. The class D amplifier designed previously by Hall [5] has enabled transducers to be driven to these instantaneous limits following proper design. Each amplifier has a low output impedance of < 1 Ω, allowing high peak current output. Furthermore, the boards are low-cost and can be joined in parallel to increase total output capabilities or can be used to individually drive an array of elements. This low impedance driver also allows the transducer to be matched to any impedance within its limits electrically.

One limitation of the class D amplifier is that options for high-voltage transistors for its construction are limited. The present systems are limited to outputting about 400 V. However, as will be demonstrated in the results, transducer elements can be driven beyond 1000 Volts/mm thickness. For the case

of typical piezoceramics, this means for any transducer < 5 MHz frequency, higher voltage can be applied than can be directly supplied by the amplifier. To circumvent this limitation, a voltage gain network is applied to the output of the amplifier. While this is a 'matching network' in the traditional sense, it is more appropriate to view it as a voltage transformer circuit, since the network does not actually match the impedance of the transducer to that of the source amplifier. The following method is utilized to maximize the output from a given transducer

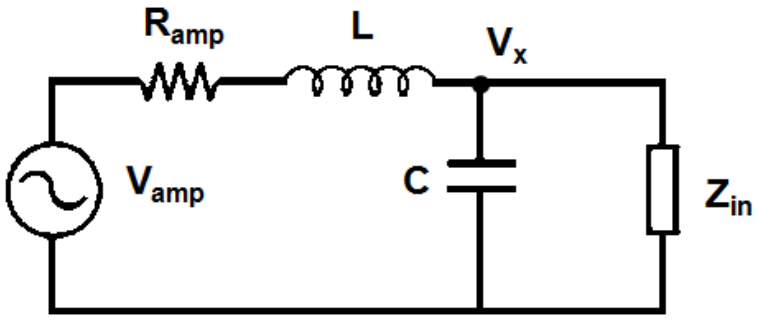

Figure A.3. Schematic of a simplified amplifier source and voltage gain network circuit attached to the combined impedance of the transducer element and cable, Z_{in}.

Each element within the constructed transducer is first measured to obtain the electrical impedance at the operating frequency using an impedance analyzer (VNA 2180, Array Solutions, Sunnyvale, TX). While the class D amplifier has been demonstrated to drive loads < 1 Ω, it is ideal to divide the transducer into small sections with higher impedance and drive these sections separately. This minimizes internal loss in the amplifier and other components due to high current draw. It is recommended to keep the impedance > 10 Ω per amplifier channel. For a typical matching network, it is important to specify the matching impedance. However, the maximum voltage achieved across the element as a

result of the network (the transfer function) is of more interest here. Figure A.3 shows a voltage transformer circuit applied between a transducer and amplifier. Assuming the output resistance of the amplifier is very low, the transfer function for this circuit can be expressed by a simple voltage divider law:

$$\frac{V_x}{V_{amp}} = \frac{Z_C \| Z_t}{Z_C \| Z_t + Z_L} \tag{A.17}$$

Where Z_t, Z_c, and Z_l are transducer, capacitor, and inductor impedance, and Z_t can be expressed as $Z_t = R + jX$. One constraint to the design of the network is that it should increase the voltage by a specified amount, i.e. it should have a set 'gain' value *G*. This means the voltage transfer function defined in Eq. A.17 is set to a given value. One important note is that *G* is complex because the voltage phase at the transducer is not equal to the voltage phase out of the amplifier for a given network. The other constraint is that the inductor impedance cancels the imaginary part of the combination of Z_t and Z_c:

$$G = \frac{V_x}{V_{amp}} = \frac{Z_C \| Z_t}{\mathrm{Re}\left(Z_C \| Z_t\right)} \tag{A.18}$$

$$G = G_0 \exp\left(-j\phi\right) \tag{A.19}$$

By expanding the terms in A.18, an expression for *G* in terms of R, X, and C is given:

$$G = \frac{R + jX\left(1 - \omega CX\right) - j\omega CR^2}{R} \tag{A.20}$$

Given that the real and imaginary parts of *G* are separable, an expression of the magnitude G_0 can be determined:

$$G_0 = \sqrt{1 + \left(\frac{X\left(1 - \omega CX\right) - \omega CR^2}{R}\right)^2} \tag{A.21}$$

Solving for *C* yields:

$$C = \frac{R\sqrt{G_0^{\,2} - 1} + X}{\left(\omega X^{\,2} + \omega R^{2}\right)} \qquad \text{A.22}$$

With the specification of *C* based on the desired voltage gain G_0, one can specify $L = -\operatorname{Im}\left(Z_t \| Z_c\right)/\omega$. These equations hold under the condition that the gain is high enough that the inductor completely cancels the imaginary part of the impedance. Using this method, voltages of over 2000 V peak-peak have been applied to 1 MHz transducers.

A.4 Elliptical lens

A KLM model has been recently developed for a flat element transducer with a spherically-curved acoustic lens for focusing. For the case of strong focusing in histotripsy, however, a spherical lens will introduce focusing aberration. According to geometric optics, a generalized ideal curvature for focusing of a plane wave through the lens is that of an ellipse. In this section, the equations for the acoustic propagation through an axis-symmetric elliptical lens interface are derived to accurately determine the electrical impedance and surface pressure of the transducer, following the method of Marechal[3].

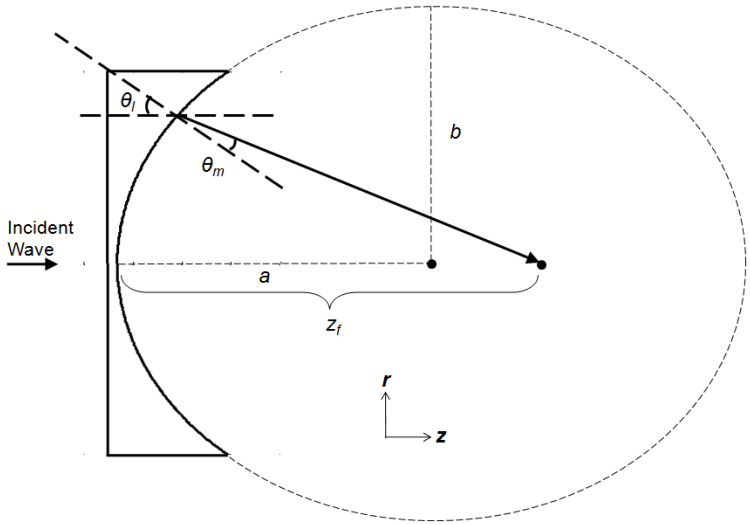

Figure A.4. Coordinate system from the axisymmetric elliptical lens with major and minor axes a and b, respectively. The incident wave propagates to the elliptical surface with an angle θ_l relative the surface normal, and is transmitted into the medium at angle θ_m relative to the surface normal, towards the focus at a distance z_f from the lens surface along the major axis.

For the situation that the sound speed of the lens c_l is faster than the sound speed of the load medium c_m, the surface in contact with the load is concave, and the surface along the element is flat. If one considers the propagation of part of an acoustic wave on the lens/load interface, the pressure transmission coefficient through the interface can be given as:

$$T(r) = \frac{Z_{mi}}{Z_{mi} + Z_{ti}}, \qquad \text{A.23}$$

where Z_{mi} and Z_{li} are the load medium and lens material effective impedance, defined by:

$$Z_{mi} = \frac{Z_m}{\cos(\theta_m)} \qquad Z_{li} = \frac{Z_l}{\cos(\theta_l)} \qquad \text{A.24}$$

In Eq. A.24, Z_m and Z_l are the impedances of the lens and load as described in the previous section. Eq. A.23 holds for a fluid/fluid interface, which does not include the development of shear waves which would occur in a solid medium,

such as the lens. However, Eq. A.23 has been shown to accurately predict the propagation with small error in the case of a polymer lens with propagation into water, as is the case for the designs described here[6]. The incident and refracted angles must be found to determine the transmission coefficient and effective impedances. Once the transmission coefficient is found vs. radial position *r* along the lens surface, the pressure output from each point on the lens can be calculated.

For an ellipsoidal surface with major axis length *a* and minor axes length *b*, the equation for the surface is given by rotation of an ellipse about its major axis:

$$\frac{x^2+y^2}{a^2}+\frac{z^2}{b^2}=\frac{r^2}{a^2}+\frac{z^2}{b^2}=1 \qquad \text{A.25}$$

The elliptic surface has an eccentricity, ε, which defines its relative length of the major and minor axes:

$$\varepsilon=\frac{\sqrt{a^2-b^2}}{a} \qquad \text{A.26}$$

The eccentricity is also related by the ratio of sound speeds between the media: $\varepsilon = c_m/c_l$. For design of a specified transducer with focal length z_f, the *a* and *b* must be chosen such that the parallel acoustic rays at the lens interface refract such that their transmission angle is in the direction of the focus. The focal length is found by [7]:

$$z_f = a+\sqrt{a^2-b^2} \qquad \text{A.27}$$

With the specifications of the eccentricity based on sound velocities and focal length, Eqs. A.26 and A.27 form a two-equation system which can be solved for *a* and *b* in terms of z_f and ε to yield:

$$a=\frac{z_f}{1+\varepsilon} \qquad \text{A.28}$$

$$b = \sqrt{a^2 - \left(z_f - a\right)^2} = z_f \sqrt{\frac{2}{1+\varepsilon} - 1} \qquad \text{A.29}$$

The ellipse is fully specified by Eqs. A.25, A.28, and A.29, and the angles θ_l and θ_m can now be determined. To find these angles, a vector normal to the surface at a given position must be defined. The tangent vector can be found by implicit differentiation of the ellipse Eq. A.25,

$$\frac{\partial}{\partial z}\left(\frac{r^2}{a^2} + \frac{z^2}{b^2}\right) = \frac{\partial}{\partial z}(1) \Leftrightarrow \frac{2r}{a^2}\frac{\partial r}{\partial z} = \frac{2z}{b^2}$$

$$\frac{\partial r}{\partial z} = -\frac{b^2 z}{a^2 r}, \qquad \text{A.30}$$

and the angle of the normal to the surface,

$$\theta_\perp = \tan^{-1}\left(\frac{a^2 r}{b^2 z}\right), \qquad \text{A.31}$$

is given with respect to the +z-axis. Since the incident wave propagates in +z, the propagation is at $\theta_i = 0$, thus $\theta_l = \theta_\perp$. Finally, the refraction of the wave through the lens surface obeys Snell's Law:

$$\frac{\sin(\theta_m)}{c_m} = \frac{\sin(\theta_l)}{c_l} \qquad \text{A.32}$$

After determination of the angles by Eq. A.31 and A.32, these are entered into Eq. A.24 and Eq. A.23 is used to determine the transmission coefficient for each position and the normal surface velocity at the lens.

The KLM model is used to calculate the electrical impedance over the range $r = 0$ to r_{max}, with r_{max} being the outer diameter of the piezoelectric element. The electrical impedance is then found by a parallel summation of the electrical impedance of each ring of the transducer surface with an area $A = 2\pi r dr$. This provides an effective acoustic input impedance into the previous layer (matching layer) for the KLM model to calculate the final electrical impedance[3].

A.5 References

1. Krimholtz R, Leedom DA, Matthaei GL. New equivalent circuits for elementary piezoelectric transducers. Electron Lett. 1970;6:398-399

2. van Kervel SJH, Thijssen JM. A calculation scheme for the optimum design of ultrasonic transducers. Ultrasonics. 1983;21:134-140

3. Maréchal P, Levassort F, Tran-Huu-Hue L-P, Lethiecq M. Lens-focused transducer modeling using an extended klm model. Ultrasonics. 2007;46:155-167

4. Pozar D. Microwave engineering. 2nd Edition; Wiley: 1997.

5. Hall T, Cain C. A low cost compact 512 channel therapeutic ultrasound system for transcutaneous ultrasound surgery. AIP Conf. Proc. 2006;829:445-449

6. Maréchal P, Levassort F, Tran-Huu-Hue L-P, Lethiecq M. Effect of radial displacement of lens on response of focused ultrasonic transducer. Jap. J. Appl.Phys. 2007;46:3077

7. Akiyama M, Kamakura T. Elliptically curved acoustic lens for emitting strongly focused finite-amplitude beams: Application of the spheroidal beam equation model to the theoretical prediction. Acoust. Sci. Tech. 2005;26:279-284